GRAPHENE-DERIVED MATERIALS AS OXYGEN REDUCTION CATALYSTS IN ALKALINE CONDITIONS FOR ENERGY APPLICATIONS

by

MIGUEL ÁNGEL MOLINA GARCÍA

A thesis submitted to the University of Birmingham for the degree of DOCTOR OF PHILOSOPHY

School of Chemical Engineering
University of Birmingham
April 2018

ABSTRACT

Graphene is a relatively new carbon material increasingly finding technological applications due to its unique physical and engineering properties. Here, its application as catalyst for the oxygen reduction reaction (ORR) in alkaline media is investigated.

First, the role of graphene-related materials (including multi-walled carbon nanotubes) as catalyst supports is compared to the widely used carbon black, finding that the ORR follows a mixed behaviour between the direct 4-electron pathway and the indirect 2-step mechanism on graphene-supported platinum catalysts.

Further, different combinations of boron, nitrogen, phosphorus and sulphur metal-free doped-graphene catalysts have been systematically synthesised and evaluated, finding that dual-doped graphene catalysts yield the best ORR performance. Specifically, phosphorus and nitrogen dual-doped graphene (PN-Gr) demonstrates the highest catalytic activity, with 3.5 electrons transferred during the ORR.

Doped-graphene/perovskite oxide hybrid catalysts have been also tested, yielding PN-Gr/$La_{0.8}Sr_{0.2}MnO_3$ the best ORR activity in terms of measured current density, achieving a value that is 85% of that reported for a commercial Pt/C catalyst. Moreover, SN-Gr/$La_{0.8}Sr_{0.2}MnO_3$ produces the lowest amount of peroxide formation with only 10%.

These results confirm the graphene-derived catalysts as promising alternatives to the current platinum-based catalysts, and could enable the important issues related to its practical application to be overcome.

Publications from this work

[1] Molina-García, M. A. and Rees, N. V. *"Metal-free electrocatalysis: quaternary-doped graphene and the alkaline oxygen reduction reaction"*. Applied Catalysis A: General, 2018, 553, 107-116.

[2] Molina-García, M. A. and Rees, N. V. *"Dual-doped graphene/perovskite bifunctional catalysts and the oxygen reduction reaction"*. Electrochemistry Communications, 2017, 84, 65-70.

[3] Molina-García, M. A. and Rees, N. V. *"Effect of catalyst carbon supports on the oxygen reduction reaction in alkaline media: a comparative study"*. RSC Advances, 2016, 6, 94669-94681.

ACKNOWLEDGEMENTS

This work is the result of more than four years of dedication and sacrifice. I would like to sincerely thank all those people and organizations who have made possible this work.

First, I would like to express my inestimable debt of gratitude with my supervisor Dr. Neil V. Rees who trusted me and gave me the opportunity to undertake this PhD. I also deeply thank his cooperation and support to overcome the problems during the experiments. I think that I have been very fortunate to have such a supervisor, who is not just an excellent scientist but also a very nice person. Thanks also to Professor Robert, for rightly leading the group and providing all the support and encouragement for our work.

Furthermore, I would like also to thank my colleagues in the DTC for Fuel Cells and their Fuels. First, I would like to thank to the two colleagues who started the PhD at the same time as I did. Hal for sharing the burden of the long module lessons and exams, and Sophie for those hugs when she met me in the hall or corridors of the faculty, thanks honey! Good luck to both of you with the thesis! Thanks to Carolina, for being such a nice person and excellent investigator. To Kun, for sharing many lunchs and making me laugh a lot when he tried to pronounce my whole name (with both surnames!). To Vikrant, for those technical conversations and double meaning comments. To Bernardo, for those funny jokes and expressions: “electro-cretino!”. To Pete, for the valuable advice in the lab and sharing with me that passion for burritos.

To Alan, for the good moments in conferences and group meetings. To Yaxiang, for sharing late-night sessions in the lab (you are a really hard-worker). To Laura, for sharing my patience with the Scribner Fuel Cell Test system (although we have to thank them the stay in North Carolina…). To Aimee, for sharing the frustration with the XPS sample preparation, I really thank your advice on this. To Lois, for being such a good organizer. To James, for gladdening the office with his sense of humour. To Abby, for her friendliness and being such a nice representative. To Shangfeng, for his valuable advice about lab procedures, especially in catalyst synthesis. To Ahmed, for helping me with technical issues when I required help. To Artur, for providing support with G6 lab instruments. To María, for being a good support in the last stage of my PhD. And very especially, thanks to John Hooper, who always attended me with the best smile in spite of the annoying bureaucratic procedures. You make things easier for everybody of us! And of course, for those people of the group who have helped me in one way or another to finish my PhD but I cannot mention expressly here due to space limitations.

I also thank the EPSRC for providing the financial support that has made this work possible.

Entre todos mis compañeros de trabajo, quiero hacer mención especial a Dani Escalera, mi colega por excelencia durante el doctorado y un apoyo enorme en el laboratorio. Cuántas horas no habré pasado mirando cómo te comes esos guisantes o ese brócoli mientras yo me metía mis burritos entre pecho y espalda. Pero sí, las verduritas son más sanas, muy a mi pesar. También muchas gracias por proporcionarme el RRDE, sin ese aparatillo del demonio mi tesis no existiría. Y por todos tus consejos en el laboratorio y durante la redacción de las publicaciones. Pero sobre todo, por nuestra amistad fuera del laboratorio y por esas fiestas por la Universidad. Me llevo muy buenas experiencias y un gran amigo.

Entre las personas que no han sido compañeros de trabajo pero a las que quiero agradecer especialmente su apoyo durante estos años de doctorado, no quiero dejar de mencionar muy especialmente a la persona que ha estado a mi lado en todo momento durante la elaboración de esta tesis. Ella ha sufrido conmigo, ha tenido una paciencia infinita en los momentos más duros y sobre todo, ha estado siempre ahí para apoyarme cuando pensaba que ya no podia más. Sinceramente, no sé si habría podido acabar este trabajo si no hubiese sido por ti. Desde que te conocí eres una fuente de inspiración para todo lo que hago, y todas las cosas que llevo a cabo tienen más sentido porque tú estás a mi lado. Muchas gracias Patri, nunca sabré agradecerte suficientemente todo lo que haces por mí.

A mis padres, sobre todo y ante todo, por confiar siempre en mí y por apoyarme siempre aunque las cosas fueran difíciles. Sin vuestra educación y sin vuestro ejemplo ni esta tesis, ni nada de lo que tengo existiría. Parece mentira aquel día que entré a la Universidad a matricularme y pensaba “madre mía, dónde me he metido..” y mira por dónde vamos. Aunque estemos lejos, nunca dejo de teneros como referencia para todo lo que hago. Muchas gracias por todo lo que me habéis dado y me seguís dando.

A mi hermana Elena, que siempre ha creído en mis posibilidades (muchas veces incluso más que yo mismo) y por haber crecido conmigo y haber visto cómo me iba formando como persona. Hace poco me ha dado uno de los mayores regalos que me ha dado la vida, ¡nuestro Fran! Es tan listo que con un año ya sabía señalar en la bola del mundo donde vivía su tito, en Birmingham, en Génova… estoy deseando que pegue otro estirón y pueda venir ya solo a visitarme.

Cómo no, a mi “sobrino” Daniel. Una de las personas más íntegras que he conocido en mi vida y un crack que siempre me ha apoyado desde la distancia. Cuánto se echan de menos, compañero, esas noches viendo vídeos en el youtube, haciendo ato en el paseo, echando la postura en el pichi, tirao en la tronera compartiendo temblores, cuántas cositas sobrino… Y por supuesto, la prima Che. Mi prima del alma, que lo primero que me dijo cuando se enteró de que empezaba el doctorado fue: “Primo, pero tú tómate esto en serio eh, no vayas a poner cara de meimportaunamierda”. Seguir tu consejo me ha permitido poder terminar esto.

Desde luego, tengo que hacer mención honorífica al gran Primo Tomás. Gracias por estar siempre ahí para todo y para todos. Perfectamente podría aplicarse a ti esa frase de Nietzsche: “Yo no soy un hombre, soy dinamita”. Sin tu ayuda, tanto material como emocional, no habría podido emprender mi aventura británica. Muchas gracias primo, también por tantas cosas que compartimos y por hacerme partícipe de tus proyectos y alegrías.

Me gustaría también agradecer a todos los miembros de la CERU todos los buenos ratos que hemos pasado juntos. A su actual presidente, el Zelu, por todas esas discusiones políticas y por hacer tan bien la tortuga, y por lo bien que iba vestido de Super Mario. A su antiguo presi, Xavi, con quien tan buenos momentos he pasado también. A Claudia, por enseñarme las cosas tan divertidas que hacen en su trabajo. A Sara, una gaditana-yanki que ahora se nos ha ido a hacer las Américas. A Laura, que se nos fue a hacer las Américas hace ya tiempo. A María, nuestra manchega de Fuentealbilla que tuvo la decencia de dejarme su móvil en Londres cuando más lo necesitaba (¡noche épica!). A Adrián, por aquellos buenos ratos en la embajada y luego después por Londres… ¡Gracias a todos! Sinceramente, creo que hemos contribuido a mejorar la figura del investigador español exiliado.

Y aquí quiero hacer especial mención a Manolo, una de esas personas que merece la pena conocer, con el que no me canso de hablar una vez y otra y otra, de política sobre todo. Cómo echo de menos cuando me dices eso de: “Miguelillo, ¡queeh..!” Te deseo lo mejor en tu andadura londinense, lo de Tailandia no ha podido ser, pero te quiero ver por Génova con tu Mariquilla más pronto que tarde.

En esta última etapa de mi doctorado, quizás la más difícil, quiero agradecer también a esta pequeña familia que me ha acogido con los brazos abiertos en Génova, y que me ha dado todo su apoyo para la terminación de esta tesis y la defensa. ¡Y sobre todo por esa cena sorpresa donde recibí mi merecida banda de Dottore! A Jandra, por tantas conversaciones y aperitivos, y por presentarme a su perro Sucre, al que le mando un “Guau” muy fuerte desde aquí. A Aide, gracias también por tus ánimos mientras preparaba mi defensa y por esas birras en el Kamun. A Ander, un tío auténtico donde los haya, con el que se puede hablar de todo y, desde luego, también beber de todo. A Sion, por ser una de las personas más generosas que conozco, no sabes cómo me han ayudado tus consejos para la defensa y para terminar mi tesis. Y a Viryi, un apoyo excepcional en estos últimos meses. Gracias por animarme a plasmar por escrito mis agradecimientos, desde luego sin ti esta sección sería diez veces más corta. ¡No sabes cómo me voy a alegrar cuando te me hagas doctora dentro de poco! Recuerda, ¡la Doctor, Doctor Party nos está esperando!

Y finalmente, quiero también agradecer a todas las personas que de un modo u otro han hecho possible que haya llegado hasta aquí. Es imposible mencionaros a todos en estas líneas, pero os estaré eternamente agradecido por hacerme cada día mejor persona.

TABLE OF CONTENTS

LIST OF FIGURES

LIST OF TABLES

LIST OF ABBREVIATIONS

AC Alternating Current

AEMFC Anion Exchange Membrane Fuel Cell

AFC Alkaline Fuel Cell

AFM Atomic Force Microscopy

BBCF $Ba_{0.8}Bi_{0.2}Co_{0.6}Fe_{0.4}O_{3-\delta}$

BDS Benzyl Disulphide

BET Brunauer, Emmett and Teller theory

BJH Barrett-Joyner-Halenda method

B-Gr Boron-doped Graphene

BN-Gr Boron-nitrogen dual-doped Graphene

BNS-Gr Boron-nitrogen-sulphur ternary-doped Graphene

BNPS-Gr Boron-nitrogen-phosphorus-sulphur quaternary-doped Graphene

BPS-Gr Boron-phosphorus-sulphur ternary-doped Graphene

BSBCF $Ba_{0.7}Sr_{0.2}$ $Bi_{0.1}Co_{0.6}Fe_{0.4}O_{3-\delta}$

B-V Butler-Volmer

CB Carbon Black

CCD Charge Couple Device

CE Counter Electrode

CFSM $CaFe_{0.7}Si_{0.2}Mn_{0.1}O_{3-\delta}$

CHP Combined Heat and Power

CMTS $CaMn_{0.7}Ti_{0.2}Si_{0.1}O_{3-\delta}$

CV Cyclic Voltammetry

CVD Chemical Vapour Deposition

DFT Density Functional Theory

d_p Particle Diameter

$E_{1/2}$ Half-wave Potential

ECSA Electrochemical Surface Area

EDX Energy Dispersive X-ray Spectroscopy

EG Ethylene Glycol

EIS Electrochemical Impedance Spectroscopy

E_{onset} Onset Potential

FCV Fuel Cell Vehicle

Fe-N-Gr Iron-nitrogen doped-graphene

FTIR Fourier Transform Infra-red Spectroscopy

GC Glassy Carbon

GO Graphene Oxide

GrO Graphite Oxide

HFR High Frequency Resistance

HOMO Highest Occupied Molecular Orbital

HOR Hydrogen Oxidation Reaction

HR-TEM High-resolution Transmission Electron Microscopy

H_{upd} Hydrogen Underpotential Deposition

I_D Disk Current

IPA Isopropyl Alcohol

I_R Ring Current

IR Infra-red

j Measured Current Density

j_K Kinetic-limiting Current Density

j_L Diffusion-limiting Current Density

K-L Koutecky-Levich Equation

L_a Mean Crystallite Size

LSM $La_{0.8}Sr_{0.2}MnO_3$

LSV Linear Sweep Voltammetry

LUMO Lowest Unoccupied Molecular Orbital

MEA Membrane Electrode Assembly

MWAPRP Microwave-assisted Polyol Reduction Process

MWCNT Multi-Walled Carbon Nanotubes

n number of electrons transferred during the electrochemical reaction

N Collection Efficiency

$NaBH_4$-CRP Sodium Borohydride Chemical Reduction Process

NHE Normal Hydrogen Electrode

N-Gr Nitrogen-doped Graphene

ORR Oxygen Reduction Reaction

PEMFC Polymer Exchange Membrane Fuel Cell

P-Gr Phosphorus-doped Graphene

PN-Gr Phosphorus-nitrogen dual-doped Graphene

RDE Rotating Disk Electrode

rds rate determining step

RE Reference Electrode

rGO reduced Graphene Oxide

RHE Reversible Hydrogen Electrode

RRDE Rotating Ring-Disk Electrode

SHE Standard Hydrogen Electrode

SWCNT Single-Walled Carbon Nanotubes

S-Gr Sulphur-doped Graphene

SN-Gr Sulphur-nitrogen dual-doped Graphene

TEM Transmission Electron Microscopy

TGA Thermogravimetric Analysis

TGA	Thermogravimetric Analysis
TPB	Triple Phase Boundary
T_{onset}	Onset Temperature
WE	Working Electrode
XANES	X-ray Absorption Near Edge Spectroscopy
X_{H2O2}	Fraction of Peroxide Intermediate produced in ORR
XPS	X-ray Photoelectron Spectroscopy
XRD	X-ray Diffraction
XRF	X-ray Fluorescence

1 INTRODUCTION

In the present world, there is an increasing energy demand due to the rise of global population and the technology developments. The use of combustion engines for automotive applications involves the depletion of oil reserves and increased carbon dioxide emissions contributing to global warming and raising the levels of environmental pollution.

The issues associated to this situation encourage the development of renewable energy technologies, including conversion and storage devices. Among the new technologies for energy generation, fuel cells are promising electricity generators that convert the chemical energy stored in a fuel into electricity. Supercapacitors and advanced metal-air batteries are technologies that are being also developed for electrical storage. The development of these technologies have triggered the search for new engineering materials that can be applied on this field [1].

One of the advantages of fuel cells is that, when they use hydrogen as fuel, the only by-product generated is water. Due to its low operating temperature and high power density, the polymer exchange membrane fuel cell (PEMFC) has been proposed from among the different types of fuel cells as ideal for automotive applications, as well as portable devices and combined heat and power (CHP) systems [2]. This makes PEMFCs ideal candidates as clean energy technologies. In addition, some other advantages of fuel cells with respect to combustion engines are very high efficiency and unlimited reactant resources. Nevertheless, although PEMFCs have become promising candidates to substitute current combustion engines in the short-medium term for automotive applications [3], there are some problems related to their use which should be overcome.

The oxygen reduction reaction (ORR) is a crucial factor in the development of the fuel cell technology. The present thesis will tackle the development of new catalysts for ORR applications, using as starting point a relatively new material that is being subject of increasing interest: graphene.

1.1 The oxygen reduction reaction and its application to fuel cell technology

The ORR has been one of the most studied topics in electrochemistry. It is a very complex reaction, highly irreversible, involving multiple adsorption/desorption steps and intermediate products. The ORR is a crucial reaction in several of the current renewable energy technologies energy, including conversion and storage devices, such as fuel cells [4].

This section is focused on the application of the ORR to the fuel cell technology. A brief review over the evolution of fuel cell applications along the years is developed, and the fundamentals of one particular type of fuel cell: the PEMFC, is presented.

1.1.1 Brief historical review of fuel cells

Since the theoretical explanation of the working principle of fuel cells by the German chemist Christian Friedrich Schönbein (1839) and its first real demonstration by the Welsh scientist William Robert Grove (1842) the research and development of fuel cells technology have been sluggish and arduous, being always put in the shade of combustion engines [5].

Fuel cells were not considered important in 19th century but became subject of intensive research during the last century. They were first put into practice in Apollo space programs of NASA in the 1960s with magnificent results [6]. In this stage, the use and application of fuel cells were not highly developed yet and the cost of using them was exorbitant. Nevertheless, fuel cells had already certain advantages that made these devices viable for special applications.

In general, fuel cells are successfully applied to very diverse fields: from stationary systems, such as co-generation plants, to portable and transportation devices, such as electric prototype cars, ecological buses or even military planes [7]. Although a detailed explanation about fuel cells applications is beyond the scope of the present study, it would be interesting to have a quick look at one of the most promising applications of fuel cells: fuel cell vehicles (FCV).

General Motors was the first company to use a fuel cell to power the wheels of a vehicle in 1966. The GM Electrovan, as it was called, used a 5 kW fuel cell produced by Union

Carbide, which was fuelled by both super-cooled liquid hydrogen and liquid oxygen, reaching top speeds between 100 and 110 Km/h [8]. In 2002 the Japanese motor company Honda developed a model of fuel cell vehicle, called Honda FCX. The type of fuel cell used was a PEMFC, with a power of 78 kW. The hydrogen was stored into two separate containers behind the rear seat at 350 atm, storing a maximum capacity of 156.6 L. The maximum speed was 150 km/h and the vehicle range was 355 km [9]. In 2011, the German company Audi developed a new hybrid vehicle called Audi Q5 Hybrid Fuel Cell which incorporates a fuel cell. It also contains two 680 atm compressed hydrogen tanks in order to get an extended driving range. The PEMFC is rated at 90 kW and it works in parallel with a 1.3 kWh lithium ion battery pack [10].

More recently, the Toyota Mirai (“future” in Japanese) has become the first mass-produced FCV. It was launched for commercialisation in 2014 in Japan and is being sold in North America from 2015 at a price of 57,000 US dollars [2]. Therefore, fuel cells are increasing its application in automobile field every year and it is expected that they will be predominant in the future. Nevertheless, the high cost of the fuel cell stack due, among other reasons, to the use of a platinum catalyst to boost the electrochemical reaction, is driving the research in alternatives catalysts for fuel cell applications.

1.1.2 Working principle of low-temperature fuel cells

As it has been mentioned previously, fuel cells convert the chemical energy of a fuel into electrical energy. Although several different fuels can be used in the anode side, such as methanol, ethanol or formic acid, in this section hydrogen will be considered as the anode fuel. In the cathode, the reduction of oxygen provides the second reaction needed.

The reactions taking place in a PEMFC are:

$$\text{ANODE:} \quad H_2 \leftrightarrows 2H^+ + 2e^- \qquad (1.1)$$

$$\text{CATHODE:} \quad 2H^+ + \tfrac{1}{2}O_2 + 2e^- \leftrightarrows H_2O \qquad (1.2)$$

$$\text{OVERALL:} \quad H_2 + \tfrac{1}{2}O_2 \leftrightarrows H_2O \qquad (1.3)$$

As shown in Figure 1.1 (left), the protons generated in the anode side move through the polymeric membrane (a sulfonated tetrafluoroethylene-based membrane called Nafion) towards the cathode, while the electrons generated in the anode are conducted through an external circuit producing electricity. Platinum based catalysts are used in both the anode and the cathode to increase the reaction rates. The hydrogen oxidation reaction (HOR) taking place at the anode is extremely fast, and very low Pt loadings are required (as low as 0.05 mg cm^{-2}), whereas the sluggish ORR in the cathode requires much higher loadings (0.4 mg cm^{-2}) [2].

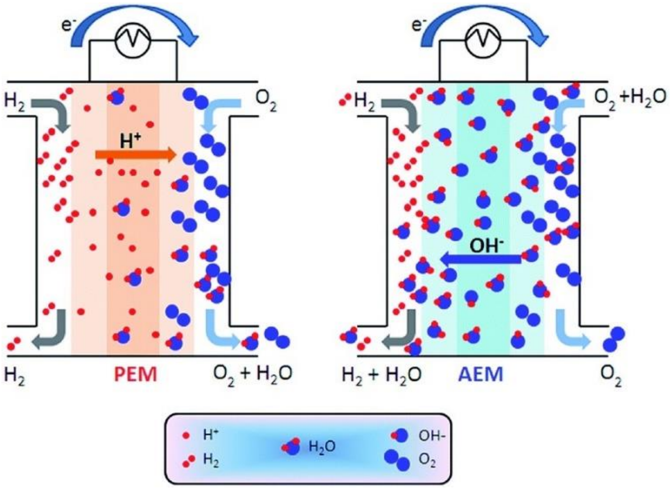

Figure 1.1. *Comparison of a proton exchange membrane fuel cell (left) and an alkaline exchange membrane fuel cell (right) [11].*

As it can be inferred from the catalyst loadings mentioned, the most limiting issue related to expansion of fuel cell market is the sluggish nature of the oxygen reduction taking place in the cathode side. Due to that the double bond of the O_2 molecule is much stronger than the weak single bond of the H_2 molecule, it can be easily understood that the ORR will be much slower than the HOR [12]. This requires the use of a higher amount of Pt catalyst in the cathode with respect to the anode, which increases considerably the cost of the system. In fact, the slow kinetics of the ORR in acidic conditions is one of the main challenges that should be overcome in the fuel cell development [13].

Due to that the ORR kinetics are more rapid in alkaline media than in acid and that the alkaline media provides a less corrosive environment [4], the shift from acid to alkaline media has been proposed. Alkaline fuel cells (AFC) were in fact the first fuel cells put into practice. These first AFC employed a liquid KOH electrolyte, but in these fuel cells the problem of carbonate/bicarbonate precipitation due to a reaction of the ambient CO_2 with the dissociated KOH electrolyte was a very important handicap for its practical application [14]. In order to solve this problem, anion exchange membrane fuel cells (AEMFC) have been developed, being fuel cells very similar to PEMFCs (comparison between the two types is shown in Figure 1.1). Nevertheless, although the overall reaction *1.3* remains the same with respect to PEMFC, the reactions in the anode and the cathode are different [15]:

ANODE: $H_2 + 2OH^- \leftrightarrows 2H_2O + 2e^-$ *(1.4)*

CATHODE: $1/2O_2 + H_2O + 2e^- \rightarrow 2OH^-$ *(1.5)*

The ORR in alkaline media (Reaction *1.5*) has several advantages with respect to the ORR in acid (Reaction *1.2*). First, the standard reduction potential is +0.401 versus the standard hydrogen electrode (SHE) in the alkaline ORR, whereas it is +1.229 V in the acid ORR. This difference in the overpotential has been proposed to be behind the thermodynamic applicability of non-Pt group materials for the ORR in alkaline media [16], including silver, manganese oxides, perovskites and carbon surfaces [17], since only platinum offers the high energy free adsorption of O_2 in acid media.

1.2 Graphene as a novel material for energy applications

Intensive research has been devoted to the development of novel carbon materials, due to its abundance, accessibility and easy processability. Among the carbon materials, graphene has recently attracted great interest due to its unique properties and the possibility of producing different morphological materials using it as the starting point.

The investigation on the field of graphene has undergone an exponential growth since it was isolated from graphite and characterised by Geim and Novoselov in 2004. Among the increasing applications of graphene it can be found long-life batteries, solar cells, display panels and medicinal technologies [18].

1.2.1 Properties of graphene

Graphene consists of a two-dimensional structure where each carbon atom is sp^2 bonded to other three, forming an one atom-thick honeycomb lattice. The main property of graphene is its excellent electrical conductivity, which makes it very suitable for engineering applications. Other characteristics are its extremely high strength and a superb surface area (2630 $m^2\ g^{-1}$) [1]. The importance of graphene research lies in that the present (and future) graphene applications depend on the advances in graphene production, and the different produced graphene qualities should meet each specific requirement. To date, there are around a dozen of methods used for graphene production, leading to a variety of shapes, quality and dimensions [19].

Some characteristics of graphene are close to the theoretically predicted limit: intrinsic strength of 130 GPa, Young modulus of 1 TPa, electron mobility (at room temperature) of $2.5\text{x}10^5$ cm^2 V^{-1} s^{-1} and thermal conductivity above 3000 W mK^{-1}. In addition, it is completely impermeable to any gas, it can withstand extremely high electric currents and can be chemically functionalised [19]. This features are only reported for high-quality graphene obtained by a mechanical exfoliation method [20] and graphene deposited in hexagonal boron nitride substrates [21]. Nevertheless, these methods are not available for mass-scale production yet.

The two-dimensional graphene was first isolated from three-dimensional graphene using a mechanical exfoliation technique, resulting in single- or few-layered graphene. Previously to this discovery, it was thought that two-dimensional structures were thermodynamically unstable, which was a limitation for the development of graphene [22].

It is very difficult to produce high-quality two-dimensional layers of graphene in a scalable fashion. The Van der Waals interactions between two adjacent layers of graphene should be overcome without altering the honeycomb structure in order to obtain a single layer of graphene. The highest quality samples of graphene have been obtained using a top-down method based on mechanical exfoliation. In spite of tremendous efforts with other synthesis methods, up to date the graphene obtained by other ways have not reported the high quality reported for exfoliated graphene yet [22].

1.2.2 From graphite to graphene: the story of a new old material

The history of graphene is inevitably linked to the material which it comes from: graphite. In this regard, graphite has been known and used as mineral for at least 500 years, being used for marking instruments similar to the current pencils. Nevertheless, graphite had been already reported to be used 6000 years ago, when Marican in Europe used it to decorate pottery [23]. More recently, the properties of graphite have driven its use as dry lubricant, heating component and electrodes for industrial furnaces and in carbon fibre reinforced composites, raising the annual demand of graphene to more than 1 million tons worldwide [22].

The history of graphite derivatives driving to graphene began in 1840s. By that date, the German scientist Schafhaeutl synthesised the first graphite intercalation compounds, inserting small molecules, such as alkali metals, between adjacent layers of graphite [24]. The graphite structure remained, but the space between consecutive layers was widened, producing a surprising increase in the electric conductivity of the material and foreseeing some of the future properties of graphene [25].

In 1859, graphite oxide (GrO) was first prepared by the British chemist Brodie using strong nitric and sulphuric acids and oxidants, such as $KClO_3$, leading not only to the intercalation of molecules between graphite layers, but also a chemical functionalisation (oxidation) of its surface. This modification of the surface weakens the interaction between layers, being possible the exfoliation by further thermal or ultrasonic treatment. This method was further modified by Staudenmaier with the addition of the chlorate salt gradually during the chemical reaction [24].

One century later, Boehm et al. achieved to synthesise lamellar carbon by the reduction of GrO with hydrazine, hydrogen sulphide or iron (II) salts in alkaline media. The pioneer experiment of measuring the number of graphene layers was carried out by densitometry, comparing the sample with films of well-known thicknesses using a transmission electron microscopy (TEM), obtaining a value of 4.6 Å (very close to the real value obtained in recent studies) [26]. Although this methodology does not permit to obtain pure graphene (strictly speaking), the procedure of oxidising graphite followed by a reduction to obtain few-layered reduced graphene oxide is still used nowadays. In fact, this is one of the methods proposed in the present study to obtain reduced graphene oxide.

The term “graphene” was proposed by Boehm et al in 1986 [27]. In 1999, a micromechanical method consisting of a lithographic patterning of pyrolytic graphite was combined with oxygen-plasma etching to create a few-layered graphene [28]. Finally, in 2004 Geim and Novoselov used a variation of this method, where pyrolitic graphite was pressed against a silicon wafer substrate and then removed, to obtain a

0.8 nm thick graphene layer confirmed by atomic force microscopy (AFM) measurements [20]. This was the first graphene layer reported ever, completely free from functional groups, and their authors were awarded with the Nobel Prize in 2010 “for ground breaking experiments regarding the two-dimensional material graphene” [23]. Although new methods for graphene production have been developed after this, the micromechanical exfoliation remains as the main method to produce high-quality defect-free graphene [29]. Nevertheless, the scalability of this method does not permit to produce graphene in large quantities [24].

1.3 Aims and objectives of the present work

The main goals stablished for the present study are described below:

- Identification and evaluation of mechanisms for the oxygen reduction reaction on platinum-based catalysts supported on different carbon supports. A comparison between the different catalytic behaviour of several carbon configurations, namely Carbon Black, multi-walled carbon nanotubes, graphene oxide and reduced-graphene oxide, acting as catalyst supports is developed, with especial regard to the catalytic activity and the number of electrons involved in the electrochemical reaction.

- Evaluation of two different methods for Pt deposition on carbon supports in terms of efficiency of deposition and particle size distribution.
- Comparison of two different methods for reduction of graphene oxide in terms of overall oxide reduction efficiency and effect on the individual oxide moieties elimination.
- Composition optimisation of metal-free graphene-based catalysts doped with different heteroatoms *via* a systematic physical and electrochemical characterisation. Single, dual, ternary and quaternary-doped graphene catalysts are evaluated using boron, nitrogen, phosphorus and sulphur as dopant heteroatoms.
- Thorough study of the oxygen reduction performance of metal/doped-graphene hybrid catalysts, being a transition-metal and perovskites the metal components. Several theories are proposed and discussed to explain the different catalytic activities observed, and the optimisation of composition of the best perovskite/doped-graphene hybrid catalyst is carried out.

Through the completion of the objectives described above, a more efficient environmentally-friendly catalyst is expected to be developed for its application in fuel cell systems. Both *ex-situ* and *in-situ* experiments have been carried out to obtain realistic and representative results which permit the application of the optimised catalyst in practical energy applications.

2 THEORETICAL BACKGROUND

In this chapter the fundamentals of the ORR and the graphene-derived materials are described, excluding the description of the experimental procedures that are analysed in the next chapter.

First, the oxygen reduction reaction is described in terms of thermodynamic and kinetic factors, going in depth into the oxygen reduction mechanisms and the application of the theoretical expressions in the electrochemical characterisation.

The structural configuration of graphene will be also extensively reviewed, emphasising the multiple possibilities of graphene for catalytic applications, such as its role as catalyst support, its catalytic properties by itself and the possibility of combining it with different types metals to form hybrid catalysts.

2.1 The oxygen reduction reaction

The ORR takes place in the cathodic electrode of a number of energy conversion technologies. It is a complex, highly irreversible reaction, which includes the formation of many reaction intermediate species (such as, HO_2^-, H_2O_2, O_2^-, O or $OH^•$) in several adsorption/desorption steps [30].

The ORR can take place in alkaline media according to the overall, direct four-electron pathway *2.1* [31]:

$$O_2 + 2H_2O + 4e^- \leftrightarrows 4OH^- \qquad E^0 = +0.401\ V\ vs\ SHE \qquad (2.1)$$

However, the reaction can also proceed stepwise, via the following two-electron processes [4]:

$$O_2 + H_2O + 2e^- \leftrightarrows HO_2^- + OH^- \qquad E^0 = -0.076\ V\ vs\ SHE \qquad (2.2)$$

followed by either further reduction of the peroxide generated:

$$HO_2^- + H_2O + 2e^- \leftrightarrows 3OH^- \qquad E^0 = +0.878\ V\ vs\ SHE \qquad (2.3)$$

or a disproportionation:

$$2\ HO_2^- \leftrightarrows 2\ OH^- + O_2 \qquad (2.4)$$

As it can be seen, the alternative 2-step pathway produces peroxide intermediates. This is a problem in alkaline media, as the lower working potential of the ORR electrode in this environment favours the desorption of HO_2^-, whereas in acidic conditions the high working potential avoids the peroxide desorption thus facilitating the further reduction to OH^- [32]. The ORR takes place mainly through HO_2^- formation at graphite and most carbon surfaces, whereas it follows the 4-electron pathway in Pt catalysts [31]. As a result, in catalytic systems formed by Pt particles deposited on carbon supports it is expected to find a mixed behaviour between the two proposed mechanisms, depending on the behaviour of the carbon support. In order to determine which mechanism is predominant the peroxide intermediate production should be monitored. This can be done with a rotating-ring disk electrode (RRDE), setting the ring potential at the peroxide diffusion-limiting value. This methodology has been successfully proven in former work carried out by Damjanovic and co-workers [33] and then developed by subsequent investigations [34–36]. The application of RRDE to determine the ORR mechanism will be described in detail in Section 3.2.2.

2.1.1 Thermodynamics

Considering the general reaction:

$$O + e^- \leftrightarrows R \qquad (2.5)$$

the maximum work is given by the change in the Gibbs' free energy, which is dependent on the temperature and concentrations of reactants in accordance with the following equation:

$$\Delta G = \Delta G^0 + R\,T \ln \frac{[R]}{[O]} \qquad (2.6)$$

where ΔG is the Gibbs' free energy change, ΔG^0 is the standard Gibbs' free energy change, R is the gas constant (8.314 J K^{-1} mol^{-1}), T is the temperature (in K), and $[R]$ and $[O]$ are the concentrations of reduced and oxidised species, respectively. The Gibbs' free energy can also be expressed as follows:

$$\Delta G = -n\,F\,E \qquad (2.7)$$

where n is the number of electrons transferred, F is the Faraday constant (96485 C mol^{-1}) and E is the reaction potential. Combining Eq. *2.6* and Eq. *2.7* the equilibrium potential of the ORR is obtained, giving the **Nernst equation**:

$$\boldsymbol{E = E^0 - \frac{R\,T}{n\,F} ln \frac{a_{Red}}{a_{Ox}}} \qquad (2.8)$$

where, E^0 is the standard cell potential, and a_{Red} and a_{Ox} are the activities of the oxidised and reduced species, respectively.

Under the conditions of the experiments carried out in the present study, at a temperature of 25 °C and O_2-saturated solution, the potential of the SHE is related to the pH according to the following equation:

$$E_{SHE} = E_{RHE} + 0.059\,pH \qquad (2.9)$$

where E_{RHE} is the potential of the Reversible Hydrogen Electrode (RHE). Therefore, the potential at which the ORR takes place depends on the pH of the aqueous solution. This relationship is shown in Figure 2.1:

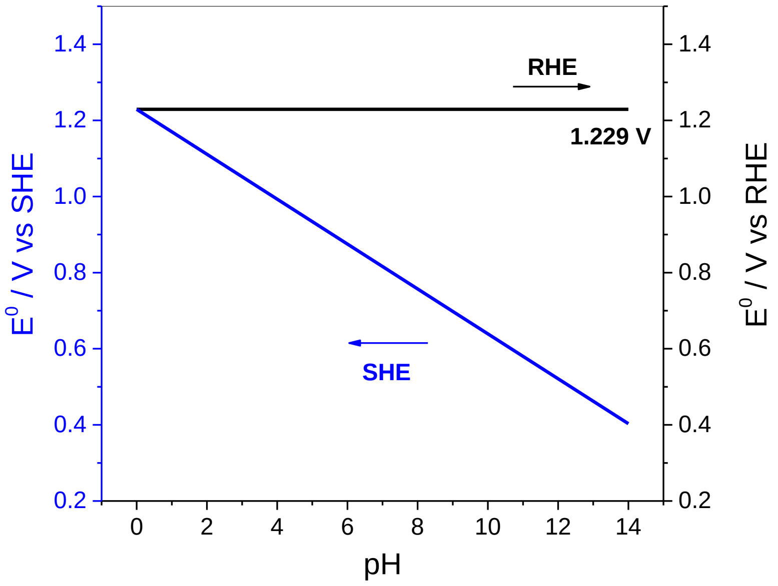

Figure 2.1. *Potential of SHE (blue) and RHE (black) versus pH of solution.*

This permits the calculation of the potential of the ORR at any pH. In the case of the present study, most of the electrochemical measurements are carried out at pH 13.

2.1.2 Electrode kinetics

2.1.2.1 The Butler-Volmer equation

The electrochemical reactions involve the transfer of electrons to or from the electrode to the reactants. The reaction rate directly determines the flow of electrical current, which can be expressed by the reaction rates in anodic and cathodic directions.

$$j_c = j_0\, e^{\frac{-\alpha\, n\, F\, \eta}{R\, T}} \tag{2.10}$$

$$j_a = j_0\, e^{\frac{(1-\alpha)\, n\, F\, \eta}{R\, T}} \tag{2.11}$$

where j is the current density with “c” and “a” referring to “cathodic” and “anodic” respectively, j_0 is the exchange current density, α is the charge transfer coefficient ($0 < \alpha < 1$) and η is the overpotential ($\eta = E - E_{eq}$, where E is the applied potential and E_{eq} is the equilibrium potential).

The net current is obtained by subtracting the anodic current to the cathodic current, to give Eq. *2.13*:

$$j = j_c - j_a \tag{2.12}$$

$$\boldsymbol{j = j_0 \left[e^{\frac{-\alpha\, n\, F\, \eta}{R\, T}} - e^{\frac{(1-\alpha)\, n\, F\, \eta}{R\, T}} \right]} \tag{2.13}$$

This is the **Butler-Volmer (B-V) equation**, which describes the correlation between the overpotential (η) and the current density.

2.1.2.2 The Tafel equation

At highly negative overpotentials (mass transport region), the second term of the B-V equation approaches zero, and the B-V can be simplified to the kinetic component of current density (j_K):

$$j_K = j_0\, e^{\frac{-\alpha\, n\, F\, \eta}{R\, T}} \tag{2.14}$$

$$\ln j_K = \ln j_0 - \frac{\alpha\, n\, F\, \eta}{R\, T} \tag{2.15}$$

$$\log j_K = \log j_0 - \frac{\alpha\, n\, F\, \eta}{2.303\, R\, T} \tag{2.16}$$

$$\eta = \frac{2.303\, R\, T}{\alpha\, n\, F} \log j_0 - \frac{2.303\, R\, T}{\alpha\, n\, F} \log j_K \tag{2.17}$$

$$\boldsymbol{\eta = a - b \log j_K} \qquad (2.18)$$

where:

$$a = \frac{2.303\, R\, T}{\alpha\, n\, F} \log j_0 \qquad (2.19)$$

$$b = \frac{2.303\, R\, T}{\alpha\, n\, F} \qquad (2.20)$$

Eq *2.18* is known as **Tafel equation**. If the overpotential (η) is plotted versus log j_K is obtained a straight line, where the values of exchange current density j_0 and the electrons transferred in the reaction n can be calculated from the intercept (a) and the slope ($-b$), respectively.

The values of j_K can be calculated from the measured values of current density j (see Appendix 1 for detailed obtention of j_k from j):

$$\boldsymbol{j_K = \frac{j\, j_L}{j_L - j}} \qquad (2.21)$$

where j_L is the limited current density and j_K is the component of the measured current that should be plotted in the abscisa axis to obtain the Tafel plot.

2.1.2.3 The Tafel slope and the rate determining step

As it was explained previously, the Tafel equation permits to calculate the value of n from the slope of the straight line. However, the slope of the Tafel plot can also provide valuable information by itself. In particular, the Tafel slope has been stated to be closely linked to the ORR mechanism, and more precisely it can be used to determine the rate determining step (rds). Although several mechanisms have been proposed to describe the ORR [17,37], in the present study the following steps are considered [38,39]:

$$M + O_2 \leftrightarrows MO_2 \qquad (2.22)$$

$$MO_2 + e^- \leftrightarrows MO_2^- \qquad (2.23)$$

$$MO_2^- + H_2O \leftrightarrows MO_2H + OH^- \qquad (2.24)$$

$$MO_2H + e^- \leftrightarrows MO + OH^- \quad or \quad MO_2H + e^- \leftrightarrows MOOH^- \qquad (2.25)$$

where *M* is an empty site on the surface.

When Reaction *2.23*, related to the *MOO^-* formation, determines the overall reaction rate, Figure 2.2 represents the behaviour of the Tafel plot and the Tafel slope value is 120 mV dec^{-1}.

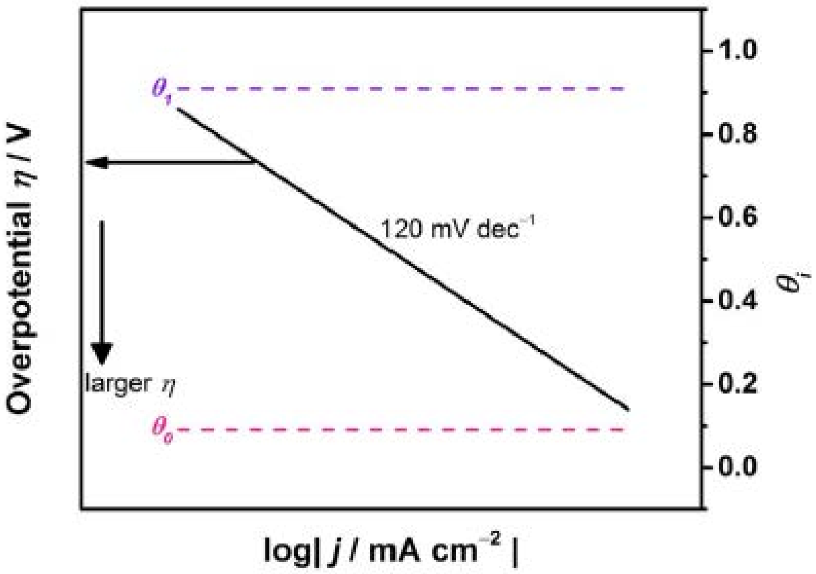

Figure 2.2. *Simulated behaviour of the Tafel relation for the oxygen reduction reaction assuming Reaction 2.23 as the rate determining step [38].*

When Reaction *2.24*, which is not an electron-transfer reaction, determines the overall reaction rate, Figure 2.3 represents the overpotential-current relationship and the Tafel slope value is 60 mV dec^{-1}.

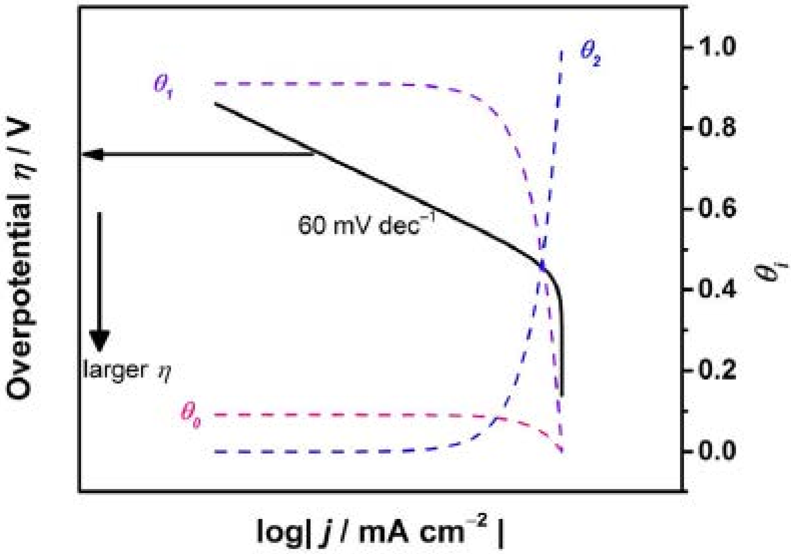

Figure 2.3. *Simulated behaviour of the Tafel relation for the oxygen reduction reaction assuming Reaction 2.24 as the rate determining step [38].*

When Reaction *2.25* determines the overall reaction rate, Figure 2.4 represents the behaviour of the Tafel plot and the Tafel slope value is 40 mV dec^{-1} at lower overpotentials and 120 mV dec^{-1} at higher overpotentials.

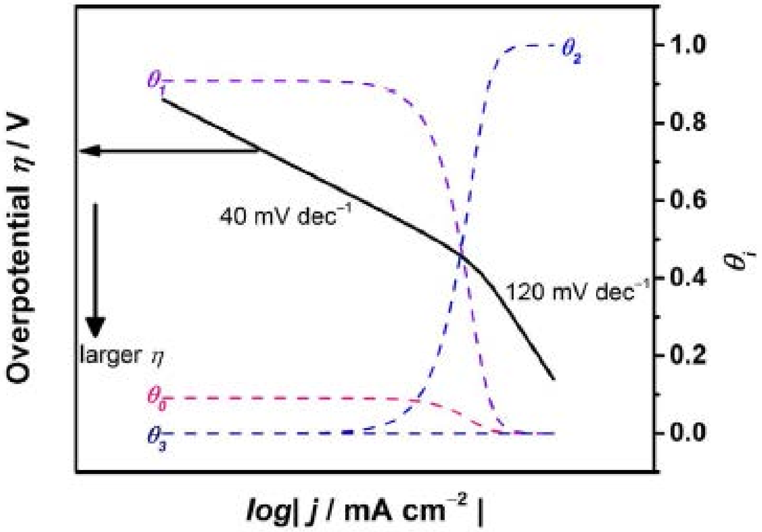

Figure 2.4. *Simulated behaviour of the Tafel relation for the oxygen reduction reaction assuming Reaction 2.25 as the rate determining step [38].*

In conclusion, the Tafel slope is 120 mV dec^{-1} when the rds is the first discharge step, whereas in the rest of the cases the Tafel slope is always lower than 120 mV dec^{-1}. This information permits to establish the mechanism by which the ORR takes place for each individual catalyst. The ORR mechanism is highly sensitive to the catalyst used and the pH of the O_2-saturated solution. Under alkaline conditions, the Tafel slope reported in the low overpotential region for a Pt catalyst is approximately 60 mV dec^{-1} in a 0.1 M KOH solution [40], which increases to 200-490 mV dec^{-1} at higher overpotentials. Under acidic conditions, a bare Pt disk shows a two-step Tafel slope: 60 mV dec^{-1} at low overpotential that increases to 120 mV dec^{-1} at higher overpotentials [41]. In addition, an ORR active carbon material consisting of pyrolytic graphite has reported a Tafel slope of 110 mV dec^{-1} under alkaline conditions [40].

2.2 Graphene as catalyst support

In this section, the use of graphene as carbon support for ORR platinum catalysts is compared with other carbon materials. It is discussed how the carbon support can enhance the catalytic properties of platinum, and how the configuration and morphology of the carbon support can affect the performance of the catalyst.

2.2.1 Platinum as ORR catalyst

For a determining metal to be successful as catalyst, it must adsorb the involved species with sufficient strength to permit the dissociation of the chemical bonds, but not too strong to avoid the release the products once the reaction has took place [42]. This implies an equilibrium predicted by the Sabatier's principle, which describes the ideal interaction between the substrate and the catalyst [43]. This principle is well reflected in the Balandin's volcano plot, where the catalytic activity is plotted versus the adsorption energy. The Balandin's volcano plot for the ORR is shown in Figure 2.5, where it is clearly observed an activity peak at the optimal binding energy. As it can be seen, platinum is the catalyst that is closest to the theoretical activity peak, which explains that platinum is generally recognised as the best metal catalyst currently available for the ORR.

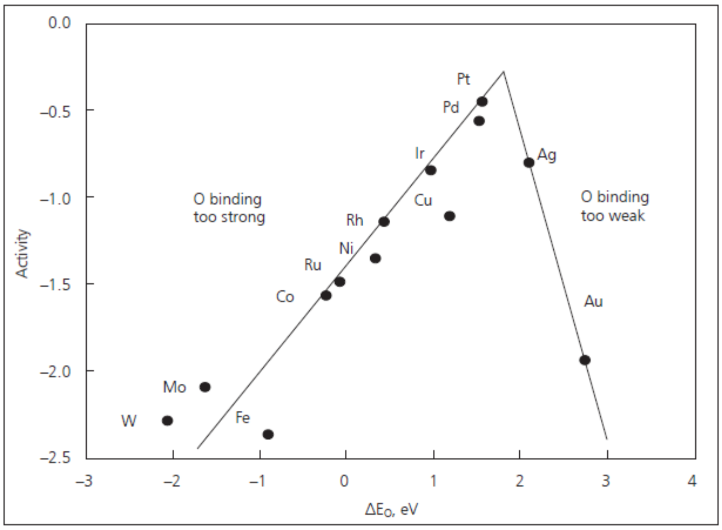

Figure 2.5. *Trends in ORR activity plotted versus the oxygen binding energy. Reprinted with permission from Ref. [44]. Copyright 2018, American Chemical Society.*

In addition, platinum has been traditionally considered the most catalytically active metal towards the oxygen reduction, due to its very high selectivity towards the 4-electron mechanism without peroxide intermediate formation [45]. Moreover, it shows excellent thermodynamic stability, even at very low pH [42].

Nevertheless, there are a number of problems related to the use of Pt catalyst, which limit its application. First, platinum is one of the most expensive and scarce elements on Earth [46]. The current catalyst loadings employed in PEMFCs must be reduced in a factor of at least ten to become economically acceptable [47]. Although intensive research is devoted to reach this goal, the unique possibility to avoid the Pt dependence is to use other less expensive and scarce catalysts to substitute Pt. The problem is that in the highly acidic conditions of PEMFC only noble metal catalyst such as Pt can be used. These Pt nanocatalysts suffer several degradation processes that limit the stability and durability of this catalyst in practical applications. These processes include Ostwald ripening, where the small particles are dissolved and redeposited forming higher agglomerations [48], as well as catalyst loss or particle migration. Moreover, Pt is extremely sensitive to the presence of carbon monoxide, which can poison the Pt catalyst and make it inactive, even at levels as low as 10 ppm [49]. Minute amounts of CO are normally present in the H_2 supplied to the anode due to the process of H_2 production. This CO undergoes a process of chemisorption onto the catalytic sites of Pt particles impeding the H_2 dissociation [50]. Although the presence of a second element, especially Ru, improves the tolerance of the Pt catalyst to CO poisoning, Pt still shows a low tolerance to CO even at very low levels [51]. Since the CO poisoning effect is more associated to methanol fuelled fuel cells, a detailed description of the CO poisoning mechanism is beyond the scope of the present work.

In order to overcome these issues several solutions have been proposed, such as developing Pt-alloy electrocatalysts [52]. Nevertheless, the cost remains high. Other solutions, such as synthesising novel Pt-free metal catalysts, has been proposed [53]. As an example, tungsten monocarbide has been prepared, being a competitive catalyst for the methanol oxidation reaction [54], but no activity has been reported for the ORR.

The use of carbon supports can mitigate some of the problems mentioned above, and in particular can reduce the high costs derived of using bulk platinum.

2.2.2 Carbon as catalyst support:

The use of catalysts supports is currently a normal strategy to improve the application of Pt catalysts for a number of reasons [55]:

- a more homogeneous catalyst distribution along the surface area is attained. The high Pt dispersion on Vulcan XC-72 (one of the most widespread carbon supports) is attributed to its high internal porosity [56]. The catalyst distribution on the catalyst support is crucial in order to maximise the so-called triple phase boundaries (TPBs), which are the points where the O_2, the alkaline electrolyte and the electrically conductive catalyst meet to produce the electrochemical reaction. A higher amount of TPBs can be obtained from an improved catalyst distribution on the catalyst support, leading to a better catalytic activity.
- there is an improvement in the electrical conductivity due to the capacity of carbon to conduct the electrons. In the case of carbon black, this type of catalyst support has been selected in the industry based on its conductive properties [57]. The high electron conductivity typical of carbon supports facilitates the incorporation of electrons towards the points of reaction, which increases the efficiency of the electrochemical reaction.
- there is an enhancement of the catalytic activity and the efficiency. This is due to that the activity of a catalyst increases when the reaction surface area is higher, which is a consequence of the reduced catalyst particle size when a carbon catalyst support is used [58].

- increase of the catalyst durability, since the loss and dissolution processes affecting the catalyst are mitigated. However, it has been demonstrated that the particle detachment is not due to the possible oxidation of the carbon support to carbon dioxide [59].

Moreover, the catalyst-support interaction results in increased number of catalytic sites for the adsorption-desorption of reactants. Among the different materials proposed to act as catalyst supports, carbon has been widely used due to several reasons, such as its abundance, potential low cost, availability in a variety of forms with different properties, excellent electronic conductivity, high surface area and relatively inert surface [60].

Carbon black (CB) is the most widespread carbon support, being commonly present under the commercial name of Vulcan XC-72. It consists of quasi-spherical carbon particles with diameters <50 nm and polycrystalline structures of several layers with an interplanar separation of 0.35-0.38 nm, reaching a high surface area of around 250 m^2 g^{-1} [55]. The behaviour of CB as a catalyst support depends strongly on its specific characteristics, as well as on the application of different preparatory treatments [61]. Regarding the physical properties, the specific surface area [62] and the porosity [63] of the carbon support has been proven to be a crucial factor in the catalytic activity.

Several methods have been proposed for the deposition of the Pt catalyst onto the carbon supports [64,65]. Figure 2.6 shows a TEM image showing Pt particles randomly distributed over CB spheres. The Pt particle size has been demonstrated to have an important influence on the ORR activity of the catalyst, with some studies showing a particle size in the range of 4-5 nm to yield the best performance in 20% wt. Pt on CB [66,67].

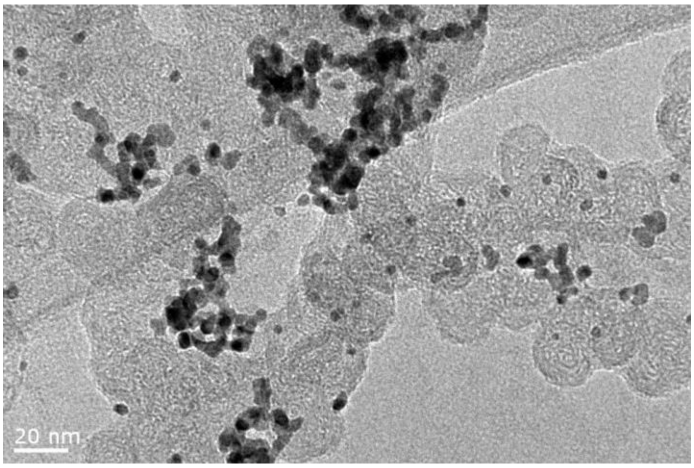

Figure 2.6. *TEM image showing Pt particles deposited onto CB spheres.*

In spite of the mentioned advantages of using carbon as material for catalyst support, there are some issues related with its practical application [68]. The most studied is the possible carbon corrosion of carbon under certain electrochemical conditions, which could limit the lifetime of the catalyst. Attending to thermodynamic criteria, carbon can be oxidised to carbon dioxide at potentials higher than +0.207 V (vs. Normal Hydrogen Electrode (NHE)). Nevertheless, the slow kinetics of the corrosion process guarantee the stability of the catalyst under the conditions of operation, especially at low temperature [69].

The performance of the catalyst support is also affected by the carbon structure and configuration of the carbon material. This has motivated the research into new carbon allotropes, such as graphene [70] and carbon nanotubes [61], which could improve the performance of Pt/carbon systems.

2.2.3 Graphene-derivatives as carbon catalyst supports

The main characteristics of graphene have been explained in Section 1.2.1. Here it will be mentioned that the structure of graphene consists of an one-atom thick layer formed by carbon atoms distributed in a honeycomb lattice structure, where each carbon atom is bonded to three others by σ- bonds. The three electrons of each carbon atom participating in these bonds experience sp^2-hybridisation, leaving the fourth electron in the valence layer to form a π-cloud where the electrons are free to move along the structure, which confers on graphene its typical excellent conductivity [70–72]. The characteristic honeycomb structure of graphene is shown in Figure 2.7.

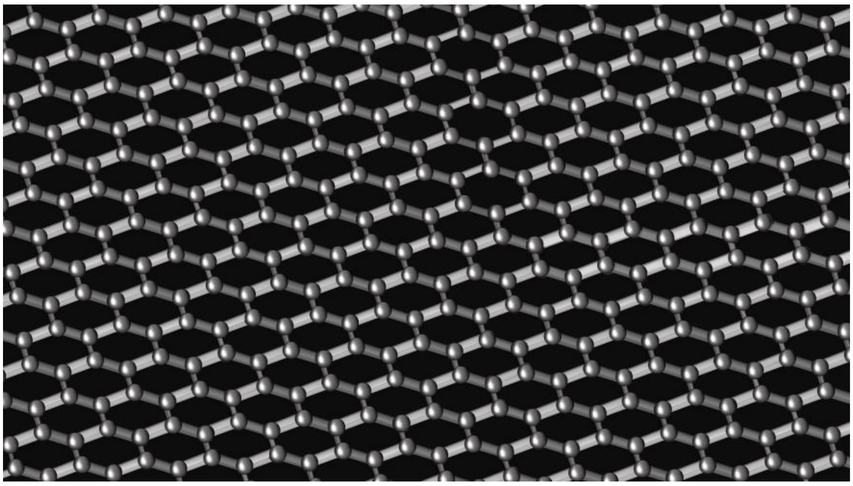

Figure 2.7. *Schematic illustration of graphene structure.*

Although graphene has been proposed as catalyst support itself [73], it cannot be produced for large-scale by micromechanical exfoliation from graphite [74]. Therefore, there is increasing interest on two graphene derivatives: graphene oxide (GO) and reduced-graphene oxide (rGO), which can be easily obtained from abundant graphite crystal using well-known oxidation methods [75], followed by a reduction in the case of rGO [76]. The main characteristic of GO with respect to graphene is the loss of electronic conductivity due to the partial transition from sp^2 to sp^3 configuration of carbon atoms [77].

The reduction of GO would recover part of the characteristic conductivity of graphene by partially restoring the π-network [78]. Moreover, the elimination of oxide groups (either carbonyl, epoxy, alkoxy and carboxylic groups) would create vacancies along the sp^2 carbon structure, as observed in Figure 2.8, which could favour the deposition and dispersion of the catalyst particles [79]. GO reduction can be achieved via thermal, electrochemical or chemical methods [80]. Of the latter, hydrazine is a selective reagent to reduce GO [76], but has the disadvantages of toxicity and the aggregation of rGO layers leading to the increasing use of L-ascorbic acid as a more benign reductant [81].

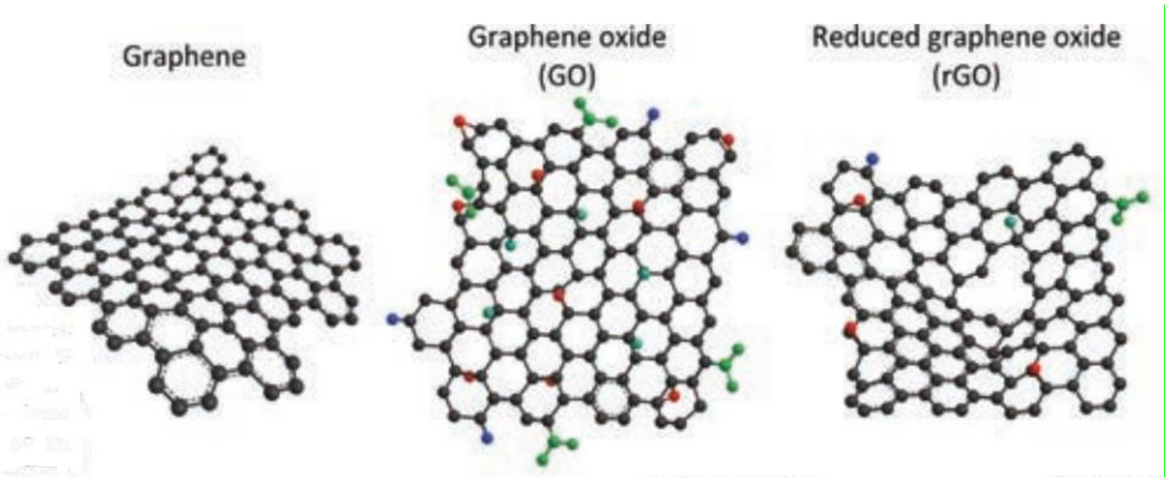

Figure 2.8. *Schematic chemical structures of graphene, graphene oxide and reduced-graphene oxide* [82].

The reduction of graphene oxide creates different types of defects on the graphene structure, which have also demonstrated to be catalytically active towards the ORR by themselves [83]. The defects created in the graphene structure during the reduction procedure can be generally classified into two types: defects created on the carbon plane, which are more related to a decrease in the conductivity, and defects formed on the edges, which have less influence in the conductivity [76]. Obviously, the presence of in-plane or in-edge defects will depend on the nature of the original oxide groups present in the GO precursor, and where these groups are located within the graphene structure. Figure 2.9 shows the six different types of oxygen functionalities, which are described in the caption of the figure.

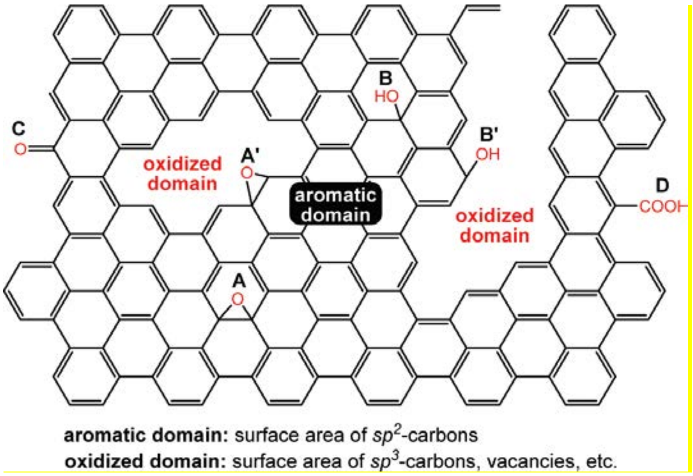

Figure 2.9. *Schematic illustration of oxygen-containing groups in GO: **A**, epoxy groups located at the interior of an aromatic domain; **A'**, epoxy groups located at the edge of an aromatic domain; **B**, hydroxyls located at the interior of an aromatic domain; **B'**, hydroxyls at the edge of an aromatic domain; **C**, carbonyls at the edge of an aromatic domain; and **D**, carboxyls at the edge of an aromatic domain. Reprinted with permission from [84]. Copyright (2010) American Chemical Society.*

The elimination of each particular group will be determined by the method used for the reduction of graphene oxide. For example, a thermal annealing at temperatures between 700 and 1200 °C favours the removal of hydroxyl and carboxylic groups, whereas a chemical reduction with hydrazine will eliminate the epoxy groups while the hydroxils located on the edges will not be affected [76]. The importance of the choice of the GO reduction procedure lies in that the defects created on the edges are considered active sites for the ORR due to the higher charge density with respect to the carbon atoms located on the basal plane, which show negligible charge [83].

In addition, these graphene-derived supports have some advantages with respect to CB. First, the much higher surface area (2630 m^2 g^{-1}) [85], which is only 250 m^2 g^{-1} in the case of CB [55]. Nevertheless, the value for multilayer graphene is reduced to 70-130 m^2 g^{-1}, hence the importance of synthesising high-quality graphene [72]. Another advantage of graphene supports is that the platinum-support interaction is strengthened with respect to CB, due to the electronic configuration of graphene. This allows the enhancement of the stability of the catalyst-support system [71]. Finally, due to the intrinsically high electronic conductivity of graphene, this property is considerably improved in catalyst-graphene systems with respect to Pt/CB [70].

2.2.4 Carbon nanotubes

Another carbon material increasingly finding application as a catalyst support are carbon nanotubes in either single-walled (SWCNT) or the most common multi-walled (MWCNT) forms. MWCNTs have been used as carbon supports for a variety of metal catalysts, such as Ag [86] and Pt-Co alloys [87]. They have been even shown to display excellent electrocatalytic activity towards ORR in alkaline media by themselves [88], although Pumera et al. link this behaviour to metal impurities remaining from the process of fabrication [89].

Nanotubes are fabricated from graphene layers that have been modified to adopt a tubular shape, in such a way that SWCNT is a single graphene layer rolled as a cylinder, whereas MWCNT results from the winding of several coaxially arranged graphene sheets with an interlayer space between them of 0.34 nm [68]. A comparison of the morphology of SWCNT and MWCNT can be observed in Figure 2.10. The features of carbon nanotubes when used as catalyst supports are a length of 10-50 µm, outer diameter between 10 and 50 nm, and an inner diameter of 3-15 nm. The specific surface area are normally reported in a wide range between 200 and 900 m^2 g^{-1}, which is significantly higher than carbon black and multi-layered graphene [68].

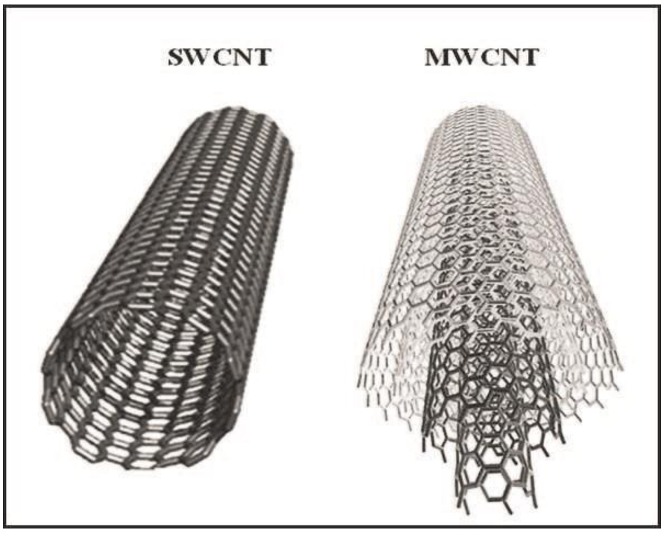

Figure 2.10. *Schematic diagrams of single-walled (SWCNT) and multi-walled carbon nanotubes (MWCNT) [90].*

Among the different methods available for the synthesis of SWCNT and MWCNT it can be cited carbon-arc discharge, laser ablation of carbon and chemical vapour deposition (CVD) [91]. SWCNT produced by these methods can only be produced in small scale and are very expensive, also having a high concentration of impurities. These impurities can be reduced through the application of acid treatments, but these procedures can introduce other impurities and degrade nanotube quality [92]. On the contrary, MWCNT can be produced in mass scale using a versatile CVD procedure. Basically, this method consists on passing a hydrocarbon vapour through a tubular furnace containing a catalyst at temperatures between 600 and 1200 ˚C to decompose the hydrocarbon. By this way, CNTs grow on the catalyst inside the reactor and are collected after cooling down the system at room temperature [93].

Carbon nanotubes can be also classified according to their structural configuration (Figure 2.11), that can be armchair (a), zigzag (b) and chiral (c), depending on the direction along which the graphite sheet is rolled up. This has huge implications in the conductivity of the nanotube, determining if it behaves like a metal or a semiconductor [94]. In addition, if carbon nanotubes are unzipped to produce carbon nanoribbons, they became catalytically active due to the catalytic behaviour of the edges created, being the zigzag configuration the most active one for the oxygen reduction among the different configurations mentioned above [95].

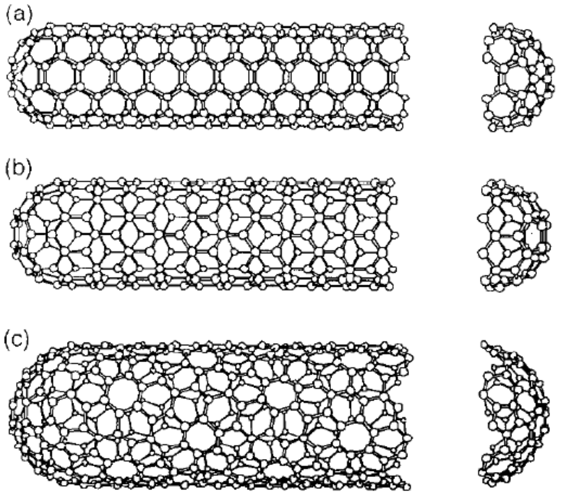

Figure 2.11. *Schematic illustration of carbon nanotubes configuration, which can be (a) armchair, (b) zigzag, and (c) chiral. Reprinted with permission from [96]. Copyright (1995) Elsevier.*

The catalytic performance of MWCNT can be also modified by chemical functionalization of the nanotubes. As an example, Dumitru and co-workers demonstrated that the ORR in alkaline media proceeds by a two-electron mechanism when MWCNT are functionalised with citric acid, whereas it undergoes a four-electron mechanism when the nanotubes are treated with peroxymonosulfuric acid, due to an increase in the number of C-O groups [97]. However, without chemical functionalisation there is a scarcity of binding sites for anchoring the catalyst nanoparticles, leading to poor particle distribution and agglomeration of Pt particles [98].

2.3 Doped-graphene as catalyst for the ORR

The ORR is a persistent challenge for researchers on energy applications (e.g. fuel cells, metal-air batteries) due to its slow kinetics [99,100]. Pristine graphene has demonstrated a limited ORR performance due to its zero band gap, which implies the lack of active functional groups or defects in the graphene structure that are considered active sites for the ORR [53,101]. A promising strategy to make graphene more catalytically active towards the ORR is doping the graphene structure with *p*-block heteroatoms, such as nitrogen [102–108], boron [109–113], phosphorus [114–116] or sulphur [117–120], since the inclusion of dopant atoms in the 2D graphene structure can modify the electroneutrality of the sp^2 carbon lattice and create sites for the O_2 adsorption [121]. It has been suggested that the formation of carbon active sites induced by the heteroatoms alters the binding energy of the molecule of O_2, favouring the dissociation of the O=O bond [4]. Several methods have been proposed for the doping of graphene with heteroatoms, including chemical vapour deposition (CVD), ball milling, bottom-up synthesis, thermal annealing, wet chemical method, plasma treatment with heteroatom atmosphere or arc-discharge [122]. Among these methods, CVD is one of the most widespread, in spite of being a relatively complex process whose application entails the use of hazardous precursors and gases, contamination by transition metal reagents, high cost of the process and a low yield [123]. Most of these problems can be overcome using a thermal annealing treatment of a mixture of precursors under an inert atmosphere for the synthesis of the catalyst [124].

Abundant literature exists in metal-free doped-graphene catalysis for ORR applications, there being reported single [111,114,120,125], dual [126–129] and ternary-doped [130–132] compounds. However, these catalysts are produced under a vast variety of synthesis and experimental conditions, and therefore the obtained results cannot be compared to each other. Chapter 5 presents a systematic synthesis and characterisation of single, dual, ternary, and even a novel metal-free quaternary-doped graphene under reproducible conditions, in such a way that conclusions about the mechanism and performances of the different doped-graphene catalysts towards the ORR can be obtained.

In this section, a brief review is presented about the four most used dopants for graphene-derived catalysts, stating their main characteristics, as well as methods of doping and particular influence in the ORR mechanism.

2.3.1 Boron

Boron is peculiar compared with the rest of the common dopants due to the fact of being electron-deficient with respect to carbon. It is the most studied graphene dopant (after nitrogen) since its atomic radius is very similar to that of carbon. The fact of being less electronegative than carbon implies that boron-doped graphene (B-Gr) undergoes p-type conductivity [111].

The synthesis of B-Gr is favoured due to the fact that boron is very efficient in substituting the carbon atoms from the graphene structure, in spite of the high activation energy barrier (1.3 eV) associated to this process [133]. The procedures for boron-doping of graphene can be classified in bottom-up methods, where B-Gr is synthesised from molecular boron and carbon precursors, and chemical modification of graphene oxide with boron precursors [133]. Among the most used synthesis methods it can be mentioned the solid state synthesis, which is a top-down method where very different graphene precursors are incorporated into graphene materials via arc discharge [134] or thermal treatments [109,112]. In this regard, it should be noted that the synthesis temperature has important implications in the resulting products, with operational temperatures higher than 2000 °C producing substitutional doping [109], whereas average temperatures of 900 °C produce a variety of functional groups [112]. Hydrothermal methods at temperatures between 150 to 270 °C [135,136] and CVD in presence of gaseous sources of boron [137] have been also reported.

Among the precursors used for boron-doping of graphene it can be found a vast number of chemicals from simple inorganic compounds, such as boric acid (H_3BO_3) [138], B_2O_3 [139], B_4C [140], BCl_3 [141], BBr_3 [136] or $NaBH_4$ [111], to more complex organic compounds, such as boron trifluoride diethyl etherate (BF_3Et_2O) [111], borane tetrahydrofuran (BH_3-THF) [142] or tetraphenylborate [143]. The B-Gr catalysts obtained from these methods report a wide range of boron incorporation into the graphene structure, with compositions ranging between 0.5 and 10%.

The incorporation of boron into the graphene structure induces a profound change in its electronic configuration, generating a small energy band gap and p-type conductivity [111]. Raman measurements have also demonstrated that boron produces a distortion of the translational symmetry in the graphene structure [111]. Boron is present in B-Gr catalysts as a broad variety of moieties. For example, CVD procedures lead in substitutional atoms [144], whereas that borinic (C_2BO) and boronic (CBO_2) species are found in GO treated with boron precursors [145].

When boron is incorporated into the graphene structure as substitutional boron (BC_3), it undergoes sp^2 hybridisation with highly polarised B-C σ-bonds due to the higher electronegativity of C with respect to B (2.55 and 2.04, respectively), involving a strong positive charge in the B atom. These positive atoms tend to attract the O_2 molecule, decreasing the adsorption distance and strengthening further the interaction between the B atom and the O_2 molecule [146]. Once the O_2 molecule is adsorbed, the active site weakens the O=O double bond and promotes the formation of reactive intermediates [111]. The incorporation of boron into the carbon matrix transforms the electron-deficient boron into an electron-donating site by taking advantage of the abundant π-electrons in the carbon system. More precisely, the active electrons are transferred from the C-C π* antibonding orbital to the vacant $2p_z$ orbital of boron. When the boron dopant is in the form of boronic and borinic, i.e. in oxidised states, this mechanism is still valid [146]. In addition, boron-doped graphene has demonstrated excellent tolerance against CO poisoning with respect to a typical platinum-based catalyst in methanol-fuelled fuel cells [147].

2.3.2 Nitrogen

Nitrogen is by far the most studied and reported heteroatom for graphene doping. Due to its atomic radius being very similar to graphene, the nitrogen atoms can be easily incorporated into the graphene lattice using a number of doping methods. The incorporated nitrogen species enhance the interactions between the graphene surface and the O_2 molecule, thus improving the catalytic activity with respect to non-doped graphene [148].

The synthesis of nitrogen-doped graphene (N-Gr) can be carried out by two different approaches: direct synthesis and post-treatment methods. Among the first it is found the CVD procedure, where N-Gr is generated onto a Cu or Ni substrate at high temperature under a mixed nitrogen-carbon gases atmosphere [149]. This category includes the segregation growth approach, consisting of the sequential deposition of nitrogen and carbon-containing Ni layers onto a SiO_2/Si substrate by electron beam evaporation [150]. The solvothermal method produces N-Gr in gram-scale with varying compositions by mixing different amounts of nitrogen and carbon precursors at 300 °C [151]. The last method in the direct synthesis approach is the arc-discharge procedure, where this source of energy is employed to obtain N-Gr by evaporating graphite in the presence of a pyridine or NH_3 atmosphere [134].

Among the post-synthesis methods it can be found the thermal treatments. As an example, heating graphene at high temperatures under NH_3 atmosphere produces N-Gr with varying compositions depending on the temperature applied, obtaining 1.1%

at 1100 °C [152] and 2.8% at 800-900 °C [153]. Another example of post-synthesis would be the plasma treatment, where N-Gr with nitrogen contents varying from 3 to 8.5% is produced by exposing GO in a NH_3 plasma atmosphere [154]. Finally, N-Gr with nitrogen compositions up to 5% has been also obtained by treating GO with a hydrazine (N_2H_4) solution at temperatures between 80 and 160 °C [125].

The introduction of nitrogen into the graphene structure produces four different bonding configurations (Figure 2.12) [153,155]:

- Pyridinic N: it refers to the sp^2 hybridised N atom bonded to two carbon atoms of a six-membered ring located at the edges or defects of the graphene lattice, contributing one p-electron to the π-system. It appears at 398.2 eV in the XPS spectra.
- Pyrrolic N: they are the sp^3 hybridised N atoms bonded to two carbon atoms of a pyrrolic five-membered ring present in the edges of the graphene structure. Pyrrolic N-atoms contribute two electrons to the π-cloud system. They typically appears in the 399.5 eV position of the XPS spectra.
- Graphitic N: also called quaternary N. They substitute a carbon atom in the hexagonal ring not located at the edges or defects, thus being sp^2 hybridised. In the XPS spectra graphitic N appears at 400.8 eV.
- Pyridinic N-oxide: here the N atom bonds to two C and one O atoms. This group appears at 403.6 eV in the XPS spectra.

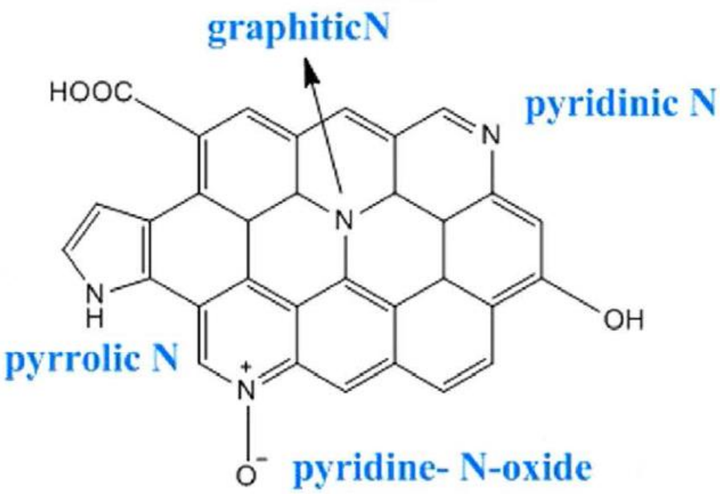

Figure 2.12. *Scheme of the characteristic nitrogen groups in nitrogen-doped graphene [156].*

The fact of that doped-graphene shows higher catalytic activity than pure graphene can be also explained from the point of view of their respective chemical reactivity. The kinetic stability can be considered in terms of the energy separation between the highest occupied molecular orbital (HOMO) and the lowest unoccupied molecular orbital (LUMO). A small HOMO-LUMO gap implies high chemical reactivity due to the favoured transition of electrons between the two levels and the subsequent formation of activated complexes [157]. In fact, the substitution of one carbon atom in pure graphene ($C_{46}H_{20}$) by a nitrogen atom to give $C_{45}NH_{20}$ reduces two times the HOMO-LUMO gap [158]. As a consequence, the catalytic activity of nitrogen-doped graphene is improved due to the easier mobility of electrons from valence to conduction band.

The incorporation of nitrogen into graphene also increases the catalytic activity by a mechanism in which there is an enhancement of the electron transfer from the electronic bands of carbon atoms to the σ* antibonding orbital of the O_2 molecule. This mechanism is mediated by the increase of the electronic density states near the Fermi level induced by the introduction of N atoms in the graphene lattice [159]. In addition, activation regions are induced in the graphene surface due to the influence on the spin density and charge distribution of the carbon atoms by the neighbour nitrogen dopants. These activated regions can participate directly in the ORR or create sites for anchoring metal nanoparticles [158].

2.3.3 Phosphorus

Phosphorus is an element of the nitrogen group, with the same number of electrons in the valence layer. Doping graphene with phosphorus has been less studied than the boron and nitrogen doping of graphene, and, as a consequence, the mechanisms and the role of phosphorus incorporation into graphene remain mostly unknown. In addition, only a few papers report the single-doping of phosphorus into carbon materials [116,160,161] (even less in phosphorus-doped graphene (P-Gr) [114,115]), with the most of literature available on this topic reporting dual [127,129,162–165] and ternary-doping [132,166,167] of graphene in combination with B and N, especially the latter.

The larger covalent radius and lower electronegativity of P compared to B, N and S can modify more effectively the carbon structure and the resulting catalytic activity [160]. It has been also predicted a more intense bandgap effect in P-Gr and a more energetically favoured incorporation of P heteroatoms into the graphene structure [168]. Moreover, the increased catalytic activity has been proposed to be linked to increased electron-donor properties, due to the intrinsic lower electronegativity of phosphorus with respect to carbon [169]. Another work suggests that the asymmetric spin density of carbon atoms induced by the P dopants, or the P^+ charged sites by themselves, are the active regions where the ORR takes place [116].

Several methods have been reported for the preparation of phosphorus-doped carbons. P-Gr has been synthesised by pyrolising triphenylphosphine and phenol (acting as phosphorus and carbon precursors, respectively) in a mesoporous silica template, obtaining a catalyst with a P content of 1.36% [160]. A hydrothermal method has been also proposed for the production P-doped hollow spheres, using tetraphenylphosphonium as the P source. The resulting product reported a P composition of 1.61% and a very high surface area (>500 $m^2 g^{-1}$) [116]. CVD has been also employed to synthesise a P-Gr catalyst, although this method reported a poor yield and contamination with metal impurities that could interfere the role of P in the catalytic activity [170].

Phosphorus is incorporated into the graphene lattice as P-C and P-O moieties. Phosphorus at higher oxidation levels is assumed to be remaining unaltered from the phosphoric acid precursor [171], when used. Metaphosphates are also reported, being presumably produced by the condensation of phosphates [172], whereas other P-O species [116], where an oxygen bridge is formed between C and P [165], are also reported. Finally, oxygen-free P-C moieties are also found [173], especially when oxygen-free organic phosphogypsum compounds are used as precursors.

2.3.4 Sulphur

Sulphur has been more recently reported as heteroatom dopant for graphene. The S-doping has been predicted to be more complicated than the rest of dopants due to the different size and binding features with respect to carbon. However, unlike the rest of the dopants, the electronegativity of sulphur (2.58) is very similar to that observed in carbon (2.55) [119]. Therefore, in this case, breaking the electroneutrality of the carbon lattice to create charged sites for O_2 adsorption is not the reason behind a possible improvement of the ORR activity.

In contrast to the previously discussed phosphorus dopant, single sulphur-doped graphene (S-Gr) has been more extensively reported in the literature for different applications, apart from ORR catalysts [117,118,120,174]. Sulphur is also commonly reported as co-doped with nitrogen in dual-doped graphene catalysts [128,175–178]. All of them have demonstrated excellent ORR activity, with catalytic performance even comparable to platinum [119]. It has been also proposed that the ORR take place in the high charge density S atoms following the 2-electron pathway, whereas that it follows a 4-electron mechanism in the high spin density C atoms [117].

S-Gr can be synthesised using different methods. It has been produced with a low S content of 0.6% by CVD is a solution of sulphur in hexane, exhibiting the resultant S-Gr lower conductivity and characteristic p-type properties compared to graphene [179]. A higher S composition (2.2%) has been reported using a phosphorus pentasulphide precursor, showing the produced S-Gr much higher catalytic activity in alkaline media than in acid [118]. Yang et al. synthesised various S-Gr catalysts by annealing GO and benzyl disulphide (BDS) in an Ar atmosphere at different temperatures, finding that lower temperatures (600 °C) produces S-Gr with higher S content (1.53%) than at higher temperatures (1.30% at 1050 °C) [119]. The influence of the annealing temperature on the sulphur content of the produced catalyst was confirmed by Schmidt et al., using poly(1,3,5-tris(thienyl)benzene) as the sulphur precursor [174].

Density functional theory (DFT) calculations show that the sulphur atoms mainly substitute carbon atoms at the edge of graphene layers in the form of sulphur or sulphur oxide, even connecting two graphene layers by the formation of a sulphur cluster ring [117]. These observations are confirmed by XPS measurements, where, unlike the boron and phosphorus dopants, the sulphur moieties are well established, with low variability between different studies, and they appear at well-reported positions in the XPS spectra. Most of sulphur atoms are in the form of -C-S-C- species, where the S atoms can adopt two different spin-orbit coupling positions: $S2p_{3/2}$ (164.1

eV) and S2$p_{1/2}$ (165.2 eV) [175,176]. The rest corresponds to -C-SO_x-C- moieties, with x=2 (167.5 eV), x=3 (169.4 eV) or x=4 (171.2 eV) [119].

The catalytic activity of S-doped graphene towards the ORR is believed to take place on the C-S bonds located on the edges of defect sites [119]. Since the electronegativity of C and S atoms is similar (2.55 and 2.58, respectively), it is speculated that a change of the charge distribution of graphene due to the S incorporation is not a probable cause for the improved catalytic behaviour shown by S-doped graphene with respect to pure graphene [119]. On the contrary, the increased spin density (influenced by the bigger size of the S atoms compared to other dopants) could play a crucial role on the ORR activity observed in S-doped graphene [180].

2.4 Metal/doped-graphene hybrid catalysts for the ORR

In this section the incorporation of two different metals into the doped-graphene catalysts is discussed. One of these metals under study is a transition-metal (Fe) which is a very cheap and abundant material, with poor catalytic activity by itself but with promising results when it is combined with activated carbon materials. The other is perovskite oxides, which have been reported for a number of applications, but here they will be analysed in terms of ORR performance. Their compositions and structures are introduced here, and a brief review about synthesis and ORR performance is also discussed.

2.4.1 Transition metal/nitrogen-doped carbon hybrid as ORR catalysts

Transition metals have been reported to form active ORR catalysts when they are combined with nitrogen-doped carbons. Among the available transition metals, Fe is the most studied for this purpose, although Co has been also reported in the form of Co/N/C hybrid systems. Co/N/C catalysts have been reported in the form of mesoporous hybrids [181] or hollow spheres [182]. Nevertheless, it is generally assumed that Co/N/C systems yield lower ORR performance than Fe/N/C [4].

It should be noted that Fe has yielded very poor results when it has been tested as a single-catalyst, mainly due to the low number of active sites [183]. However, the addition of Fe to N-doped carbon materials has been reported to increase the ORR activity with respect its metal-free counterpart [184]. One of the roles of Fe in the transition has been stated to be to facilitate the incorporation of the nitrogen dopant into the carbon structure [185]. Nevertheless, another study proposed that the ORR suffers a double mechanism in Fe-N-CNT hybrids, where the O_2 is reduced to peroxide on the carbon surface, being the peroxide immediately disproportionated on the Fe surface [186].

Several methods for the synthesis of Fe-N-C systems have been proposed. A method consisting in the pyrolysis and the ammonia activation of a ferrocene precursor yielded a good ORR activity, with a calculated number of electrons transferred during the ORR of 3.5 [187]. Another study reported the fabrication of a mesoporous carbon material co-doped with Fe and N, prepared using a mesoporous silica template, $FeCl_3$ as the Fe precursor and aniline as the simultaneous N and C precursor. Some features of the obtained catalyst were a 4.9 nm pore size and a specific surface area of 236 m^2 g^{-1} [188]. A Fe-N-Gr catalyst has been also prepared by pyrolysis of a hybrid precursor under an inert atmosphere, being the precursor formed by $FeCl_3$, melamine and aniline. The resulting product reported a very high active area 702 m^2 g^{-1}, and high N-pyridinic and N-graphitic content [184].

In the present work, a Fe-N-Gr catalyst will be prepared by simultaneous doping under a thermal treatment at inert atmosphere, using $FeCl_3$, melamine and GO as Fe, N and graphene precursors, respectively. The obtained hybrid catalyst will be physically and electrochemically characterised, comparing the most characteristic features, such as the ORR performance and N-species composition, with its metal-free N-doped graphene equivalent.

2.4.2 Perovskite oxide/doped-graphene hybrid catalysts

Perovskite oxides were first reported as ORR catalysts in the 1970s. Since then, abundant research has been devoted to develop these materials as electrochemical catalysts. In this section, a brief review on perovskite composition and structure will be carried out, as well as a brief introduction to perovskite/carbon hybrid systems.

2.4.2.1 Structure and design of perovskite oxides

The simplified formula of perovskites is ABO_3, where the A-cation is either a rare-earth metal from the group of lanthanides and/or a group II (alkaline earth) metal, whereas the B-cation is one (or combination of several) transition-metal [189]. The configuration of a typical perovskite is a corner shared BO_6 octahedra, with the A-site cations acting as the corners of a unit cell (Figure 2.13). This type of structure is flexible, permitting a lattice mismatch between the A-O and B-O bond lengths [4]. This implies the possibility of partial substitution of the A and B-cations, giving the more general formula $A_{1-x}A'_xB_{1-y}B'_yO_{3-\delta}$, which also reflects the formation of oxygen vacancies. This high compositional flexibility offers tuneable physical and chemical properties [190,191], with very interesting applications in ORR catalysis.

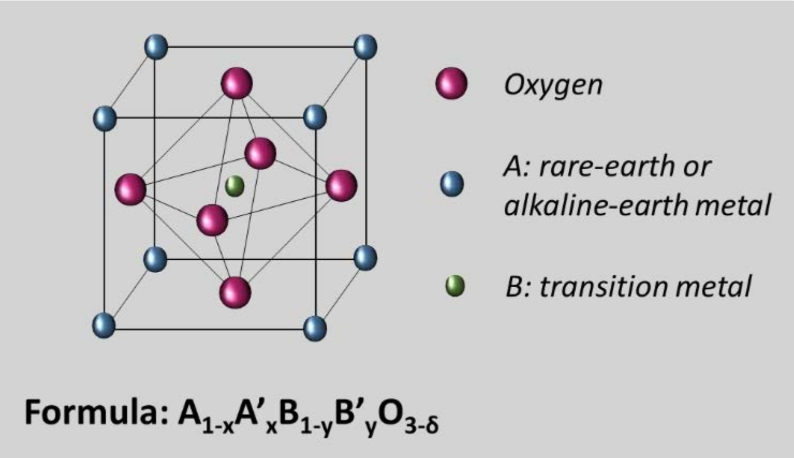

Figure 2.13. *Illustration of a unit cell of the perovskite structure.*

In an ideal cubic perovskite without oxygen vacancies, the B-site transition metals are octohedrally coordinated to oxygen, while the A-site cations are 12-fold coordinated to oxygen [189]. Substitutions of the A and B-cation sites will modify this ideal structure, leading to oxygen vacancies and structural distortion. This deviation can be quantified using the Goldschmidt tolerance factor [192]:

$$t = \frac{r_A + r_O}{\sqrt{2}\,(r_B + r_O)} \tag{2.26}$$

where r_A, r_B and r_O, are the ionic radii of the A-site cation, the B-site cation and oxygen (1.4 Å), respectively. This tolerance factor can be used to calculate the symmetry of the perovskite structure.

Perovskite oxides can be designed to obtain different chemical and physical properties. One strategy to increase the ORR activity of a perovskite catalyst is to introduce an A-site cation deficiency. This modification induces the creation of surface oxygen vacancies and modify the oxidation number of a small amount of transition metal B-cations, which is linked to the improved ORR activity [193]. On the other hand, modifying the B-site by introducing a second transition metal can also enhance the ORR activity. For example, Ciucci et al. modified a $SrCoO_{3-\delta}$ perovskite by introducing varying amounts of a Sc dopant, finding that $SrCo_{0.95}Sc_{0.05}O_{3-\delta}$ led to the optimal composition in terms of ORR kinetics. They concluded that the addition of small amounts of Sc produced the stabilisation of the oxygen-vacancy disordered structure [190]. In general, it is largely assumed that the ORR catalytic behaviour is strongly influenced by the transition metal used as B-cation site [194]. These are just two examples of how perovskite oxides can be engineered to obtain different catalytic properties. Nevertheless, a more detailed analysis on this topic is beyond the scope of the present study.

The ORR activity in perovskites is determined by the σ*-antibonding (e_g) orbital filling of surface transition-metal ions, playing the hybridisation of the B-site metal and oxygen a crucial role on this point [195]. This ORR activity shows a volcano shape as a function of the e_g-filling of the B atoms, as depicted in Figure 2.14.

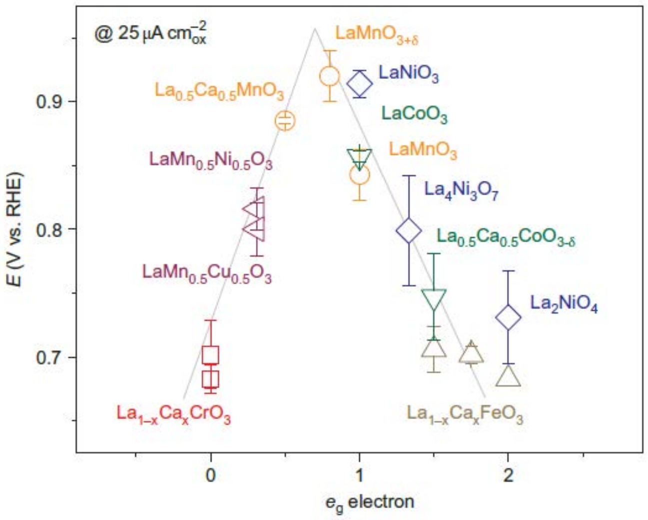

Figure 2.14. *Potentials at 25 mA cm_{ox}^{-2} as a function of e_g orbital in perovskite-based oxides. Data symbols vary with type of B ions (Cr, red; Mn, orange; Fe, grey; Co, green; Ni, blue; mixed compounds, purple), where x¼0 and 0.5 for Cr, and 0, 0.25 and 0.5 for Fe. Error bars represent standard deviations. Reprinted with permission from [195]. Copyright (2011) Nature Chemistry.*

After the adsorption of the O_2 molecule on the B-site surface, the e_g orbital overlaps the O-2p_σ orbital more strongly than the overlap between the t_{2g} and the O-2p_π orbital [195]. Figure 2.14 shows that too little e_g filling leads to very strong B-O_2 bonding, whereas much e_g filling can result in an very weak O_2 interaction. As a consequence, a moderate e_g filling of around 1 yields the optimal catalytic activity [4].

2.4.2.2 Addition of carbon materials to perovskite oxides

Although perovskites have been proposed as ORR and/or OER catalysts by themselves [196], their poor conductivity limits their extensive application as ORR catalysts [191]. Since an efficient flow of electrons is prerequisite for a good electrocatalyst to produce high current densities, several researchers have reported that the addition of highly electronic conductive carbon materials to perovskites improves the catalytic activity with respect to solely perovskite catalysts [197–200]. Most of these studies report the combination of perovskites with different inert carbon supports, such as acetylene black [197], Vulcan carbon powder [198,199], Sibunit carbon [201], graphene [200,202], with varying results. Nevertheless, very few papers report the addition of catalytically-active doped-carbons to perovskites, apart from nitrogen-doped carbons [203–206].

The preparation of perovskite/carbon hybrid catalysts can be classified into two different categories: perovskite/carbon prepared by physical mixing, where perovskites engineering and carbon functionalisation are done separately and then both compounds are mixed, and perovskite/carbon prepared by in-situ chemical synthesis, where the chemical synthesis produces a strong carbon-perovskite interaction [194]. As an example of the first type, Savinova et al. prepared some hybrid catalysts by physical mixing of perovskite and carbon, using $LaCoO_3$ and $La_{0.8}Sr_{0.2}MnO_3$ as the perovskite oxides. They compared the performance of each perovskite/carbon system with respect to the performance of their individual components, demonstrating that in both cases the perovskite/carbon systems dramatically improve the catalytic performance in terms of measured current densities and peroxide intermediate formation. $La_{0.8}Sr_{0.2}MnO_3$ also yielded a better catalytic activity than $LaCoO_3$ when carbon was added to the perovskite [201]. Another study using the physical mixing approach determined that the relation of catalytic activity with the perovskite/carbon ratio composition in a $Ba_{0.5}Sr_{0.5}Co_{0.8}Fe_{0.2}O_3$/Acetylene Black system follows a parabolic curve, reaching the optimal performance at 45% carbon content [197].

Several methods have been published on the chemical synthesis approach, for example: a CVD synthesis of $La_{0.58}Sr_{0.4}Co_{0.8}Fe_{0.2}O_3$ nanoparticle/NCNT [206], hydrothermal synthesis of $La(Co_{0.55}Mn_{0.45})_{0.99}O_{3-\delta}$ nanorod/NrGO [207], electrospinning procedure for $LaTi_{0.65}Fe_{0.35}O_{3-\delta}$ production [208] or synthesis of $Nd_{0.5}Sr_{0.5}CoO_{3-\delta}$ nanorod/edge-iodinated graphene nanoplatelets by ultrasonication [209].

The role of the carbon on the perovskite performance is still unclear. It has been proposed that the presence of carbon greatly improves the conductivity through the catalyst composite [210], whereas other workers suggest an influence of the carbon material on the ORR pathway [197,198]. In Chapter 6, novel experimental work is presented and discussed in order to elucidate the mechanisms behind the improved ORR activity in perovskite/dual-doped graphene hybrid systems.

3 EXPERIMENTAL METHODS

In this chapter, the methods used for the physical and electrochemical characterisation are described. The working principles of the techniques for the physical characterisation are reviewed, and the methods and materials for electrochemical testing are explained.

3.1 Techniques for physical characterisation

The physical characterisation techniques used in the present study are briefly reviewed in this section, explaining their theoretical background and pointing out their specific application for the characterisation of the materials.

3.1.1 Thermogravimetric analysis

Thermogravimetric Analysis (TGA) is a technique in which a sample of material is subjected to a controlled temperature program and the weight of the sample is monitored as a function of temperature or time. It is a destructive technique where the sample is burnt or destroyed under certain environmental conditions, however just few milligrams of the sample are normally required [211].

The TG analyser consists of a small pan supported on a precision balance, which is placed inside a furnace where a controlled temperature programme is applied under fixed environmental conditions, such as an oxidant or inert gas flow. The weight of the sample is monitored under the effects of the gas flow and the temperature [212].

In the resultant thermal TGA curve the weight (or weight percentage) is plotted in the y-axis as a function of the temperature or time (in the abscissa). Figure 3.1 shows a typical TGA curve:

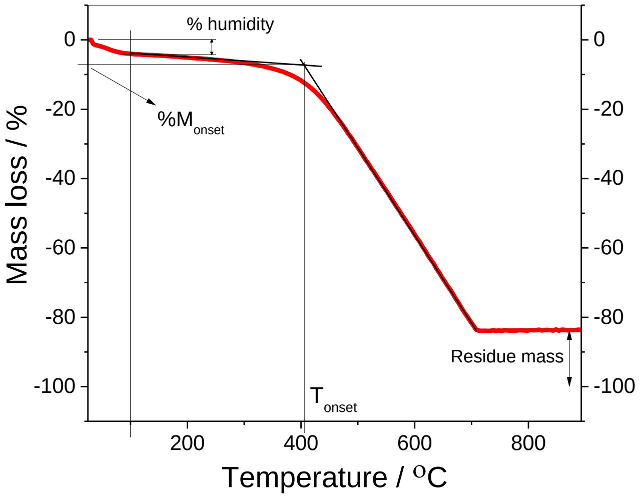

Figure 3.1. *Thermogravimetric mass loss profile of a Pt/MWCNT catalyst in air at heating rate of 10 K min*$^{-1}$.

From the TGA curve some important parameters can be obtained [212]:

- Water content: the decrease of weight of the sample when the temperature of 100 °C is reached is associated to the percentage of water contained in the sample, although this value can be imprecise when other volatile substances are present.
- Onset temperature (T_{onset}): this parameter is the value of temperature at which the weight loss of the sample begins, due to that the sample (or part of it) is burnt (in case of using an oxidant gas flow) or is decomposed (when an inert atmosphere is present).
- Residue mass: it is the final mass remaining after the application of the thermal treatment, and it is commonly associated to the metallic content of the sample. In the case of Pt-carbon catalyst analysis, this value is the percentage of Pt in the catalyst (this calculation must be complemented by another technique which can provide the purity of the residue).

In this work TGA is used to characterise the carbon materials used as catalyst support, and the Pt content in the catalysts is estimated from the value of residual mass measured.

3.1.2 Transmission Electron Microscopy/Energy Dispersive X-ray Spectroscopy

The resolution of an optical microscope is limited by the wavelength of the imaging beam (800-400 nm), due to diffraction at the lens aperture. The resolution can be increased at a given wavelength using a larger aperture, but at the expense of reducing the depth of view [213].

An electron microscope employs a beam of electrons (with wavelengths of less than 0.1 nm) to produce much higher magnifications than an optical microscope, permitting considerably greater resolution. Electron microscopes use an electromagnetic lens consisting in a solenoid through which a current is passed, thus inducing an electromagnetic field. The electron beam passes through the centre of the solenoid towards the sample, being controlled by changing the current through the lenses [214].

In the present study, a particular type of electron microscopy called Transmission Electron Microscopy (TEM) is used. In TEM the electron beam passes partially through a very thin slice sample (with the particularity of being semi-transparent to electrons), providing information about the structure of the specimen. The resulting image is then magnified by a series of magnetic lenses and recorded by a charge-couple device (CCD) camera. This technique provides black and white, two-dimensional images, in which the lighter elements are more transparent, whereas darker zones correspond to heavier components [214]. In Figure 3.2 it can be seen a TEM image displaying a platinum supported on carbon catalyst, where it is observed the darker parts corresponding to Pt particles, while the lighter zones correspond to the carbon support.

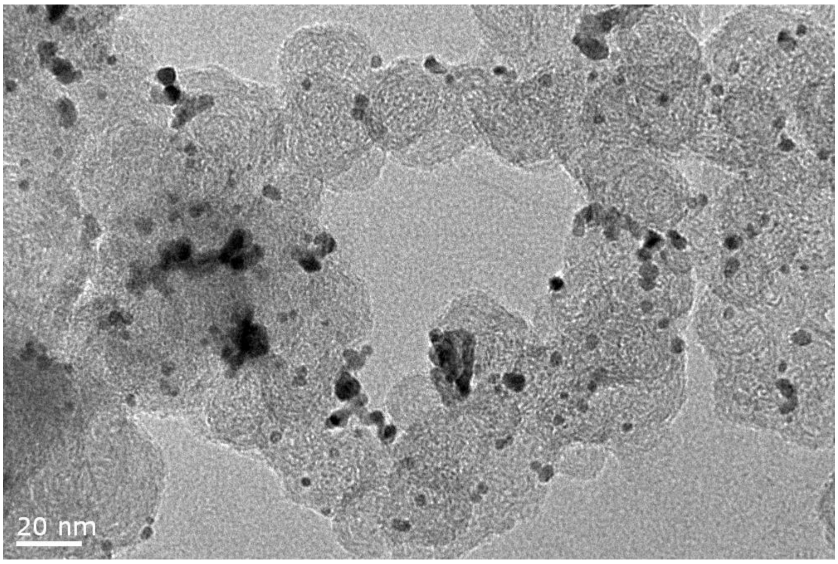

***Figure 3.2**. TEM image of a Pt/C catalyst.*

High-resolution TEM (HR-TEM) is used in this work as a good imaging technique to qualitatively determine the structure of Pt supported on different carbon supports, as well as the observation of graphene-derived materials, such as doped-graphene catalysts, carbon nanotubes and metal/graphene hybrid systems [215]. If TEM is associated to the suitable software, it can also provide quantitative information, such as the Pt particle size distribution and the calculated mean particle size.

TEM can be also coupled to an Energy Dispersive X-ray (EDX) Spectroscopy for the elemental analysis and/or the chemical characterisation of a sample. When an X-ray beam excites an electron from the inner shell, this is ejected creating an electron hole. An electron with higher energy from an outer shell can then fill the hole (with lower energy), thus releasing energy in the form of an X-ray which is detected by an energy-dispersive spectrometer. Since the energy difference between two shells is characteristic of each element, the resultant EDX spectra can be used to investigate the elemental composition of the studied sample [216].

3.1.3 Surface area determination by nitrogen adsorption-desorption analysis

A crucial parameter in the physical characterisation of porous catalysts is the surface area of the material. The physical adsorption of inert gases, such as nitrogen or argon, onto these porous surfaces is the most widespread method to calculate the active area and the morphological surface of graphene-derived catalysts. A commercial equipment provides a flow of nitrogen gas at 77 K, and contains the instruments that measure the amount of N_2 molecules adsorbed by the sample using volumetric, gravimetric or dynamic flow-through methods [217]. The resulting data are simultaneously processed and monitored.

In the experiments carried out in the present investigation, the nitrogen adsorption/desorption isotherms are analysed using the Brunauer, Emmett and Teller (BET) method. The BET theory considers that the binding energy between the surface first monolayer and the adsorbate is equal to the isosteric heat of adsorption, while a second binding energy for adsorption of all the subsequent monolayers is equal to the molar heat of condensation [218]. According to this model, the adsorption isotherms can be classified into six different types (Figure 3.3) [219,220]:

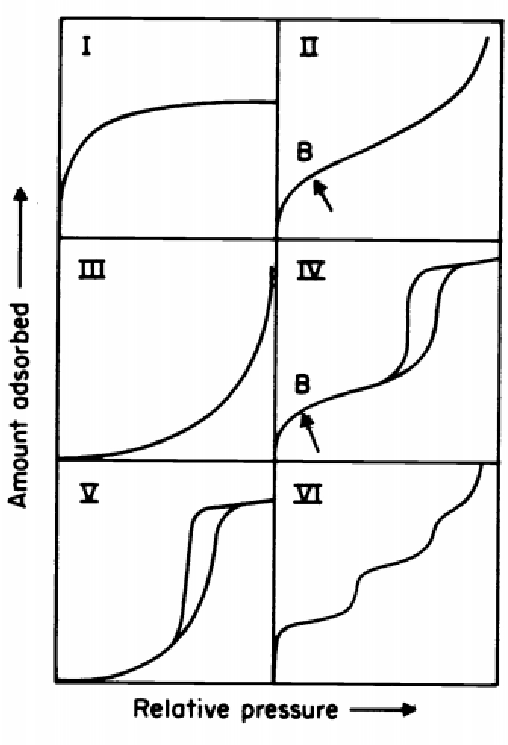

Figure 3.3. *The six types of nitrogen adsorption-desorption isotherms in the BET classification [219]. Reproduced from IUPAC©, 1985.*

- Type I isotherm: it is associated to microporous solids with small external surfaces, such as activated carbons or zeolites. The limiting uptake is determine by the accessible micropore volume rather than by the internal surface area.
- Type II isotherm: it represents unrestricted monolayer-multilayer adsorption, and it is observed in non-porous or macroporous adsorbents. Point B marks the stage at which the monolayer is fully covered, and begins the multilayer adsorption.
- Type III isotherm: it is characterised by a convexity in the whole range, being the Point B absent. It describes unusual systems where adsorbate-adsorbate interactions are important.

- Type IV isotherm: it is characterised by the presence of a hysteresis loop that is linked to capillary condensation taking place in mesopores. The initial path is similar to Type II and it is related to monolayer-multilayer adsorption. This isotherm is observed in many mesoporous industrial adsorbents.
- Type V isotherm: it is an unusual type of isotherm related to Type III. In this case the main feature is the weakness of the adsorbent-adsorbate interaction. It represents some specific porous adsorbents.
- Type VI isotherm: it describes stepwise multilayer adsorption on a uniform non-porous surface, with the height of each step representing the monolayer capacity of each adsorbed layer. It is observed in argon or krypton in graphitised carbon blacks at 77 K.

From the nitrogen adsorption-desorption isotherms the pore size distribution, together with the average pore diameter and the pore volume can be calculated, using the so-called Barrett-Joyner-Halenda (BJH) method. Although these researchers developed this technique initially to be applied to materials with high variability of pore sizes, the method can be applied to any porous materials, including graphene derivatives [221].

3.1.4 Fourier Transform Infra-red Spectroscopy

In this method, infra-red (IR) radiation (mainly that corresponding to the wavenumber range between 4000 and 670 cm^{-1}) is passed through a sample. A part of this radiation is absorbed by the sample, whereas the other part of it is transmitted, resulting in an absorption or transmission spectrum, respectively, with a pattern which is characteristic of each substance. The interferometer produces a signal in time domain that contains all the IR frequencies encoded into it. The Fourier transformation is then used to convert the time domain signals into frequency domain data, which can be interpreted by the analyst. The absorption peaks are associated to the frequency of vibrations between the bonds of the atoms forming the analysed material. Since each combination of atoms is characteristic of each material, the Fourier Transform Infra-red Spectroscopy (FTIR) spectra can provide qualitative information about the nature of the sample, while the intensity of the peaks is linked to the amount of each specific moiety [222].

IR radiation has not enough energy to induce electronic transitions, but it can alter the vibrations and rotations in a molecule, thus producing a net change in the dipole moment. If the frequency of the radiation matches the vibrational frequency of the molecule then the radiation will be absorbed, producing a variation in the amplitude of the molecular vibration. The molecular changes can be classified as follows [223]:

- Molecular rotations: rotational levels are quantised, and IR absorption by gases produces a line spectra. Nevertheless, in liquids and solids the rotational transitions are masked by molecular collisions and other interactions.
- Molecular vibrations: the positions of the atoms in a molecule are not fixed, but subjected to a number of movements that can be classified into two categories:

stretching (change in the interatomic distance along the bond axis) and bending (change in the angle between two bonds). The different subtypes of molecular vibrations are illustrated in Figure 3.4.

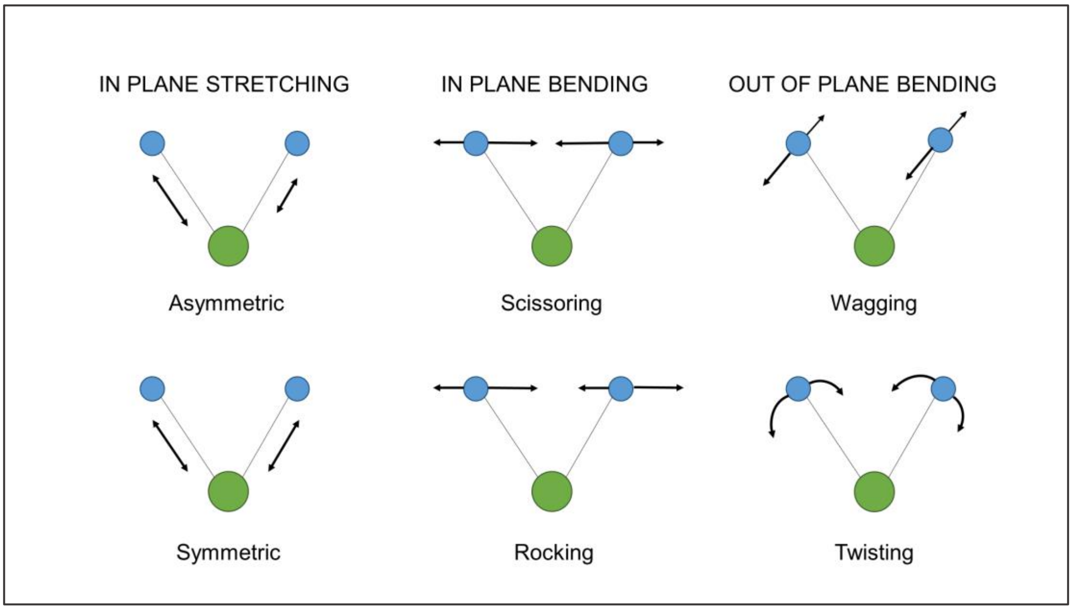

Figure 3.4. *Diagram of the types of molecular vibrations involved in FTIR characterisation.*

In this study, FTIR is applied for the identification of the different oxide groups in graphene oxide precursors, as well as the evaluation of the effect of several reductive methods in the oxide groups of graphene-derived catalysts.

3.1.5 X-ray Fluorescence

X-ray Fluorescence (XRF) is a technique suitable for bulk composition determination, which relies in the emission of characteristic secondary X-ray emission (fluorescence) from a substance that has been previously excited by high-energy X-rays or gamma rays [224]. The wavelength of the fluorescent radiation can be calculated using the Planck's law described by Eq. *3.1*, and it is characteristic of each atom [225]:

$$\lambda = \frac{h\,c}{E} \tag{3.1}$$

where λ is the wavelength of the fluorescent radiation (in m^{-1}), h is the Planck constant (6.626×10^{-34} J s), c is the speed of light in the vacuum (2.998×10^{8} m s^{-1}) and E is the energy associated to the fluorescent radiation (in J) [225].

The fluorescent radiation can be analysed by separating the wavelengths of the radiation. The intensity of the obtained peaks is proportional to the amount of each element in the material studied. This permits this technique to be applied in the detection and quantification of metals and other elements in atomic and chemical analysis [224].

With regard to its application in graphene-related materials characterisation, XRF is especially useful to complement the surface analysis carried out with XPS, which only provides information about the atoms present on the surface, whereas XRF can detect the elements trapped between adjacent layers [226]. For this reason, in the present research XRF is used to investigate the trace metals present inside the characteristic structure of multi-walled nanotubes and other graphene-materials, which cannot be detected by other surface techniques. In addition, XRF is also used in this study to determine the composition of the residue remaining after the application of the thermal treatment in the TGA experiments.

3.1.6 X-ray Diffraction

X-ray Diffraction (XRD) is widely used to obtain information about the molecular and crystalline structure of certain compounds. When a determined electromagnetic radiation beam is incident upon a crystalline sample, this beam is scattered by the atoms of the crystal producing a constructive interference following the Bragg's law, governed by Eq. *3.2* [227]:

$$2\,d\ \sin\theta = n\,\lambda \tag{3.2}$$

where d is the distance between two consecutive diffraction planes, θ is the angle of incidence of the beam with respect the diffraction plane, n is an integer describing the order of diffraction and λ is the wavelength of the beam. These parameters can be visualised in Figure 3.5.

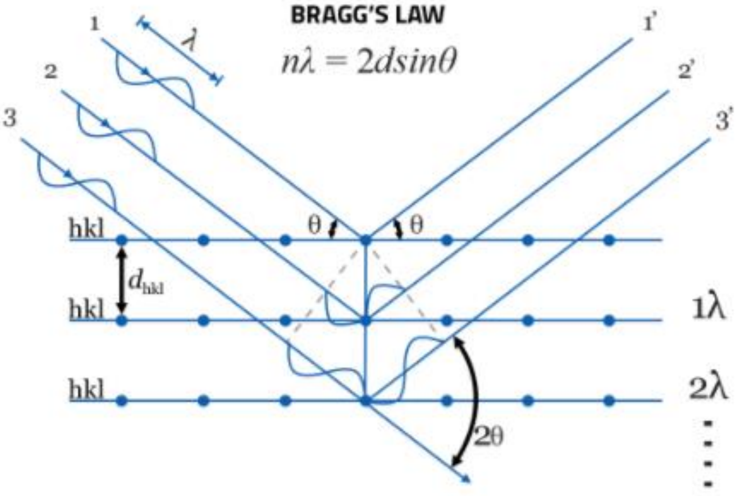

Figure 3.5. *Parameters of the Bragg's equation [228].*

XRD can be useful for characterisation of few-layered graphene-derived materials, more precisely in the calculation of the distance between adjacent graphene layers [229]. This feature is, in turn, related to the presence of oxide groups or heteroatom dopants in the graphene structure. Figure 3.6 shows an example of different graphene-derived catalysts.

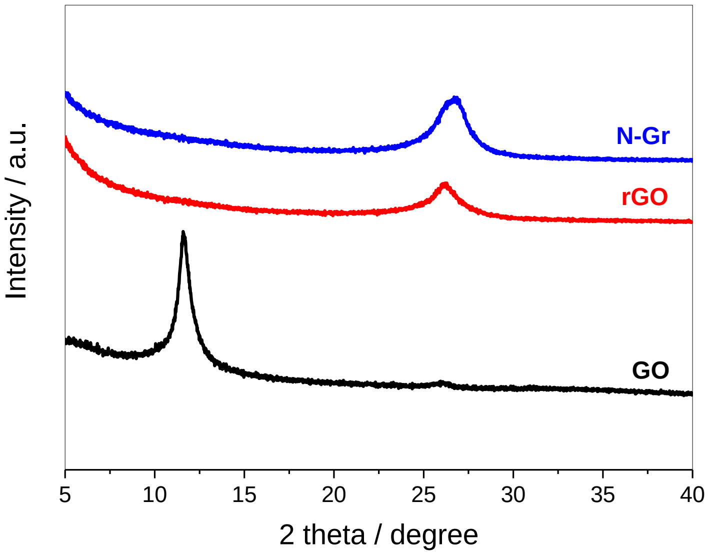

Figure 3.6. *XRD patterns of Graphene Oxide (GO), reduced-Graphene Oxide (rGO) and nitrogen-doped Graphene (N-Gr).*

A characteristic diffraction peak is observed at 11.6° in the GO catalyst corresponding to an interlayer space of 0.79 nm [164]. This peak is absent in rGO and N-Gr due to the reduction of the oxide groups, and a new peak is appearing at around 26.6° associated to a distance of 0.34 nm between adjacent layers [230]. It can be seen, however, that the peak is shifted to the right (larger value of θ) in the case of N-Gr with respect to rGO, which reflects the influence of the N atoms in the interlayer distance.

3.1.7 Raman Spectroscopy

This technique is used to detect the structural pattern of the molecules based on their specific vibrational and rotational modes, which are characteristic of the different substances. A laser energy source is used to produce a monochromatic light that interacts with the molecular vibrations or rotations of the studied sample, producing an energy shift that is linked to an inelastic scattering, also called Raman effect. Since this Raman scattering is very weak compared with the intense Rayleigh scattered light, the latter should be filtered by an edge or band pass filter, being the rest of the light collected by a detector [231].

This technique has been widely applied in the characterisation of graphene related catalysts, due to the well-known Raman spectra of graphene with some characteristic peaks that provide very precise information about the configuration of these materials. In a Raman spectra the intensity of the signal is plotted versus the Raman shift. Figure 3.7 shows a typical Raman spectra of a graphene oxide material.

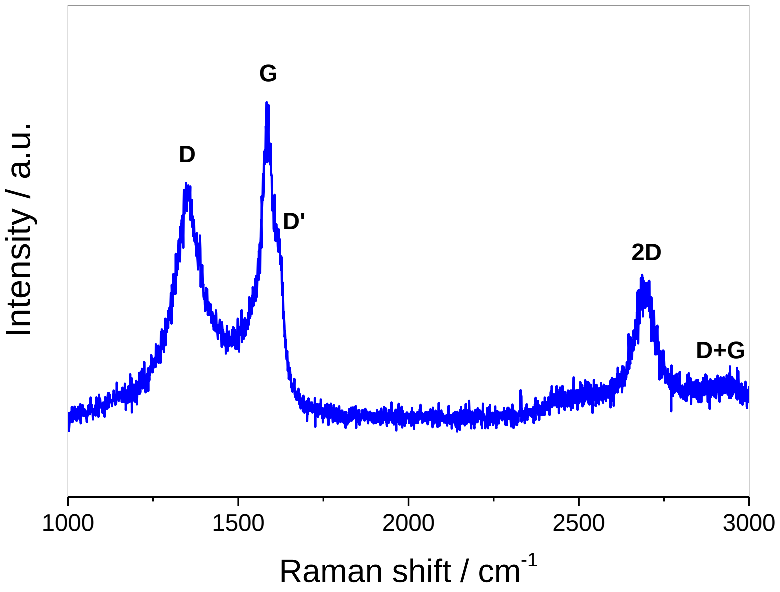

Figure 3.7. *Raman spectra of graphene oxide, using an excitation laser wavelength of 532 nm.*

In Figure 3.7 it can be identified some peaks characteristic of graphene materials [112,232]:

- D peak: it arises at around 1330 cm^{-1}. The intensity of this peak permits an estimation of the amount of defects or lattice distortion in the graphene structure.
- G peak: it appears at 1580 cm^{-1}. It arises from the in-plane bond stretching of all sp^2 C bonded pairs, and therefore is linked to the degree of graphitisation.
- D’ peak: it appears at around 1620 cm^{-1}, and it originates from the intravalley double resonance scattering process. It provides information about the nature of the defects in the graphene layer.

- 2D peak: it arises at 2650 cm^{-2}. It is the overtone of the D band and originates from a two-phonon double resonant process. It is considered to be affected by the presence of dopants in the graphene structure.
- D+G peak: it appears at 2910 cm^{-1}, and it is attributed to graphene lattice disorders.

From the intensity values of these peaks some characteristic ratios providing information about the structure of the material can be obtained. For example, the I_D/I_G ratio is related to the disorder degree of graphene, the I_{2D}/I_G relationship is strongly dependent on doping and the $I_D/I_{D'}$ is linked to the nature of the defects.

3.1.8 X-ray Photoelectron Spectroscopy

X-ray Photoelectron Spectroscopy (XPS) is based in the photoelectric effect discovered by Albert Einstein (for which he received the Nobel prize in 1921) [233] and developed by Kai Siegbahn in the 1960s at the University of Uppsala, Sweden. A monochromatic X-ray source (usually Al(Kα): hv = 1486.6 eV, or Mg(Kα): hv = 1253.6 eV) is generated and interacts with the surface of the sample, being an electron ejected from this surface (as displayed in Figure 3.8) [234]:

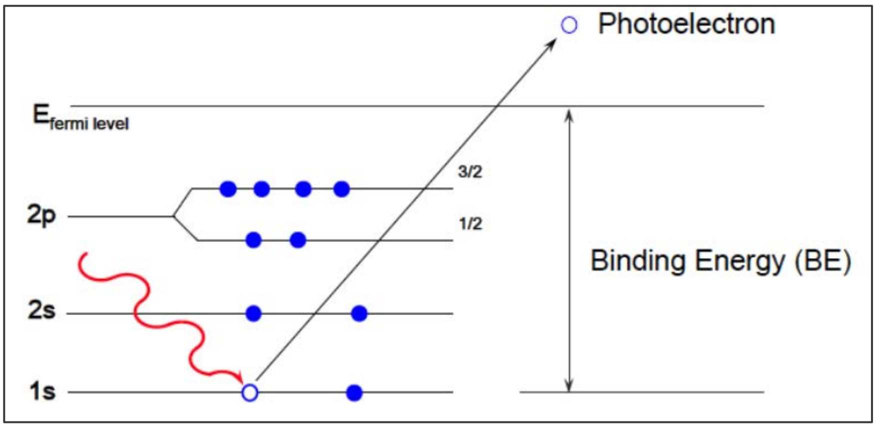

Figure 3.8. *Diagram of the working principle of the photoelectric effect as applied in the XPS technique [235].*

The kinetic energy of the electron ejected from the surface is described by Eq. *3.3* [234]:

$$KE = h\,\nu - BE - \varphi \tag{3.3}$$

where KE is the kinetic energy of the ejected electron, $h\,\nu$ is the energy of the incident X-ray beam, BE is the binding energy of the atomic orbital from which the electron is ejected, and φ is the minimum energy to extract an electron from the surface, usually called the work-function. In a characteristic XPS spectra the intensity of the signal is plotted versus the binding energy calculated from Eq. *3.3*, being the positions of the different peaks assigned to the corresponding species.

XPS can provide valuable information of the analysed sample, such as [236]:

- Study of the surface composition and identification of elements on the surface, from lithium to uranium, with a detection limit ranging from 0.01 to 0.5 atom percent.
- Determination of the electronic structure of the valence band.
- Identification of the oxidation states of transition metals.
- Study of the chemical environmental, for example in corrosion investigations.

It should be mentioned, however, that this technique is suitable for surface analysis, but *not* for the determination of elemental bulk compositions [236]. This makes XPS particularly appropriate for the characterisation of graphene materials.

3.2 Electrochemical methods

Here the methodology used to evaluate the ORR activity of the different catalysts is described. A detailed description of the materials and equipment used in the experiments is provided, paying special attention to the procedures employed for the synthesis and electrochemical characterisation of the catalysts.

3.2.1 Three-electrode system

A three-electrode system as depicted in Figure 3.9 is required to perform the voltammetry experiments in which the catalysts are characterised in terms of their catalytic behaviour by measuring the current density generated under the application of a potential range. The electrodes are immersed in an aqueous electrolyte solution saturated with the reactant of interest, in this case an O_2-saturated (1.26×10^{-6} mol cm^{-3} at 25 °C [237]) 0.1 M KOH solution, with a pH of 13, which is the standard solution reported in the literature to study the ORR catalysis in alkaline media. Each of the three electrodes has a determined function that makes the system to work properly, as described below [238]:

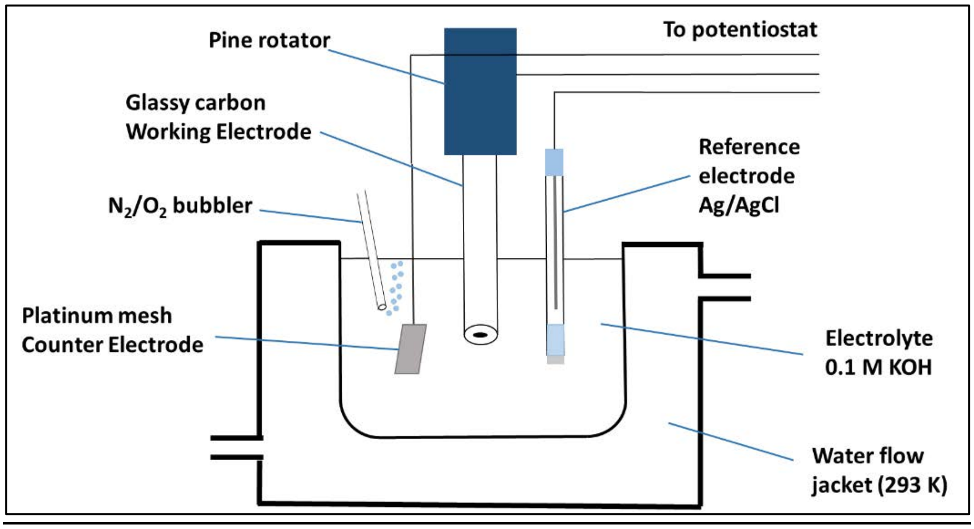

Figure 3.9. Diagram of three-electrode system used for electrochemical characterisation of catalysts.

The reference electrode (RE) is needed because the potential of the working electrode does not have an absolute value and should be measured versus a standard electrode with a well-known potential [238]. There are different reference electrodes with well-known potentials, but in the present study an Ag/AgCl (KCl sat. or 3 M) reference electrode is used, with a potential of +0.197 V or +0.210 V versus the Standard Hydrogen Electrode (SHE), respectively. This electrode consists on an Ag wire submerged in a KCl solution (3 M or saturated, depending on the experiment), where a semipermeable frit separates the KCl solution from the external 0.1 M KOH electrolyte [239].

The counter electrode (CE) also known as auxiliary electrode, passes all the current needed to balance the current observed at the working electrode, permitting the potential of the working electrode to be measured against a known reference electrode without compromising the stability of that reference electrode by passing current over it. The key properties that a good counter electrode should hold are [238]:

- It must be a very good electrical conductor.
- It should be made of an electrochemically inert material, such as platinum, carbon or gold.
- It should have a surface much larger than the working electrode in order to ensure that it does not limit the reaction at the working electrode.

In the experiments carried out in this work, a platinum mesh is used due to its inertness, stability, large surface area and excellent electrical conductivity.

The working electrode (WE) is the electrode where the reaction of interest takes place. It consists of a chemically inert and catalytically active metal, such as platinum, gold or silver, or non-metal, such as glassy carbon. The working electrode can be modified, for example by drop-casting a catalytic ink, being this a common methodology to analyse the catalytic behaviour of both organic or inorganic samples [240]. In the present study, the different catalysts are tested by depositing a certain amount of the corresponding catalytic ink into a glassy carbon WE. After this the electrode is left to dry under rotation, in order to get a uniform catalyst layer, and then the electrode is submerged into the electrolyte to perform the electrochemical tests.

Taking into account the very low solubility of O_2 in water at 25 °C (1.26×10^{-6} mol cm^{-3} [237]), the ORR activity can be only successfully evaluated if a convective method is used for the measurements. To this effect, the rotating disk electrode (RDE), consisting in a disk electrode mounted in a rotating shaft, is a valuable technique which permits to obtain a convective system for ORR evaluation. The rotating speed can be either manually or automatically controlled from the rotator. A typical current density-potential (iV) curve is shown in Figure 3.10 [4]:

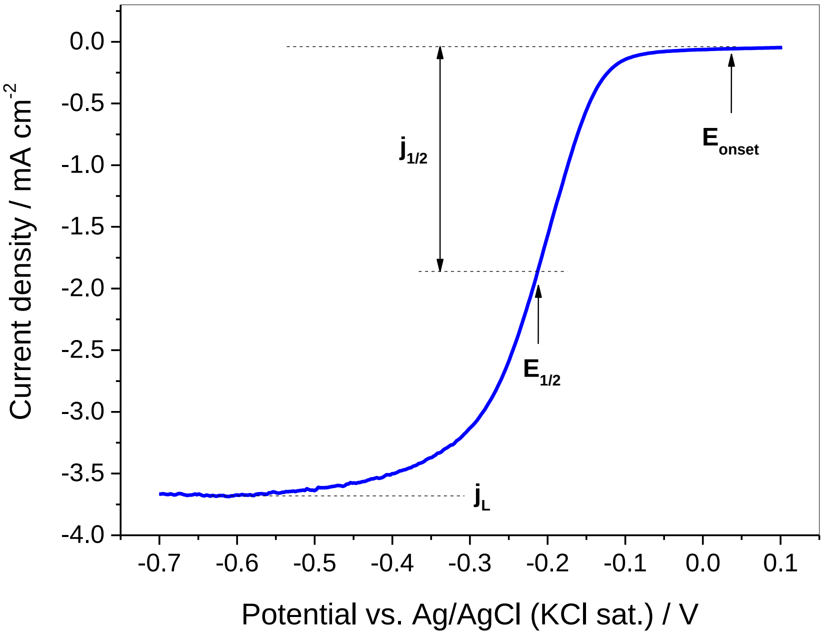

Figure 3.10. *ORR polarisation curve of a perovskite/doped-graphene hybrid catalyst from a RRDE system at 1600 rpm, showing some parameters of the reaction kinetics.*

Some important parameters can be obtained from Figure 3.10. The onset potential (E_{onset}), that is the potential at which the current density starts to move from zero; the half-wave potential ($E_{1/2}$), that is the potential at which the current density reaches a value that is the half of the limited current density; and the diffusion-limited current density (j_L), that is the value of current at which the concentration of reactants on the electrode surface reaches a maximum due to mass transport limitations [4].

3.2.2 Calculation of the number of electrons transferred in the electrochemical reaction

The number of electrons transferred during the ORR (n) is a crucial parameter that informs about the ORR mechanism taking place for a given catalyst. There are two proposed methods to calculate the value of n: one indirect method where this value is calculated from measurements at different rotation speeds, using the Koutecky-Levich (K-L) equation; and another direct method, where the value of n is determined by direct measurement of the peroxide intermediate formation. Both methods are described in this section.

3.2.2.1 Indirect calculation of n using the Koutecky-Levich equation

One very widespread method to calculate the value of n is based in the application of different rotation speeds in order to obtain different values of diffusion-limited current densities. One example of iV curves obtained at different rotation speeds is shown in Figure 3.11:

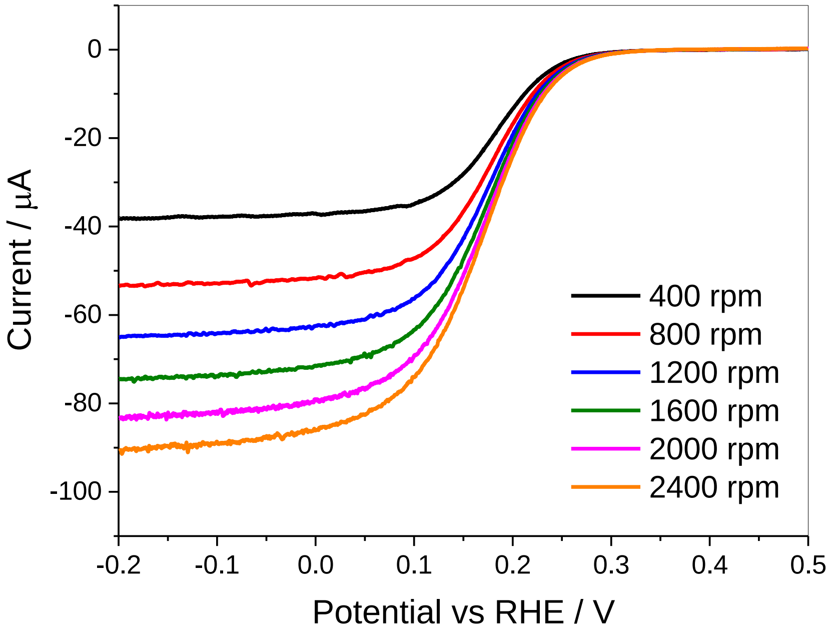

Figure 3.11. *Linear sweep voltammetry (LSV) measurements at different rotation speeds of a Pt RDE in O_2-saturated 0.1 M $HClO_4$ solution.*

The values of the measured current densities are related to the applied rotation speeds by the Koutecky-Levich (K-L) equation (Eq. *3.4*) [241]:

$$\frac{1}{j} = \frac{1}{j_L} + \frac{1}{j_K} = \frac{1}{0.62\, n\, F\, D_0^{\frac{2}{3}}\, \nu^{-\frac{1}{6}}\, C_0\, \omega^{\frac{1}{2}}} + \frac{1}{n\, F\, k\, C_0} \qquad (3.4)$$

where j is the measured current density, j_L is the diffusion-limiting current density, j_K is the kinetic-limiting current density, n is the number of electrons transferred in the reaction, F is the Faraday constant (96485.3 C mol^{-1}), D_0 is the diffusion coefficient (1.93 x 10^{-5} cm^2 s^{-1} [35]), v is the kinematic viscosity of the solution (0.01009 cm^2 s^{-1}

[35]), C_0 is the concentration of O_2 (saturated) in the aqueous solution (1.26×10^{-6} mol cm^{-3} at 25 °C [237]), ω is the rotation rate of the electrode (in rad s^{-1}) and k is the electron-transfer rate constant.

The K-L equation permits to separate the kinetic and mass transport contributions from the measured current densities. Therefore, the values of n and k can be calculated from the slope and intercept, respectively, of the K-L equation when $1/j$ is plotted versus $1/\omega^{1/2}$, as displayed in Figure 3.12.

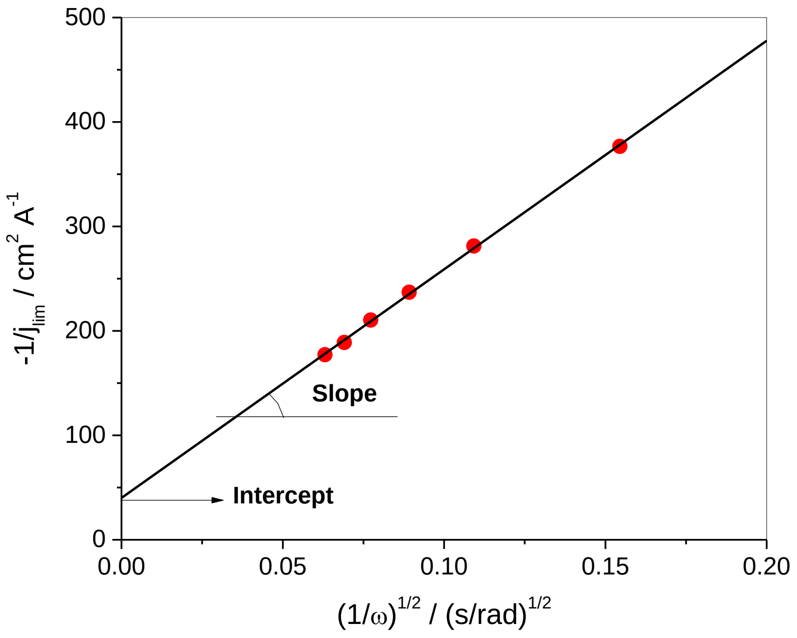

Figure 3.12. *Koutecky-Levich plot at -0.9 V of a Pt/C catalyst in O_2-saturated 0.1 M $HClO_4$ solution.*

The application of the K-L method for the determination of n has been questioned. The K-L method can be only applied if it is assumed that the ORR is a one-step process. Nevertheless, the ORR has been demonstrated to be a multi-step process. In addition, the K-L method should not be applied to rough surface catalysts, which limits its suitability in the characterisation of porous graphene materials [242–245].

3.2.2.2 Direct determination of n by peroxide intermediate measurement

For the detection of the peroxide intermediates produced during the ORR a rotating ring-disk electrode (RRDE) like that shown in Figure 3.13 is used.

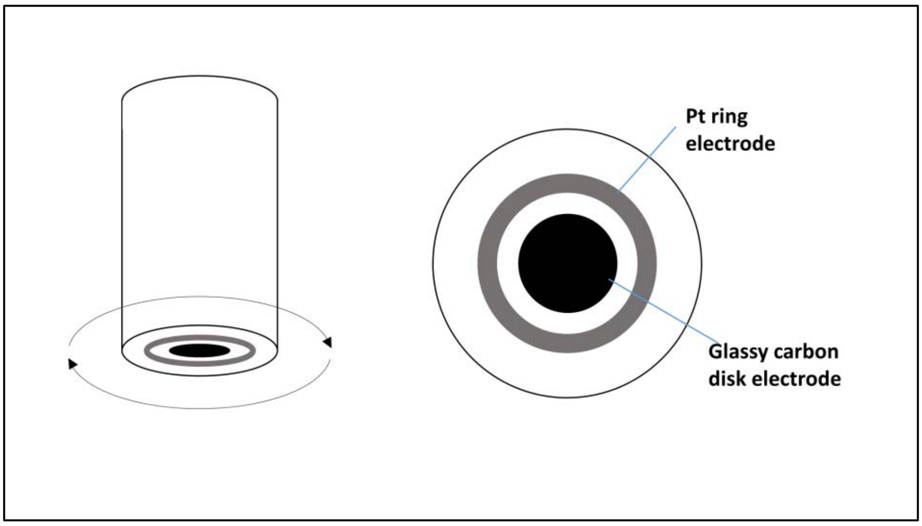

Figure 3.13. *Schematic diagram of a RRDE.*

The RRDE is formed by a central disk where the electrochemical reaction takes place (in this work a glassy carbon (GC) disk modified by drop-casting the catalyst ink), surrounded by a concentric ring, normally made of gold or platinum, whose potential is fixed in such a way that all the peroxide can be oxidised. The peroxide moves from the central disk towards the concentric ring due to the convective forces created by the rotation.

The resulting iV curves from the RRDE measurement are normally displayed in two adjacent graphs, showing the measured disk current j_D at the bottom and the measured ring current j_R at the top, as shown in Figure 3.14.

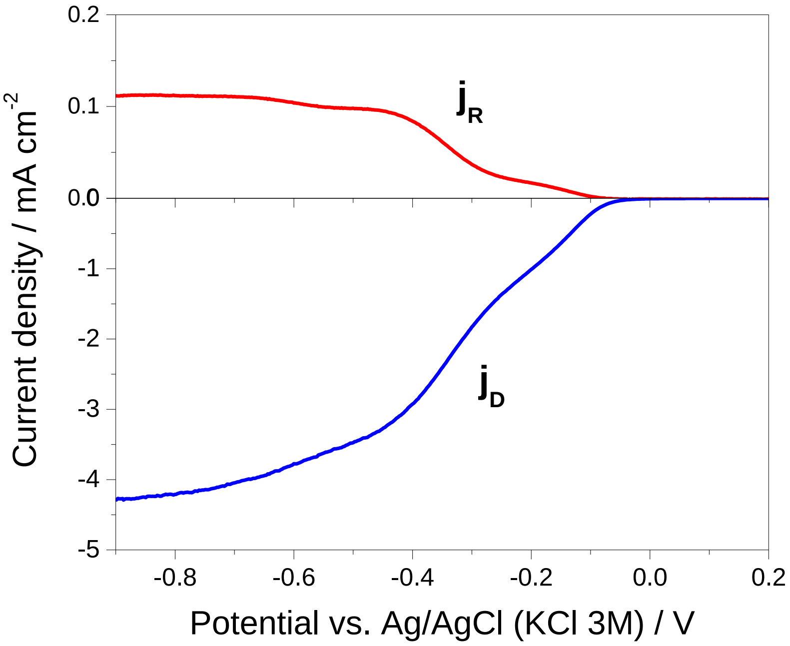

Figure 3.14. *RRDE measurements of a Pt/C catalyst at loading of 20 µg Pt/C cm^{-2} on 0.2475 cm^2 area GC working electrode in O_2-saturated 0.1 M KOH at 25 °C. j_R ring current (in red, ring potential fixed at +0.47 V) is displayed at the top (ring area 0.1866 cm^2) and j_D disk current (in blue) is displayed at the bottom.*

From the data derived from these graphs, the values of *n* can be calculated using Eq. *3.5* [36]:

$$n = \frac{4\,I_D}{I_D + \left(\frac{I_R}{N}\right)} \qquad (3.5)$$

where *n* is the number of electrons transferred, I_D the current measured at the GC disk ($I_D(H_2O)+I_D(H_2O_2)$), I_R the current measured at the Pt ring (related to the oxidation of H_2O_2) and *N* the collection efficiency which is a design parameter provided by the RRDE manufacturer (for the equipment used in this thesis, N=0.37).

These values of n are closely related to the selectivity of the reaction, which can be quantified by the fraction of peroxide intermediate produced in the reaction (X_{H2O2}) using the Eq. *3.6* [246]:

$$X_{H_2O_2} = \frac{2\left(\frac{I_R}{N}\right)}{I_D + \left(\frac{I_R}{N}\right)} \qquad (3.6)$$

This method for the direct determination of n via peroxide intermediate measurement is more straightforward and has fewer limitations than the indirect method based in the K-L equation, as long as the fixed ring potential ensures complete peroxide decomposition. Therefore, it has been chosen as the preferred method for calculation of n in the present study.

3.2.3 Calculation of the electrochemical surface area

The electrochemical surface area (ECSA) is one important parameter in catalyst characterisation and refers to the area of the catalyst that is catalytically active towards the reaction of interest. There are two main methods to obtain the ECSA in Pt/carbon support systems: hydrogen underpotential deposition (H_{upd}) and carbon monoxide stripping voltammetry [247]. In this study, H_{upd} is employed to calculate the ECSA, and will be described in the present section.

In the H_{upd} process, a monolayer of hydrogen is adsorbed-desorbed onto the surface of the catalytically active platinum catalyst [248], according to Reaction *3.7*.

$$Pt + H^+ + e^- \leftrightarrows Pt\text{-}H_{ads} \qquad (3.7)$$

Figure 3.15 shows the typical cyclic voltammetry (CV) curve of a platinum supported on carbon catalyst in a 0.1 M $HClO_4$ electrolyte. The areas marked in red correspond to the anodic process of the hydrogen desorption and the cathodic adsorption charge.

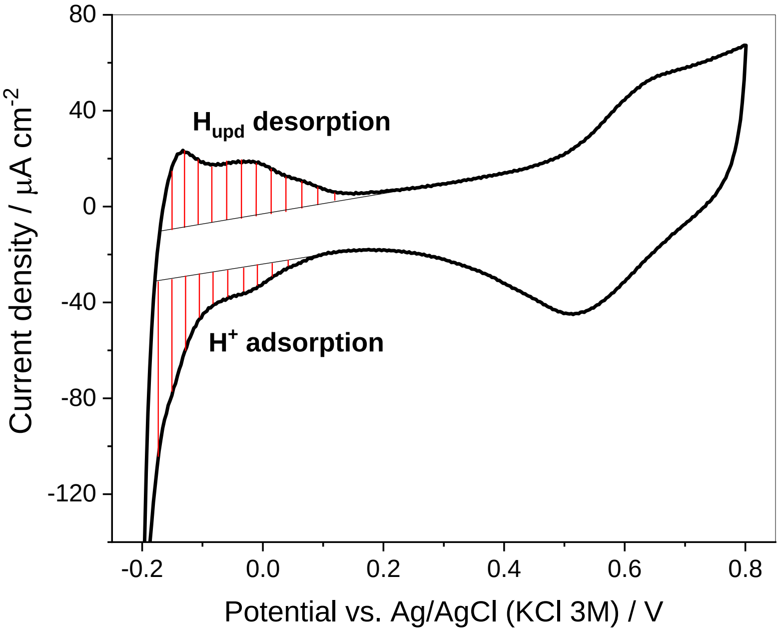

Figure 3.15. *CV obtained in N_2-saturated 0.1 M $HClO_4$ solution at 20 mV s^{-1} and 293 K for a Pt/C catalyst, with a catalyst loading of 0.13 mg cm^{-2} (sloping baselines are due to resistivity of the sample [241]).*

In order to calculate the ECSA using this method, some assumptions should be done [249]. First, one hydrogen atom is adsorbed on a single Pt surface centre. Second, an equal distribution of the three low-index planes (100), (110) and (111) is assumed.

The ECSA is preferably calculated from the area under the anodic hydrogen desorption curve (Q_{Hupd}). The ECSA is then calculated using Eq. *3.8* [250]:

$$ECSA = \frac{Q_{Hupd}}{Q_{ML}\, L_{Pt}\, A_{geo}} \tag{3.8}$$

where *ECSA* is the electrochemical surface area (in m^2 g_{Pt}), Q_{Hupd} is the anodic hydrogen desorption charge (in μC), Q_{ML} is the area-normalised charge for removing a complete monolayer of the species (210 μC cm^{-2} for Pt [251]), L_{Pt} is the platinum loading (in g_{Pt} cm^{-2}) and A_{geo} is the glassy carbon electrode geometric area (in cm^2). A correction factor of 10^4 cm^2 m^{-2} should be inserted in the denominator to keep the homogeneity of the units.

The H_{upd} method for ECSA determination has been established as a standard for Pt and Rh electrodes, being the accuracy of this method estimated to be within 10% [249].

3.2.4 Electrochemical Impedance Spectroscopy

Electrochemical Impedance Spectroscopy (EIS) is a sophisticated technique that permits to study the complex electrochemical processes taking place in the catalytic system, being able to separate the activation, ohmic and mass transport losses which characterise the performance of a catalyst [252]. EIS uses a small amplitude sinusoidal alternating current (AC) signal over a wide range of frequencies to create the impedance spectrum, where the amplitude and the phase shift of the resultant current are shown. For this reason, this technique is sometimes called AC Impedance. In this work, EIS is used to determine the resistance of the catalyst layer deposited onto the GC electrode, and therefore a detailed description of the EIS technique is beyond the scope of this section.

Among the impedance spectrum modes for the visualisation of the AC Impedance measurements, Nyquist plots are the most widespread due to their simplicity and capacity to show all the information in one single graph [253]. A typical Nyquist plot represents the negative value of imaginary component of impedance ($-Z_{imag}$) in the Y axis versus the real component of impedance (Z_{real}) in the abscissa. Figure 3.16 shows the Nyquist plot of two graphene-derived catalysts:

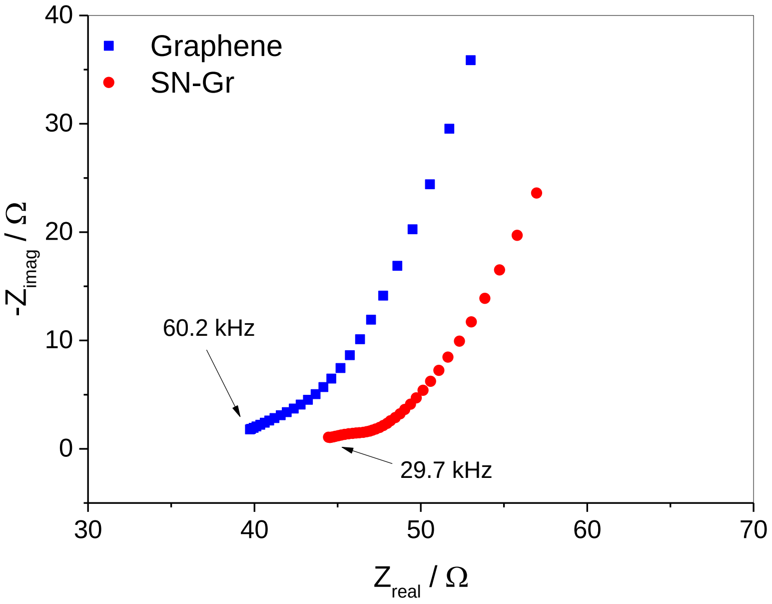

Figure 3.16. *Example Nyquist plot of pure graphene and nitrogen, sulphur-dual doped graphene catalyst, showing the frequencies corresponding to the High Frequency Resistance value.*

From this graph, the ohmic resistance contribution of the overall impedance can be obtained from the high frequency resistance (HFR), which is the value of Z_{real} at which $-Z_{imag}$ equals zero (or approximately zero) at higher frequencies [254]. Unlike the capacitance and mass transport contributions, the ohmic resistance is characterised by that the imaginary component of the impedance is null, i.e. the phase shift is zero.

The ohmic resistance is commonly attributed to three main factors: resistance to ion migration in the electrolyte, resistance to electron transport in the cell components and contact resistances [254]. The ohmic resistance calculated by this method is used in graphene-derived materials to study the presence of defects in the graphene layers.

3.3 Materials, equipment and procedures

In this section the materials and equipment are described, and their providers and technical specifications are detailed. The procedures are also thoroughly described.

3.3.1 Carbon support materials

Carbon Black is Ensaco Conductive Carbon Black (CB) provided by TIMCAL Graphite & Carbon (a member of IMERYS). Multi-walled carbon nanotubes (MWCNT) is provided by Nanostructured & Amorphous Materials INC (Los Alamos, NM 87544, USA), having the next properties: Purity: 95%, length: 10-20 µm, diameter: 20-40 nm, SSA>360 $m^2 g^{-1}$. Graphene oxide (GO) is purchased to Nanoinnova (ref.: GO.M.10.29-1), whereas reduced GO (rGO) is obtained by a chemical reduction with L-ascorbic acid following the procedure described in Section 3.3.2 below.

3.3.2 Procedures for GO reduction

Two methods are proposed for the reduction of GO: a chemical reduction with L-ascorbic acid and an annealing method based in the thermal reduction of GO under inert atmosphere.

The chemical reduction of GO with L-ascorbic acid is based in the procedure described by Zhang et al. [255]. First, 300 mg of commercial GO (Nanoinnova, ref.: GO.M.10.29-1) are deposited into 300 mL of ultrapure water together with 3 g of L-ascorbic acid at room temperature (ca. 298 K). The mixture is left to stir overnight at 500 rpm and then filtered 3 times, washing with copious amount of ultrapure water between filtrations. The catalyst is then dried in the oven at 80 ˚C overnight and finally weighed to check the amount of rGO obtained.

For the annealing method, a catalyst ink is produced by dissolving 100 mg of the same GO in 30 mL of ultrapure water (resistivity ≥18.2 MΩ cm, milli-Q Millipore). The ink is then sonicated (Ultrawave, 50 Hz) for 1 hour and then stirred for 15 hours, before being concentrated by centrifugation at 20000 rpm for 10 minutes at room temperature (Centrifuge Sigma 3K-30 refrigerated). The resulting mixture is placed on an alumina crucible and pyrolised in a quartz tubular furnace (Vecstan Ltd. F400414) at 900 °C for 2 hours, heating rate of 5 °C min^{-1} from room temperature, under 50 mL min^{-1} N_2 atmosphere (BOC gases, O_2 free, 99.998% purity). Finally, the sample is left to cool at room temperature under N_2 atmosphere before being collected and weighed.

3.3.3 Methods for platinum deposition on carbon supports

Two methods are proposed for the deposition of Pt onto the different carbon supports: a microwave-assisted polyol reduction process (MWAPRP) and a sodium borohydride chemical reduction process ($NaBH_4$-CRP).

The deposition of Pt nanoparticles onto a carbon support by MWAPRP is based on the work of Yu and co-workers [256]. 50 mg of carbon supports are suspended in a solution of 24 mL of ethylene glycol (EG) and 6 mL of isopropyl alcohol (IPA), and sonicated for 1 hour in a 30 kHz sonic bath. After this, 31.2 mg of $K_2PtCl_6 \cdot 6\ H_2O$ is added and sonicated for a further 1 hour to obtain an uniform distribution. After sonication, KOH is added to the solution to set the pH at 12, using universal indicator paper to monitor the pH. The solution is then stirred at 400 rpm for 30 minutes under a N_2 atmosphere and then placed in a microwave where 800 W are applied for 40 seconds. Afterwards, the pH is adjusted to 2 by addition of concentrated HNO_3 and then the solution is stirred at 400 rpm overnight. The catalyst is then separated from the solution by three consecutive centrifugations (21,000 rpm for 3 minutes) and acetone wash cycles. Finally, the catalyst is dried in a vacuum oven at 60 ^{o}C for 2 hours.

The synthesis of Pt/C catalysts by $NaBH_4$-CRP follows a procedure based in Fang and co-workers [257]. 195.2 mg of carbon support are dissolved into 200 mL of ultrapure water. After 30 minutes of sonication, 5 mL of 0.05 M K_2PtCl_6 aqueous solution (121.5 mg of K_2PtCl_6 in 5 mL ultrapure water) is added and stirred at 500 rpm for 3 hours. Next, KOH was added to adjust the pH at 8 and then 5 mL of an aqueous solution containing 94.6 mg of $NaBH_4$ (the amount is calculated to provide a $NaBH_4$:Pt molar ratio of 10:1) is added to the solution. After stirring at 500 rpm overnight the solution is filtered, thoroughly washing the catalyst with ultrapure water. Finally, the catalyst is left to dry in the oven at 80 ˚C overnight and then weighed.

3.3.4 Graphene-doping procedure

The graphene-doped catalysts are prepared *via* a thermal annealing of a mixture formed by GO and the precursors of the different doping agents. The precursors are boric acid, melamine, dibenzyl disulphide, iron (III) chloride (all Sigma Aldrich, ≥98%), and orthophosphoric acid (Fisher Scientific, 86.75%). For the single-doped catalysts 100 mg of GO are mixed with 500 mg of precursor (except 100 mg in the case of dibenzyl disulphide) in 30 mL of ultrapure water (resistivity ≥18.2 MΩ cm, milli-Q Millipore). For the dual-doped graphenes, 100 mg of GO are mixed with 500 mg of melamine plus 100 mg of the corresponding second precursor (except 76.5 mg for $FeCl_3$). For the ternary-doped catalysts, 100 mg of GO are mixed with 300 mg of boric acid, 150 of dibenzyl disulphide and 500 mg of the third precursor. For the quaternary-doped catalyst, the composition of the mixture is 100 mg of GO, 200 mg of boric acid, 300 mg of melamine, 500 mg of phosphoric acid and 100 mg of benzyl disulphide in 30 mL of ultrapure water. The inks are sonicated (Ultrawave, 50 Hz) for 1 hour and then stirred for 15 hours, before being concentrated by centrifugation at 20000 rpm for 10 minutes at room temperature (Centrifuge Sigma 3K-30 refrigerated). The resulting mixture is placed on an alumina crucible and pyrolised in a quartz tubular furnace (Vecstan Ltd. F400414) at 900 °C for 2 hours, heating rate of 5 °C min^{-1} from room temperature, under 50 mL min^{-1} N_2 atmosphere (BOC gases, O_2 free, 99.998% purity). Finally, the sample is left to cool at room temperature under N_2 atmosphere before being collected and weighed.

3.3.5 Synthesis of perovskites

For the synthesis of $Ba_{0.8}Bi_{0.2}Co_{0.6}Fe_{0.4}O_{3-\delta}$ (BBCF) and $Ba_{0.7}Sr_{0.2}Bi_{0.1}Co_{0.6}Fe_{0.4}O_{3-\delta}$ (BSBCF) perovskites, stoichiometric amounts of $BaCO_3$, Bi_2O_3, Co_3O_4, Fe_2O_3 and $SrCO_3$ powders (Sigma Aldrich, ≥99%) were intimately ground and heated at 5 ˚C min^{-1} to 850 ˚C in air and held at that temperature for 12 hours. The powders were then reground and reheated (5 ˚C min^{-1}) to 950 ˚C for 6 hours.

For the synthesis of $CaFe_{0.7}Si_{0.2}Mn_{0.1}O_{3-\delta}$ (CFSM) and $CaMn_{0.7}Ti_{0.2}Si_{0.1}O_{3-\delta}$ (CMTS) perovskites, stoichiometric amounts of $CaCO_3$, Fe_2O_3, SiO_2, MnO_2 and TiO_2 powders (Sigma Aldrich, ≥99%) were intimately ground and heated at 5 ˚C min^{-1} to 1100 ˚C in air and held at that temperature for 12 hours. The powders were then reground and reheated (5 ˚C min^{-1}) to 1200 ˚C ($CaFe_{0.7}Si_{0.2}Mn_{0.1}O_{3-\delta}$) or 1300 ˚C ($CaMn_{0.7}Ti_{0.2}Si_{0.1}O_{3-\delta}$) for 12 hours.

3.3.6 Equipment for physical characterisation

TGA is carried out using a TG 209 F1 Libra thermo-gravimetric analyser (TA Instruments). The samples are placed in an alumina crucible and then heated from 25 to 900 °C with a heating rate of 10 °C min^{-1} under a flow of air at 50 mL min^{-1}.

The different catalysts are imaged by a TEM using a JEOL 2100F at 200 kV, equipped with a FEG source and a Gatan Orius CCD camera in order to obtain images with 0.025 nm pixel resolution. The EDX spectra are taken on a Tecnai F20 FEG (S)TEM operating at 200 kV, equipped with an Oxford Instruments X-Ma SDD EDX system. The TEM and STEM-EDS samples are prepared by drying a 10 µL droplet of catalyst aqueous suspension on a Cu grid.

The specific surface areas and porous structures of the quaternary-doped catalyst are measured with a Micromeritics TriStar II Plus adsorption instrument by physical adsorption-desorption of N_2 at 77 K in order to get the N_2 adsorption-desorption isotherms. The BET and BHJ methods are used to calculate the active surface area and the pore size area and volume, respectively, from the N_2 isotherm data.

Catalysts based on GO and rGO carbon supports are characterised by FTIR using a PerkinElmer FT-IR Spectrum 100.

XRF is performed using a Niton XL3T TYPE 980 portable XRF analyser + Helium GOLDD for light element analysis. An X-Ray tube with a 50 kv Ag anode is used for precious metal spectra evaluation.

XRD measurements are obtained using a PANalytican Empyrean Pro X-ray powder diffractometer with a not monochromated Cu X-ray source.

Raman spectra are recorded using a Raman Microscope Renishaw inVia system with an excitation laser wavelength of 532 nm.

X-ray photoelectron spectroscopy (XPS) spectra are obtained at the National EPSRC XPS Users' Service (NEXUS) at Newcastle University using a Thermo Scientific K-Alpha XPS instrument with a monochromatic Al Kα X-ray source.

3.3.7 Equipment and procedures for electrochemical characterisation

Due to the inherent experimental conditions for each different catalysts, the electrochemical procedures are detailed separately for the three sections.

3.3.7.1 Electrochemical characterisation of carbon supports

Several catalyst inks are prepared with the different catalysts. The ink is made by mixing 4 mg of the required catalyst with 0.8 mL of IPA, 3.18 mL of ultrapure water and 0.02 mL of the commercial I2 ionomer solution (Acta S.p.a.) to act as a binder, obtaining an ink with 1 mg mL^{-1} of catalyst concentration and 0.02% of I2 ionomer. This mixture is then sonicated for 1 hour and after this a 5 µL aliquot is pipetted onto the GC disk, to give a loading of 20 µg cm^{-2}. After the ink deposition the droplet is left to dry at room temperature for 30 minutes at 700 rpm as described in literature [258] in order to get an uniform layer. In the case of ECSA determination, the ink is formed by 5 mg of the catalyst, 1.6 mL of ultrapure water, 0.4 mL of IPA and 20 µL of 5% Nafion solution (Fluka 117-Nafion Solution in a mixture of water and aliphatic alcohols), with a final concentration of 2.5 mg catalyst per mL (1 hour sonication). 10 µL of this ink is pipetted onto a GC electrode (5 mm diameter) and let dry for 30 min at 700 rpm.

For the *ex-situ* characterisation of the catalysts rotating ring-disk voltammetry is performed using a Metrohm AutoLAB PGSTAT128N potentiostat in a Faraday cage. The reference electrode is an Ag/AgCl (KCl 3 M or KCl sat.) electrode (E^0 = +0.210 or +0.197 V vs SHE, respectively) and the counter electrode is a Pt mesh. The RRDE (E7R9 Series, Pine Instruments Inc., USA) is formed by a GC disk (5.61 mm diameter) and a Pt ring with an area of 0.1866 cm^2, with a collection efficiency of 37%. Prior to each experiment the RRDE is thoroughly polished with consecutive alumina slurries of 1, 0.3 and 0.05 µm and then sonicated to remove any impurities. All the experiments are carried out in 0.1 M KOH solution made with ultrapure water (resistivity ≥18.2 MΩ cm, milli-Q Millipore), except for electrochemical surface area (ECSA) characterisation carried out in 0.1 M $HClO_4$ solution.

The RRDE is immersed in the alkaline solution and cycled between -1.2 and +1.0 V at 100 mV s^{-1} until a stable response is observed. The solution is then thoroughly purged with N_2 (BOC gases, O_2 free, 99.998% purity) and voltammograms are measured to determine the capacitive current and ohmic resistance of the solution. The solution is then bubbled with O_2 (BOC gases, N5, 99.999% purity) for 45 minutes until saturation. Linear sweep voltammograms (LSV) are then recorded at 25 mV s^{-1} between -0.4 and +1.0 V at the rotation speeds from 400 to 2400 rpm. The Pt ring voltage is fixed at +0.47 V to ensure complete HO_2^- decomposition [259]. For the ECSA experiment, the solution is purged with N_2 for 30 minutes and cycled between -0.2 V and +0.8 V at 20 mV s^{-1}.

AC impedance measurements are also taken in potentiostatic mode at 0 V vs. the same Ag/AgCl (3 mol dm^{-3}) ref. electrode in 0.1 M KOH solution purged with N_2, with the frequency varying from 100 to 0.01 kHz. The volume of the catalyst solution deposited onto the GC electrode is in this case 6 µL for all the samples, with the rest of the procedure remaining the same as previously explained. The resistance of the layers are not found to depend on the dropcast volume (and hence thickness) in the range from 3 to 12µL. All the measurements are carried out at 293 ± 2 K.

For the *in-situ* fuel cell testing of the catalysts four membrane electrode assemblies (MEAs) are prepared for testing the four synthesised catalysts. In all cases the anode is made with a commercial Pt/CB 20% (Fuel Cell Store®) with a catalyst loading of 0.4 mg cm^{-2} and an ionomer:catalyst ratio of 0.24:1. The ionomer is the Acta I2 commercialised as precursor polymer (4% wt%) dissolved in a mixture of solvents composed by 20% N,N-dimethylformamide and 80% of 1-Propanol. On the cathode side the conditions are the same using the homemade catalysts. The catalyst ink is fabricated mixing 3.75 mg of the desired catalyst (50% in excess to compensate brushing losses), 50 µL of milli-Q water, 22.5 mg of Acta I2 ionomer solution and 2 mL of IPA. This mixture is sonicated for 1 hour before being applied directly onto the microporous side of a Sigracet GDL 35 BC (Ion Power, Inc.) with an area of 6.25 cm^2 (2.5 x 2.5 cm^2) by a brush procedure. Once the ink solvent is evaporated, the electrode is weighed to ensure that the desired catalyst loading is reached. Once both electrodes are made they are stored in ultrapure water for at least 24 hours until use. The membrane is also submerged in ultrapure water for at least 24 hours and then converted to OH^- form immediately before use by immersing it in 1 M KOH solution for 1 hour changing the solution every 20 minutes, as the alkaline exchange membrane cannot be entirely exchanged to OH^- form by only one immersion [11].

Fuel cell tests are carried out in a Scribner 850e Multirange at an operation temperature of 50 °C with fully humidified (100% RH) H_2 at the anode and fully humidified pure O_2 at the cathode (BOC Gases, CO_2 free, purity of N5.0) at 0.4 L min^{-1}, 50 °C and atmospheric pressure. No back pressure is applied and the torque pressure of the fuel cell is adjusted at 200 Ncm. MEAs are pretreated by cycling between OCV and 100 mV for 15 min per cycle until constant performance between two cycles is observed. Performance curves are obtained in incremental steps of 10 mA cm^{-2} per minute from OCV until 100 mV.

3.3.7.2 Electrochemical characterisation of doped-graphene catalysts

The catalyst inks are prepared dispersing 5 mg of the required catalyst in 0.2 mL of IPA (VWR Chemicals), 0.78 mL of ultrapure water and 0.02 mL of 10 wt% Nafion (Ion Power Inc.), obtaining a resulting catalyst concentration of 5 mg mL^{-1}. This mixture is sonicated for 1 hour and then a 15 µL aliquot is pipetted onto the GC disk to give a catalyst loading of 0.3 mg cm^{-2}. The droplet is left to dry at room temperature for 30 minutes at 500 rpm as described in literature [258] in order to get an uniform layer.

The RRDE is then immersed in the O_2-saturated (BOC gases, N5, 99.999% purity) 0.1 M KOH (Sigma-Aldrich, 99.99%) alkaline solution and cycled between +0.4 and -1.0 V at 100 mV s^{-1} until a stable response is observed. Linear sweep voltammograms (LSV) are then recorded at 10 mV s^{-1} between +0.4 and -1.0 V at rotation speeds from 400 to 2400 rpm. The Pt ring voltage is fixed at +0.5 V to ensure complete HO_2^- decomposition [178]. Methanol tolerance is tested by current-time chronoamperometry at -0.5 V (vs. Ag/AgCl) and 1600 rpm rotation rate for 300 s. 4.36 mL of methanol (Fisher Chemical, 99.99%) is added after 60 s into the alkaline solution (175 mL) to give a 0.6 M methanol concentration. All measurements are carried out at 293 ± 2 K.

3.3.7.3 Electrochemical characterisation of doped-graphene/metal hybrid catalysts

The catalyst inks are prepared by dispersing different amounts of the as-prepared dual-doped graphene (or pure graphene sourced from PiKem Ltd.), and $La_{0.8}Sr_{0.2}MnO_3$ (LSM, PRAXAIR Surf. Tech., surface area: 4.19 m^2 g^{-1}), $Ba_{0.8}Bi_{0.2}Co_{0.6}Fe_{0.4}O_{3-\delta}$, $Ba_{0.7}Sr_{0.2}Bi_{0.1}Co_{0.6}Fe_{0.4}O_{3-\delta}$, $CaFe_{0.7}Si_{0.2}Mn_{0.1}O_{3-\delta}$, $CaMn_{0.7}Ti_{0.2}Si_{0.1}O_{3-\delta}$ (BBCF, BSBCF, CFSM and CMTS, respectively, provided by Prof. Peter Raymond Slater from the Birmingham Centre for Energy Storage) or manganese (IV) oxide (MnO_2, Sigma-Aldrich, 99%), to give a total amount of 5 mg (with the desired composition) in 0.2 mL of isopropyl alcohol (VWR Chemicals), 0.78 mL of ultrapure water and 0.02 mL of 10 wt% Nafion (Ion Power Inc.). This mixture is sonicated for 1 hour and then a 15 µL aliquot is pipetted onto the GC disk to give a catalyst loading of 0.3 mg cm^{-2}. The droplet is left to dry at room temperature for 60 minutes at 400 rpm as described in literature [258] in order to get an uniform layer.

The RRDE is then immersed in the O_2-saturated (BOC gases, N5, 99.999% purity) 0.1 M KOH (Sigma-Aldrich, 99.99%) alkaline solution and cycled between +0.4 and -1.0 V at 100 mV s^{-1} until a stable response is observed. Linear sweep voltammograms (LSV) are then recorded at 10 mV s^{-1} between +0.4 and -1.0 V at rotation speeds from 400 to 2400 rpm. The Pt ring voltage is fixed at +0.5 V to ensure complete HO_2^- decomposition.

The AC impedance spectra are also measured via a Metrohm Autolab FRA32M analyser between 500 kHz and 0.1 Hz at 0 V vs Ag/AgCl (KCl sat.) with a signal amplitude of 10 mV. All measurements are carried out at 293±1 K.

4 EVALUATION OF DIFFERENT CARBON MATERIALS AS CATALYST SUPPORTS

In this chapter, four different carbon materials are evaluated as platinum catalyst supports towards the oxygen reduction reaction in alkaline media. The carbon materials are carbon black (CB), multi-walled carbon nanotubes (MWCNT), graphene oxide (GO) and partially-reduced graphene oxide (rGO), obtained by reduction of the same GO with L-ascorbic acid (as described in Section 3.3.2). Platinum is deposited on them, and the resultant catalysts are physically characterised and their catalytic performances towards the ORR in alkaline media evaluated and compared.

4.1 Assessment of methods for Pt deposition on the carbon supports

Two different methods for Pt deposition on the carbon supports are evaluated. The first method is a microwave-assisted polyol reduction process (MWAPRP) based on the method proposed by Yu and co-workers [256], where microwave heating is applied to a mixture of ethylene glycol (EG) and isopropyl alcohol (IPA) in a proportion 4:1, to cause the reduction of the Pt precursor. The second method is a sodium borohydride chemical reduction process ($NaBH_4$-CRP), based on the procedure described by Yu and co-workers [257], where this more reducing agent is used to directly reduce the Pt precursor. In both methods the quantity of reactants is chosen to obtain a theoretical Pt loading of 20% in the total catalyst. Nevertheless, the actual amount of Pt could differ from these values due to inefficiencies of the methods proposed. To find out the actual amount of Pt deposited TGA analysis are carried out, paying special attention to the residual mass remaining after the application of the thermal treatment. These experiments are carried out under ambient (oxidising) atmosphere and temperatures up to 900 °C in such a way that the carbon support would be completely burnt and only the metal should remain as a residue after the application of the thermal treatment.

The results of TGA analysis are shown in Figure 4.1. Thermogravimetric mass loss profiles in air at heating rate of 10 K min-1 of (a) CB, (b) MWCNT, (c) GO and (d) rGO, before (continuous line) and after Pt deposition by MWAPRP (dashed line) and NaBH4-CRP (dotted line).

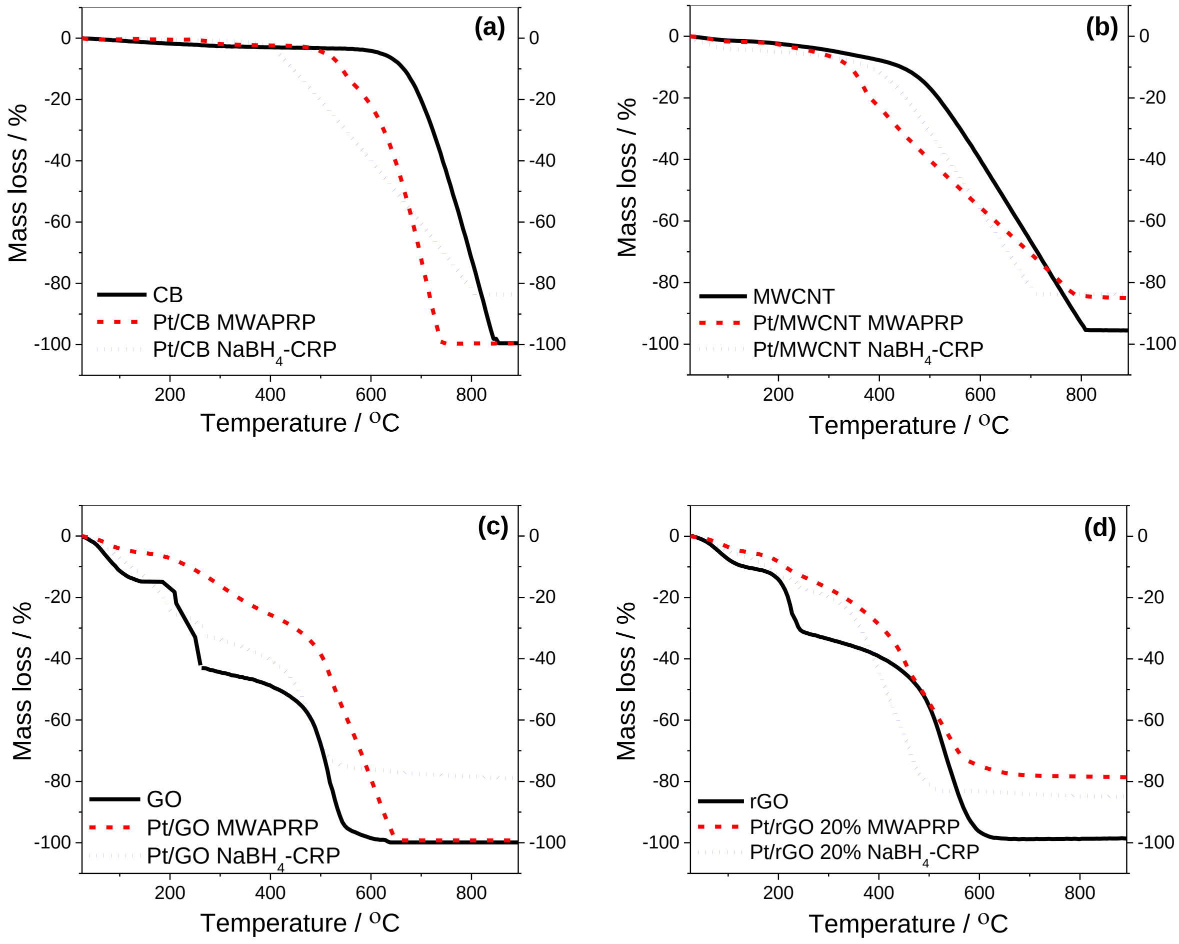

Figure 4.1. *Thermogravimetric mass loss profiles in air at heating rate of 10 K min*$^{-1}$ *of (a) CB, (b) MWCNT, (c) GO and (d) rGO, before (continuous line) and after Pt deposition by MWAPRP (dashed line) and* $NaBH_4$*-CRP (dotted line).*

The continuous black lines reflecting the pure carbon supports before Pt deposition show that CB and MWCNT display a similar pattern with no significant presence of water and further gradual combustion of carbon until the final residue. It is observed in CB (Figure 4.1. Thermogravimetric mass loss profiles in air at heating rate of 10 K min-1 of (a) CB, (b) MWCNT, (c) GO and (d) rGO, before (continuous line) and after Pt deposition by MWAPRP (dashed line) and NaBH4-CRP (dotted line).a) that the onset temperature (T_{onset}) is 684 °C, with no residue remaining after the thermal treatment. In MWCNT (Figure 4.1. Thermogravimetric mass loss profiles in air at heating rate of 10 K min-1 of (a) CB, (b) MWCNT, (c) GO and (d) rGO, before (continuous line) and after Pt deposition by MWAPRP (dashed line) and NaBH4-CRP (dotted line).b) the T_{onset} is 484 °C, presumably due to the easier accessibility of the oxidant to carbon in the nanotube structure [260], thus the oxidation is more gradual compared to CB. In this case, the residual mass is 4.5% which is consistent with the observations of Antunes et al. [261] who reported transition-metal impurities, mainly Fe, remaining from the process of production of nanotubes. The behaviour of GO and rGO is different with respect to CB and MWCNT due to the presence of oxide groups [262]. In GO (Figure 4.1. Thermogravimetric mass loss profiles in air at heating rate of 10 K min-1 of (a) CB, (b) MWCNT, (c) GO and (d) rGO, before (continuous line) and after Pt deposition by MWAPRP (dashed line) and NaBH4-CRP (dotted line).c) there is an initial weight loss of 14.9% until 150 °C, due to evaporation of water trapped in the GO bulk, followed by a decrease of 27.1% until 260 °C due to decarboxylation processes [263]. Further loss of mass at T_{onset} of 470 °C is due to complete carbon combustion until no residue is remaining at the end of the thermal treatment. A similar pattern is observed in rGO (Figure 4.1. Thermogravimetric mass loss profiles in air at heating rate of 10 K min-1 of (a) CB, (b) MWCNT, (c) GO and (d) rGO, before (continuous line) and after Pt deposition by MWAPRP (dashed line) and NaBH4-CRP (dotted line).d), there being a significant difference in the mass loss at 260 °C (related to the degree of decarboxylation) with respect to GO, being in this case only 19.1%. This (together with the fact of that no distortion in the graph is observed) points to a minor presence of oxide species in the case of rGO, just as expected after the reduction of GO with L-ascorbic acid.

In the same graphs, the red dashed and blue dotted lines reflect the effect of the thermal treatment on the catalysts prepared by MWAPRP and $NaBH_4$-CRP, respectively. The residual mass obtained with the MWAPRP is 14.9% for Pt/MWCNT and 21.4% for Pt/rGO, being null for Pt/CB and Pt/GO. The blue dotted lines show the behaviour of the catalysts synthesized by $NaBH_4$-CRP, showing residual masses of 16.3% for Pt/CB, 16.4% for Pt/MWCNT, 20.8% for Pt/GO and 14.9% for Pt/rGO. It is observed that $NaBH_4$-CRP is more efficient for the reduction of K_2PtCl_6 than MWAPRP, especially for CB and GO where no residual mass is detected in MWAPRP. This indicates that $NaBH_4$ performs as a more appropriate reducing agent for Pt deposition than the polyol mixture (80% EG+20% IPA), despite microwave activation in the latter. The high selectivity of $NaBH_4$, previously reported in the literature [264], is clearly reflected in Figure 4.1. Thermogravimetric mass loss profiles in air at heating rate of 10 K min-1 of (a) CB, (b) MWCNT, (c) GO and (d) rGO, before (continuous line) and after Pt deposition by MWAPRP (dashed line) and NaBH4-CRP (dotted line).c, where the polyol mixture spends its reductive potential in the reduction of oxide groups present in GO, then being unable to further reduce the K_2PtCl_6 to Pt particles. Unlike this, $NaBH_4$ only reduces a small part of the oxide groups but deposits the entire Pt present. In the case of rGO (with lower oxide content than GO), the MWAPRP is powerful enough to subsequently produce the Pt deposition. In addition, the surface defects created in rGO during the previous reduction with L-ascorbic acid act as nucleation sites for the Pt nanoparticles deposition [265]. The weakness of the polyol mixture as reducing agent [266] can be seen in Figure 4.1. Thermogravimetric mass loss profiles in air at heating rate of 10 K min-1 of (a) CB, (b) MWCNT, (c) GO and (d) rGO, before (continuous line) and after Pt deposition by MWAPRP (dashed line) and NaBH4-CRP (dotted line).a, where it is observed that the residual mass of the catalyst prepared by MWAPRP is null. On the other hand, the structure of MWCNTs (Figure 4.1. Thermogravimetric mass loss profiles in air at heating rate of 10 K min-1 of (a) CB, (b) MWCNT, (c) GO and (d) rGO, before (continuous line) and after Pt deposition by MWAPRP (dashed line) and NaBH4-CRP (dotted line).b) seems to play a role to facilitate the Pt deposition with this method [267].

In the light of these results, the main conclusion is that the chemical reduction of the Pt precursor with $NaBH_4$ is more efficient than the reduction with a polyol mixture assisted by microwave. The MWAPRP is demonstrated to be efficient with MWCNT and rGO only, highlighting the influence of the carbon material used as catalyst support in the procedure for Pt precursor reduction and further deposition. Due to that the $NaBH_4$-CRP is successful for the four types of carbon analysed, thereinafter only the catalysts prepared by $NaBH_4$-CRP are considered for further study.

Finally, in order to establish the real Pt content in the catalysts prepared by $NaBH_4$-CRP, it should be considered that the Pt particles deposited onto the carbon supports could contain some metal impurities, especially other Pt-group metals (such as Pd, Rh and Ir) which are commonly found in platinum rough materials [268]. XRF has been commonly used as a suitable technique for the determination of metal impurities in different materials [269,270], and it is employed in the present study to determine the

Pt composition of the catalyst particles deposited onto the carbon supports. The main noble metal impurities detected by XRF are Ir, Rh, Pd and Ru, with maximum measured contents of 0.92 ± 0.09 %, 0.56 ± 0.01 %, 0.38 ± 0.01 % and 0.13 ± 0.01 % with respect to the total amount of metal, respectively. The Pt contents in the different catalysts are calculated from the values of residual mass obtained by TGA and the Pt compositions measured in the residue analysis by XRF, and are shown in Table 4.1. Amount of Pt (in percentage with respect to the total amount of metal) of the different catalysts prepared by NaBH4-CRP, calculated from the values of residual mass obtained by TGA and the XRF analysis of the residue..

Table 4.1. *Amount of Pt (in percentage with respect to the total amount of metal) of the different catalysts prepared by $NaBH_4$-CRP, calculated from the values of residual mass obtained by TGA and the XRF analysis of the residue.*

	Pt/CB	**Pt/MWCNT**	**Pt/GO**	**Pt/rGO**
Residual mass (TGA) / %	16.28	16.37	20.80	14.92
Pt in residue (XRF) / %	97.54	91.26	91.83	92.38
Pt loading / %	**15.9**	**14.9**	**19.1**	**13.8**

A considerably higher Pt composition in Pt/GO with respect to the other catalysts is observed, presumably due to the role of the oxide groups anchoring the Pt particles on the support [271]. For the rest of the catalysts the Pt loading can be considered the same, with an average Pt composition of 14.9 ± 1.1 %, which is a significant lower amount than the theoretical 20% for which the reactants were calculated. This permits to estimate the efficiency of the $NaBH_4$-CRP deposition method as approximately 75%.

4.2 Physical characterisation of the catalysts

First, HR-TEM images are taken in order to see the catalyst configuration and the particle size distribution. Figure 4.2 shows the TEM images of the different catalysts together with their corresponding particle size distribution.

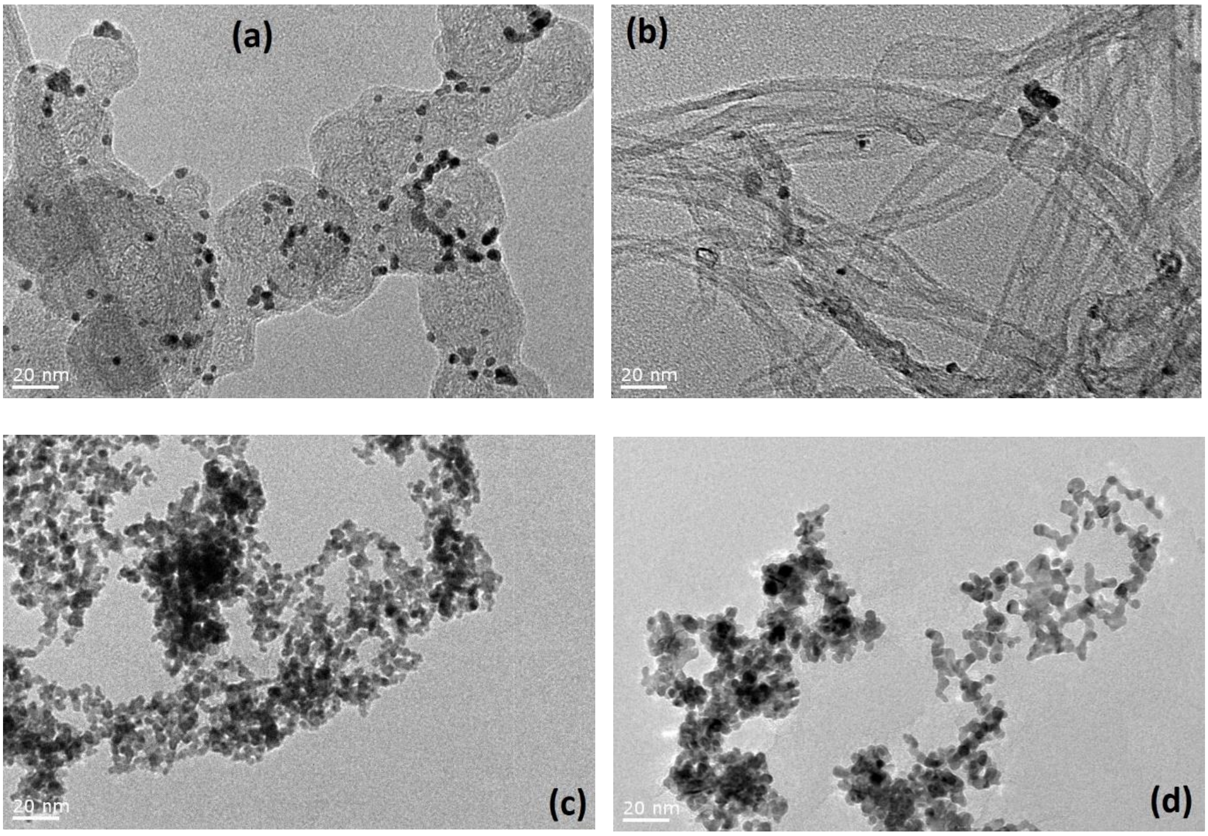

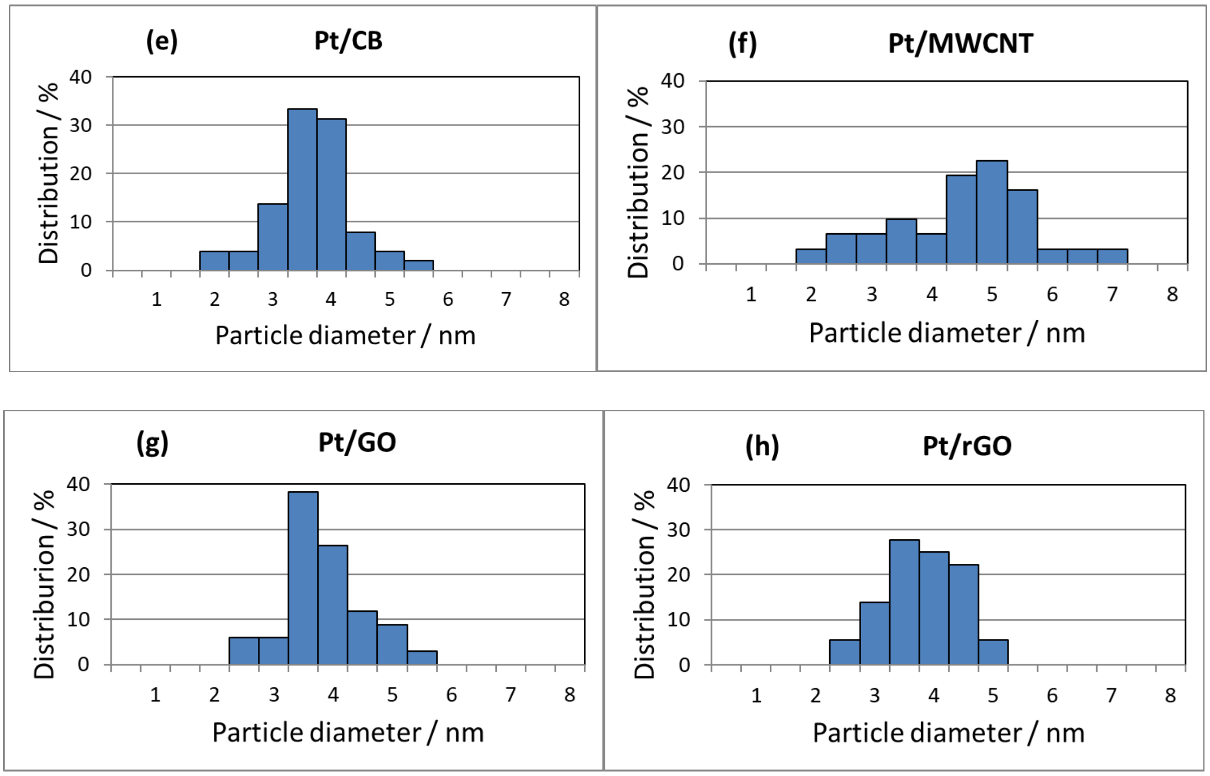

Figure 4.2. *TEM images and particle size distribution of: (a, e) Pt/CB, (b, f) Pt/MWCNT, (c, g) Pt/GO and (d,h) Pt/rGO.*

The homogeneity of the particle size in the Pt/CB catalyst is noteworthy, with 80% of the particles being in the range between 3-4 nm and a mean particle diameter (d_p) of 3.7 nm. On the contrary, Pt/MWCNT shows very high particle size dispersion with particles up to 7 nm of diameter, with a value of d_p of 4.5 nm. This observation highlights the importance of functionalisation of nanotubes, for example by a chemical modification with H_2SO_4 and/or HNO_3, to create nucleation sites which favour a more homogenous Pt distribution [265]. The TEM images for Pt/GO and Pt/rGO show a homogeneous particle size in both catalysts with identical value of d_p: 3.8 nm. Nevertheless, a higher particle agglomeration effect in the case of Pt/GO with respect to Pt/rGO can be seen. This may be related to the vacancies created during the reduction of GO with L-ascorbic acid when the oxide groups leave the graphene structure. These have been reported to create binding sites to anchor the Pt precursor ions which are subsequently reduced to Pt particles [272], reducing by this way the particle agglomeration. In addition, it has been reported that rGO sheets are more hydrophobic, showing stronger π-π stacking interaction and weaker electrostatic repulsion with respect to GO [273], which also favours the Pt deposition on the rGO support. This good dispersion of Pt particles on rGO structures has been already reported in previous investigations [274–276]. It is observed that the Pt particle diameters are in the range between 2 and 7 nm for all the catalysts. According to some investigations, this range is beyond the particle size that can influence the catalytic behaviour [277], especially regarding the mass activity [278] and the ORR performance [279].

FTIR spectra (Figure 4.3. FTIR spectra of GO, rGO, Pt/GO and Pt/rGO in the range: (a) 4000-600 cm-1 and (b) 2000-800 cm-1.) are also recorded to evaluate the influence of the reductive treatments on the oxide groups present in the GO-derived carbon supports. The attenuation of peaks in the characteristic spectra of oxygen-containing moieties (Figure 4.2. *TEM images and particle size distribution of: (a, e) Pt/CB, (b, f) Pt/MWCNT, (c, g) Pt/GO and (d,h) Pt/rGO.*) in the case of rGO, Pt/GO and Pt/rGO with respect to GO indicates the extent of reduction of the support that has occurred.

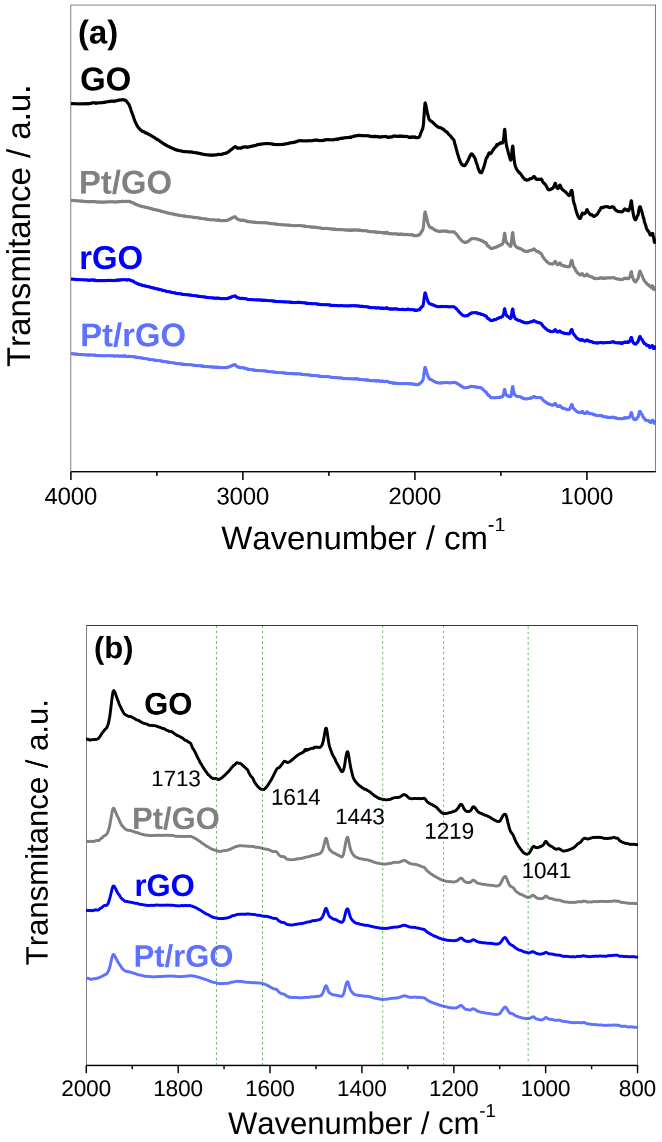

Figure 4.3. *FTIR spectra of GO, rGO, Pt/GO and Pt/rGO in the range: (a) 4000-600 cm^{-1} and (b) 2000-800 cm^{-1}.*

Table 4.2. *Characteristic IR absorptions.*

Frequency, cm^{-1}	Bond	Functional group	Refs.
3100-3700	O-H stretch	alcohol, phenol	[75,255,280,281]
1713	C=O stretch	carbonyl	[75,255,280,281]
1443	O-H stretch	alcohol, carboxyl	[255]
1219	C-O stretch	epoxy	[75,255,281]
1041	C-O stretch	alkoxy	[75,255]

The peak at 1614 cm^{-1} in GO supports Montes-Morán and co-workers, who assign this peak to cyclic ethers or C=C stretching related to carbon rings decorated with phenolic groups rather than to aromatic ring vibrations [282]. Dékány and co-workers discovered that a drying process modified the intensity of this peak, suggesting that it could be related to water present in the GO structure [280]. Another study independently confirms that the peak in this region is related to vibrations of adsorbed water molecules [281]. In our case, this could explain why this peak does not appear in the samples that were subjected to a thorough drying procedure as part of the processes for GO reduction and/or Pt deposition.

The results obtained by FTIR are qualitative, and further characterisation is required in order to gain insight into the changes occurred during the reductive treatments applied to the graphene-derived species. In this regard, XPS is used to quantify the effect of the reductive treatment applied to GO and the Pt deposition procedure on the carbon and oxygen composition. First, the XPS survey spectra shown in Figure 4.4. Survey XPS spectra of GO, rGO, Pt/GO and Pt/rGO, showing the C and O composition of each catalyst. exhibit two characteristic peaks at 284 and 532 eV corresponding to C1s and O1s, respectively [283], revealing that the oxygen content decreases in rGO and the Pt-containing catalysts with respect to the GO precursor.

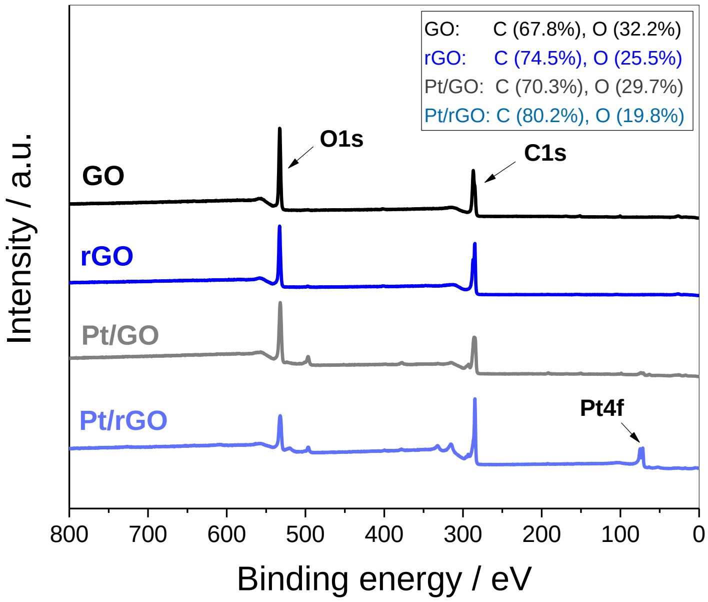

Figure 4.4. Survey XPS spectra of GO, rGO, Pt/GO and Pt/rGO, showing the C and O composition of each catalyst.

It is observed that the reduction of the oxygen content produced in rGO by the reductive treatment with L-ascorbic acid is higher than the collateral oxygen content reduction produced by the $NaBH_4$ used for the Pt deposition in Pt/GO. It is also seen that Pt/rGO exhibits the lowest oxygen content due to the two consecutive reductive treatments. In addition, the XPS survey spectra show a peak appearing at 72 eV that corresponds to Pt4f [265], confirming that the Pt deposition treatment is successful. This peak, however, is more intense in Pt/rGO than in Pt/GO, in spite of that TGA results reveals the higher Pt content in the latter. One possible explanation could be the higher presence of oxygen species in the Pt/GO catalyst that could alter the actual Pt composition detected by XPS. Nevertheless, it should be remembered that XPS is a surface technique, not being suitable for bulk component detection [284], since the Pt particles lodged between adjacent graphene layers may not be detected. Finally, the peak observed at 496 eV in the Pt-containing catalysts can be ascribed to iridium (Ir4p) [285], which is found (by XRF) to be the main metal impurity in the Pt particles.

According to the literature, the different carbon groups contributing to the C1s peak, namely oxygen-free C-C/C=C bonds, hydroxyl C-OH (including phenols), epoxy C-O-C, carbonyl >C=O and carboxyl HO-C=O, are assigned to the corresponding binding energies 284.49, 285.86, 286.55, 287.54 and 288.94 eV, respectively [262]. It has been reported that epoxy and hydroxyl groups are normally found on the basal plane of the GO layer, while carboxyls are present on the edges and carbonyls can be found on both basal plane and edges [286,287]. Figure 4.5. C1s core-level XPS spectra of: (a) GO, (b) rGO, (c) Pt/GO and (d) Pt/rGO. shows that the proportion of C-C/C=C bonds in the rGO-containing samples increases with respect to GO due to the effect of L-ascorbic acid used in the GO reduction treatment.

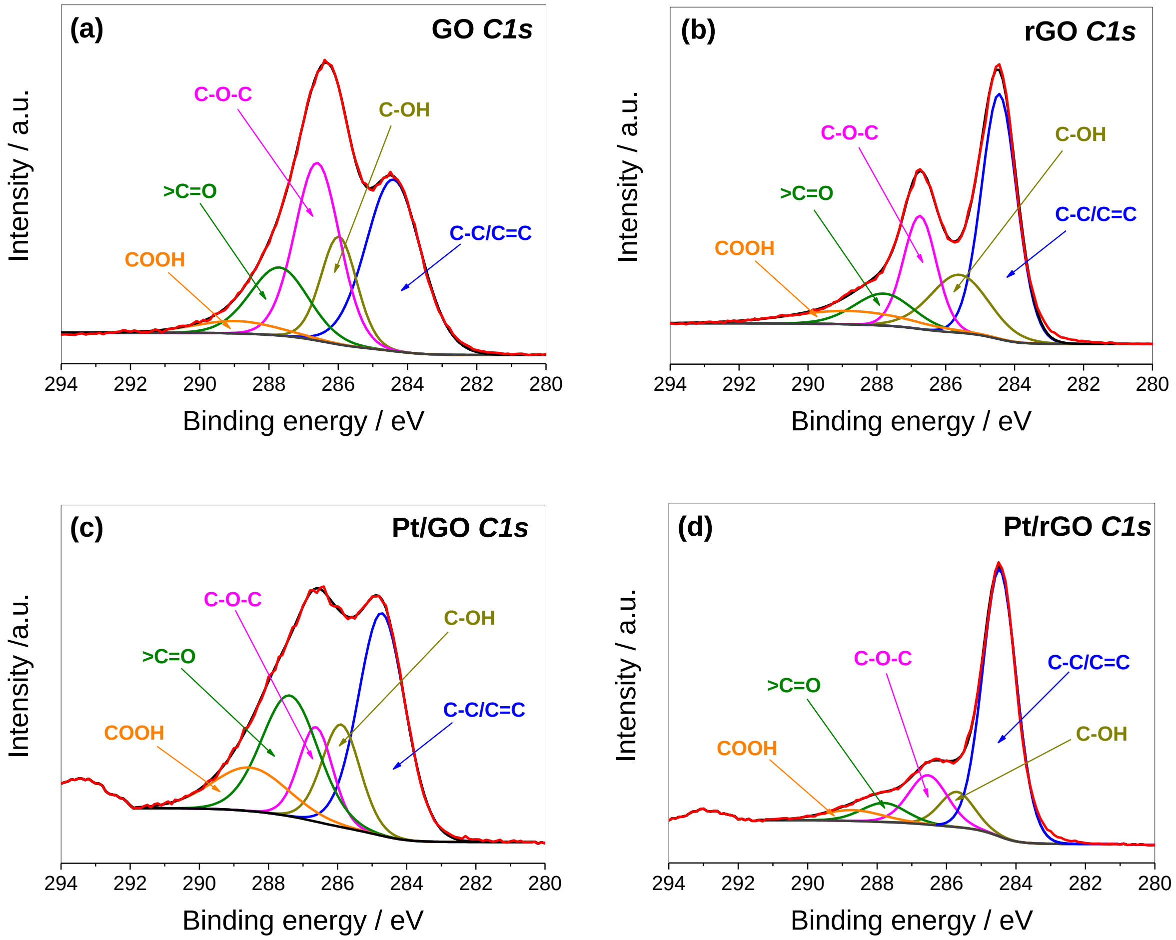

Figure 4.5. *C1s core-level XPS spectra of: (a) GO, (b) rGO, (c) Pt/GO and (d) Pt/rGO.*

$NaBH_4$ used in the treatment for Pt deposition also increases the proportion of C-C/C=C bonds in the Pt-containing catalysts with respect to their Pt-free equivalents, due to collateral reduction of oxide groups, although in a lesser extent than L-ascorbic acid (see Appendix 2). With regard to the oxygen-carbon bonds, the epoxy groups are the main contributors to the oxide species in GO with 30.3%, whereas carboxyls are the less abundant specie, representing only 3.9%. Nevertheless, a comparison of Figure 4.5. C1s core-level XPS spectra of: (a) GO, (b) rGO, (c) Pt/GO and (d) Pt/rGO.a and 4.5b reveals that the carboxyl moieties are the less affected by the L-ascorbic acid, while the rest of oxide species are reduced in the same extent. With regard to the Pt deposition treatment, the comparison between Figure 4.5. C1s core-level XPS spectra of: (a) GO, (b) rGO, (c) Pt/GO and (d) Pt/rGO.a and 4.5c shows that $NaBH_4$ collaterally reduces the epoxy species mainly, whereas the proportion of carbonyl and carboxyl moieties is increased. This observation seems to point out that the C=O bond is resistant to the action of borohydride. Finally, it should be also mentioned that the peak at 293.3 eV present in Pt/GO and Pt/rGO is due to the presence of potassium species ($K2p_{3/2}$) remaining from the K_2PtCl_6 precursor used in the Pt deposition [288].

4.3 Electrochemical characterisation

After the physical characterisation, the catalytic behaviour of the carbon catalyst-supports towards the ORR in alkaline media is studied. First, in order to obtain a complete characterisation of the four different Pt-supported catalysts, the ECSA is determined using the H_{upd} method (described in Section 3.2.3). Figure 4.6 displays the CV curves measured in N_2-saturated 0.1 M $HClO_4$ solution at 20 mV s^{-1}, and the ECSA is calculated by measuring the coulombic charge in the hydrogen desorption region, ranging between -0.2 and +0.15 V.

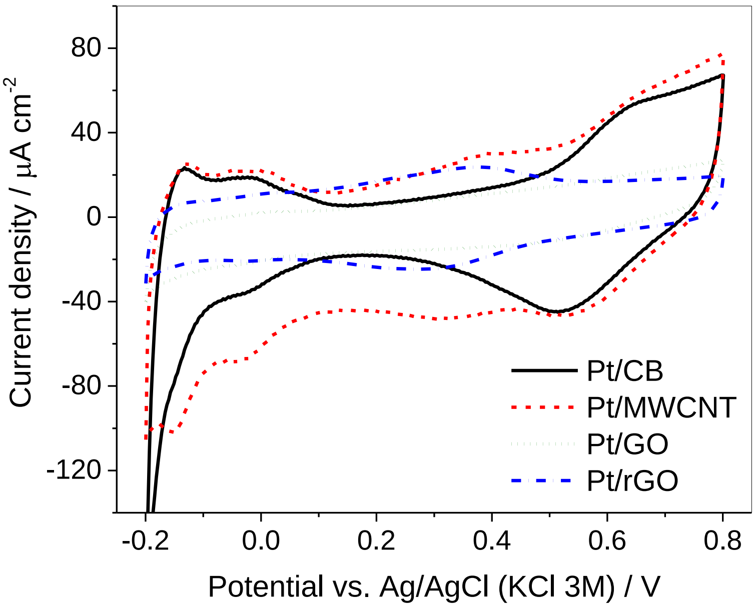

Figure 4.6. *CV obtained in N_2-saturated 0.1 M $HClO_4$ solution at 20 mV s^{-1} and 293 K, with a catalyst loading of 0.13 mg cm^{-2}.*

The ECSA calculated for Pt/CB, Pt/MWCNT, Pt/GO and Pt/rGO are 20.6, 15.3, 1.8 and 3.5 m^2 g^{-1}, respectively. It is observed that the ECSA measured for Pt/GO and Pt/rGO is very low compared to Pt/CB and Pt/MWCNT, which is attributed to the presence of Pt in oxidised form, i.e. Pt^{2+} and Pt^{4+}, in the graphene oxide supports [289], whereas it remains as Pt^0 in the Pt/CB and Pt/MWCNT catalysts.

In order to compare the ORR activity of each catalyst, voltammograms are measured at a voltage scan rate of 25 mV s^{-1} over the range from +0.4 to -1.0 V vs. Ag/AgCl (KCl 3 M) in O_2-saturated 0.1 M KOH solution, using a RRDE modified with the catalyst as described in Section 3.3.7.1. Figure 4.7a shows the voltammograms of the different catalysts at a rotation speed of 1600 rpm. If the ORR activity is considered in terms of more positive onset potential, it can be seen that this parameter is in good correlation with the values of ECSA previously reported (Table 4.3). A similar pattern is shown in terms of half-wave potential, except for the case of Pt/MWCNT and Pt/rGO, which swap their positions with respect to the onset values. The behaviour of Pt/MWCNT at more negative potentials could be influenced by the presence of metal impurities in its structure, as it will be discussed later.

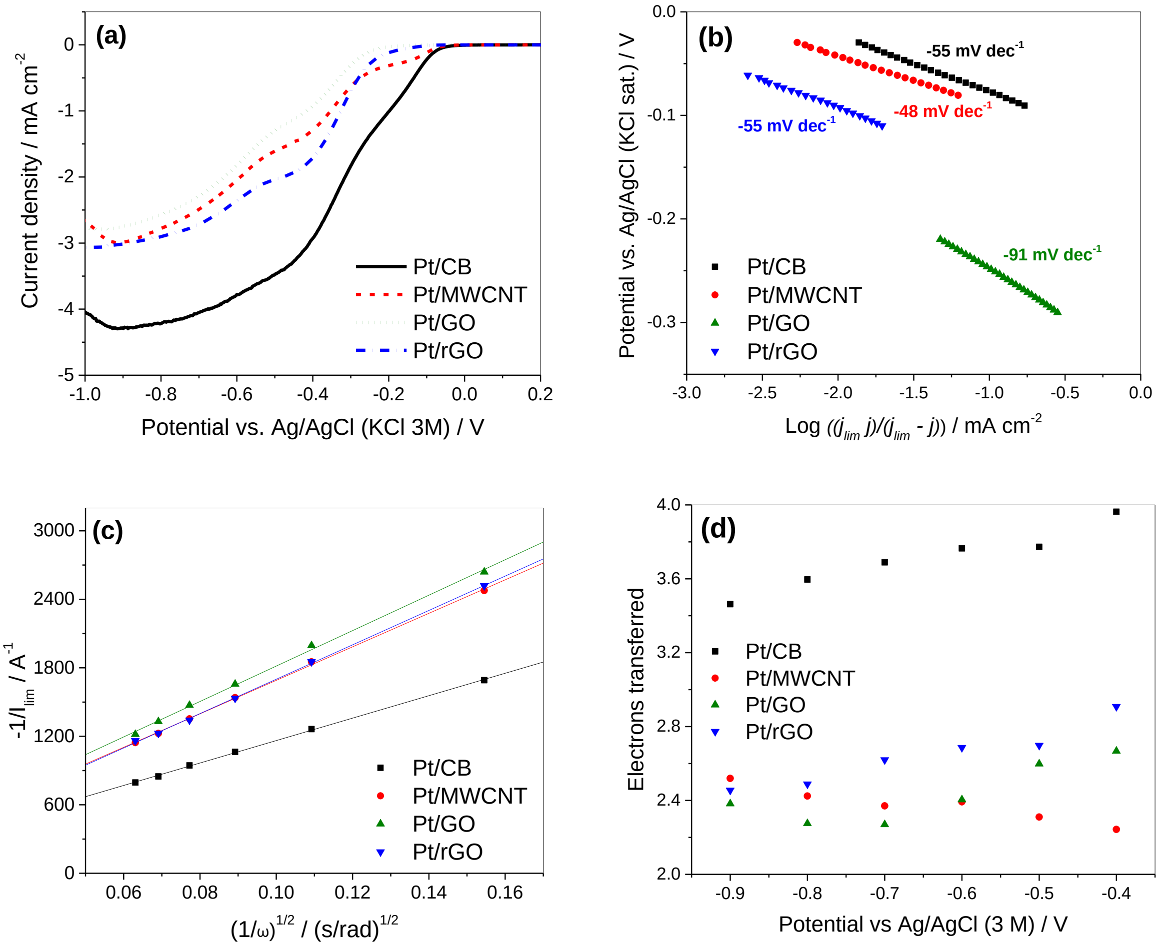

Figure 4.7. *(a) LSV measurements of the four different synthesised catalysts at a rotation speed of 1600 rpm. (b) Tafel plots showing the Tafel slope values. (c) Koutecky-Levich plots obtained from the values of measured current at -0.9 V. (d) Electrons transferred obtained from the application of the Koutecky-Levich equation.*

Table 4.3. Electrochemical parameters of the different catalysts. [a]Calculated by application of the Koutecky-Levich equation. [b]Calculated by direct peroxide determination with RRDE.

Catalyst	ECSA / m^2 g^{-1}	E_{onset} / V	$E_{1/2}$ / V	j_L / mA cm^{-2}	-b / mV dec^{-1}	n (at -0.5)[a]
Pt/CB	20.6	-0.05	-0.33	-4.30	55	3.77 [a] , 3.78 [b]
Pt/MWCNT	15.3	-0.07	-0.46	-3.00	48	2.31 [a] , 3.23 [b]
Pt/GO	1.8	-0.20	-0.52	-2.80	91	2.60 [a] , 2.86 [b]
Pt/rGO	3.5	-0.09	-0.38	-3.07	55	2.70 [a] , 3.18 [b]

In order to gain insight into the ORR mechanism (and more precisely in the determination of the rds) taking place at the different catalysts, the Tafel slopes are calculated from the Tafel plots displayed in Figure 4.7b. It is seen that Pt/CB and Pt/rGO show a Tafel slope value of -55 mV dec^{-1}, which is closed to the theoretical -60 mV dec^{-1} value exhibited by Pt in 0.1 M KOH solution in the low overpotential region [39,40,290], corresponding to a mechanism in which the reaction *2.22* is the rds [38] (see Section 2.1.2.3). The Tafel slope calculated for Pt/MWCNT is -48 mV dec^{-1}, which is an intermediate value between -40 and -60 mV dec^{-1}, corresponding to reaction *2.25* and reaction *2.24* being the rds, respectively [38]. This implies that in Pt/MWCNT the reaction *2.24* is faster than in Pt/CB and Pt/rGO. On the other hand, Pt/GO exhibits a higher Tafel slope value of -91 mV dec^{-1}, which lies between -60 and -120 mV dec^{-1}, corresponding to reaction *2.24* and reaction *2.23* being the rds, respectively [38]. Unlike reaction *2.24*, reaction *2.23* is an electron transfer reaction, which suggests that the higher oxide content of the GO support hinders the electron conductivity through the Pt/GO catalyst, producing a lack of electrons in the reaction sites.

Another important parameter in electrochemical characterisation is the number of electrons transferred during the electrochemical reaction (n). As it was explained in Section 3.2.2, the ORR can proceed by two different mechanisms: one direct mechanism in one-step with the transfer of four electrons, and a second mechanism in two steps involving the production of peroxide intermediates. To investigate the dominant ORR mechanism, the number of electrons involved in the electrochemical reaction is determined via Koutecky-Levich (K-L) analysis (Eq. *3.4*, Section 3.2.2.1) [241].

Figure 4.7c shows the K-L plots for each catalyst at -0.9 V, which is approximately the region where the limited currents are reached. It is observed that Pt/CB exhibits a lower slope with respect to the rest of the catalysts, which implies a higher number of electrons transferred in the reaction. In fact, the values of n calculated from the slope are 3.46 for Pt/CB, 2.52 for Pt/MWCNT, 2.38 for Pt/GO and 2.46 for Pt/rGO. In order to see how the applied potential can affect the values of n, the same procedure is applied to other currents measured at different potentials in the range -0.9 to -0.4 V, and the calculated values of n are plotted versus the potential in Figure 4.7d. It can be seen that there is a slight decrease in the value of n as the potential becomes more negative for Pt/CB, Pt/rGO and Pt/GO (in this case until -0.7 V only), whereas it slightly increases as the potential is more negative for Pt/MWCNT. According to these results, the ORR seems to proceed by a direct 4-electron mechanism for Pt/CB while there is a mixed behaviour between the two proposed mechanisms for the rest of the catalysts. Nevertheless, several investigations claim that the K-L method is not suitable for the calculation of the number of electrons transferred in the ORR due to several reasons

[242–245]. First, strictly speaking, the K-L equation is only applicable to single-step reactions, whereas the ORR is a multi-step reaction [242]. Second, the K-L equation has been demonstrated not being suitable for rough or porous surfaces [244]. Another incongruity is that the K-L theory assumes a constant value of n, whereas n is actually dependent on the angular velocity of the rotating electrode [243].

A more straightforward method to calculate the number of electrons transferred in the ORR is to use a rotating ring-disk electrode (RRDE) to directly measure the rate of peroxide intermediate formation. Here the ORR takes place in the central glassy carbon disk (where the different catalysts are deposited) and the concentric Pt ring detects peroxide produced. In Figure 4.8, the RRDE plots for each catalyst are shown, displaying the measured disk current density j_D at the bottom and the measured ring current density j_R at the top. These graphs provide a quick visualisation on which catalyst produces more peroxide, since the measured I_R current is directly proportional to the amount of peroxide detected. Therefore, it is seen that Pt/GO generates the most peroxide intermediate, whereas Pt/CB produces the lowest amount.

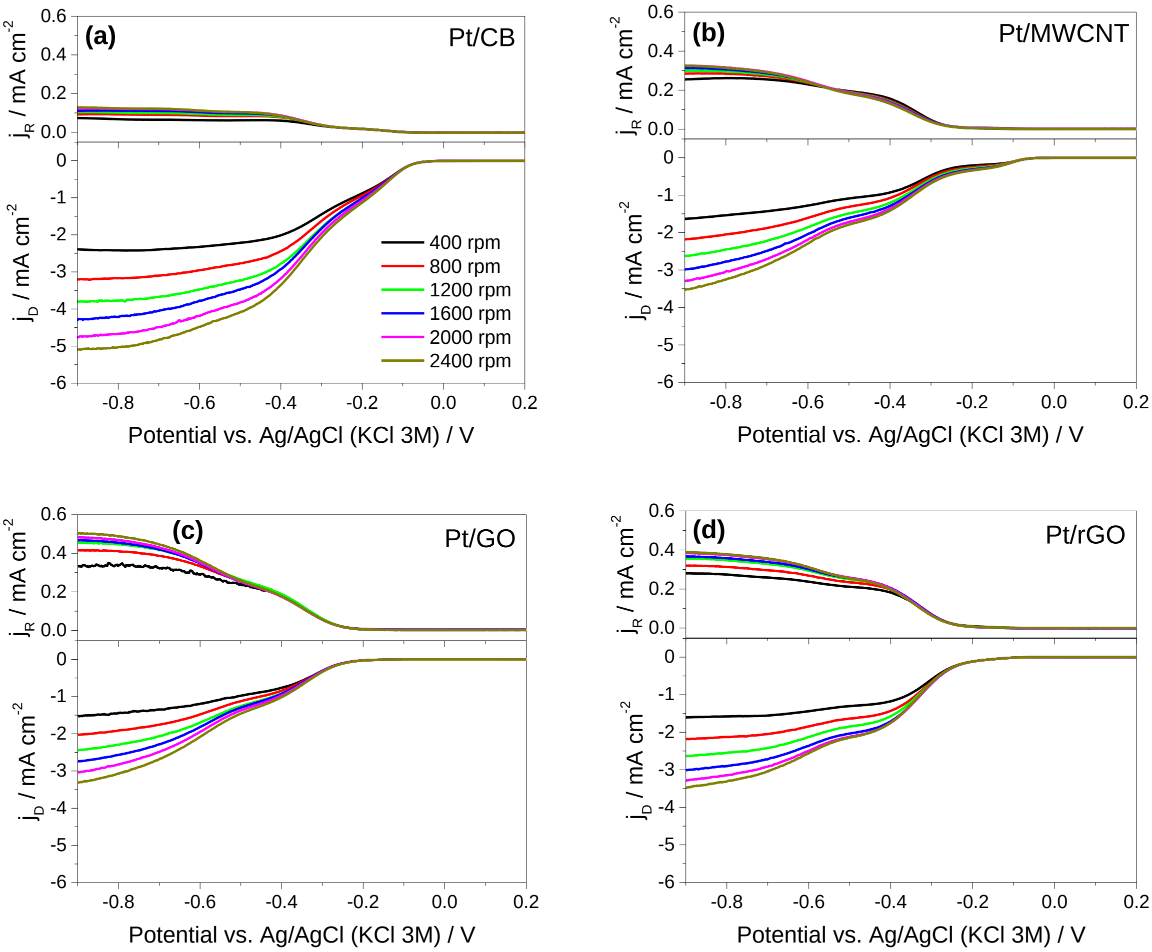

Figure 4.8. *Background-subtracted RRDE measurements at different rotation rates for the four catalysts at loadings of 20 µg Pt/C cm^{-2} on 0.2475 cm^2 area GC working electrode in O_2-saturated 0.1 M KOH at 25 °C. I_R ring current (ring potential fixed at +0.47 V) is displayed at the top (ring area 0.1866 cm^2) and I_D disk current is displayed at the bottom.*

From these graphs, the number of electrons transferred in the electrochemical reaction can be calculated from the values of I_R and I_D using Eq. *3.5* (see Section 3.2.2.2) [36]. Figure 4.9a shows the values of n calculated by this method versus the potential applied at 1600 rpm.

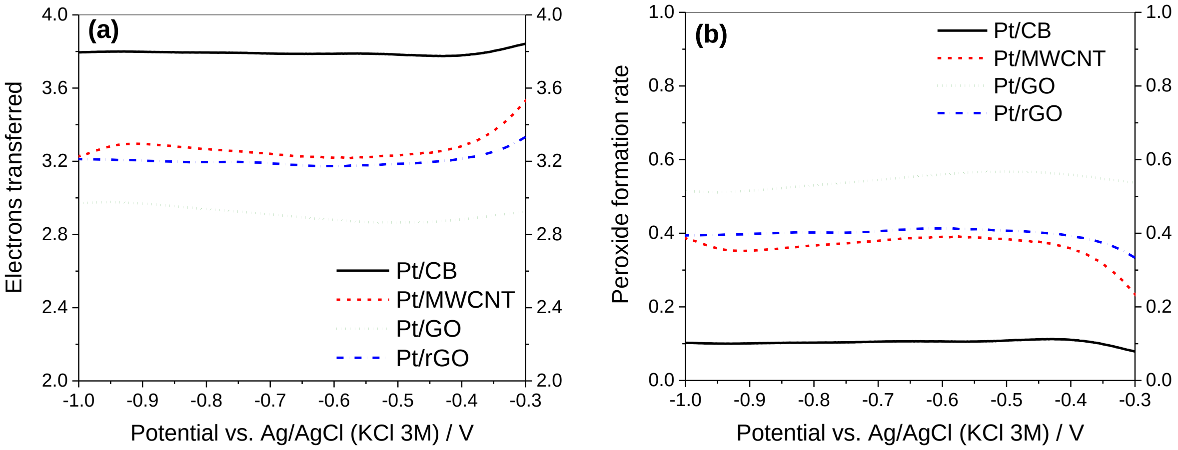

Figure 4.9. *(a) Electrons transferred vs. the potential calculated from the RRDE measurements at 1600 rpm, using Equation 3.5. (b) Peroxide formation rate vs. potential calculated from RRDE measurements at 1600 rpm, using Equation 3.6.*

If these values are compared to those obtained by the K-L equation, it is seen that the RRDE method provides higher values of n (Table 4.3). For Pt/CB the ORR involved 3.78 electrons, which is independent of the potential applied in the range between -0.4 and -1.0 V. This stability of n in that potential range is also observed in Pt/rGO with a constant value of 3.18. The value of n is more fluctuating in the case of Pt/MWCNT, indicating that the OR is more sensitive to changes in the potential for this catalyst. Finally, Pt/GO confirmed its lowest catalytic activity with a value of n oscillating between 2.86 at -0.5 V and 2.97 at -0.9 V.

These values of n are closely linked to the selectivity of the reaction, which can be quantified by the fraction of peroxide intermediate produced in the reaction (X_{H2O2}) obtained from the values of I_R and I_D using the Equation *3.6* (see Section 3.2.2.2). The values of X_{H2O2} versus the potential applied at 1600 rpm are plotted in Figure 4.9b. The peroxide intermediate production at -0.5 V is 10.9% for Pt/CB, 38.3% for Pt/MWCNT, 56.8% for Pt/GO and 40.7% for Pt/rGO, which is in accordance with the catalytic behaviour showed by each catalyst in previous measurements.

The variation of the values of n and X_{H2O2} with the applied voltage is significant in the case of Pt/MWCNT. There could be two different explanations for this. First, this could be attributed to metal impurities remaining in the MWCNTs from the fabrication process [291,292]. In the present investigation, XRF analysis has been carried out in order to determine the nature of these metal impurities [293], showing that Fe is by far the main contributor with 11130 ± 90 ppm, followed in a lesser extent by Cd (270 ± 10 ppm), Ni (200 ± 20 ppm), In (130 ± 10 ppm), Zn (130 ± 10 ppm) and Pb (110 ± 30 ppm). All these impurities are also found in the rest of the carbon supports but only Fe impurities are 10 times higher in MWCNT with respect to the others, suggesting that Fe plays an important role on the catalytic activity of MWCNT [294]. The fact of that no Fe impurities are detected in XPS studies (which is a surface technique) carried out on the Pt/MWCNT catalyst clearly indicates that the Fe particles are embedded *inside* the nanotube structure [295]. Most of available literature on the topic points to that these Fe impurities are in the form of Fe_3O_4 [296], being this specie more catalytically active at potentials around -0.8 V (vs. Ag/AgCl) [297]. This could explain why the value of n is higher (and consequently X_{H2O2} is lower) in the case of Pt/MWCNT at more negative potentials. The second possibility is related to the role of the 1D structure of MWCNT on the catalytic performance. It has been proposed that in some types of carbon nanotubes the number of electrons transferred during the ORR is function of the potential applied, increasing the value of n at more negative potentials [298].

Nevertheless, Pumera and Wang demonstrated that the catalytic activity of these supposedly “metal-free” materials is, in fact, due to metal impurities remaining from the process of fabrication [297].

We can also observe that Pt/GO undergoes a considerably lower catalytic activity in spite of its relatively higher Pt loading (almost 20%) compared to the rest of the catalysts (around 15%). The reason of this poor performance of the Pt/GO catalyst should be obviously related to the intrinsic characteristics of the carbon support. Especially remarkable are the differences of catalytic activity in Pt/GO and Pt/rGO taking into account that they were synthesised from the same GO carbon support, but subjected to a previous reductive method in the case of rGO. XPS studies (see Figure 4.5c and 4.5d) demonstrates that the oxide groups have been removed in a larger extent in Pt/rGO with respect to Pt/GO. Although it is commonly accepted that the electrical conductivity of GO can be improved by partially restoring the sp^2 structure through oxide group elimination (especially epoxy and hydroxyl species located on the basal plane [76]), this is not our case. AC impedance measurements carried out as described in Section 3.3.7.1 show that the ohmic resistance of the Pt/GO layer deposited on the RDE is 2.8 ± 0.7 Ω *versus* 3.2 ± 0.4 Ω for Pt/rGO. Clearly, the ohmic resistance measurements for Pt/GO and Pt/rGO include the three factors previously described (see Section 3.2.4), namely, resistance to ion migration in the electrolyte, contact resistances in the cell components and resistance to electron transport. Since the first two of these factors are common for all the catalysts, any difference in the ohmic resistances measured are attributable to the resistance to electron transport through the different carbon supports, and more precisely, to the influence on the electronic conductivity of the amount of oxide species present in each individual catalyst support. This indicates that the oxide groups in the basal plane (epoxy and hydroxyl) involved in the electronic conductivity are less affected by the reduction treatment. This is also supported by the observation (see Figure 4.5 and Appendix 2) of that the main oxide groups being removed in Pt/rGO with respect to Pt/GO were carbonyl and carboxyl, which are located on the edges. Another study verifies the influence of quinones (containing the carbonyl group) on the ORR performance [299], confirming that the oxygen reduction in rGO takes place mainly on the active reduced sites located on the edges of the graphene layers.

In addition, the values of ohmic resistance obtained for Pt/CB and Pt/MWCNT are 8.1 ± 1.2 Ω and 6.5 ± 1.4 Ω respectively, which confirms that the conductivity played just a secondary role on the catalytic activity observed. Considering the number of electrons involved in the ORR, the higher value of n calculated for Pt/CB suggests that the catalytic activity of the Pt dominates the ORR in Pt/CB, since it is well-known that the oxygen reduction follows a 4-electron mechanism on Pt surfaces in both alkaline and acid media, while the 2-electron mechanism is preferred on carbon surfaces [31,300]. For example, Mao et al. reported that the ORR takes place in MWCNT by the 2-electron mechanism in alkaline media [88], while Papakonstantinou at al. concluded that electrochemically reduced graphene oxide follows a more predominant 2e pathway [299]. Likewise, the lower value of n for Pt on MWCNT, GO and rGO reveals a greater contribution of the carbon-mediated pathway and thus reflects that these forms of carbon are more active towards the ORR than CB. In conclusion, in the supports where the carbon configuration is derived from the graphene structure

(MWCNT, GO and rGO), the ORR seems to take place on both carbon and Pt particles, thus showing a mixed behaviour between the two proposed mechanisms.

In order to evaluate the catalytic behaviour of the catalysts in practical fuel cell tests, these are applied in the cathode side (where the ORR takes place) of the MEA and tested in a real AEMFC, under the conditions described in Section 3.3.7.1. Figure 4.10 shows the iV curves obtained in galvanostatic mode (where the measured potential is plotted *versus* the applied current density) and the power curves (where the calculated power density is plotted *versus* the applied current density) of the different catalysts.

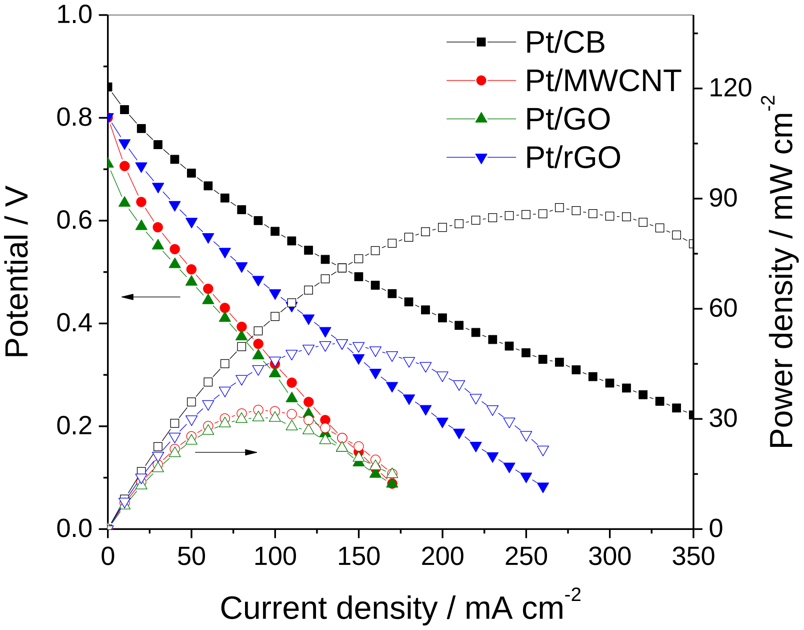

Figure 4.10. *iV curves (solid symbols) and power density curves (open symbols) of the four synthesized catalyst in the cathode side, and a commercial Pt/C 20% catalyst in the anode side in all cases. MEAs made with commercial Tokuyama A201 alkaline exchange membrane and Acta I2 exchange ionomer, catalyst loading 0.4 mg$_{Pt}$ cm^{-2} with ionomer/catalyst 0.24:1 in both anode and cathode, Sigracet GDL 35 BC used as GDL. Test conditions: H_2 (100% RH) at 0.4 L min^{-1} and 50 °C at the anode, O_2 (100% RH, CO_2-free) at 0.4 L min^{-1} and 50 °C at the cathode. T$_{cell}$: 50 °C, torque pressure: 200 cnm, no back pressure applied.*

At lower current densities it is found the activation region, where the kinetic effects are predominant over other characteristic fuel cell parameters, such as the ohmic or mass transport losses [6]. In this regard, it is seen a similar pattern to that observed in Figure 4.7a, i.e. Pt/CB is clearly the best catalyst, showing the highest open circuit voltage (OCV) and maximum power density (P_{max}) with values of 860 mV and 87.6 mW cm^{-2}, respectively. On the other hand, Pt/GO and Pt/MWCNT show the poorest performance, with a considerably lower P_{max} of around 30 mW cm^{-2}. Pt/rGO exhibit an average catalytic activity, with a value of P_{max} of 50.7 mW cm^{-2}.

Therefore, it is concluded that the catalytic performance results of the different catalysts obtained with the RRDE experiments using *ex-situ* characterisation techniques, truly reflect the real behaviour in practical fuel cell applications.

4.4 Conclusions

Four different carbon materials, namely Carbon Black (CB), Multi-walled Carbon Nanotubes (MWCNT), Graphene Oxide (GO) and reduced Graphene Oxide (rGO), are evaluated as Pt catalyst supports towards the oxygen reduction in alkaline media. Two methods have been proposed and tested for Pt deposition onto the carbon supports, showing the TGA analysis that the reduction of potassium hexachloroplatinate with sodium borohydride is a more efficient method for Pt deposition than a polyol reduction process assisted by microwaves. The oxide groups of the GO carbon support seem to favour the Pt deposition and increase the final Pt loading of the catalyst, whereas MWCNT (not functionalised) exhibits a poor homogeneity in the distribution of the Pt particles on the carbon support.

FTIR and XPS measurements have been carried out to qualitative and quantitatively determine how the methods for GO reduction and Pt deposition affect the oxide composition of the graphene-derived carbon supports. It is concluded that L-ascorbic acid is an effective reducing agent for GO reduction, whereas the sodium borohydride used in the Pt deposition procedure collaterally reduces a certain amount of the oxide groups present in GO.

Regarding the catalytic activity, it is observed that the Pt/CB catalyst performs a *quasi* 4-electron pathway for the oxygen reduction, whereas Pt/MWCNT, Pt/GO and Pt/rGO undergo a mixed behaviour between the 4e and the 2e proposed mechanisms. These observations seem to be related to the catalytic activity of the carbon supports, in such a way that in the catalysts containing graphene-derived materials, i.e. MWCNT, GO and rGO, the ORR takes place on both the Pt particles and the carbon support, thus showing a mixed mechanism. On the contrary, the low catalytic activity of CB induces the ORR to take place on the Pt particles only, thus favouring the 4e mechanism in Pt/CB. These results have been obtained by indirect calculation using the Koutecky-Levich equation and confirmed by direct determination of peroxide intermediate formation with RRDE measurements.

In addition, the carbon support composition is shown to play a role on the ORR performance observed. In this regard, the Pt/GO catalyst yields a poorer performance than Pt/rGO, presumably due to the presence of carbonyl and carboxyl species on the edges hindering the oxygen reduction reaction. Moreover, the catalytic behaviour of MWCNT as carbon support seems to be influenced by the presence of Fe impurities remaining from the fabrication process, particularly with regard to the peroxide intermediate formation.

Finally, *in-situ* fuel cell tests have yielded similar results to those obtained using the RRDE measurements, which demonstrates that the electrochemical methods employed in the present study, such as CV and LSV, accurately reflect the catalytic behaviour of Pt supported on carbon catalysts for the ORR in alkaline media, and the results can be applicable to practical fuel cell systems.

5 DOPED-GRAPHENE AS METAL FREE ORR CATALYST

In this chapter, the fabrication of different single, dual, ternary and quaternary-doped graphene catalysts is thoroughly analysed in terms of physical and electrochemical characterisation. A comparison between two different methods for the reduction of GO is developed as a brief introductory section.

5.1 GO reduction methods

Before proceeding with the comparison of the different doped-graphene catalysts, two different methods applied for the reduction of oxide groups in GO [301] are compared in terms of C and O composition. Since the reduction of oxide groups in GO takes place in the same step as the addition of the doping heteroatoms [302,303], it is important to check which method is more efficient in terms of reduction and selectivity of oxide groups. Here two methods are proposed: first, a purely chemical reduction using a mild reducing agent, L-ascorbic acid, which has been previously reported as an efficient and selective method for GO reduction [81,255]. Secondly, a thermal method in which the GO is annealed at 900 °C for 2 hours under a protective N_2 atmosphere [304,305]. Both procedures are described in detail in Section 3.3.2. The present section does not analyse the structure and features of the resultant rGOs, as the main interest is to determine how the two different treatments affect to the reduction of the oxide groups present in the GO precursor. In this regard, XPS is a suitable technique that provides information about the resultant rGO composition, and enables information on the nature of the C-O bonding groups affected by the treatments applied to be obtained [262].

First, a sample of GO is analysed by XPS to provide a control measurement. Next, certain amounts of the same batch of GO are subjected to the chemical reduction and the annealing reduction methods, respectively. The resulting rGO samples are then analysed via XPS to ascertain changes in its oxide content. These results are given in Figure 5.1a, which shows that the annealing method is more efficient in reducing the oxide groups of GO, being these reduced from the 32.2% observed in the oxidised precursor to 25.5% for the L-ascorbic acid reduced GO and 5.2% of the annealed rGO.

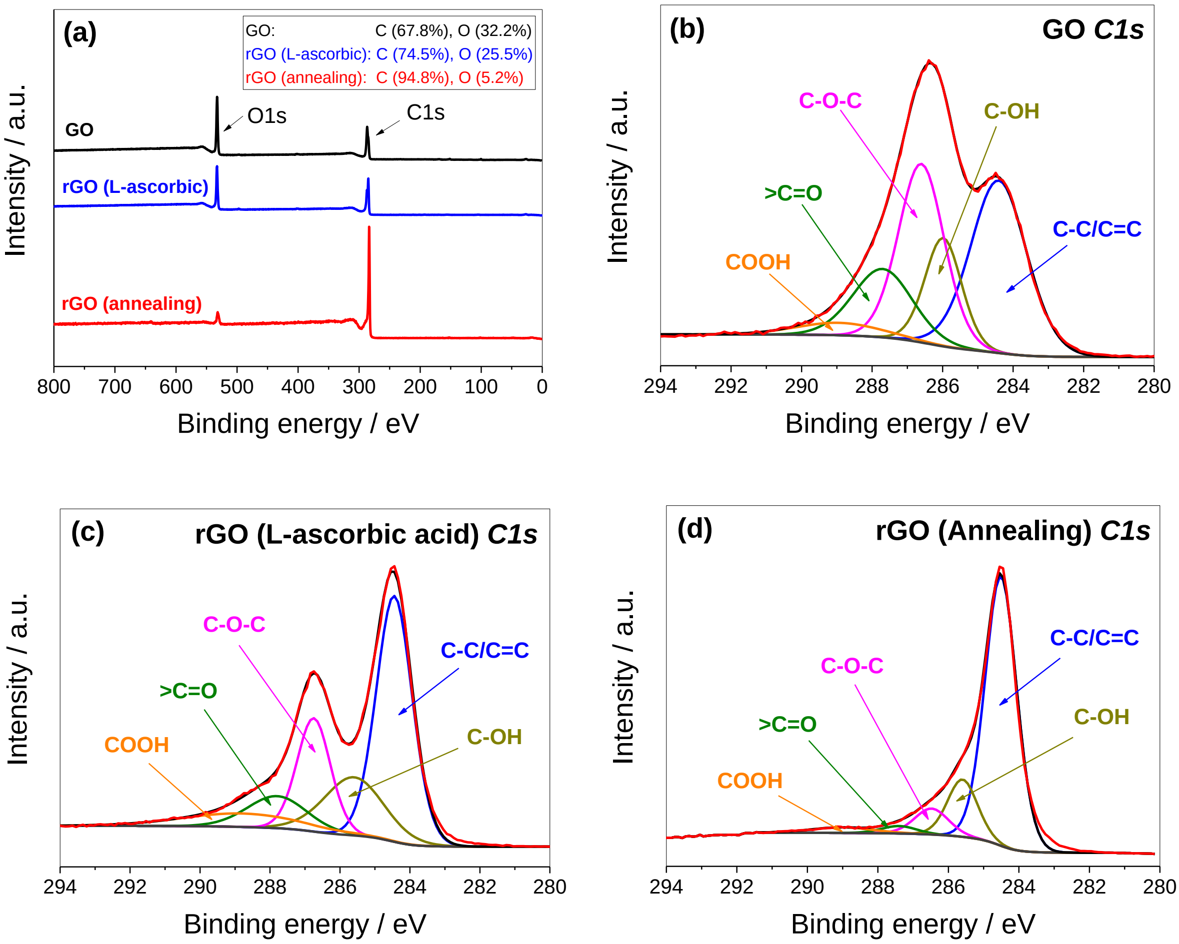

Figure 5.1. *(a) Survey XPS spectra of the GO, rGO (L-ascorbic acid) and rGO (Annealing), showing the corresponding C and O compositions. C1s deconvolution XPS spectra of (b) GO, (c) rGO (L-ascorbic acid) and (d) rGO (Annealing).*

Figure 5.1b, c, and d show the C1s peak deconvolution obtained by XPS. As previously mentioned in Section 4.2, the different carbon groups contributing to the C1s peak, namely oxygen-free C-C/C=C bonds, hydroxyl C-OH (including phenols), epoxy C-O-C, carbonyl >C=O and carboxyl HO-C=O, are assigned to the corresponding binding energies 284.49, 285.86, 286.55, 287.54 and 288.94 eV, respectively [262]. It has been reported that epoxy and hydroxyl groups are normally found on the basal plane of the GO layer, while carboxyls are present on the edges and ketones can be found on both basal plane and edges [286,287]. In Figure 5.1b it is seen that in GO the oxygen-free C-C/C=C bonds represent only 35.9% of the bonding groups, with -C-O-C- being the main oxide contributors with 30.3% (see Appendix 3 for compositions). Figure 5.1c reveals that all the oxide groups are moderately reduced by the L-ascorbic acid, with C-OH and COOH being less affected by this reduction. In contrast, it can be seen in Figure 5.1d that all oxide groups are drastically reduced by the thermal annealing, increasing the C-C/C=C composition to 72.7% of the total bonds. It is also observed that the -C-O-C- and >C=O species are especially attacked by the thermal treatment. These results reveal that the annealing procedure is more effective than the chemical reduction with L-ascorbic acid for the reduction of GO.

5.2 Single-doped graphene

In this section, the single-doped graphene catalysts synthesised as described in Section 3.3.4; boron-doped graphene (B-Gr), nitrogen-doped graphene (N-Gr), phosphorus-doped graphene (P-Gr) and sulphur-doped graphene (S-Gr) are characterised in terms of composition and structure, and the results are compared with the graphene oxide (GO) precursor and the reduced graphene oxide (rGO) prepared following the annealing procedure.

First, in order to investigate the chemical composition of the synthesised catalysts, XPS measurements are performed and shown in Figure 5.2, revealing the typical peaks for C, O, B, N, P and S and confirming that the doping precursors are effectively incorporated into the graphene structure. The composition of the different catalysts is calculated from the area under the peaks (Table 5.1).

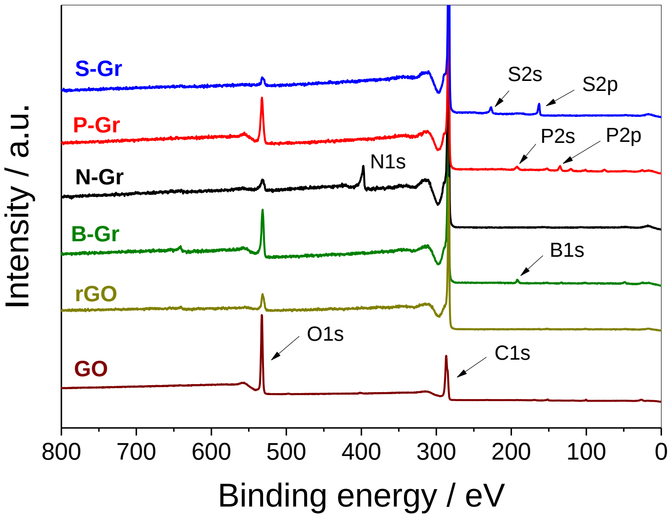

Figure 5.2. *Survey XPS spectra of the single-doped graphene catalysts plus GO and rGO, showing the peaks corresponding to the dopants.*

Table 5.1. *Single-doped graphene catalyst compositions (calculated from XPS measurements) with their corresponding errors.*

Catalyst	C	O	B	N	P	S
GO	68.0 ± 0.2	32.0 ± 0.2				
rGO	94.8 ± 0.3	5.2 ± 0.3				
B-Gr	88.1 ± 0.1	9.1 ± 0.1	2.8 ± 0.1			
N-Gr	91.8 ± 0.5	2.6 ± 0.6		5.6 ± 0.5		
P-Gr	88.8 ± 0.3	9.4 ± 0.3			1.8 ± 0.2	
S-Gr	95.8 ± 0.1	1.6 ± 0.2				2.6 ± 0.1

There is a significant variability in the composition of the different doped-graphene catalysts. Even for each individual single-doped graphene catalyst there is a wide range of compositions reported in the literature, depending on the nature of the synthesis method, the doping-precursor and the synthesis temperature [153,306]. For the B-Gr catalyst a peak can be seen at ~192 eV corresponding to B1s species introduced in the graphene structure, obtaining a boron composition of 2.8%. This value is similar to that reported in the literature under similar conditions [139], with other B-doped graphenes ranging between 2.5% and 6.0% synthesised under diverse methods [110,112,113]. In the case of the N-Gr catalyst, the characteristic N1s appears at ~398 eV, giving a nitrogen content of 5.6%, which is an average value compared to the wide nitrogen composition range between 1.1 and 10.8% reported in the literature [153]. The P-Gr catalyst composition is obtained from the P2s and P2p peaks at ~194 eV and ~136 eV, respectively, giving a total value of 1.8%. This value is in accordance with those previously reported, which are between 1.36 and 1.81% using different phosphorus precursors [115,116,160]. Finally, the S-Gr catalyst shows two distinctive peaks, S2s at ~227 eV and S2p at ~163 eV, giving a composition of 2.6%. In this case, the sulphur contents in previously reported S-Gr range between 1.30 and 3.95% [118,119,174,307].

In addition, it is observed a substantial lowering of the oxygen content observed in the GO precursor after the application of the thermal treatment. The oxygen content of the GO precursor is calculated to be 32.2%, whereas the oxygen composition of rGO after the annealing (without dopants) is 5.2%. In the case of the doped graphenes, there is a variability in the oxygen content, suggesting that the mechanism of dopant incorporation into the graphene 2D structure may be different depending on the identity of the dopant species. In this way, the N-Gr and S-Gr catalysts show an oxygen content lower than rGO, while B-Gr and P-Gr exhibit a higher oxygen composition than rGO. This can be related to the nature of the different dopant precursors, since N and S precursors are melamine and benzyl disulphide respectively, which are oxygen-free, whereas B and P precursors are boric acid and phosphoric acid, respectively, both with significant oxygen content.

Following the structural characterisation of the single-doped catalysts, XRD and Raman spectroscopy measurements are carried out to characterise their structure (Figure 5.3).

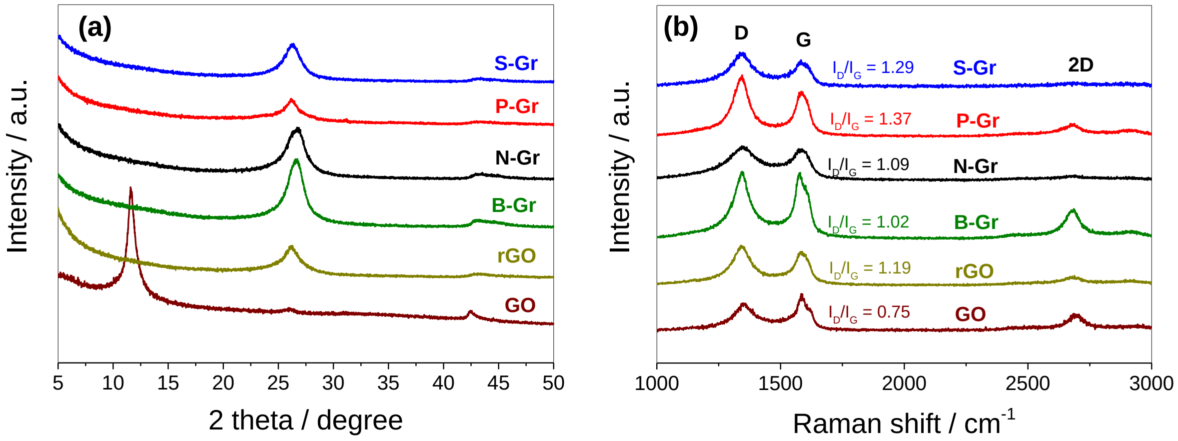

Figure 5.3. *(a) XRD patterns of all single-doped catalysts, including rGO and the GO precursor. (b) Raman spectra of the prepared catalysts using an excitation laser wavelength of 532 nm. The calculated* I_D/I_G *values are also presented.*

The rGO catalyst synthesised under the same conditions but without dopants is also shown for comparison, as well as the GO precursor. The XRD patterns (Figure 5.3a) show a distinctive diffraction peak at 2θ = 11.6° for the GO precursor corresponding to a (002) index related to an interlayer space of 0.79 nm. This feature points to the presence of oxide groups located in the basal space between layers [164]. After pyrolysis, this peak disappears and a new broader peak arises at around 2θ = 26.5°, which is in agreement with the intense narrow peak observed in pristine graphene at 26.6° associated to a basal space between consecutive layers of 0.34 nm [230]. It should be noted that the values of 2θ corresponding to the C(002) peak are in inverse correlation to the distance between consecutive graphene layers [308]. Figure 5.3a shows that the value of 2θ for the C(002) peak is 26.7° for B-Gr and N-Gr, whereas that for P-Gr and S-Gr it is around 26.3°. Since B and N have a smaller atomic radius than P and S, the interlayer space is decreased (thus 2θ bigger) in B-Gr and N-Gr with respect to P-Gr and S-Gr. For rGO the 2θ value of the C(002) peak is 26.2 due to the oxygen groups remaining from the GO precursor after the thermal treatment. Beside this, the width and intensity of the C(002) peak in the doped graphene catalysts and rGO compared to graphite [309] indicate that the restoration of the graphene structure is only partial. The conclusion of these results is that annealing partially recovers the crystal structure of pristine graphene due to the reduction of the oxide groups present in the GO precursor. The faint peak appearing at around 43° corresponds to (101) reflections in the carbon phase [116].

The Raman spectra (Figure 5.3b) are obtained under ambient conditions and show the characteristic peaks corresponding to the D and G bands at 1340 and 1580 cm^{-1}, respectively. The D band is attributed to the presence of defects or distortion of the 2D graphene lattice, whereas the G band is produced by stretching of the sp^2 bonds between carbon atoms and it is commonly associated to the degree of graphitization [112]. The ratio of D and G bands (I_D/I_G) is a good indicator of the degree of structural disorder of a material and values are indicated in Figure 5.3b for all the catalysts. The I_D/I_G ratio is lower for B-Gr and N-Gr (ca. 1.05) with respect to P-Gr and S-Gr (ca. 1.35). This suggests that the integrity of the graphene structure is dependent on the size of the doping atoms, rather than the amount of doping species incorporated into the graphene layers. rGO shows an I_D/I_G ratio of 1.19, which reflects the presence of remaining oxide groups (see Table 5.1). It is observed that the values of I_D/I_G ratio in the Raman spectra keep an inverse correlation with the intensity of the C (002) peaks reflected in the XRD graph, noting that both features are closely related to defects present on the graphene structure [308]. Raman spectra can also provide information about the mean crystallite size (L_a) of the different doped-graphenes via the Tuinstra-Koenig (T-K) equation [310]:

$$\frac{I_D}{I_G} = \frac{C(\lambda)}{L_a} \tag{5.1}$$

where C(532 nm) is ~ 49.56 Å [311] (however, it should be noted that the T-K method has been questioned in the literature [312], where it is stated not being valid over all ranges of L_a and wavelengths). The values of L_a are shown in Table 5.2.

Table 5.2. *I_D/I_G ratios and mean crystallite size (L_a) of the different catalysts obtained from the Raman spectra.*

	GO	rGO	B-Gr	N-Gr	P-Gr	S-Gr
I_D/I_G	0.75	1.19	1.02	1.09	1.37	1.29
L_a (Å)	**66.1**	**41.6**	**48.6**	**45.5**	**36.2**	**38.4**

It can be seen that the mean crystallite size of the different doped-graphene catalysts has been reduced with respect to GO due to the thermal treatment applied and the incorporation of the different heteroatoms into the graphene structure [311]. This is in agreement with the higher I_D band observed in doped graphenes with respect to GO, as a consequence of the hexagonal symmetry distortion of graphene due to the incorporation of heteroatoms [308].

To gather insight into the mechanism of doping and the nature of the bonds formed during the thermal treatment, XPS is used to determine the different species, and the XPS survey spectra are displayed in Figure 5.4.

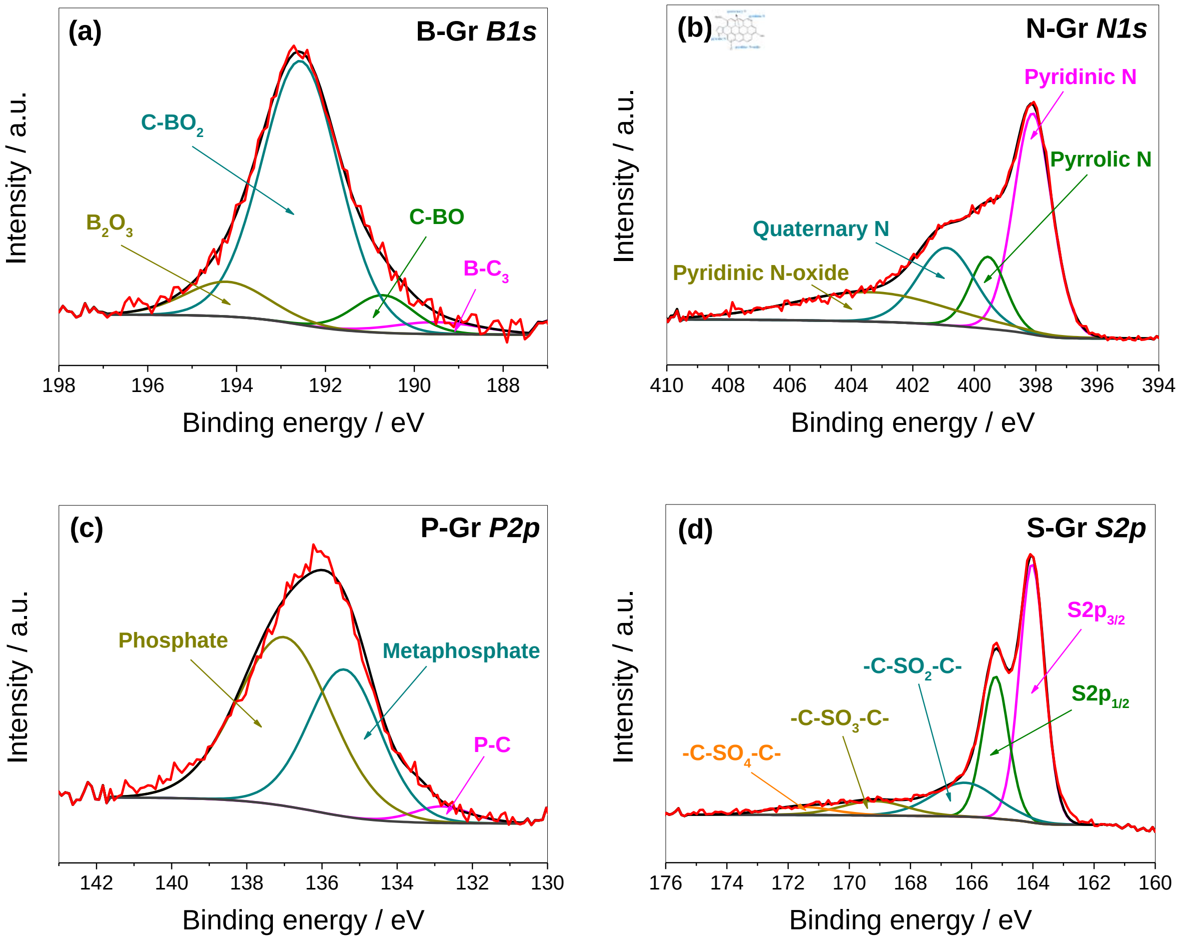

Figure 5.4. *Deconvolution XPS spectra of (a) B1s in B-Gr, (b) N1s in N-Gr (inset: description of N-bonding species* [156]*), (c) P2p in P-Gr and (d) S2p in S-Gr.*

The deconvoluted B1s spectrum (Figure 5.4a) for the B-Gr catalyst is fitted to four peaks at 189.5, 190.6, 192.5 and 194.1 eV, attributable to B-C_3 (*sp*^{2}), C-BO, C-BO_2 and B_2O_3, respectively [113,313], being C-BO_2 the predominant B moiety, with 76.6%. The deconvolution of the N1s spectrum (Figure 5.4b) generates four N species, namely pyridinic N (398.2 eV), pyrrolic N (399.5 eV), quaternary N (400.8 eV, also called graphitic) and pyridinic N-oxide (403.6 eV), which are represented in the inset of Figure 5.4b [156]. In this case, pyridinic species are predominant with 40.0%, followed by N-oxide species with 24.0%. The composition of N bond species seems to be significantly influenced by the precursors used [108], duration of the thermal treatment [124] and the combination of precursors and temperature of operation [106]. For example, a study found that the quaternary N bonds appear at 800 °C and increase at 900 °C, whereas pyrrolic N decreases with the temperature in the range between 700 and 900 °C and pyridinic N remains constant as the main N bonding specie [105]. The P2p peak observed in P-Gr (Figure 5.4c) can be mainly deconvoluted into two oxidised species, namely phosphorus at high oxidation levels (137.2 eV) [173] representing the 57.8% of the composition, which are basically phosphates remaining unaltered from the phosphoric acid precursor [171], and metaphosphates (135.2 eV) with 38.7%, caused by the condensation of phosphates [172], followed by a very small contribution of the P-C bond (132.7 eV) [173] with 3.5%. Titirici et al. argue that the P atom is too large to be incorporated in the graphitic surface, and can only be lodged at edge sites [314]. Finally, the S2p feature (Figure 5.4d) has 73.6% of -C-S-C-, in which the S atoms can adopt two different spin-orbit coupling positions: $S2p_{3/2}$ (164.1 eV) and $S2p_{1/2}$ (165.2 eV) [175,176], and 26.4% of $-C-SO_x-C-$, with x=2 (167.5 eV), x=3 (169.4 eV) or x=4 (171.2 eV) [119]. This pattern is predominant in the sulphur-doped graphenes reported in the literature [119,174–176], suggesting that, unlike the rest of dopants analysed, the different S precursors and synthesis procedures do not produce significant variability on the final catalyst.

In order to investigate the catalytic performance, the single-doped catalysts are compared with rGO by RRDE voltammetry for the ORR in O_2-saturated 0.1 M KOH electrolyte, and the results are shown in Figure 5.5a. The RRDE measurements are taken at a scan rate of 10 mV s^{-1} and a rotation speed of 1600 rpm.

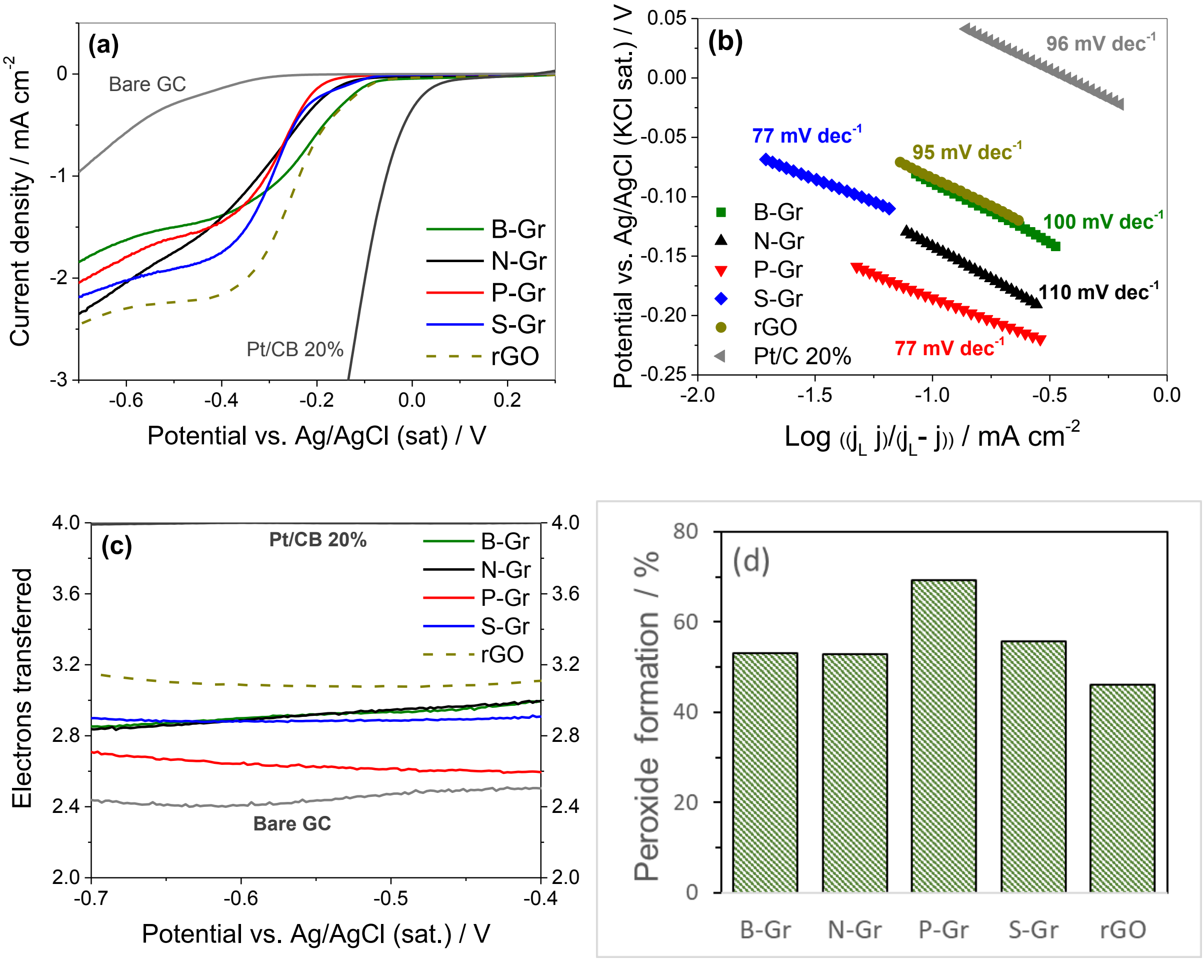

Figure 5.5. *(a) LSV measurements of the single-doped graphene catalysts, including rGO, in O_2-saturated 0.1 M KOH solution, measured at 10 mV s^{-1} and 1600 rpm. A commercial Pt/C 20% and Bare GC electrode are also shown for comparison. (b) Tafel plots corresponding to the data shown in (a). (c) Number of electrons transferred during the ORR vs. the applied potential calculated from RRDE measurements at 1600 rpm using Eq 3.5. (d) Peroxide formed during the ORR at -0.5 V obtained from the values shown in (a) using Eq 3.6.*

It is observed that all the catalysts are active towards the ORR under alkaline conditions, with lower overpotentials and increased magnitude of current densities than for GC, but not as catalytic as rGO. Nevertheless, some small differences are reported in the single-doped catalysts. For example, B-Gr exhibits the earliest onset potential, similar to that observed in rGO, whereas N-Gr and S-Gr show the highest current density at -0.6 V, although lower than that observed in rGO.

The mechanism of reaction and the identification of the rate determining step (rds) are studied using the calculated Tafel slopes shown in Figure 5.5b, as discussed in Section 2.1.2.3. It is observed that all the single-doped and rGO catalysts show values between 60 and 120 mV dec^{-1}, corresponding to Reaction *2.24* and Reaction *2.23* as rds, respectively. In this context, the Tafel slopes of P-Gr and S-Gr, with values of 77 mV dec^{-1} in both cases, are lower than that reported for rGO (95 mV dec^{-1}), whereas B-Gr and N-Gr exhibit higher Tafel slopes, with values of 100 and 110 mV dec^{-1}, respectively. Taking into account that, unlike Reaction *2.24*, Reaction *2.23* is an electron-transfer reaction, those catalysts with Tafel slopes closer to 120 mV dec^{-1} (B-Gr and N-Gr) are considered less efficient in terms of electron transfer than those with Tafel slope values closer to 60 mV dec^{-1} (P-Gr and S-Gr).

One important feature to take into account when analysing the catalytic activity of a nanomaterial for the ORR is the number of electrons transferred (*n*) during the electrochemical reaction. As discussed in Section 3.2.2, this gives valuable information about the predominant mechanism, with n values closer to 2 indicating a 2-step mechanism with high peroxide intermediate production, whereas a n value closer to 4 points to a direct 1-step mechanism with lower peroxide formation rate. From the RRDE measurements n is calculated using Eq *3.5*, and Figure 5.5c shows the values of n at 1600 rpm versus the potential applied. These values are quite stable in the range from -0.4 to -0.7 V, showing a similar result for B-Gr and N-Gr with values of

2.93 and 2.95 at -0.5 V, respectively, whereas it is 2.88 for S-Gr and significantly lower for P-Gr (2.62). In agreement with the behaviour observed in Figure 5.5a, the value of n is higher for rGO (3.08) with respect to the single-doped graphenes. In a similar manner to the calculation of n, the production rate of peroxide intermediate can be also calculated from RRDE measurements using the Eq *3.6*. The results are displayed in Figure 5.5d for an applied potential of -0.5 V, showing P-Gr the highest peroxide production rate with 69.2%, while the values for S-Gr, B-Gr and N-Gr are 55.8%, 53.1% and 52.8% respectively. rGO is the only one showing a value below 50%, with 46.1%.

In conclusion, the single-doped graphene catalysts do not show an improved catalytic activity with respect to a catalyst prepared under the same annealing conditions but without the addition of dopants. In all cases, the single-doped catalysts show a mixed behaviour between the two proposed mechanisms, with peroxide production rates above 50%, whereas the catalytic performance of rGO is slightly better but still showing a mixed ORR mechanism. Despite the high variability in the quality of the graphene layers of the different catalysts, indirectly measured by Raman spectra, it is observed that the presence of defects in the graphene structure has no significant influence in the catalytic behaviour. For example, B-Gr and P-Gr exhibit I_D/I_G ratios of 1.02 and 1.37, respectively, but they show a similar catalytic performance. On the other hand, rGO shows an average I_D/I_G ratio compared to the rest of the catalysts. In terms of the activities of the specific bonding groups, it is not identified any bonding group linked to a specific dopant which makes a substantial difference in terms of catalytic activity. Therefore, it is worth to explore combinations of dopants in order to analyse if the interaction of the different atoms can create an improved catalytic activity towards the ORR.

5.3 Dual-doped graphene

In order to continue with the analysis and discussion of graphene doped with heteroatoms, in this section the structure, composition and ORR performance of several dual-doped graphene catalysts are thoroughly studied. Three different dual-doped graphenes have been synthesised, being the first dopant B, P or S, and fixing the second dopant as N, obtaining BN-Gr, PN-Gr and SN-Gr.

In order to continue with the same structure, the characterisation of the three dual-doped graphene catalysts in terms of composition is developed using XPS measurements. In Figure 5.6 it can be seen the characteristic peaks, showing that the doping procedure is successful. Table 5.3 exhibits the compositions of the different catalysts with their corresponding errors.

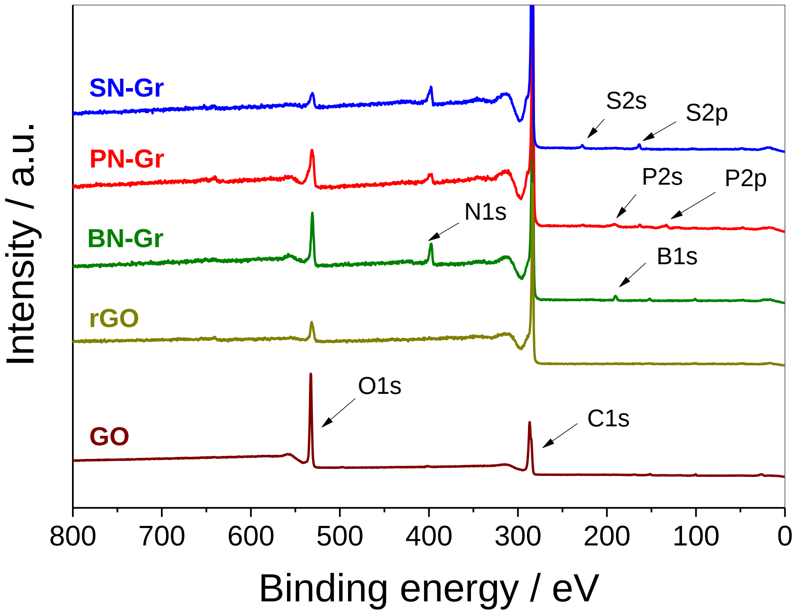

Figure 5.6. *Survey XPS spectra of the dual-doped graphene catalysts plus GO and rGO, showing the peaks corresponding to the dopants.*

Table 5.3. *Dual-doped graphene catalyst compositions (calculated from XPS measurements) with their corresponding errors.*

Catalyst	C	O	B	N	P	S
GO	67.8 ± 0.2	32.2 ± 0.2				
rGO	94.8 ± 0.3	5.2 ± 0.3				
BN-Gr	83.5 ± 0.5	7.5 ± 0.2	3.1 ± 0.4	5.7 ± 0.1		
PN-Gr	88.0 ± 1.7	6.9 ± 1.5		2.5 ± 0.4	1.2 ± 0.1	
SN-Gr	92.1 ± 0.6	2.6 ± 0.6		4.1 ± 0.1		0.9 ± 0.1

Among the different dopants, it is observed that nitrogen is the most easily assimilated into the graphene structure, confirming the results observed in the single-doped graphenes. Nevertheless, the nitrogen content varies depending on the second dopant, being the BN-Gr the catalyst which shows the highest nitrogen content. This result confirms the conclusions of a previous similar study [315]. In terms of oxide reduction, it is observed that only SN-Gr displays a lower oxygen content than rGO, in agreement with the observations in single-doped graphenes where only N-Gr and S-Gr show lower oxygen content than rGO.

The XRD patterns of the dual-doped graphene catalysts, together with the GO precursor and rGO, are shown in Figure 5.7a.

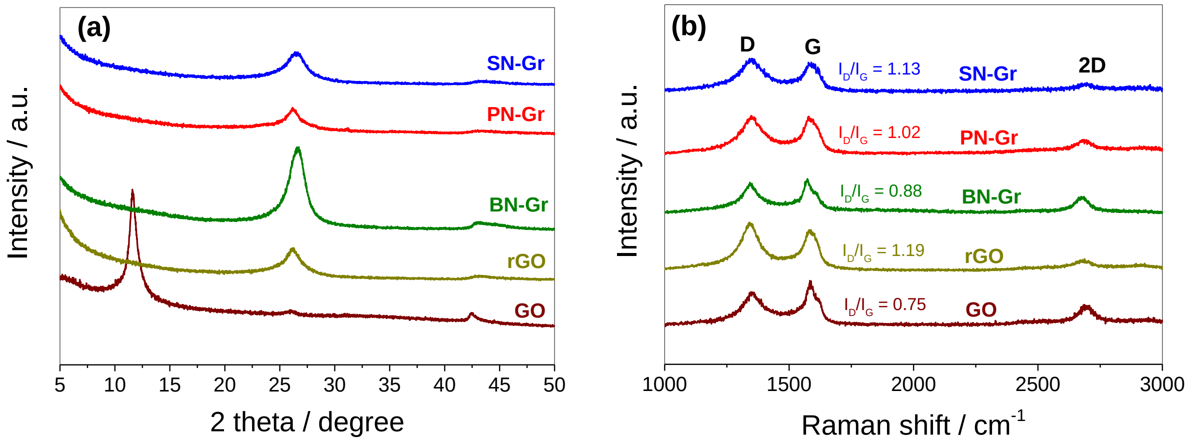

Figure 5.7. *(a) XRD patterns of all dual-doped catalysts, including rGO and the GO precursor. (b) Raman spectra of the prepared catalysts using an excitation laser wavelength of 532 nm. The calculated* I_D/I_G *values are also presented.*

In the same way that single-doped graphenes, the GO diffraction peak at 2θ = 11.6° disappears and a new value at around 26.5° (corresponding to C(002)) arises after the thermal treatment. Following the same pattern observed in single-doped graphenes, the value of 2θ corresponding to the C(002) peak of BN-Gr is shifted to the right with respect to the other dual-doped graphenes, due to the smaller atomic radius of B and the subsequent smaller distance between graphene layers. Here, it is also observed that the synthesised catalysts show less sharp peaks than GO, due to the partial recovery of the graphene structure after the thermal treatment.

This can be further confirmed by the Raman spectra (Figure 5.7b). It is clearly observed that the BN-Gr catalyst shows the lowest I_D/I_G ratio among the dual-doped graphenes, confirming that the smaller boron atoms are linked to fewer defects in the graphene structure. This positive effect of boron in reducing the defects and favouring the restoration of the sp^2 graphene structure has been previously observed in dual-doped graphene catalysts [315]. However, it is surprising to observe that the dopant-free rGO shows the highest value of I_D/I_G, as it would be expected that the absence of foreign atoms in the structure would lead a more free-of-defects structure. One posible explanation could be that there are voids and vacancies in the rGO structure due to the loss of oxide groups during the thermal treatment. The values of L_a obtained from the T-K equation (Eq. *5.1*) are shown in Table 5.4 and confirm that the mean crystallite size decreases with respect to GO after the application of the annealing.

Table 5.4. *I_D/I_G ratios and mean crystallite size (L_a) of the dual-doped graphenes obtained from the Raman spectra.*

	GO	rGO	BN-Gr	PN-Gr	SN-Gr
I_D/I_G	0.75	1.19	0.88	1.02	1.13
L_a (Å)	**66.1**	**41.6**	**56.3**	**48.6**	**43.9**

The XPS spectra (Figure 5.8) show the deconvolution of the characteristic peaks of the dual-doped graphenes.

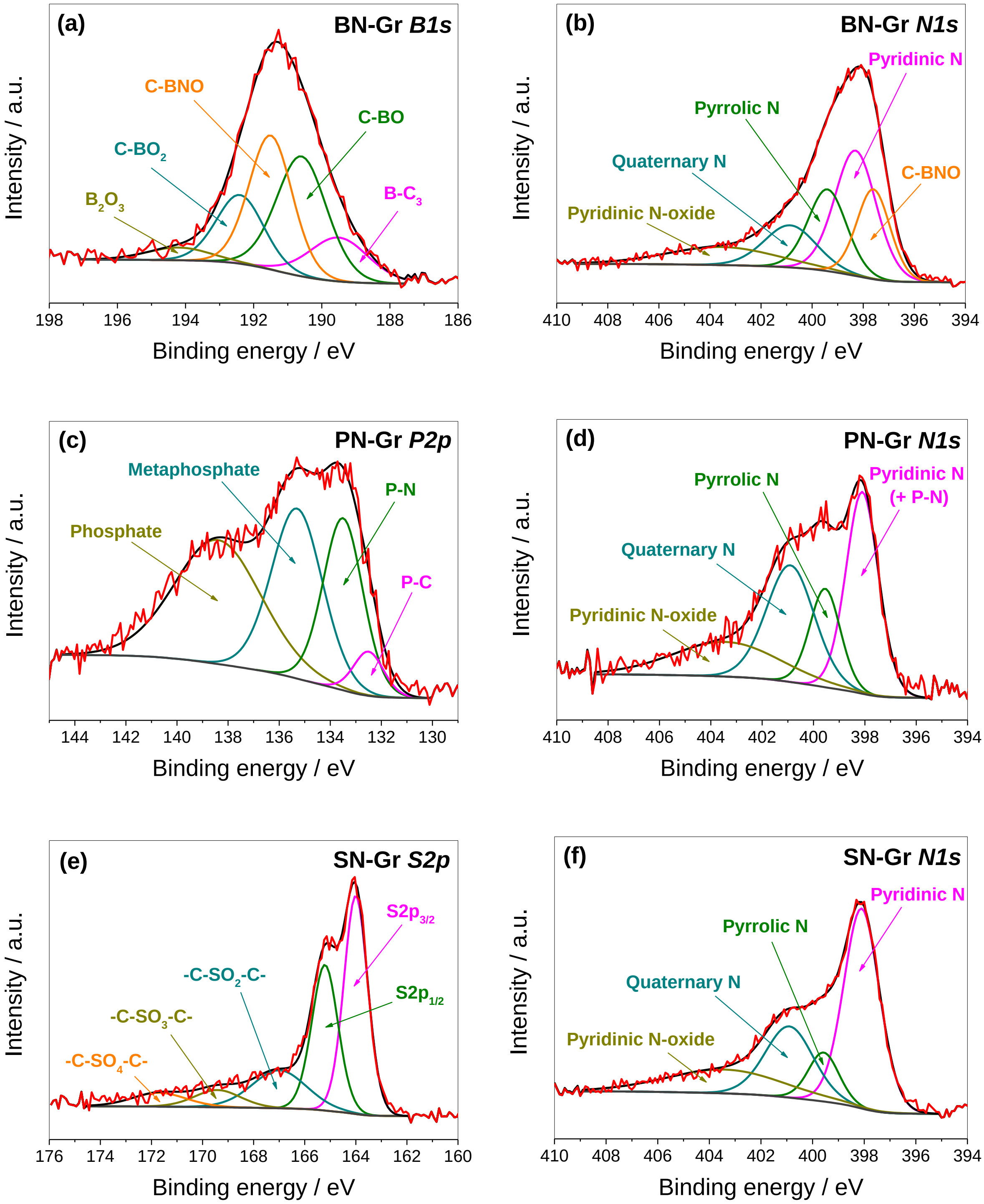

Figure 5.8. *Deconvolution XPS spectra of (a) B1s and (b) N1s in BN-Gr, (c) P2p and (d) N1s in PN-Gr, and (e) S2p and (f) N1s in SN-Gr.*

In BN-Gr the B1s peak (Figure 5.8a) shows significant differences with respect to that observed in B-Gr (see Figure 5.4a). First, due to the simultaneous incorporation of B and N, a new peak arises at 191.5 eV corresponding to C-BNO [313] representing the 31.4%. C-BO also increases to 32.7%, whereas C-BO$_2$ decreases from 76.6% observed in B-Gr to 17.6%. This is in agreement with the lower oxygen content observed in BN-Gr with respect to B-Gr. Regarding the deconvolution of the N1s peak (Figure 5.8b), the C-BNO peak appears in BN-Gr at 397.5 eV [316] at the expense of pyridinic N, thus sweeping the N1s peak to the right. The P2p peak of PN-Gr (Figure 5.8c) shows a widening to the right with respect to P-Gr due to the inclusion of P-N species at 133.7 eV [314], thus decreasing the contribution of the phosphate and metaphosphate moieties to the overall composition. This indicates that the presence of N dopants modifies the way in which the P dopants are incorporated into the graphene structure. The P dopants in turn alter the N1s peak of PN-Gr (Figure 5.8d) with respect to N-Gr, displaying a higher contribution of the quaternary N moieties. It should be noted that the P-N moieties appear at 398.1 eV [314], which is the same position that N-pyridinic species. In the case of the SN-Gr catalyst, the S2p peak (Figure 5.8e) does not exhibit significant variations with respect to that seen in S-Gr, with the -C-S-C- species representing the 71.6%, only noting a slight increase of the S2p$_{1/2}$ contribution with respect to S2p$_{3/2}$. On the other hand, the N1s deconvolution (Figure 5.8f) is similar to that observed in N-Gr, only reporting a small decrease of the pyrrolic N contribution.

The electrochemical performance of the dual-doped graphene catalysts is investigated using RRDE measurements in O$_2$-saturated 0.1 M KOH electrolyte under the conditions described in Section 3.3.6.2. The LSV measurements are displayed in Figure 5.9a.

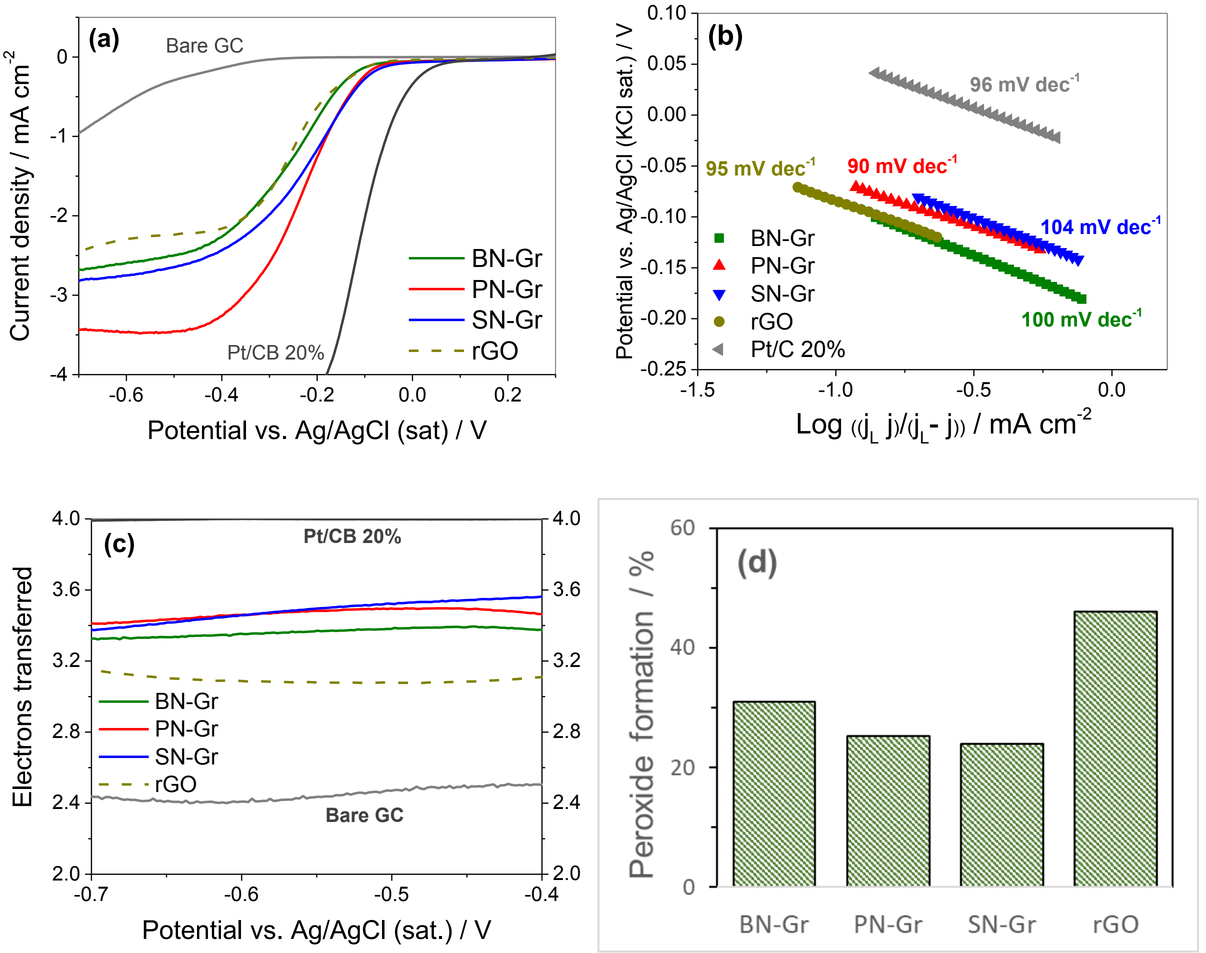

Figure 5.9. *(a) LSV measurements of the dual-doped graphene catalysts, including rGO, in O_2-saturated 0.1 M KOH solution, measured at 10 mV s^{-1} and 1600 rpm. A commercial Pt/C 20% and Bare GC electrode are also shown for comparison. (b) Tafel plots corresponding to the data shown in (a). (c) Number of electrons transferred during the ORR vs. the applied potential calculated from RRDE measurements at 1600 rpm using Eq (3.5). (d) Peroxide formed during the ORR at -0.5 V obtained from the values shown in (a) using Eq (3.6).*

The LSV measurements show that the three dual-doped catalysts exhibit higher current density than that observed in rGO. BN-Gr shows an onset potential similar to rGO, whereas PN-Gr and SN-Gr exhibit earlier values of onset potential. Regarding the current density, PN-Gr is by far the most active catalyst with a value of current density at -0.6 V of -3.48 mA cm^{-2}, while the corresponding values for BN-Gr and SN-Gr are -2.60 and and -2.75 mA cm^{-2}, respectively. All these values are higher in absolute terms than that reported for rGO: -2.29 mA cm^{-2}.

The calculated Tafel slopes of the dual-doped graphenes displayed in Figure 5.9b show values between 60 and 120 mV dec^{-1}, corresponding to Reaction *2.24* and Reaction *2.23* as rds, respectively. However, it is observed that PN-Gr displays the lowest value (90 mV dec^{-1}), while BN-Gr and SN-Gr yield 100 and 104 mV dec^{-1}, respectively. This implies that in BN-Gr and SN-Gr the rds is determined by the electron-transfer step (Reaction *2.23*), whereas PN-Gr shows a mixed rds between both reactions, indicating a more efficient electron transfer.

The calculated number of electrons transferred during the ORR for the dual-doped catalysts follows a similar pattern to that observed in Figure 5.9a. The values of n (Figure 5.9c) calculated for BN-Gr, PN-Gr and SN-Gr at -0.5 V are 3.38, 3.49 and 3.52, respectively, whereas rGO exhibits a value of 3.08. This demonstrates that the dual-doped graphenes follow a mixed mechanism closer to the direct 1-step route. The peroxide formation rate at -0.5 V is displayed in Figure 5.9d for all the catalysts, showing SN-Gr the lowest peroxide production with 23.9%, and followed by PN-Gr (25.2%) and BN-Gr (31.0%). In contrast, the peroxide production of rGO is considerably higher, with 46.1%.

In summary, it has been reported that the dual-doped graphene catalysts exhibit a better catalytic performance with respect to the dopant-free rGO, especially PN-Gr which shows a significantly higher activity in terms of current density and ORR kinetics. All the dual-doped catalysts yield a lower peroxide intermediate formation than rGO, producing SN-Gr the lowest peroxide formation. Although the quality of the graphene layer can play a role in the performance observed (in fact, all dual-doped graphenes showed lower I_D/I_G ratios than rGO), this conclusion should be taken with caution. For example, BN-Gr exhibits a lower I_D/I_G ratio than PN-Gr (0.88 vs 1.02), but the measured current densities of the latter are higher. Since PN-Gr has demonstrated a considerably higher activity than the single-doped N-Gr and P-Gr, with a value of current density at -0.6 V of -3.48 mA cm^{-2} for PN-Gr versus -2.04 and -1.79 mA cm^{-2} for N-Gr and P-Gr, respectively, it would be interesting to compare the binding species of the different catalysts measured by XPS. Figure 5.10 shows the comparison of the N1s and P2p deconvoluted peaks of PN-Gr, N-Gr and P-Gr.

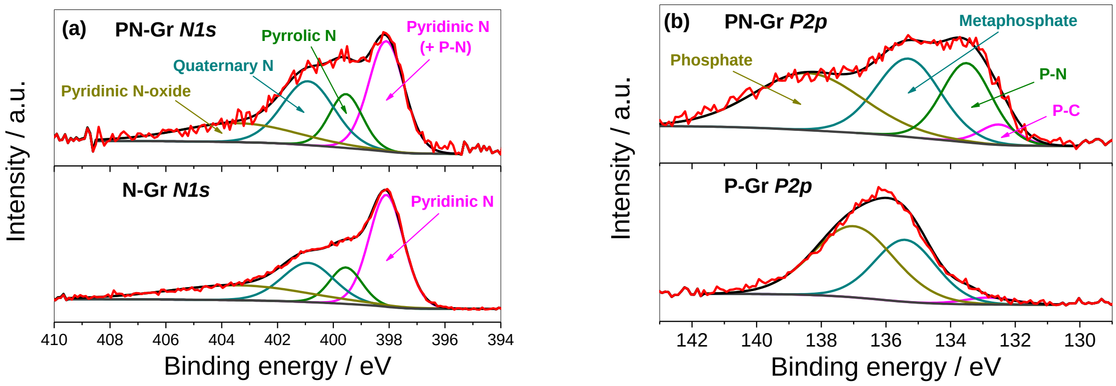

Figure 5.10. *Deconvolution XPS spectra of (a) N1s and (b) P2p of PN-Gr (top) and N-Gr (bottom).*

In Figure 5.10b marked changes are reported in the P2p peak observed in PN-Gr with respect to P-Gr, namely there is a pronounced distortion in PN-Gr at lower binding energies, associated to the rise of P-N and P-C moieties. In addition, in Figure 5.10a it is observed that there are not significant differences in N1s other than a slight increase of quaternary and pyrrolic N in PN-Gr, with minor importance. It should be noted that P-N species appear at the same binding energy that N-pyridinic [314]. At the light of these observations, two possible theories are proposed for the excellent ORR activity observed in the PN-Gr catalyst. Titirici et al. suggest that, when a P site is oxidised and bound to a N co-dopant, it stabilises the graphitic N and activates a neighbouring C site [314]. Furthermore, it is possible that the higher presence of P-C bonds in PN-Gr could be linked to an enhanced catalytic activity. Liao et al. proposed a mechanism for the improved performance according to which, while P-C covalent bonds could induce negatively delocalised C atoms adjacent to P, meanwhile P-O with an O bridge between P and C can induce an electron deficiency in the C atoms [165]. Nevertheless, these conclusions should be confirmed by the results obtained for ternary and quaternary-doped graphenes involving the same groups, which is studied in the next section.

5.4 Ternary- and quaternary-doped graphene

In this section two different ternary-doped graphenes and a novel quaternary-doped doped graphene catalyst are analysed. The ternary-doped graphenes are doped with boron, nitrogen and sulphur (BNS-Gr) and boron, phosphorus and sulphur (BPS-Gr), whereas the quaternary-doped graphene is doped with boron, nitrogen, phosphorus and sulphur (BNPS-Gr).

XPS measurements (Figure 5.11) are used to obtain the compositions of the catalysts, which are displayed in Table 5.5.

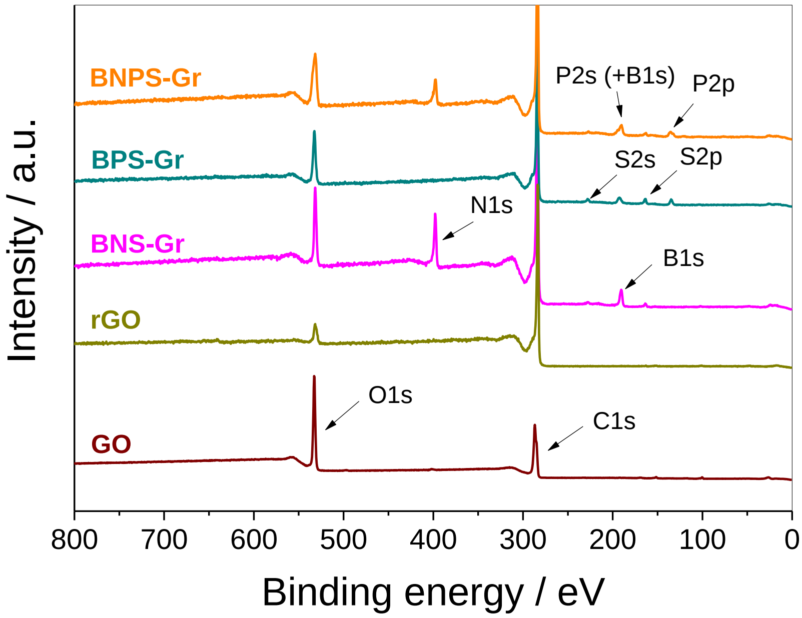

Figure 5.11. *XPS survey spectra of the ternary and quaternary-doped graphene catalysts plus GO and rGO, showing the peaks corresponding to the dopants.*

Table 5.5. *Ternary and quaternary-doped graphene catalyst compositions (calculated from XPS measurements) with their corresponding errors.*

Catalyst	C	O	B	N	P	S
GO	67.8 ± 0.2	32.2 ± 0.2				
rGO	94.8 ± 0.3	5.2 ± 0.3				
BNS-Gr	71.0 ± 1.7	8.4 ± 0.4	10.7 ± 1.0	9.3 ± 0.6		0.6 ± 0.1
BPS-Gr	82.1 ± 5.0	10.7 ± 1.9	3.2 ± 0.5		2.4 ± 0.8	1.6 ± 0.2
BNPS-Gr	74.1 ± 4.4	10.8 ± 1.9	6.4 ± 0.7	6.1 ± 0.1	2.2 ± 0.8	0.4 ± 0.2

For the calculation of boron content in BPS-Gr and BNPS-Gr, it is noted that the broader peak appearing at around 195 eV in those catalysts is consistent with a combination of both the B1s and the P2s moieties, therefore the P2s contribution is calculated from the P2p peak (using the same P2s/P2p ratio calculated for P-Gr) and subtracted to the (P2s+B1s) peak in order to obtain the content of B.

A general increase in the level of the dopant incorporation is observed in the ternary and quaternary catalysts, especially B and N atoms, suggesting that the precursors have a synergistic doping effect. It is also observed that this synergistic effect is not homogeneous, for example, the B content is more than three times higher in BNS-Gr with respect to BPS-Gr, indicating that N facilitates more than P the incorporation of B. Conversely, the S content in BPS-Gr is four times higher than in BNPS-Gr, pointing out that in this case the N atoms hinder the incorporation of S. In addition, it is observed that the oxygen content in all the analysed catalysts remains higher than in rGO, indicating that the presence of a high number of simultaneous dopants hampers the reduction of the oxide groups.

The XRD patterns of the ternary and the quaternary-doped graphene catalysts are shown in Figure 5.12. (a) XRD patterns of ternary- and quaternary-doped catalysts, including rGO and the GO precursor. (b) Raman spectra of the prepared catalysts using an excitation laser wavelength of 532 nm. The calculated ID/IG values are also presented.a, and compared with the GO precursor and rGO.

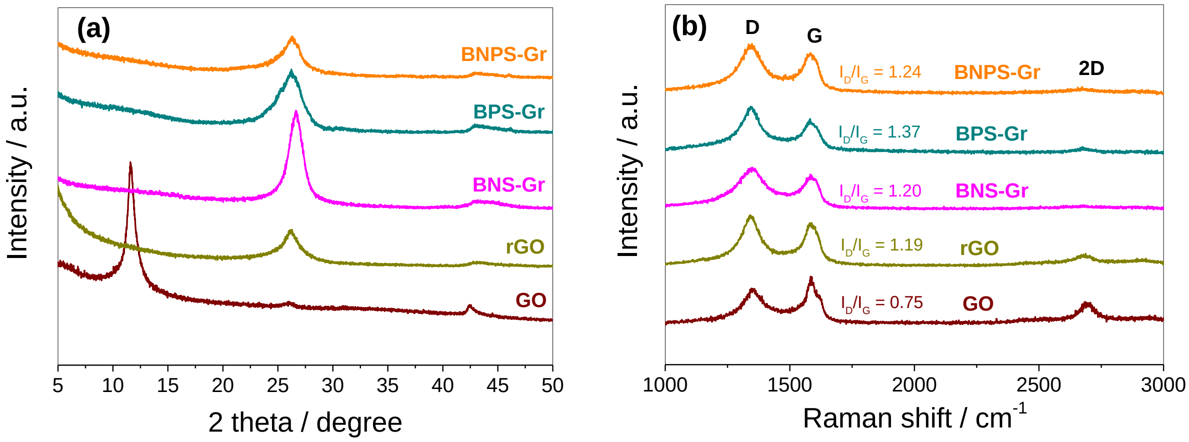

Figure 5.12. *(a) XRD patterns of ternary- and quaternary-doped catalysts, including rGO and the GO precursor. (b) Raman spectra of the prepared catalysts using an excitation laser wavelength of 532 nm. The calculated* I_D/I_G *values are also presented.*

The values of 2θ corresponding to the C(002) peak of the ternary-doped graphenes are 26.7° and 26.2° for BNS-Gr and BPS-Gr, respectively. This difference can be attributed to the N atoms being smaller than P, thus producing a smaller interlayer distance between consecutive layers and a higher value of 2θ for BNS-Gr. The corresponding value for the quaternary-doped graphene is closer to that of BPS-Gr, due to that the value of 2θ for the C(002) peak is determined by the larger atoms present in the structure (P in this case).

The Raman spectra (Figure 5.12b) and the mean crystallite sizes calculated in Table 5.6 reflect that the I_D/I_G ratio of BNS-Gr is lower than that of BPS-Gr.

Table 5.6. *ID/IG ratios and mean crystallite size (La) of the different catalysts obtained from the Raman spectra.*

	GO	rGO	BNS-Gr	BPS-Gr	BNPS-Gr
I_D/I_G	0.75	1.19	1.20	1.37	1.24
L_a (Å)	**66.1**	**41.6**	**41.3**	**36.2**	**40.0**

One possible explanation could be that the N atoms seem to be more effective than P in restoring the sp^2 structure and repairing the defects created during the thermal treatment [315]. This observation is in agreement with the Raman results reported for the single-doped catalysts, where the I_D/I_G ratios were 1.09 and 1.37 for N-Gr and P-Gr, respectively. Regarding the quaternary-doped graphene, the I_D/I_G ratio is significantly lower than in BPS-Gr, probably due to the higher incorporation of B (exactly the double, according to XPS measurements, see Table 5.5), which has a positive effect on the restoration of the sp^2 structure (as previously mentioned for the dual-doped graphene catalysts).

The XPS deconvoluted peaks of the ternary-doped graphene catalysts are displayed in Figure 5.13.

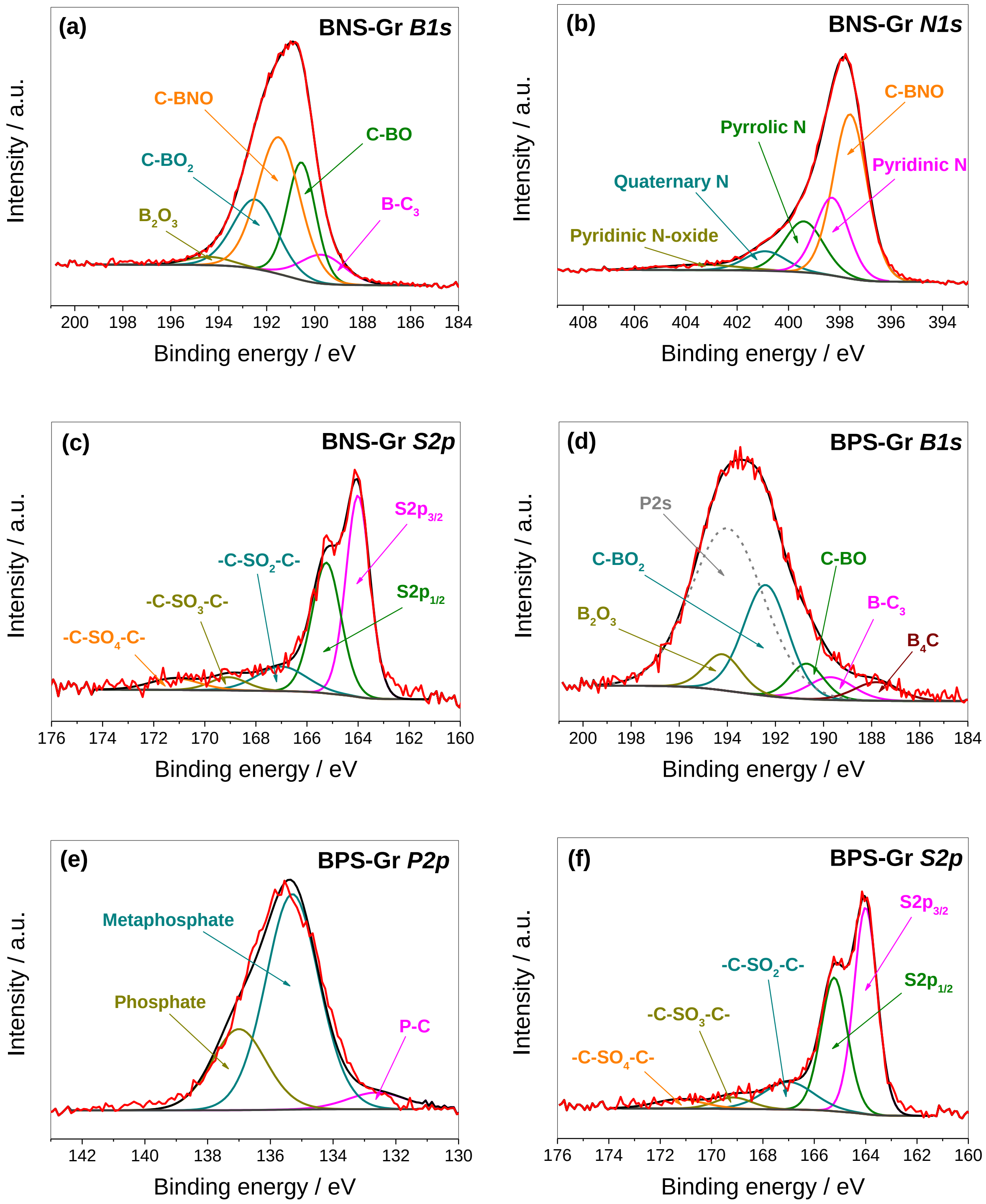

Figure 5.13. *Deconvolution XPS spectra of (a) B1s, (b) N1s and (c) S2p in BNS-Gr, and (d) B1s, (e) P2p and (f) S2p in BPS-Gr.*

In a similar way that the behaviour observed in BN-Gr, the deconvoluted B1s peak of the BNS-Gr catalyst shows the great contribution of the C-BNO moiety, with 41.7%. This peak is also the largest one in the N1s peak, while the quaternary N and the N-oxide pyridinic compositions exhibit very low values, representing 7.1% and 3.7%, respectively. Regarding the S2p peak, there are no important differences with respect to S-Gr other than a further decrease in the contribution of -C-SO_x-C groups, with 20.9%.

With regard to BPS-Gr, the B1s peak is wider than those reported for B-Gr, BN-Gr and BNS-Gr due to the overlap of the P2s peak at 193.8 eV, contributing with the 55.9% of the overall area. In addition, there is a distortion of the B1s peak at lower binding energies, corresponding to a new B_4C moiety (187.9 eV) [313], which does not appear in the rest of boron-containing doped-graphenes. Since N dopants are not present, C-BO_2 is once again the main contributor with 53.2% (after S2p subtraction), due to the absence of the C-BNO moeity. In the P2p peak, the main feature is that, unlike in P-Gr and PN-Gr, metaphosphates are by far the main contributors (66.1%) to the overall area. The S2p does not display any significant difference with respect to the other catalysts studied.

The quaternary-doped graphene catalyst shows simultaneously all the used dopants, as shown in the deconvoluted peaks displayed in Figure 5.14.

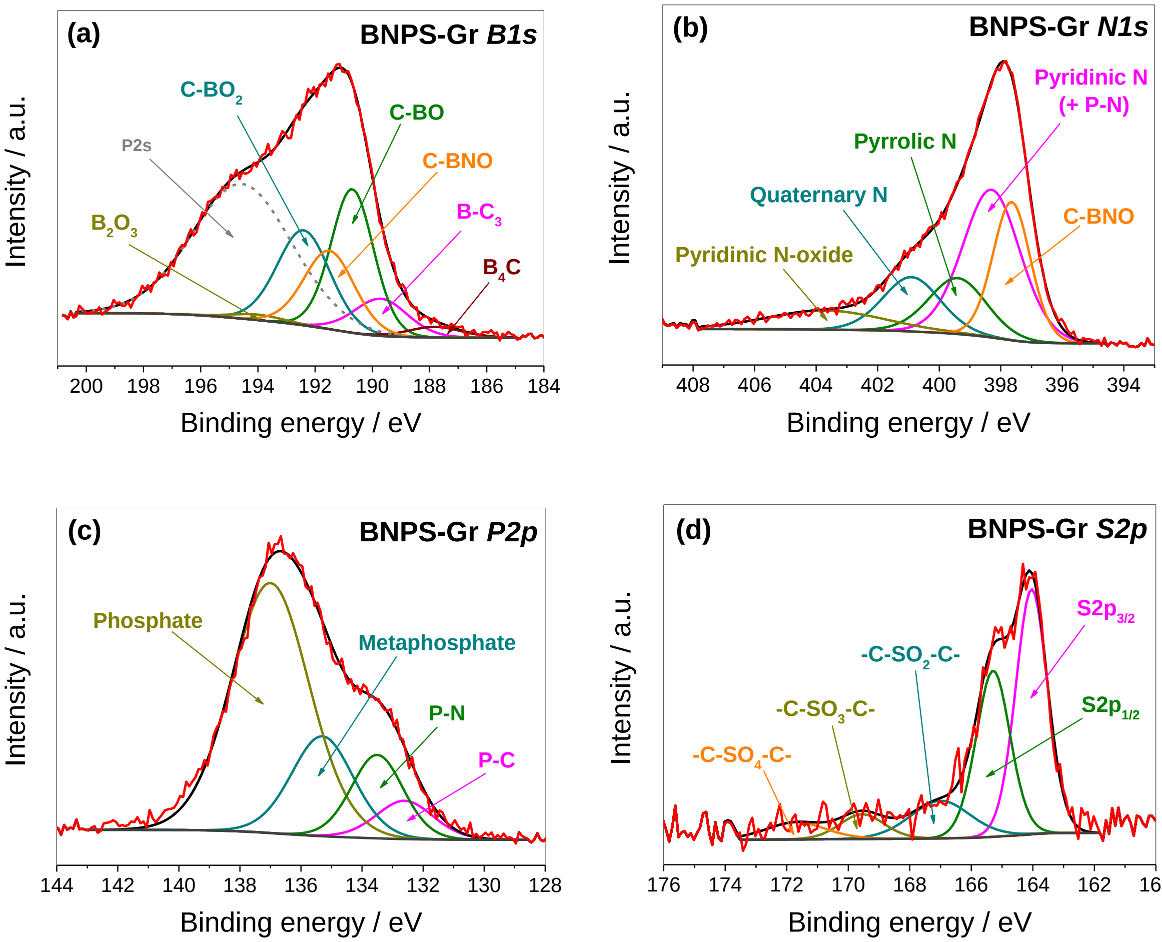

Figure 5.14. *Deconvolution XPS spectra of (a) B1s, (b) N1s, (c) P2p and (d) S2p peaks in the BNPS-Gr catalyst.*

First, in the same way that in BPS-Gr, the B1s peak overlap with the P2s, which shows a contribution of 42.8%. The C-BNO is also present due to the simultaneous doping of B and N, although in this case it has a smaller contribution than the other oxidised species (C-BO and C-BO$_2$). As it is observed in BPS-Gr and unlike in B-Gr, BN-Gr and BNS-Gr, the B$_4$C moiety is also present, suggesting that its presence is related to the simultaneous doping of B and P. In the N1s peak, the C-BNO counts 23.4% of the overall area, showing the rest of the moieties a similar proportion than that reported for

N-Gr. P has been incorporated into the catalyst mainly as phosphates (60.4%), while the P-C bond proportion is relatively high, with 6.8%. It is also noticeable the rise of P-N moieties, but in a lesser extent that in the PN-Gr catalyst. Finally, the S2p peak does not seem to be affected by the presence of other dopants and show a similar behaviour to that reported for S-Gr, with -C-S-C- contributing with 75% of the overall area.

The electrochemical behaviour of the ternary and quaternary-doped graphenes is studied by LSV measurements (Figure 5.15a).

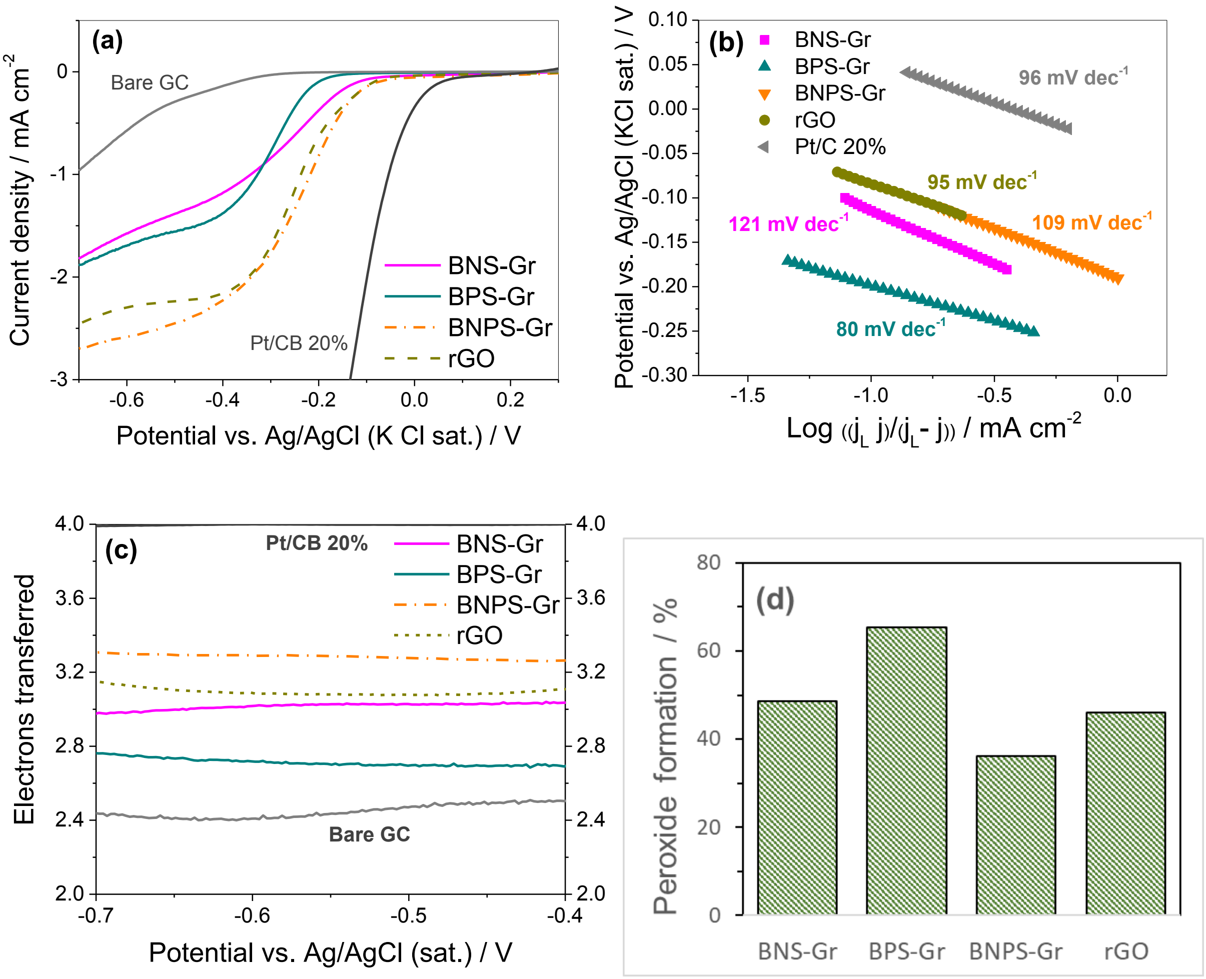

Figure 5.15. *(a) LSV measurements of the ternary and quaternary-doped graphene catalysts, including rGO, in O_2-saturated 0.1 M KOH solution, measured at 10 mV s^{-1} and 1600 rpm. A commercial Pt/C 20% and Bare GC electrode are also shown for comparison. (b) Tafel plots corresponding to the data shown in (a). (c) Number of electrons transferred during the ORR vs. the applied potential calculated from RRDE measurements at 1600 rpm using Eq. 3.5. (d) Peroxide formed during the ORR at -0.5 V obtained from the values shown in (a) using Eq. 3.6.*

It can be seen that the ternary-doped catalysts exhibit lower current densities than rGO, with BNS-Gr having an earlier onset potential than BPS-Gr, but the latter showing higher overpotential than BNS-Gr, with -1.69 and -1.57 mA cm^{-2} at -0.6 V, respectively. Conversely, the catalytic performance of the quaternary catalyst exhibits a similar behaviour than rGO with practically the same onset potential. Nevertheless, BNPS-Gr leads rGO in terms of current density beyond -0.4 V, yielding 2.58 and 2.30 mA cm^{-2} at -0.6 V, respectively.

The Tafel slopes are calculated and displayed in Figure 5.15b, revealing that BNS-Gr and BNPS-Gr yield both a value similar to 120 mV dec^{-1} that corresponds to the electron-transfer reaction *2.23* being the rds. Surprisingly, BPS-Gr shows a significantly lower Tafel slope (80 mV dec^{-1}), reflecting a rds closer to reaction *2.24* than reaction *2.23*, which implies improved electron-transfer kinetics with respect to the other two catalysts analysed here. However, this is not reflected in an improved catalytic activity in terms of higher current densities.

The number of electrons transferred (Figure 5.15c) keeps a better correlation with the catalytic activity observed in terms of measured current densities. Thus, the values of n of the two ternary-doped catalysts (3.03 for BNS-Gr and 2.69 for BPS-Gr) are below than that reported for rGO (3.08), in the same way that they show lower overpotentials in Figure 5.15a. Similarly, the quaternary-doped catalyst exhibits a higher value of n (3.28) than rGO. The calculated peroxide production rates (Figure 5.15d) for the ternary compounds are 48.6% and 65.3% for BNS-Gr and BPS-Gr respectively, whereas this value is considerably lower for the quaternary-doped graphene (36.1%).

The main conclusion obtained from the results discussed above is that the ternary-doped graphene catalysts exhibit a poor performance, showing lower catalytic activities than that observed in rGO, whereas the incorporation of a fourth dopant into the graphene structure gets to improve the performance, even surpassing the catalytic activity of the dopant-free rGO. Once again, the results obtained in the Raman spectra regarding the defects present on the graphene layers of the different catalysts show a poor correlation with the results obtained. If we attend to the different bonding species (see Appendix 4), it is observed that N and S composition exhibits small differences among the different catalysts. Nevertheless, in the case of P it can be seen that a higher composition in phosphates and metaphosphates is linked to a lower catalytic activity, being the sum of the other two species (P-N and P-C) 20.3% for BNPS-Gr and 5.8% for BPS-Gr. This confirms the conclusion obtained in the discussion of dual-doped graphene catalysts with regard to the enhanced catalytic activity observed in PN-Gr. Regarding the B1s deconvolution, it is seen a higher composition in the C-BO moiety in BNPS-Gr (34.0%) with respect to BNS-Gr and BPS-Gr, with 24.1% and 12.8% respectively, which could be associated to the improved catalytic activity developed by the quaternary-doped graphene catalyst. This conclusion is also observed for the single and dual-doped comparison, where the C-BO compositions of B-Gr and BN-Gr were 8.5% and 32.6%, respectively, showing BN-Gr an improved catalytic performance. The mechanism behind this observation is unknown, but it could be related to the oxygen deficiency of C-BO with respect to the other predominant moiety C-BO_2, which could increase the interaction of the catalyst with the O-O molecule.

5.5 Further characterisation of the quaternary-doped graphene

A wider range of tools is available for physical and electrochemical characterisation of doped-graphene catalysts. To avoid unnecessary repetition, it has been decided to apply several more characterisation techniques to the quaternary-doped graphene only. This catalyst is selected due to that it has not been previously reported in the literature, and it contains all the dopants used for the rest of the catalysts.

The nanostructure of BNPS-Gr is investigated by HR-TEM imaging, and the corresponding images are shown in Figure 5.16.

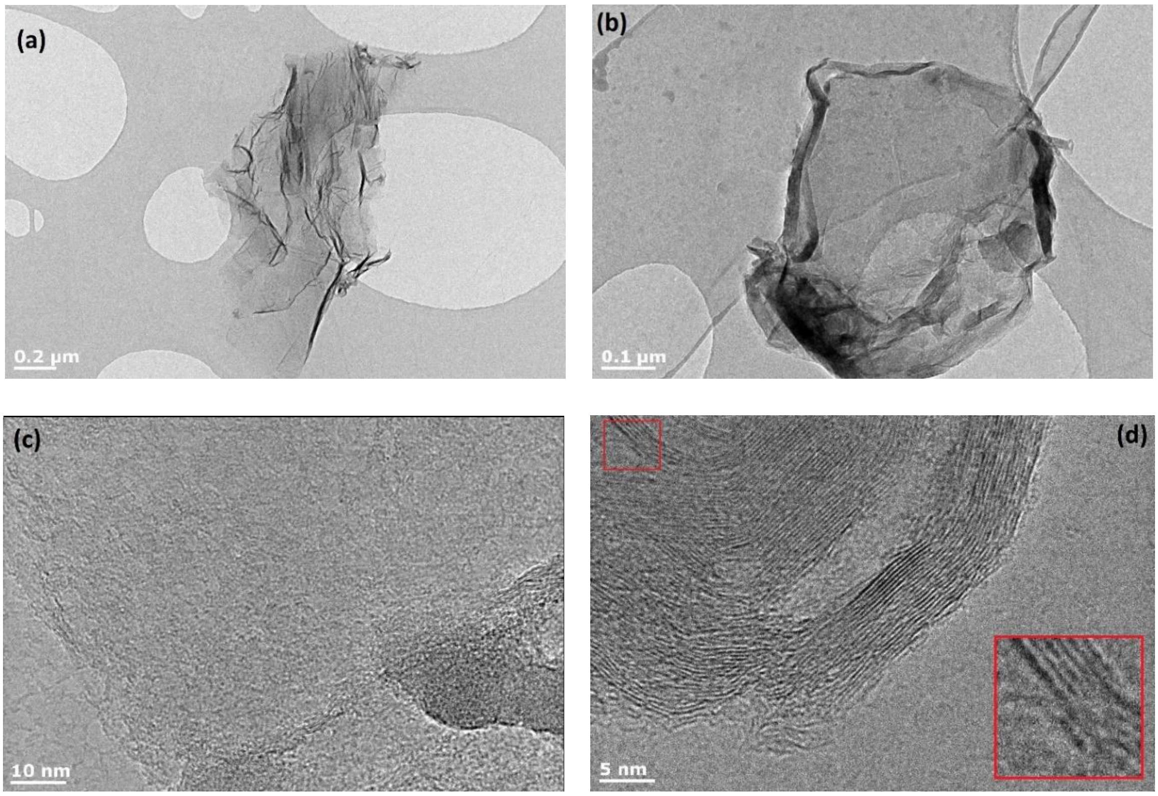

Figure 5.16. *(a) (b) Low-resolution and (c) (d) high-resolution TEM images of the quaternary-doped graphene catalyst. Inset: Higher resolution HR-TEM image showing a 6-layer graphene stack.*

Figure 5.16a and b show the characteristic wrinkled veil-like structure of the graphene sheets, with a randomly stacked and overlapped distribution of layers, and local areas exhibiting agglomeration and disorder of the 2D structure. Figure 5.16c also reflects the presence of graphene nanosheets albeit with non-uniform layer thickness, demonstrating variability in the number of graphene sheets. This feature is shown in greater detail in Figure 5.16d where the individual graphene nanosheets can be seen with theoretical thickness of 0.35 nm [317]. The inset clearly shows a 6-layer stack, although there are regions with a higher number of graphene sheets.

The elemental mapping of the dopants in the graphene is obtained by EDX and displayed in Figure 5.17.

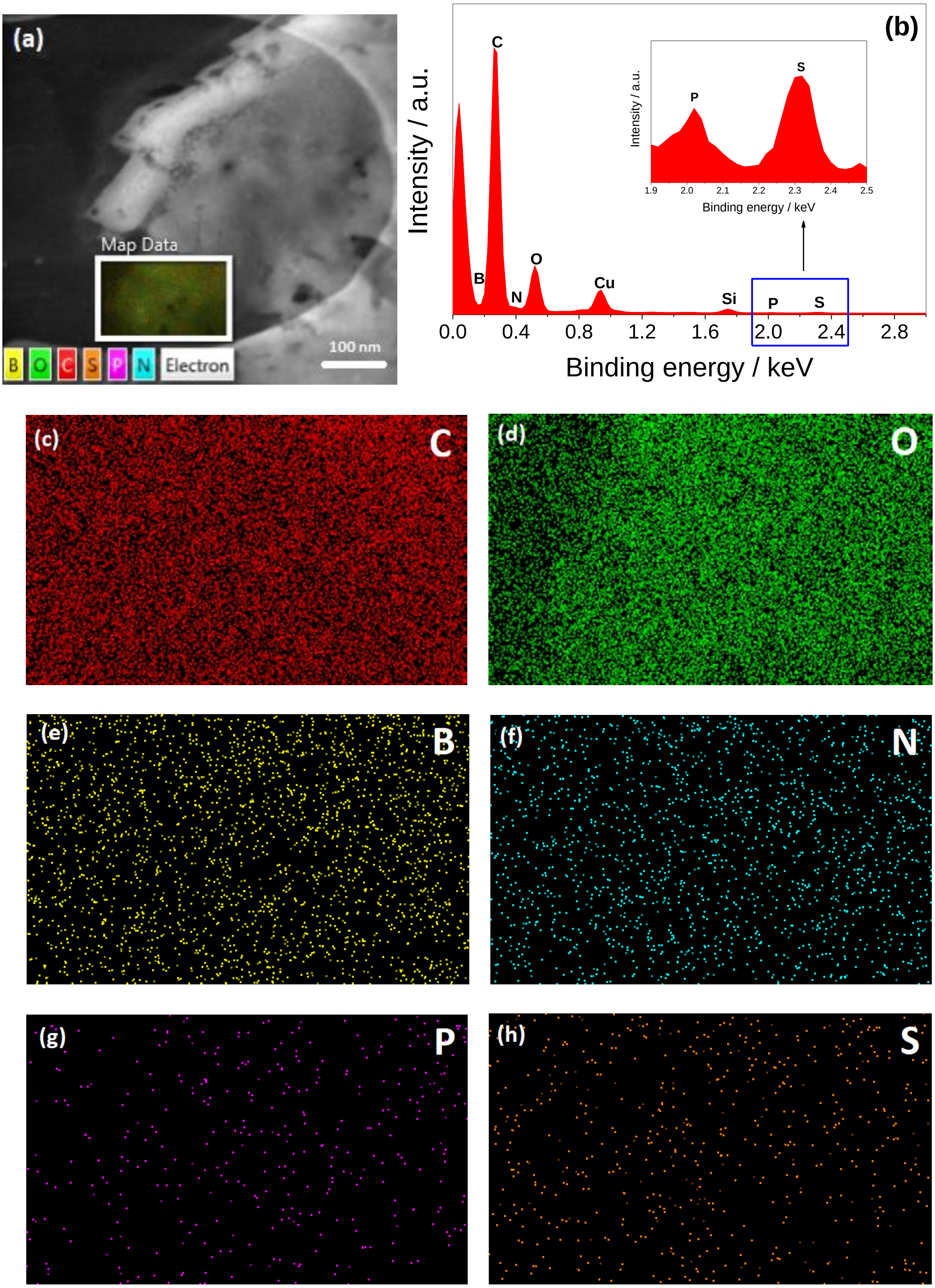

Figure 5.17. *(a) STEM image and (b) EDX spectra of BNPS-Gr, with (c-h) the corresponding C, O, B, N, P and S elemental mappings, respectively.*

It is noted that the C, O, B, N, P and S atoms are incorporated and uniformly distributed along the carbon structure. The EDX profile (Figure 5.17b) also provides evidence of the incorporation of the different dopants. Nevertheless, the B and N peaks that should appear at 0.183 and 0.392 keV, respectively, are hidden by the large C peak at 0.277 keV. In addition, the peaks appearing at 0.930 and 1.739 keV correspond to Cu and Si detected as materials from the physical support of the sample during the imaging procedure and therefore should be ignored. The inset of Figure 5.17b confirms that the P and S atoms are also added to the graphene, with the mapping images (Figure 5.17c-h) revealing that they are incorporated in a lesser extent than B and N. These results support the compositions obtained by XPS measurements.

Next, the surface area of the quaternary doped-graphene catalyst is examined by N_2 adsorption-desorption isotherms at 77 K (Figure 5.18a) and calculated according to the BET method [218], as described in Section 3.1.3.

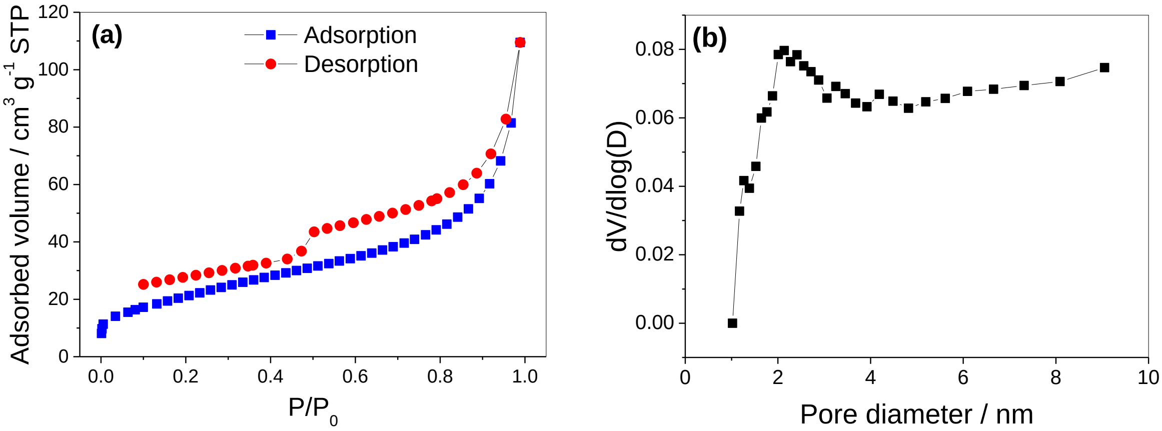

Figure 5.18. *(a) Nitrogen adsorption/desorption isotherms and (b) pore size distribution of the BNPS-Gr.*

A type-II isotherm is observed, with the intermediate flat region between the values of P/P_0 = 0.1 and 0.7 corresponding to a monolayer formation characteristic of microporous materials [220]. The calculated specific BET surface area is 78.6 ± 0.3 m^2 g^{-1}, which is higher or similar to other reported doped-graphene catalysts, such as single N-doped graphene [230] or ternary (N, P, B)-doped nanoporous carbons [318]. The pore size distribution is shown in Figure 5.18b. Using the BJH method [221], the average pore diameter is calculated to be 6.2 nm, whereas the corresponding pore volume is determined as 0.12 cm^3 g^{-1}. These results suggest that the BNPS-Gr has a mesoporous structure, with the pore size ranging between 2 and 50 nm characteristic of mesoporous materials [319].

XRF is a suitable technique which permits to obtain the concentration of elemental atoms in a sample, especially d-group transition metals [320]. Here, XRF is used to determine transition-metal traces in the BNPS-Gr catalyst, and the results are compared with those obtained for GO (Table 5.7), in order to establish if the metal impurities mainly come from the GO precursor or if they are incorporated during the doping procedure.

Table 5.7. *Transition-metal composition of BNPS-Gr and GO precursor, determined by XRF measurements. * <LOD: below limit of detection.*

Element	*Concentration in BNPS-Gr (ppm)*	*Concentration in GO (ppm)*
Mn	7340 ± 260	7010 ± 220
Fe	6740 ± 160	490 ± 70
Cr	1850 ± 140	170 ± 90
Zn	930 ± 30	200 ± 10
W	580 ± 60	270 ± 30
Cu	250 ± 50	30 ± 10
Ni	200 ± 40	<LOD*
Zr	130 ± 10	<LOD*
Cd	20 ± 10	20 ± 10
Mo	20 ± 10	20 ± 10

The results clearly demonstrate that most of the d-transition metals present in the quaternary-doped sample (except Mn, Cd and Mo) comes from impurities present in the doping agent precursors, in a different extent. For example, it is estimated that Cr is incorporated mainly from the phosphoric acid precursor used for the P-doping, while Fe is a common impurity present in all the precursors used. However, the main Mn impurity is already present in the GO precursor, due to that this is normally obtained via the Hummers' (or modified Hummers') method, which employs permanganate as oxidant [321].

The possible role of these metals on the catalytic behaviour observed has been largely discussed in the literature [89,322,323], with Pumera et al. concluding that only Mn can have a significant influence on the final catalytic activity detected in doped-graphene catalysts, mainly due to that the MnO_2 species have been shown to catalyse the ORR [323]. Nevertheless, in the present study all the prepared doped-graphenes have been synthesised using the same GO precursor, reporting very different catalytic activities. Therefore, it can be considered that the transition metal impurities present in the catalysts, including the most abundant Mn with 0.7%, have a limited influence on the final performance, as it can be seen in the current density comparison of the single-doped graphene catalysts with the dopant-free rGO (Figure 5.5a).

The catalytic behaviour of the BNPS-Gr is studied by first measuring the cyclic voltammetry at a stationary disk electrode in both N_2- and O_2-saturated 0.1 M KOH solution (Figure 5.19a), showing a clear reduction occurring at around -0.3 V in the O_2-saturated solution.

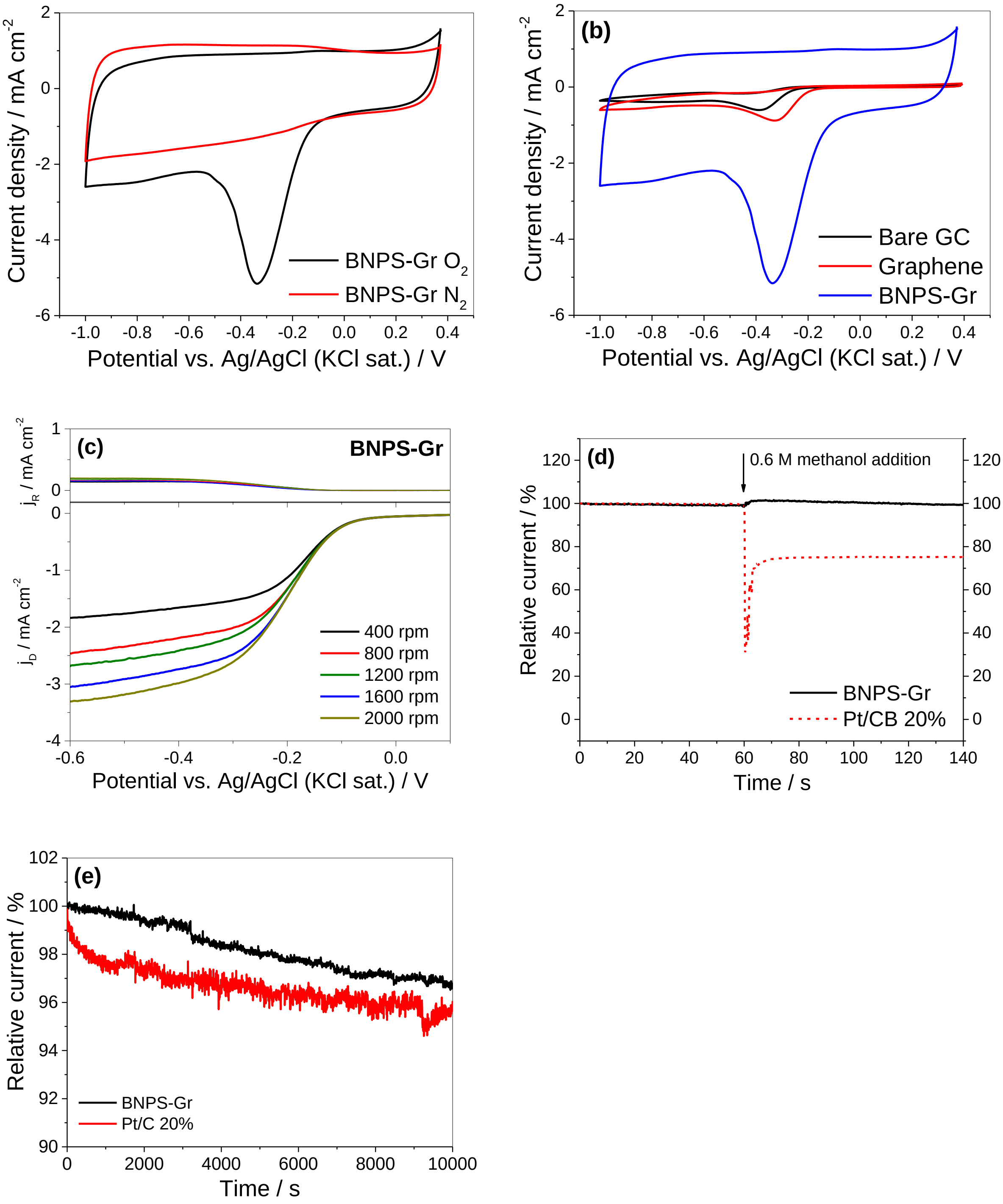

Figure 5.19. *(a) Cyclic voltammograms (CV) of BNPS-Gr catalyst in N_2 and O_2-saturated 0.1 M KOH solution, measured at 100 mV s^{-1}. (b) CVs of Bare GC, Graphene and BNPS-Gr. (c) RRDE measurements of the quaternary-doped graphene at different rotation rates, showing the ring current density (j_R) at the top and disk current density (j_D) at the bottom. Ring potential is fixed at +0.5 V. (d) Chronoamperometric responses at -0.5 V of BNPS-Gr and Pt/C 20% before and after the addition of 0.6 M methanol into the alkaline solution. (e) Durability test showing the chronoamperometric*

responses at -0.3 V of BNPS-Gr and Pt/C 20% in an O_2-saturated 0.1 M KOH solution at 1600 rpm.

Similar voltammograms are also obtained in O_2-saturated 0.1 M KOH solution at bare GC and graphene-modified (via drop-casting) GC electrodes in order to compare their performance with BNPS-Gr (Figure 5.19b). It can be seen that the current density of the quaternary-doped graphene is much higher than that of graphene, which, together with the earlier onset potential observed, indicates that the addition of dopants into the graphene structure enhances the catalytic behaviour observed.

The RRDE measurements for BNPS-Gr are displayed in Figure 5.19c for rotation speeds from 400 to 2000 rpm. As expected, the ORR current density at the disk increases with increasing the rotation rate, in the same way that the formed peroxide is oxidised at the ring. From RRDE measurements of all catalysts the number of electrons involved in the ORR, as well as the peroxide production rate can be calculated using Eq. *3.5* and Eq. *3.6*, respectively.

The quaternary-doped catalyst is also tested and compared with respect to a commercial 20% Pt/C catalyst concerning its tolerance to the presence of methanol, which can be an effect of the fuel crossover from the anode in methanol-fuelled fuel cells [324,325]. The chronoamperometric responses in an O_2-saturated 0.1 M KOH aqueous solution at fixed potential of -0.5 V and 1600 rpm electrode rotation speed are displayed in Figure 5.19d before and after the addition of a certain amount of methanol for a final composition of 0.6 M. It is observed an immediate decrease of 25% on the response in the case of Pt/C due to the poisoning effect of the CO intermediates on the Pt catalyst [326]. On the other hand, the BNPS-Gr is not affected by the presence of methanol. This points to the high selectivity of the quaternary-doped catalyst towards the ORR, which makes BNPS-Gr a promising catalyst for its application in methanol-fuelled fuel cells.

Another important feature in catalysis is the stability of a catalyst under continuous operation. A durability test is performed at a fixed potential of -0.3 V in O_2-saturated 0.1 M KOH solution for the quaternary-doped graphene catalyst and a commercial Pt/C 20% (Figure 5.19e). A decrease of around 3% is observed in the measured current density for the BNPS-Gr catalyst after 10,000 seconds of continuous operation, which is lower than that observed for the commercial Pt/C 20% under the same conditions. Similar results are reported by Titirici et al. for a nitrogen-doped carbonaceous material, which demonstrated higher durability and methanol tolerance than a commercial Pt/C catalyst [327]. Furthermore, this catalyst showed highly promising *in-situ* fuel cell performance when tested in the cathode of H_2/O_2 anion-exchange membrane fuel cells.

These results reflect the higher stability of the graphene-derived catalysts with respect to Pt-based catalysts under strongly alkaline conditions, which highlights the potential of the catalysts presented in this work for practical fuel cell applications.

5.6 Conclusions

Among the different types of doped-graphene analysed in the present study, only the dual doped catalysts have clearly demonstrated to improve the catalytic performance (in terms of both measured current density and number of electrons transferred) with respect to the dopant-free thermally reduced GO. The improved catalytic activity exhibited by the dual-doped graphene catalysts is unlikely to be mainly due to a higher electronic conductivity, since the Raman spectra shows a very similar 2D structure of dual-doped graphenes with respect to the rest of the catalysts (noting that conductivity through a graphene layer is linked to the amount of defects present in its structure).

Previously, it has been also proposed how the different bonding species can promote the catalytic activity in some specific catalysts. For example, it has been stated that the incorporation of the P precursor into the graphene structure as P-C and P-N binding species can promote the catalytic activity via a combined double mechanism. In addition, it has been observed that higher compositions in C-BO of the B containing catalysts seems to moderately improve the ORR performance. On the other hand, the composition in N bonding species has not shown a clear correlation with the activity of N-containing catalysts, while the S species composition is very similar in all the sulphur-doped catalysts.

According to some conclusions previously reported for dual-doped carbons, the simultaneous inclusion of different heteroatoms into the graphene structure can induce a synergistic effect with respect to their single-doped counterparts [167,328]. This is reportedly due to that the variability in the electronegativity of the different heteroatoms creates an asymmetry of the electronic charge density in the graphene lattice [318,329], thus increasing the adsorption of O_2 via the modulation of the π* bond of the O-O molecule [4]. Nevertheless, the experimental results of the present study seems to indicate that an excessive amount of heteroatoms acting simultaneously (especially ternary-doped catalysts) could interact negatively in terms of catalytic activity.

It has been also demonstrated that the quaternary-doped graphene (and presumably these results can be extended to the rest of doped-graphene catalysts) shows higher methanol tolerance and improved durability than a commercial Pt-based catalyst, which could have very important implications in the practical application of doped-graphenes as promising alternative catalytic materials for clean energy purposes, especially in methanol-fuelled fuel cells.

6 DOPED-GRAPHENE/METAL HYBRID ORR CATALYSTS

In this section, some doped-graphene catalysts evaluated in the previous chapter are combined with two types of metals: a transition-metal (Fe) and several perovskite oxides. The resulting hybrid catalysts are evaluated in terms of physical characterisation and electrochemical performance.

6.1 Doped-graphene/transition-metal hybrid catalyst

As a complement of the doped-graphene section, the incorporation of a transition metal into a doped-graphene catalyst is discussed here. A graphene catalyst simultaneously doped with iron and nitrogen (Fe-N-Gr) is characterised and evaluated, and its physical structure and catalytic performance is compared to that observed for N-Gr, in order to evaluate the influence of the transition metal.

The XPS survey spectra is displayed in Figure 6.1 and the composition of the Fe-N-Gr catalyst is shown and compared to N-Gr, rGO and the GO precursor in Table 6.1.

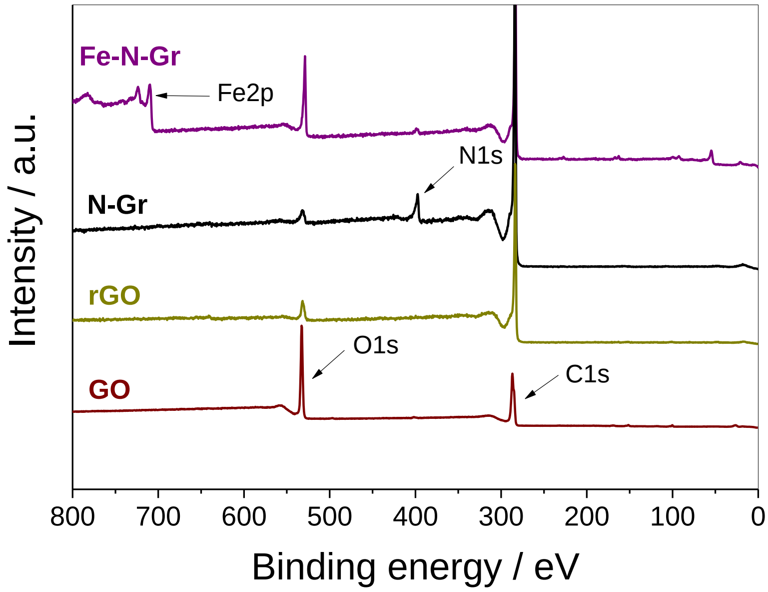

Figure 6.1. *Survey XPS spectra of the Fe-N-Gr and N-Gr catalysts plus GO and rGO, showing the peaks corresponding to the dopants.*

Table 6.1. *Fe-N-Gr and N-Gr catalyst compositions (calculated from XPS measurements) with their corresponding errors.*

Catalyst	C	O	N	Fe
GO	67.8 ± 0.2	32.2 ± 0.2		
rGO	94.8 ± 0.3	5.2 ± 0.3		
N-Gr	91.8 ± 0.5	2.6 ± 0.6	5.6 ± 0.5	
Fe-N-Gr	84.2 ± 0.7	11.9 ± 0.3	1.4 ± 0.6	2.5 ± 0.4

First, the peak reported at ~710 eV indicates that the transition metal is clearly incorporated into the catalyst. Nevertheless, the presence of Fe has dramatic consequences in the N and O content. In fact, the incorporation of N in Fe-N-Gr is four times lower than in N-Gr. Moreover, the presence of the Fe precursor decreases the efficient reduction of oxide groups reported in N-Gr, showing Fe-N-Gr an oxygen content almost 5 times higher than the metal-free single-doped catalyst.

The XRD spectrum of the Fe-N-Gr catalyst is shown in Figure 6.2a and compared with the equivalent metal-free N-Gr.

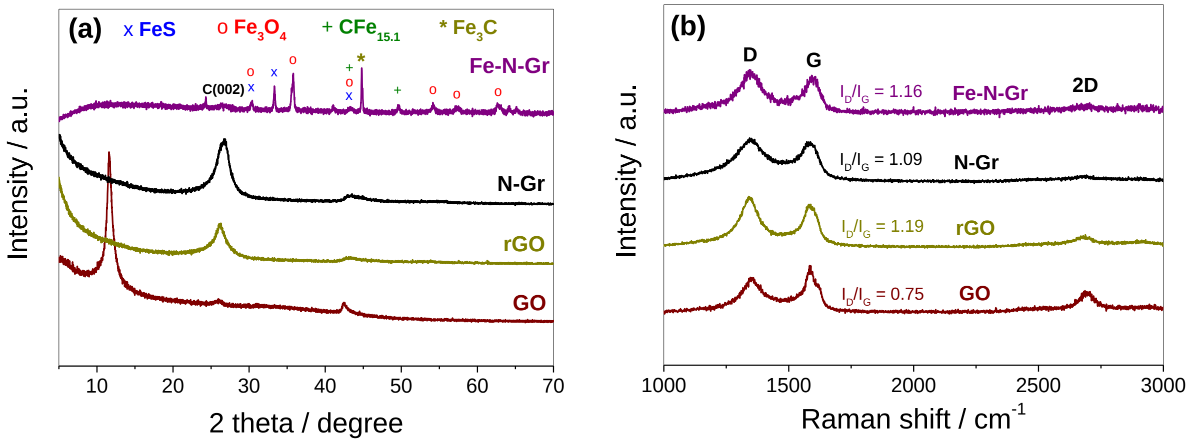

Figure 6.2. *(a) XRD patterns of GO, rGO, N-Gr and Fe-N-Gr. (b) Raman spectra of the prepared catalysts using an excitation laser wavelength of 532 nm. The calculated* I_D/I_G *values are also presented.*

Table 6.2. *Distribution of the XRD diffraction peaks observed for the different Fe species incorporated to the Fe-N-Gr catalyst [184,188].*

2θ peak	30.4°	33.4°	35.4°	43.3°	44.9°	49.7°	54.2°	57.4°	62.7°
FeS	(100)	(101)		(102)					
Fe_3O_4	(220)		(311)	(400)			(422)	(511)	(440)
$CFe_{15.1}$				(111)		(200)			
Fe_3C					x				

First, it is noted that the peak at 2θ = 26.3° present in N-Gr, which is attributed to (002) diffraction in the carbon phase [188], has almost disappeared in Fe-N-Gr, presumably due to the effects of the metal transition on the graphene structure. It can be also observed several peaks which are absent for N-Gr and, therefore, can be assigned to Fe. The characteristic diffraction patterns of these peaks are detailed in Table 6.2, where it is observed the coexistence of FeS (the source of sulphur is the traces of this element present in the $FeCl_3$ used as the iron precursor, with a concentration of 50 ppm of SO_4^{2-}), Fe_3O_4, Fe_3C and austenite ($CFe_{15.1}$) species in the prepared catalyst. The composition on these Fe species is believed to be influenced by the annealing temperature, and seems to play a role in the catalytic activity observed of Fe and N doped-graphene [184].

Regarding the influence of the Fe addition into the N-Gr on the graphene structure, the Raman spectra (Figure 6.2b) does not show pronounced changes in Fe-N-Gr with respect its metal-free counterpart. There is, however, a small increase in the I_D/I_G ratio after the addition of Fe (see Table 6.3), indicating that the presence of the metal produces a slightly more disordered structure. Nevertheless, the I_D/I_G ratio of Fe-N-Gr is still lower than that of rGO, indicating the previously mentioned capacity of N atoms for the sp^2 restoration, even in the presence of a transition metal. According to the literature, this conclusion can be extended to carbon black when it is used instead graphene [330].

Table 6.3. *I_D/I_G ratios and mean crystallite size (L_a) of the dual-doped graphenes obtained from the Raman spectra.*

	GO	rGO	N-Gr	Fe-N-Gr
I_D/I_G	0.75	1.19	1.09	1.16
L_a (Å)	**66.1**	**41.6**	**45.5**	**42.7**

In order to further investigate the incorporation of N and Fe into the graphene structure, the XPS deconvoluted spectra are shown in Figure 6.3.

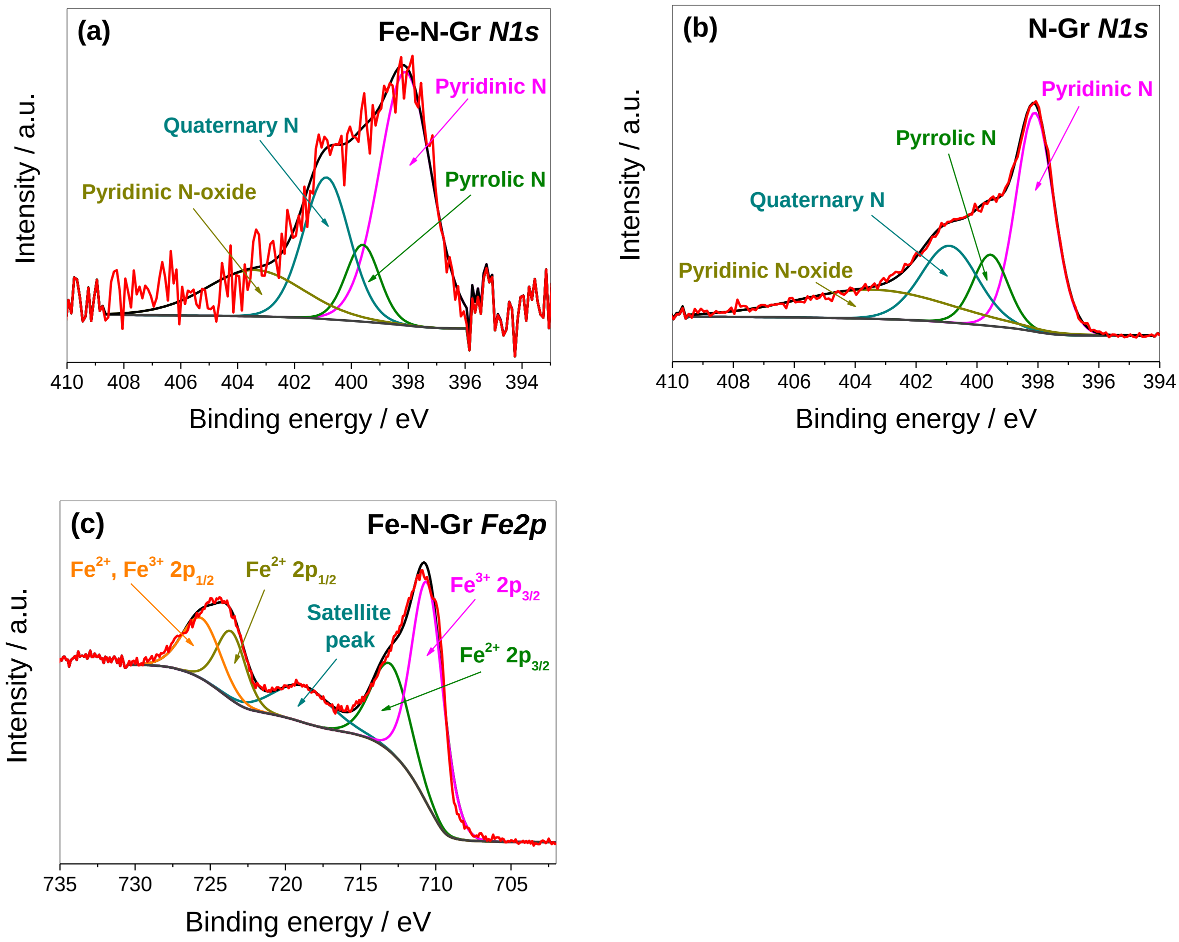

Figure 6.3. *Deconvolution XPS spectra of N1s peaks in the (a) Fe-N-Gr and (b) N-Gr catalysts (inset: description of N-bonding species [156]), and (c) Fe2p peak in the Fe-N-Gr catalyst.*

The N1s analysis shows that the presence of Fe seems to favour the promotion of quaternary N (graphitic) with respect to pyrrolic N, when Fe-N-Gr is compared with N-Gr (Figure 6.3a and b). In addition, the proportion of N-oxide species is decreased from 24.0% in N-Gr to 16.7% in Fe-N-Gr (see Appendix 4). Nevertheless, in both cases pyridinic N is the main contributor. Regarding the Fe2p peak (Figure 6.3c), it can be visualised two different peaks at around 711 eV corresponding to Fe2p$_{3/2}$ and 724 eV corresponding to Fe2p$_{1/2}$ [187]. At the same time, the Fe2p$_{3/2}$ can be split into two moieties appearing at binding energies of 710.7 and 713.6 eV, assigned to $2p_{3/2}$ of Fe^{3+} ion and $2p_{3/2}$ of Fe^{2+}, respectively. Likewise, the $Fe2p_{1/2}$ is formed by the $2p_{1/2}$ of Fe^{2+} ion, and $2p_{1/2}$ of Fe^{3+} and Fe^{2+} ions, corresponding to 723.6 and 725.5 eV, respectively. The peak at 718.8 eV is a satellite peak, indicating the coexistence of the four Fe2p species mentioned above [184].

The electrochemical behaviour of the Fe-N-Gr is compared with its metal-free counterpart in Figure 6.4a.

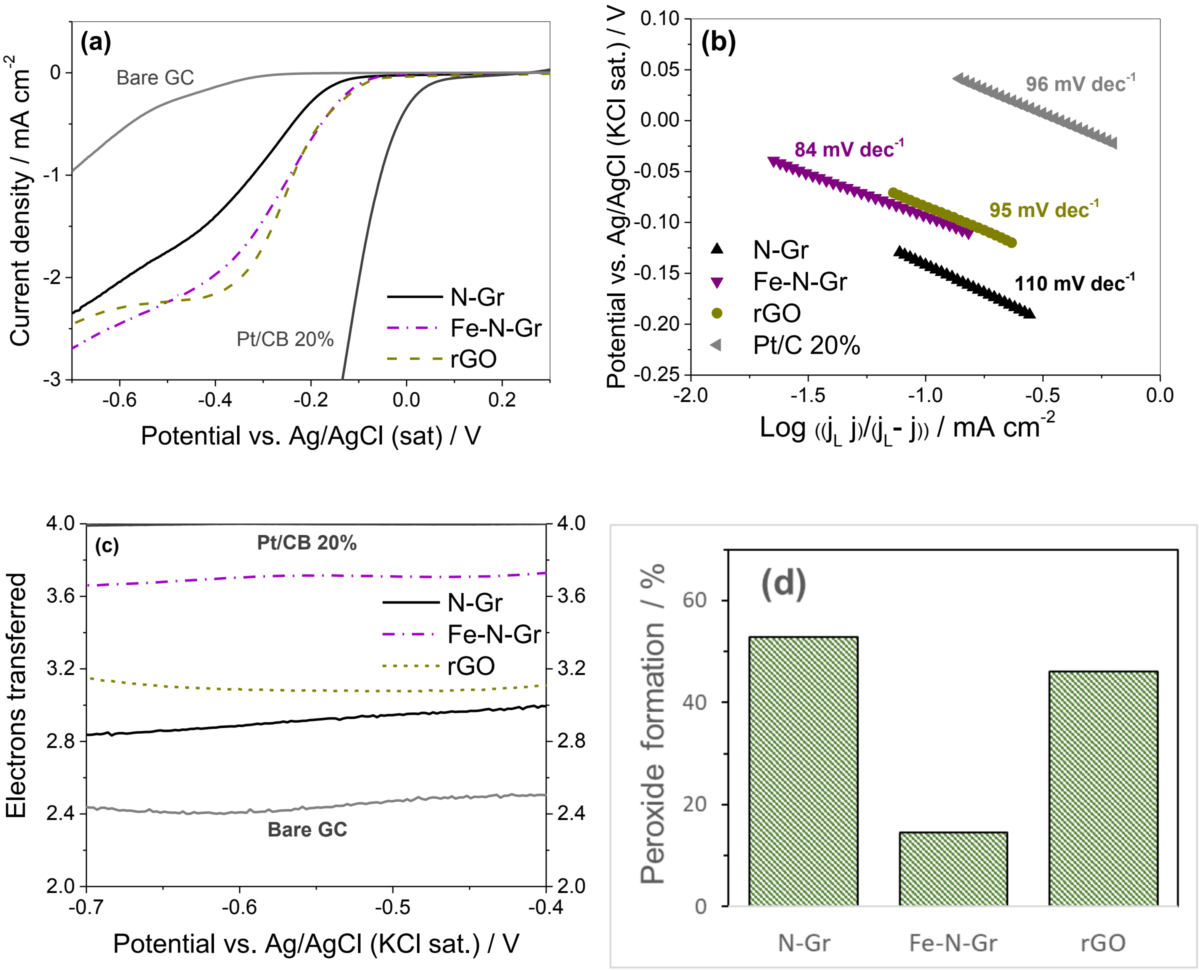

Figure 6.4. *(a) LSV measurements of the Fe-N-Gr and the N-Gr catalysts, including rGO, in* O_2*-saturated 0.1 M KOH solution, measured at 10 mV* s^{-1} *and 1600 rpm. A commercial Pt/C 20% and Bare GC electrode are also shown for comparison. (b) Tafel plots corresponding to the data shown in (a). (c) Number of electrons transferred during the ORR vs. the applied potential calculated from RRDE measurements at 1600 rpm using Eq. 3.5. (d) Peroxide formed during the ORR at -0.5 V obtained from the values shown in (a) using Eq. 3.6.*

First, it is reported an improved onset potential in the case of Fe-N-Gr with respect to N-Gr, being this value very similar to that observed in rGO. The measured current densities of Fe-N-Gr are higher (in absolute terms) than N-Gr in the whole range of applied potentials, and they even surpass those obtained for rGO beyond -0.5 V, in such a way that the current densities measured at -0.6 V are -2.04 mA cm^{-2} for N-Gr, -2.29 mA cm^{-2} for rGO and -2.45 mA cm^{-2} for Fe-N-Gr.

The calculated Tafel slopes are displayed in Figure 6.4b, and reveal that Fe-N-Gr has a value of 84 mV dec^{-1}, closer to 60 mV dec^{-1} (corresponding to Reaction 2.24 as the rds) than the Tafel slope calculated for N-Gr (110 mV dec^{-1}, closer to 120 mV dec^{-1} which corresponds to the electron-transfer Reaction *2.23* as the rds). The higher efficiency in the electron transfer shown by the Fe-N-Gr catalyst with respect to N-Gr is probably due to the presence of Fe in the first, which facilitates the electronic conductivity with respect to the metal-free catalyst. This is in good agreement with the enhanced catalytic activity shown by Fe-N-Gr in Figure 6.4a.

Regarding the number of electrons transferred during the electrochemical reaction under the different catalysts, the values of n versus the applied potential are shown in Figure 6.4c. It is noted a constant value of n in the interval of applied potentials between -0.4 V y -0.7 V for the Fe-N-Gr catalyst. However, the most important feature is the impressive increase of n when the transition metal is added to N-Gr, obtaining a value of 3.71 electrons transferred for Fe-N-Gr whereas this value is 2.95 for N-Gr. This also implies a drastic reduction in the peroxide production rate, from 52.8% for N-Gr to only 14.5% for Fe-N-Gr (Figure 6.4d).

In the light of the results reported above, it is concluded that the addition of a transition-metal into a single-doped graphene (in this case Fe added to N-Gr) can improve the catalytic activity as well as increase the reaction kinetics. Moreover, the addition of Fe promotes the transition from a mixed route between the direct and the 2-step mechanism observed in N-Gr, to a *quasi* direct 1-step mechanism reported in Fe-N-Gr, with a very low rate of peroxide intermediate production.

Although it has been argued that the main goal of the transition metal is to facilitate the incorporation of N into the carbon structure [4], this is not our case, since the N composition of Fe-N-Gr is considerably lower than the N content of N-Gr. In addition, there are no significant differences in the N1s peak deconvolution of Fe-N-Gr and its metal-free equivalent that can explain on their own the different activities observed. Nonetheless, the literature suggests that the specific Fe species could be involved in the catalytic behaviour. As an example, Liao et al found that the FeS and austenite $CFe_{15.1}$ groups (but not Fe_3O_4) are linked to a higher catalytic activity [184]. As it was observed in the XRD analysis (Figure 6.2a), all these active groups are present in the Fe-N-Gr catalyst, which can explain its improved catalytic performance.

6.2 Dual-doped graphene/perovskite composites as ORR catalysts

In Chapter 5 the ORR catalysis of metal-free doped graphene catalysts was thoroughly studied. It was concluded that dual-doped graphene catalysts show improved catalytic activity, favouring the one-step mechanism and reducing the formation of peroxide intermediates with respect to single, ternary and quaternary-doped graphenes.

In this chapter, the combination of high-performance dual-doped graphenes and perovskite oxide catalysts is studied. The structure and design of perovskite oxides have been reviewed in Section 2.4.2. Here, the graphene-derived catalyst is dually doped with a combination of a fixed N dopant, plus one of either B, P or S (Figure 6.5a).

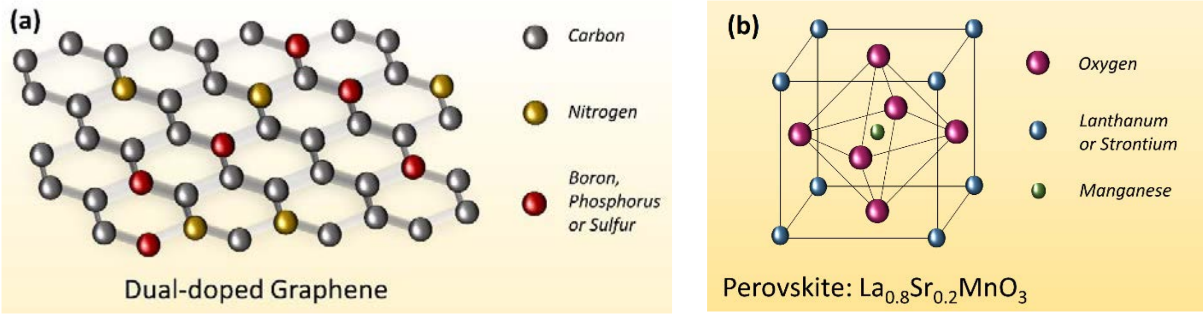

Figure 6.5. *Schematic diagram of (a) dual-doped graphene catalyst, and (b) LSM perovskite.*

In the used perovskite, the A-site cation is a combination of lanthanum and strontium in the proportion 0.8:0.2, while the B-cation is chosen to be manganese due to its reported high activity [331]. The resultant $La_{0.8}Sr_{0.2}MnO_3$ (Figure 6.5b), called thereinafter LSM for abbreviation, has been demonstrated to be catalytically active towards the ORR in previous studies [201,210].

6.2.1 Comparison of dual-doped graphene/perovskite with non-doped graphene/perovskite hybrid catalysts

First, the effect of the addition of dual-doped sulphur-nitrogen graphene (SN-Gr) to the LSM perovskite is analysed in terms of measured current densities, number of electrons transferred during the ORR and Tafel kinetics, and the results are compared with an equivalent experiment in which pure graphene is used as the carbon material instead of SN-Gr.

In Figure 6.6a it is observed that the perovskite and the pure graphene exhibit very low catalytic activity in terms of measured current density, and when both are combined this low activity remains.

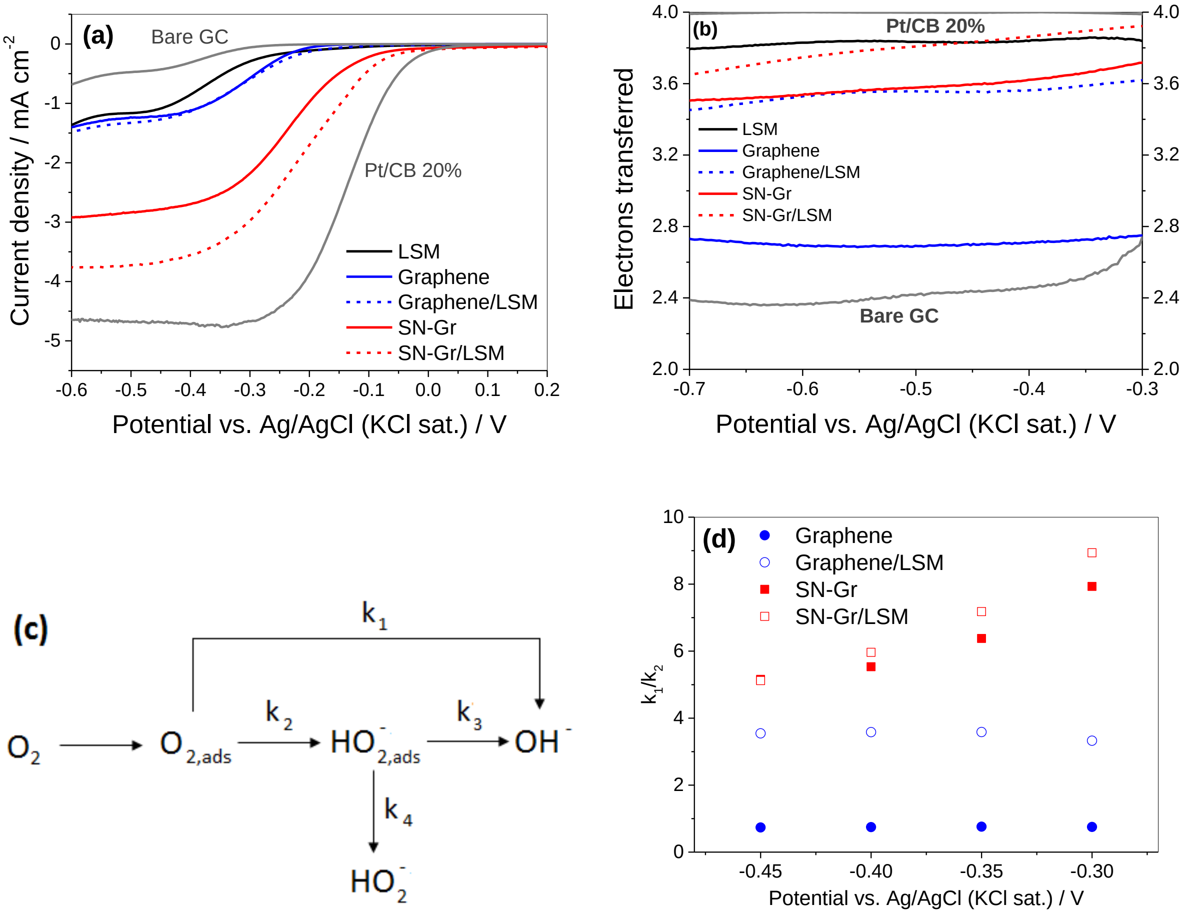

Figure 6.6. *(a) LSV of graphene and SN-Gr with and without perovskite in* O_2*-saturated 0.1 M KOH (measured at 10 mV* s^{-1} *scan rate and 1600 rpm, (doped)-graphene/LSM composites ratio 0.8:0.2, catalyst loading: 0.3 mg* cm^{-2}*). (b) Number of electrons transferred vs. potential obtained from RRDE measurements (ring potential fixed at +0.5 V). (c) ORR model suggested by Damjanovic [332]. (d)* k_1/k_2 *ratios vs. potential (vs. sat. Ag/AgCl).*

However, the dual-doped SN-Gr catalyst shows a considerably higher current density with respect to pure graphene, as it was described in Section 5.3. In this case, when the dual-doped catalyst is mixed with the perovskite, there is a noticeable increase in the measured current density, from -2.92 mA cm^{-2} to -3.77 mA cm^{-2} (measured at -0.6 V).

Regarding the number of electrons transferred during the electrochemical reaction (Figure 6.6b), the addition of LSM to pure graphene increases the observed value of *n* from 2.69 to 3.56 (at -0.5 V), although this increase is not reflected in terms of measured current density. In the case of the dual-doped graphene, the mixed SN-Gr/LSM shows a moderate increase in the value of n compared to SN-Gr (from 3.58 to 3.81). This increase in the number of the electrons involved in the ORR when the perovskite is added to the graphene materials may indicate a higher selectivity of LSM towards the direct OH^- formation from O_2 via the 4e mechanism, which is reflected in the high value of n reported for the single perovskite (3.83).

Next, the RRDE data are analysed using the method proposed by Hsueh and Chin [332] to determine the kinetics of reaction. As stated previously, the ORR can proceed in alkaline media via two different suggested mechanisms: either direct reduction of O_2 to OH^- by a 4-electron mechanism (k_1), or a 2-step process in which the O_2 is partially reduced to peroxide in a 2-electron mechanism (k_2) followed by either further reduction to OH^- (k_3) or decomposition of peroxide (k_4) [4], following the model proposed by Damjanovic (Figure 6.6c) [33]. The values of k_1 and k_2 can be calculated from the disk (I_D) and ring (I_R) measured currents, using Eq. *6.1* and Eq. *6.2* [332]:

$$k_1 = S\,Z\,\frac{I\,N-1}{I\,N+1} \qquad (6.1)$$

$$k_2 = S\,Z\,\frac{2}{I\,N+1} \qquad (6.2)$$

where:

S = slope of the plot of $I_{DL}/(I_{DL}-I_D)$ vs. $\omega^{-1/2}$

$$Z = 0.62\, \mathrm{D}_1^{\frac{2}{3}}\, \nu^{-\frac{1}{6}} \tag{6.3}$$

I = intercept of the plot of I_D/I_R vs. $\omega^{-1/2}$

N = RRDE collection efficiency (0.37, provided by the manufacturer)

I_{DL} = disc limiting current density (A cm^{-2})

ω = RRDE rotation speed (s^{-1})

D_1 = diffusivity of oxygen (1.93×10^{-5} cm^2 s^{-1} [333])

ν = kinematic viscosity (0.01009 cm^2 s^{-1} [35])

The k_1/k_2 ratios calculated using this method are plotted versus the applied potential in Figure 6.6d. It is seen that pure graphene has values of k_1/k_2 lower than 1, indicating that the 2-step mechanism is favoured over the 4e direct pathway due to its already mentioned low catalytic activity. Nevertheless, when the perovskite is added to pure graphene, the k_1/k_2 ratio increases to around 3.5, indicating that the addition of LSM significantly promotes the one-step mechanism over the stepwise 2e pathway. When dual-doped graphene is used instead of pure graphene, the addition of perovskite implies only a slight improvement in the k_1/k_2 ratio, since the single SN-Gr catalyst already shows a great preference towards the 4-e ORR mechanism. These observations are in good agreement with the results obtained for the number of electrons transferred during the electrochemical reaction (Figure 6.6b).

One reason behind the improvement in the catalytic activity of perovskite/graphene composites has been postulated to be an increase in the conductivity of the perovskite due to the addition of carbon materials [194]. Since the conductivity of graphene is closely linked to the presence of defects in its two-dimensional structure [334], XRD and Raman spectroscopy are used to investigate the conductivity in pure graphene and dual-doped graphene, and the results are displayed in Figure 6.7.

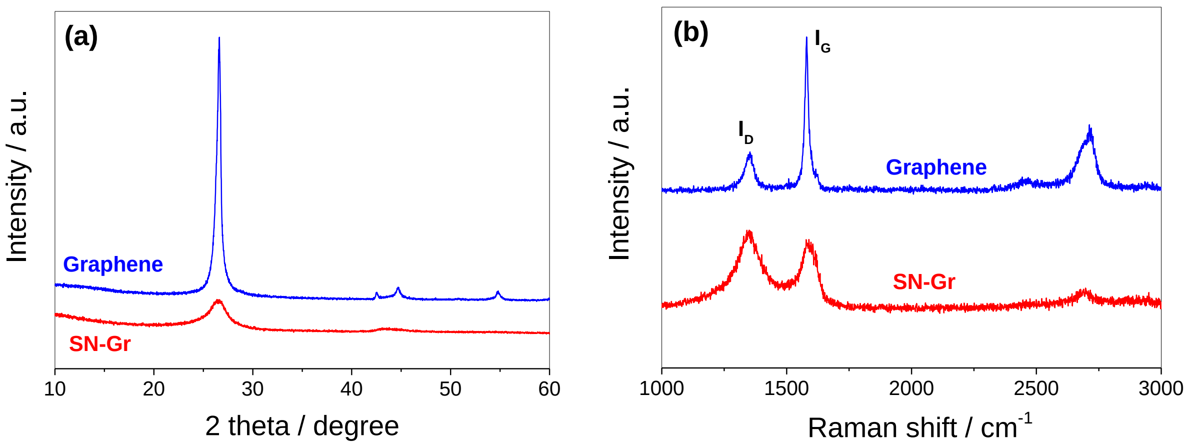

Figure 6.7. *(a) XRD patterns and (b) Raman spectra of pure graphene and SN-Gr.*

Both pure graphene and SN-Gr show a diffraction peak at 26.5° (Figure 6.7a) corresponding to a basal inter-layer spacing of 0.34 nm typical of graphene materials [230]. However, this peak is clearly more intense and sharp in pure graphene due to the absence of dopants in its structure. The defects created during the thermal annealing applied to doped-graphene catalysts are believed to influence its conductivity [335], and modify the relative intensity of the I_D (linked to defects) and I_G (related to the degree of graphitisation) peaks in the Raman spectra (Figure 6.7b) observed at 1340 and 1580 cm^{-1}, respectively [112]. The measured values of the I_D/I_G

ratio are 0.25 for graphene and 1.13 for SN-Gr, indicating fewer defects and thus higher conductivity for the graphene sample. AC impedance measurements of the high frequency resistances supports this (39.7 ± 0.1 Ω for graphene and 44.3 ± 0.2 Ω for SN-Gr). The conclusion is thus that the positive catalytic effect observed in the SN-Gr/LSM catalyst (not shown by Graphene/LSM) is not related to an increase in the conductivity of the material, but probably to the interaction between the graphene dopants and the perovskite structure [336].

Regarding the role of the perovskite composition on the observed catalytic performance, it has been stated that the transition-metal used as B-cation has a great influence in the catalytic behaviour of perovskites [195,202]. Among the different transition-metal oxide candidates, such as Co_3O_4, NiO, Fe_3O_4 or MnO_2, Pumera et al. demonstrated that the latter exhibits a significant more positive onset potential in ORR voltammograms on modified glassy carbon electrodes [323]. Since the perovskite used in the experiments carried out in this section is Mn based, an experiment comparing the ORR activities of MnO_2, SN-Gr and SN-Gr/MnO_2 is carried out to see if the catalytic performance observed in the SN-Gr/perovskite composite could be mainly attributed to the presence of Mn in the perovskite composition.

Therefore, LSV is performed to record the ORR performances of MnO_2, SN-Gr and the combination of both. The results are shown in Figure 6.8a, and reflect that, unlike the results displayed in Figure 6.6a for SN-Gr/LSM, the addition of MnO_2 to SN-Gr does not improve the current density nor the observed overpotential with respect to the dual-doped graphene alone.

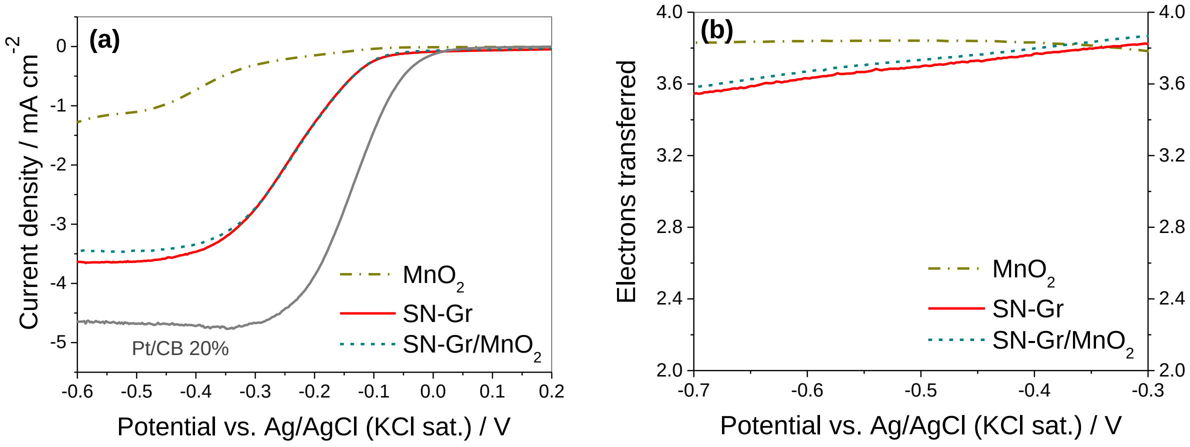

Figure 6.8. *(a) LSV of MnO_2, SN-Gr and combined SN-Gr/ MnO_2 in O_2-saturated 0.1 M KOH (measured at 10 mV s^{-1} scan rate and 1600 rpm, SN-Gr/MnO_2 composites ratio 0.8:0.2, catalyst loading: 0.4 mg cm^{-2}). (b) Number of electrons transferred vs. potential obtained from RRDE measurements (ring potential fixed at +0.5 V).*

The same result is observed in terms of electrons transferred during the ORR: Fig. Figure 6.8b shows no differences between SN-Gr and SN-Gr/MnO_2, whereas that the addition of perovskite to SN-Gr significantly increases the value of n displayed in Figure 6.6b. Nevertheless, it is noteworthy the fact of that LSM and MnO_2 (without SN-Gr) show approximately the same catalytic behaviour, i.e. both exhibit poor current densities but the values of n are very close to 4, reflecting a *quasi* 4e ORR mechanism. This indicates an excellent ability to reduce the intermediate peroxide formed, but the catalytic activity is limited by the poor electronic conductivity typical of the perovskite oxides [191].

These observations suggest that, although Mn appears to determine the electrochemical behaviour exhibited by the single LSM, the catalytic activity of the perovskite/doped-graphene bifunctional catalyst does not originate from the Mn activity only. For example, Schmidt et al. have reported that the formation of the carbon/perovskite interface could modify the electronic structure of the perovskite via altering the oxidation state of the transition metal, thus enhancing the electrochemical properties [194]. In addition, Hardin et al. suggest that the activity of functionalised carbons towards the peroxide disproportionation could also play a role in the improved catalytic activity observed in doped-carbon/perovskite composites [337]. These and other possible theories are explored more deeply in the following sections.

6.2.2 Optimisation of composition

In the previous section, it has been demonstrated that the combination of dual-doped graphene and perovskite enhances the catalytic activity towards the ORR with respect to the individual components. For a better understanding of the role played by the dual-doped graphene on the overall performance, the influence of the relative perovskite/doped-graphene composition on the electrochemical activity is analysed in terms of measured current densities, electrons involved in the reaction and Tafel kinetics. A similar experiment reported in the literature, carried out with a different perovskite ($Ba_{0.5}Sr_{0.5}Co_{0.8}Fe_{0.2}O_{3-\delta}$) and Acetylene Black® carbon instead of doped-graphene, concluded that the relative perovskite/carbon composition significantly affects the resultant catalytic performance, and found that 0.45:0.55 carbon/perovskite ratio gave the optimal composition with 28% peroxide production [197].

The influence of the doped-graphene/perovskite composition on the catalytic performance is studied by varying the ratio from pure perovskite to pure doped-graphene in 20% increments, and the resulting LSV plots are shown in Figure 6.9a.

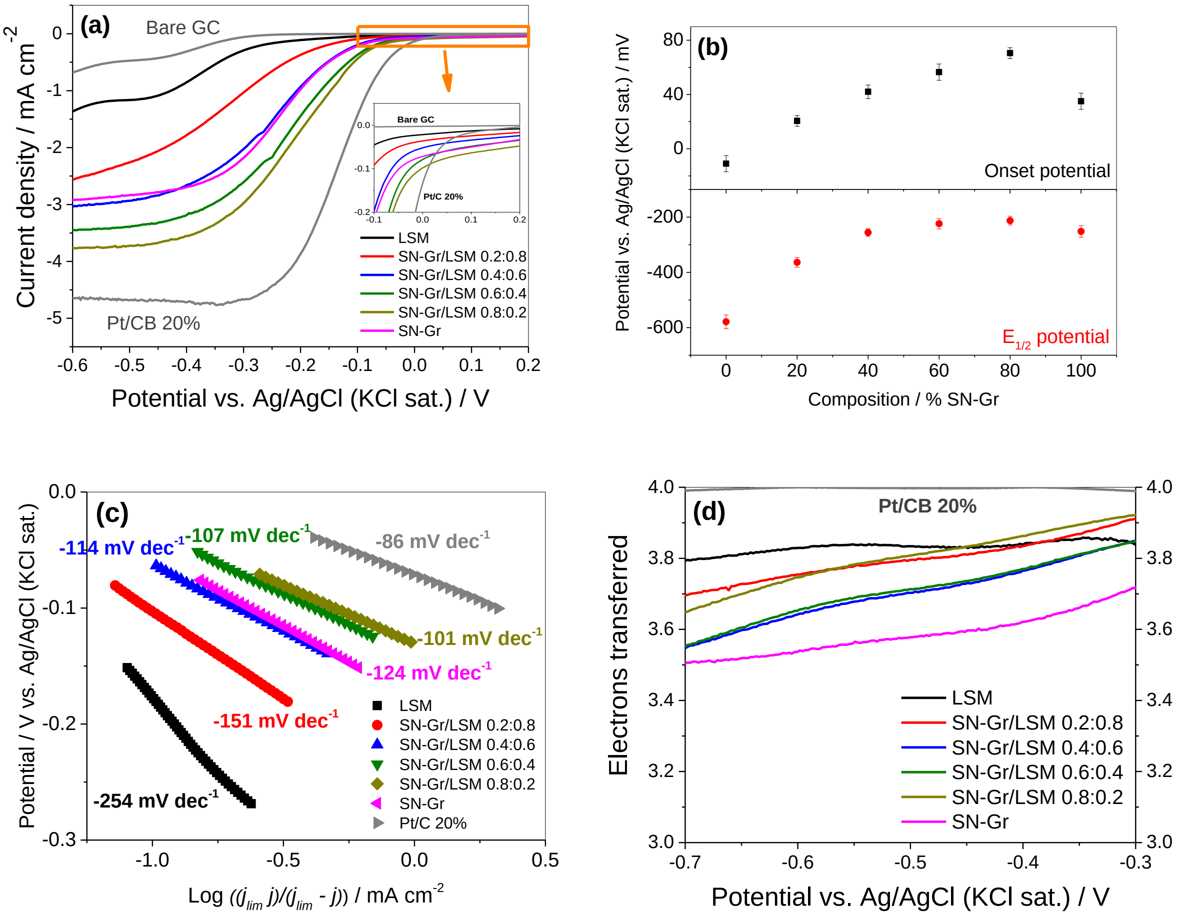

Figure 6.9. *(a) LSV of SN-Gr/perovskite at different compositions in O_2-saturated 0.1 M KOH (inset: onset potentials). (b) Onset and half-current potentials vs. composition. (c) Tafel plots showing the calculated Tafel slopes. (d) Number of transferred electrons calculated from RRDE measurements.*

It is found that the limited current density increases as the SN-Gr content rises (Figure 6.9a) from pure perovskite (-1.37 mA cm^{-2} at -0.6 V) to 80% SN-Gr content (-3.78 mA cm^{-2}), then decreasing as the SN-Gr composition is increased to 100% (-2.91 mA cm^{-2}). This trend is in agreement with the onset and half-wave potentials displayed in Figure 6.9b, with the most positive onset being +70.5 mV and the least negative half-wave potential being -213 mV, both at 80% SN-Gr content.

The calculated Tafel plots (Figure 6.9c) confirm the same trend, showing the SN-Gr/LSM 0.8:0.2 ratio the lowest value of Tafel slope with -101 mV dec^{-1} (for comparison the same value obtained for a commercial Pt/C 20% catalyst is -86 mV dec^{-1}). It is observed that the Tafel slopes of all SN-Gr/LSM compositions show a value around 120 mV dec^{-1}, corresponding to the electron-transfer Reaction *2.23* as the rds. Nevertheless, the Tafel slope obtained for pure perovskite is as low as -254 mV dec^{-1}, which confirms the poor electrical conductivity of the perovskite.

However, the correlation of the number of electrons transferred during the ORR with the perovskite/doped-graphene composition is less evident. The values of n calculated from RRDE measurements are provided in Figure 6.9d and show that the pure perovskite reaches a maximum value of 3.83 (at -0.5 V), whereas the lowest value of 3.58 corresponds to pure dual-doped graphene. For mixed SN-Gr/LSM composites n does not vary systematically between these two values, with n equals around to 3.8 for 20 and 80% dual-doped graphene composition and 3.7 for 40 and 60%. This points to the ORR occurring in the pure perovskite by a *quasi* 4e mechanism, although this selectivity towards the direct O_2 reduction into OH^- is not reflected in improved current densities, probably due to the previously mentioned poor conductivity of perovskites. The addition of SN-Gr improves the catalytic activity in terms of measured current densities especially at higher dual-doped graphene contents, in spite of being less selective towards the direct 4e mechanism than the pure perovskite. In fact, from the values of n displayed in Figure 6.9d it is calculated that the peroxide formation in pure SN-Gr is 21.1%, whereas it is only 8.3% for pure perovskite.

The principal conclusion is that the electrochemical performance mainly comes from the intrinsic catalytic activity of the doped-graphene, with the perovskite playing a role of further reducing agent of the peroxide produced by the SN-Gr catalyst. It has been proposed that the carbon facilitates the reduction of O_2 into HO_2^- in a 2e pathway, while the perovskite assists the reduction of HO_2^- into OH^- to give an overall (2e + 2e) mechanism [210]. Although this explanation has been dismissed in composites using Acetylene black® instead of doped-graphene, suggesting to those authors that the electronic interactions between the two components play a more important role in the catalytic behaviour observed [197], it is a plausible explanation for the SN-Gr/LSM catalyst.

The synergistic effect observed can also be ascribed to an interphase “ligand effect”, in which there is a covalent electronic transfer from the graphene-derived material to the transition-metal of the perovskite, thus favouring the splitting of the O-O bonding in the positive sites created. This effect has been previously reported in other carbon/metal oxide composites, such as Mn_3O_4-decorated Co_3O_4/graphene oxide [338], Mn oxide/carbon nanotube hybrid [339], Co_3O_4/N-doped mesoporous carbon/multi-walled nanotube system [340] or $CoSe_2$ nanobelt/N-doped graphene composite [341], where X-ray absorption near edge structure (XANES) spectroscopy shows the electronic interaction between the carbon and the metal oxide.

Another possible explanation for the enhanced electrochemical activity observed in dual-doped graphene/perovskite systems with respect to dual-doped graphene alone is the “spillover effect”. This phenomenon has been observed in platinum/metal oxide hybrids [342,343], where the OH^- generated by the ORR on the Pt surface spills over the adjacent metal oxide particles, due to the higher affinity of the latter towards the OH^- adsorption [344]. This would enhance the overall ORR activity of the system by the release of catalytically active sites on the Pt surface. Shao et al. demonstrated that this effect could also take place when perovskites are used instead of metal oxides [345]. Since in the previous chapter it has been shown that the ORR activity of the dual-doped graphenes is comparable to a Pt catalyst, it is presumable that the spillover effect could also contribute to the excellent catalytic performance developed by the doped-graphene/perovskite hybrid systems. In addition, considering that perovskites also possess catalytic activity towards the oxygen evolution reaction (OER) [196], the O_2 generated on the perovskite would spill over the graphene surface, thus releasing more active sites in the perovskite and increasing the synergistic effect of the doped-graphene/perovskite composite [194].

6.2.3 Comparison of different dual-doped graphenes combined with perovskite oxides

As it has been discussed before, the electronic interaction between the doped-graphene and the perovskite has been proposed to play a crucial role in the catalytic behaviour observed in these hybrid catalysts. In addition, it has been stated in Section 6.2.1 that the dual-doped graphene could modify the oxidation state of the B-cation in the perovskite, which is believed to be positive in enhancing the ORR activity [194]. Considering these two arguments, varying the heteroatoms used as graphene dopants can provide insight into the mechanisms that make possible the improved catalytic activity observed in doped-graphene/perovskite composites. Moreover, the SN-Gr catalyst that has been tested in the present chapter in combination with the LSM perovskite was found not to be the best dual-doped graphene in terms of current densities, showing PN-Gr the best catalytic performance (see Figure 5.9a). Therefore, the combination of the perovskite with dual-doped graphenes other than SN-Gr could improve the catalytic activity developed by the SN-Gr/LSM composite even further.

In addition to the already tested SN-Gr/LSM hybrid catalyst, graphene doped with boron-nitrogen (BN-Gr) and phosphorus-nitrogen (PN-Gr) are tested in combination with the LSM perovskite under the same conditions. Their compositions are determined via XPS and are shown in the inset of Figure 6.10.

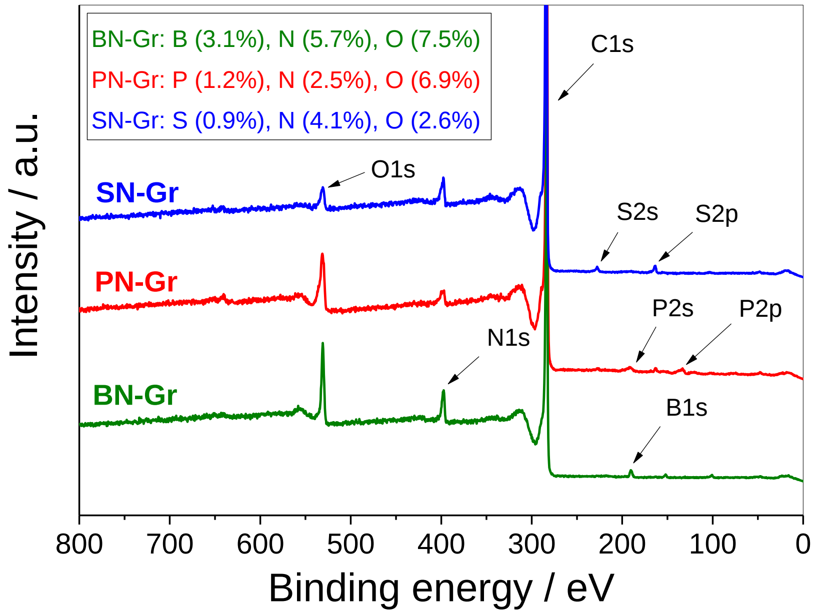

Figure 6.10. *Survey XPS spectra of the dual-doped graphene catalysts, showing (inset) the calculated compositions.*

The compositions were discussed in detail in Section 5.3, here it is just mentioned that the XPS analysis confirms the incorporation of all dopants into the different catalysts, showing different N and O compositions that could affect the catalytic activity of the different catalysts.

Figure 6.11a exhibits the measured current densities of BN-Gr, PN-Gr and SN-Gr, together with their corresponding counterparts in combination with perovskite (0.8:0.2 doped-graphene/perovskite ratio).

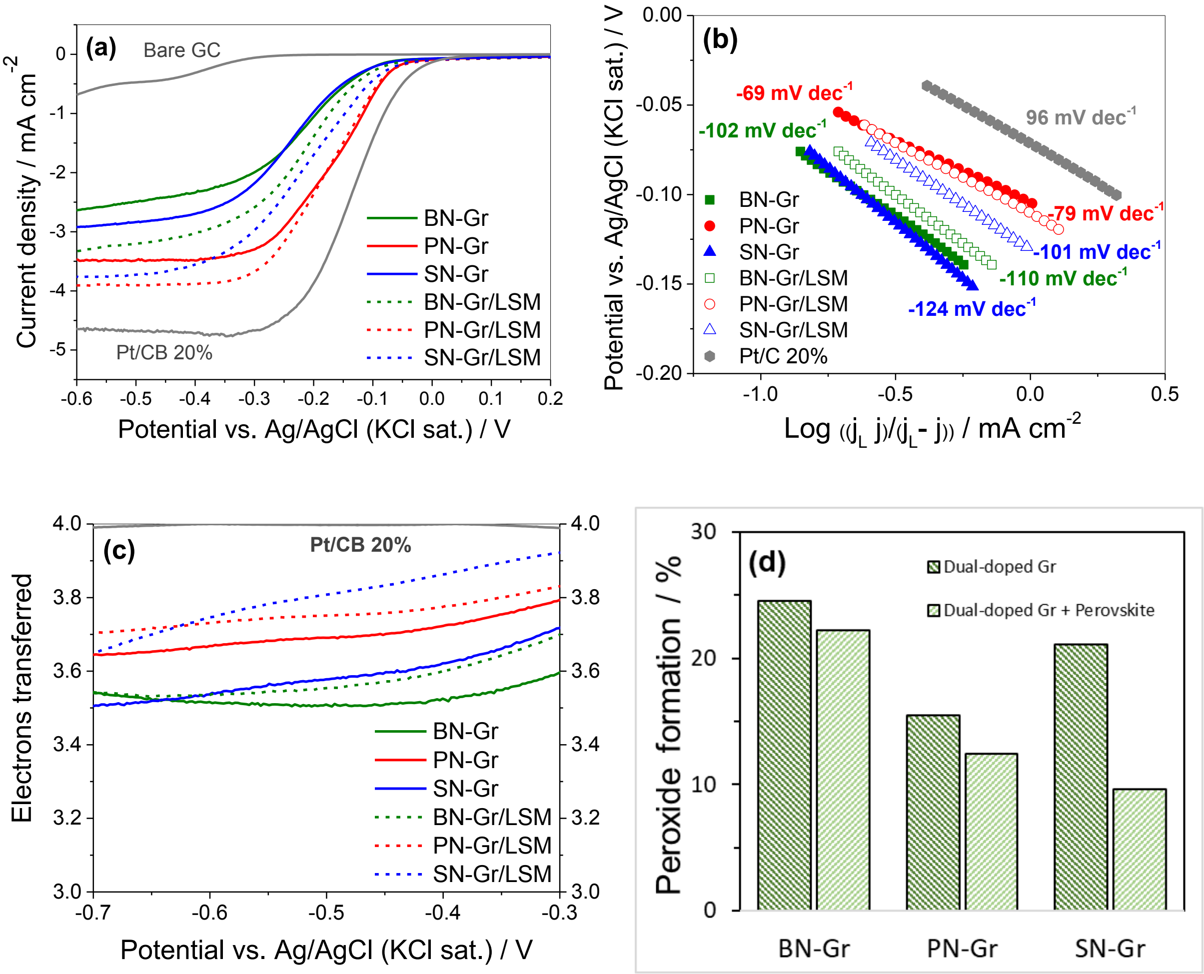

Figure 6.11. *(a) LSV of the dual-doped graphenes with and without 20% perovskite addition at different compositions in O_2-saturated 0.1 M KOH. (b) Tafel plots showing the calculated Tafel slopes. (c) Number of electrons transferred vs. potential. (d) Mole fraction (in %) of produced peroxide obtained from RRDE measurements.*

It can be seen that all the doped-graphenes boost their limiting current densities when the perovskite is added, being this increase of 0.69, 0.43 and 0.84 mA cm^{-2} at -0.6 V for BN-Gr/LSM, PN-Gr/LSM and SN-Gr/LSM, respectively. The highest limited current density is exhibited by the PN-Gr/LSM catalyst with a value of 3.91 mA cm^{-2} at -0.6 V, which is ca. 84% of the measured current density of a commercial Pt/C 20% catalyst.

In order to complement the LSV results, the reaction kinetics are studied via the Tafel slopes calculated from the plots of the applied voltage vs. the logarithm of the mass transport-corrected current densities (Figure 6.11b). It is observed that the addition of perovskite into the dual-doped graphene catalysts increases the value (in absolute terms) of the calculated Tafel slopes (except for SN-Gr/LSM), which implies a higher influence of the electron-transfer Reaction *2.23* in the rds occurring at 120 mV dec^{-1}. This is believed to be due to the poor electronic conductivity of the perovskite.

The same trend found for the measured current densities can be observed in the number of electrons involved in the ORR. Figure 6.11c shows that the addition of LSM causes an increase in the value of n (calculated at -0.5 V), with particular interest in SN-Gr where n rises from 3.58 to 3.81. In the case of BN-Gr and PN-Gr this increase is more moderate, from 3.51 to 3.55 and from 3.69 to 3.75, respectively. A consequence of this is the reduction in the production rate of peroxide intermediate (Figure 6.11d), which drops from 21.1% for the dual-doped SN-Gr to 9.6% for SN-Gr/LSM. This is an unusually low value for a Pt-free catalyst. For BN-Gr/LSM and PN-Gr/LSM the peroxide production rate is 22.2% and 12.4%, with reductions from their corresponding perovskite-free counterparts of 2.3% and 3.0%, respectively.

These results show that the significant catalytic activity observed in the SN-Gr/LSM hybrid can be extended to other similar catalysts, indicating that the improved performance of dual-doped graphene/perovskite composites does not depend exclusively on one specific graphene dopant. Nevertheless, the fact that the improvement in the catalytic features is more accentuated in the SN-Gr/LSM catalyst with respect to PN-Gr/LSM and BN-Gr/LSM suggests that the interaction between the graphene dopants and the perovskite can play an important role in the catalytic activity of these composites.

It is worthwhile to consider to what extent the previously described spillover effect is responsible for the synergistic effect observed in doped-graphene/perovskite catalysis. It should be remembered that the spillover effect consists of the release of active sites in the dual-doped graphene due to the affinity of the perovskite towards the peroxide intermediates generated during the ORR in the functionalised graphene. Since $La_{1-x}A_xMnO_3$ perovskites have demonstrated to have high affinity towards the HO_2^- adsorption [346], it can be hypothesised that, if the spillover effect is crucial in the improved doped-graphene/perovskite catalytic behaviour, the dual-doped graphenes producing a higher amount of peroxide intermediate would develop a higher ORR activity when the perovskite is added. In this regard, the peroxide formation rate of BN-Gr, PN-Gr and SN-Gr has been measured to be 24.5%, 15.5% and 21.1%, respectively (Figure 6.11d). Considering that the SN-Gr/LSM composite clearly shows the best improvement in the catalytic performance, while SN-Gr produces an intermediate peroxide production with respect to BN-Gr and PN-Gr, it can be concluded that the spillover effect is not the most crucial factor in the improved catalytic activity of doped-graphene/perovskite composites (although its influence should not be dismissed).

Conversely, the ligand effect could have a more important influence in the electrochemical performance of doped-graphene/perovskite systems. For example, Fabbri et al. suggest that the electronic interaction between the two components is the main factor that explains the enhanced catalytic activity observed in the $Ba_{0.5}Sr_{0.5}Co_{0.8}Fe_{0.2}O_{3-\delta}$/Acetylene Black carbon (BSCF/AB) composite [197]. In a similar work, using the same BSCF perovskite but N-mesoporous carbon instead of AB, Ciucci et al. detail the nature of the ligand effect via XPS and XRD measurements, demonstrating that the electronic interaction between the two components resulted in a decreased Co valence when the N-mesoporous carbon is present [204]. A different behaviour derived from the ligand effect has been also reported for carbon nanotube/Mn oxide (CNT/MnOx) hybrids, where the spontaneous electronic transfer between the two components resulted in high positive charged CNT surface favouring the O_2 adsorption, subsequent weakening of the O-O bonding and direct reduction of O_2 to OH^- via a four-electron process [339].

In conclusion, it is suggested that the different dopants used in the dual-doped graphene/perovskite hybrids reported in the present study can modulate in a different way the electronic interactions between the two components, producing slight variations in the form in which the ligand effect is expressed and thus yielding significant differences in the ORR performances. It is shown that SN-Gr/LSM clearly exhibits the best improvement with respect to its perovskite-free equivalent, suggesting that the S-dopant groups have a more positive influence in the electronic interaction with Mn than B and P dopants. The noticeably lower oxygen content of SN-Gr with respect to BN-Gr and PN-Gr (2.6%, 7.5% and 6.9%, respectively, see Figure 6.10) could also play a role on the ligand effect.

6.2.4 Composition design of perovskites and its influence in the dual-doped graphene/perovskite composites

As it was explained in Section 2.4.2, perovskite oxides encompass a vast range of possibilities due to its flexible structure and tunable characteristics. In this section, the influence of the individual components of the doped-graphene/perovskite composites are studied from the point of view of the perovskite. Different perovskite compositions are tested by varying the A- and B-cation sites, and the possible interactions between the perovskite components and the graphene dopants are analysed in order to elucidate the catalytic mechanisms.

6.2.4.1 Influence of A-cation of perovskite in the dual-doped graphene/perovskite performance

It has been demonstrated that the introduction of oxygen vacancies in stoichiometric perovskite oxides could have a positive effect towards the ORR activity [193]. Among other methods reported in the literature [347–349], the substitution of A-site cations by others A’ with lower oxidation states have been demonstrated to improve the ORR performance via the creation of oxygen vacancies and subsequent shift of B-cations to unstable higher oxidation states in order to maintain the electroneutrality [191,350]. However, this strategy must be controlled since excessive oxygen vacancies could reduce the catalytic activity due to a decrease of the electrical conductivity or changes in the crystalline structure [351].

In this study, two perovskites with different A-cation site compositions prepared as described in Section 3.3.5 are compared in terms of ORR catalytic activity, with and without the addition of dual-doped SN-Gr catalyst. The empirical composition formulae for the two perovskites are $Ba_{0.8}Bi_{0.2}Co_{0.6}Fe_{0.4}O_{3-\delta}$ and $Ba_{0.7}Sr_{0.2}$ $Bi_{0.1}Co_{0.6}Fe_{0.4}O_{3-\delta}$ that shall be abbreviated to BBCF and BSBCF, respectively, for convenience. It is noted that the B-cation is fixed as 60% Co and 40% Fe, while that the A-site is varied introducing 20% Sr in the case of BSBCF with respect to the BBCF perovskite. The introduction of the Sr cation with an oxidation state of +2 in substitution of part of the Bi cations with oxidation states of +3 or +5, results in a decrease of the overall oxidation state, thus creating oxygen vacancies.

The electrochemical performance of the SN-Gr/perovskite catalysts and their individual components are displayed in Figure 6.12.

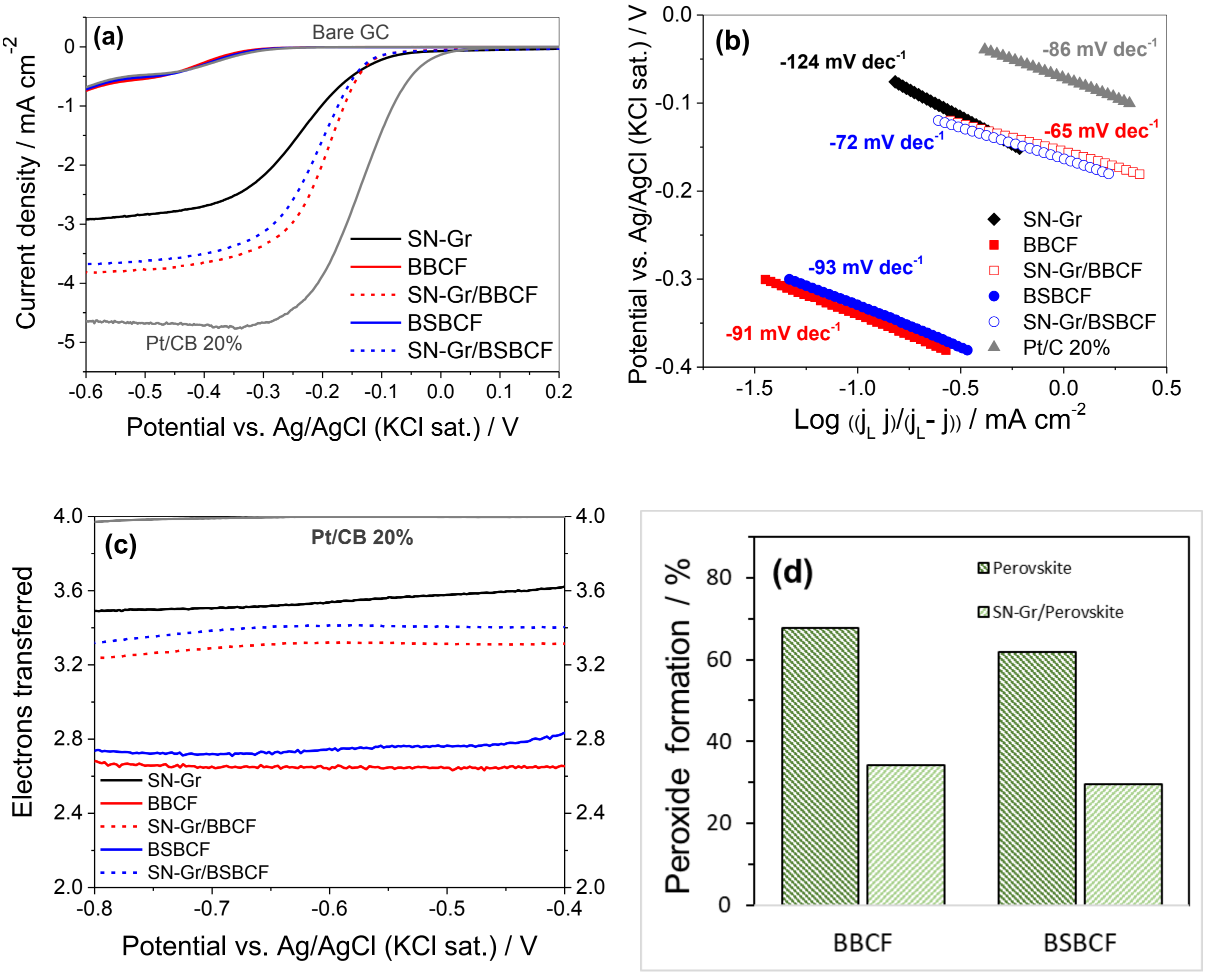

Figure 6.12. *(a) LSV of Ba$_{0.8}$Bi$_{0.2}$Co$_{0.6}$Fe$_{0.4}$ (BBCF) and Ba$_{0.7}$Sr$_{0.2}$Bi$_{0.1}$Co$_{0.6}$Fe$_{0.4}$ (BSBCF) perovskites with and without SN-Gr addition (0.2:0.8 ratio), and SN-Gr dual-doped graphene, at different compositions in O$_2$-saturated 0.1 M KOH. Bare GC electrode and a commercial Pt/C 20% are also shown for comparison. (b) Mass transport-corrected Tafel plots showing the Tafel slope values. (c) Number of electrons transferred vs. potential, obtained from RRDE measurements. (d) Mole fraction (in %) of produced peroxide intermediate.*

Figure 6.12a shows that the ORR activity of the single perovskites is insignificant, with no appreciable differences with respect to the bare GC electrode activity. Nevertheless, when they are combined with the SN-Gr catalyst (0.8:0.2 dual-doped graphene/perovskite ratio), both exhibit a considerable enhancement of the electrochemical performance. However, there is no significant difference in the measured current densities at -0.6 V of SN-Gr/BBCF and SN-Gr/BSBCF composites (-3.82 and -3.67 mA cm^{-2}, respectively), and both report a similar onset potential of around -60 mV.

The Tafel plots are displayed in Figure 6.12b. The calculated Tafel slopes are around -92 mV dec^{-1} for both BBCF and BSBCF, which implies a mixed mechanism between Reaction *2.23* and Reaction *2.24* as the rds. The addition of SN-Gr varies the calculated Tafel slopes to values closer to 60 mV dec^{-1} for the hybrid catalysts, corresponding to a rds dominated by Reaction *2.24*, which is not an electron-transfer reaction. This trend is slightly more accentuated in SN-Gr/BBCF than in SN-Gr/BSBCF. These results are in agreement with the enhanced catalytic activities observed for the hybrid catalysts in Figure 6.12a.

Regarding the number of electrons involved in the reaction, it is seen in Figure 6.12c that the doped graphene-free perovskites exhibit low values of n, being 2.65 and 2.77 (at -0.5 V) for BBCF and BSBCF, respectively. When the perovskites are combined with the dual-doped graphene both composites undergo a similar increase with respect their doped graphene-free counterparts, being the calculated values of n of 3.32 and 3.41 for SN-Gr/BBCF and SN-Gr/BSBCF, respectively. These values are even lower than that calculated for the perovskite-free SN-Gr (3.58). The corresponding peroxide formation rates calculated from the number of electrons transferred during the ORR are shown in Figure 6.12d, and confirm the high peroxide intermediate production of the pure perovskites, with 67.7% and 61.8% for BBCF and BSBCF, respectively. After the addition of the dual-doped graphene, the equivalent composites achieve both a decrease of approximately 33% to give final peroxide formation rates of 34.2% and 29.6% for SN-Gr/BBCF and SN-Gr/BSBCF, respectively.

These results show that the addition of Sr into the A-cation sites of the BBCF perovskite has low impact on the catalytic behaviour, even when both perovskites are mixed with dual-doped graphene. Nevertheless, a slight improvement is observed in the case of SN-Gr/BBCF with respect to SN-Gr/BSBCF in terms of measured current densities and Tafel slopes. Although the difference is probably too slight to be considered determining, it suggests that the addition of Sr and the corresponding changes in the perovskite structure in terms of created oxygen vacancies are not beneficial for the catalytic activity of the doped-graphene/perovskite composites.

The results also seem to indicate that the improved conductivity due to the addition of the doped-graphene into the perovskite could play a significant (although limited) role in this case. This observation is supported by the fact of that the addition of doped-graphene reveals slight changes on the ORR performance of both perovskites that are not observed in the pure perovskites. Since the B-site transition-metal composition is the same in both perovskites, these changes cannot come from any electronic transition between the doped-graphene and the B-cation of the perovskite, and it is extremely unlikely that the spillover effect (which is linked to the affinity of the transition metal used as B-cation towards the peroxide intermediates) is the reason behind these differences. Nevertheless, any conclusion should be taken with caution due to the small differences reported.

6.2.4.2 *Influence of B-cation of perovskite in the dual-doped graphene/perovskite performance*

The ORR activity of perovskite catalysts has been demonstrated to be highly dependent on the transition-metal B-site cation [195]. Analogously to the previous section that analysed the influence of the A-cation perovskite in the ORR performance of doped-graphene/perovskite composites, here two perovskites with different compositions of the B-cation site (prepared as described in Section 3.3.5) are studied regarding its ORR catalytic behaviour, and their performance is compared to their equivalent doped-graphene composites. In this case, the A-cation is fixed as 100% Ca, being the B-site composition of the first perovskite 70% Fe, 20% Si and 10% Mn. In the second perovskite 20% Ti is added, whereas the Mn composition is increased to 70% at the expense of removing all the Fe. Therefore, the formulae of the perovskites are $CaFe_{0.7}Si_{0.2}Mn_{0.1}O_{3-\delta}$ and $CaMn_{0.7}Ti_{0.2}Si_{0.1}O_{3-\delta}$, being abbreviated hereafter as CFSM and CMTS, respectively.

The low catalytic activity of the single perovskites is displayed in Figure 6.13a, which shows that only the CFSM slightly improves that activity with respect the bare GC electrode.

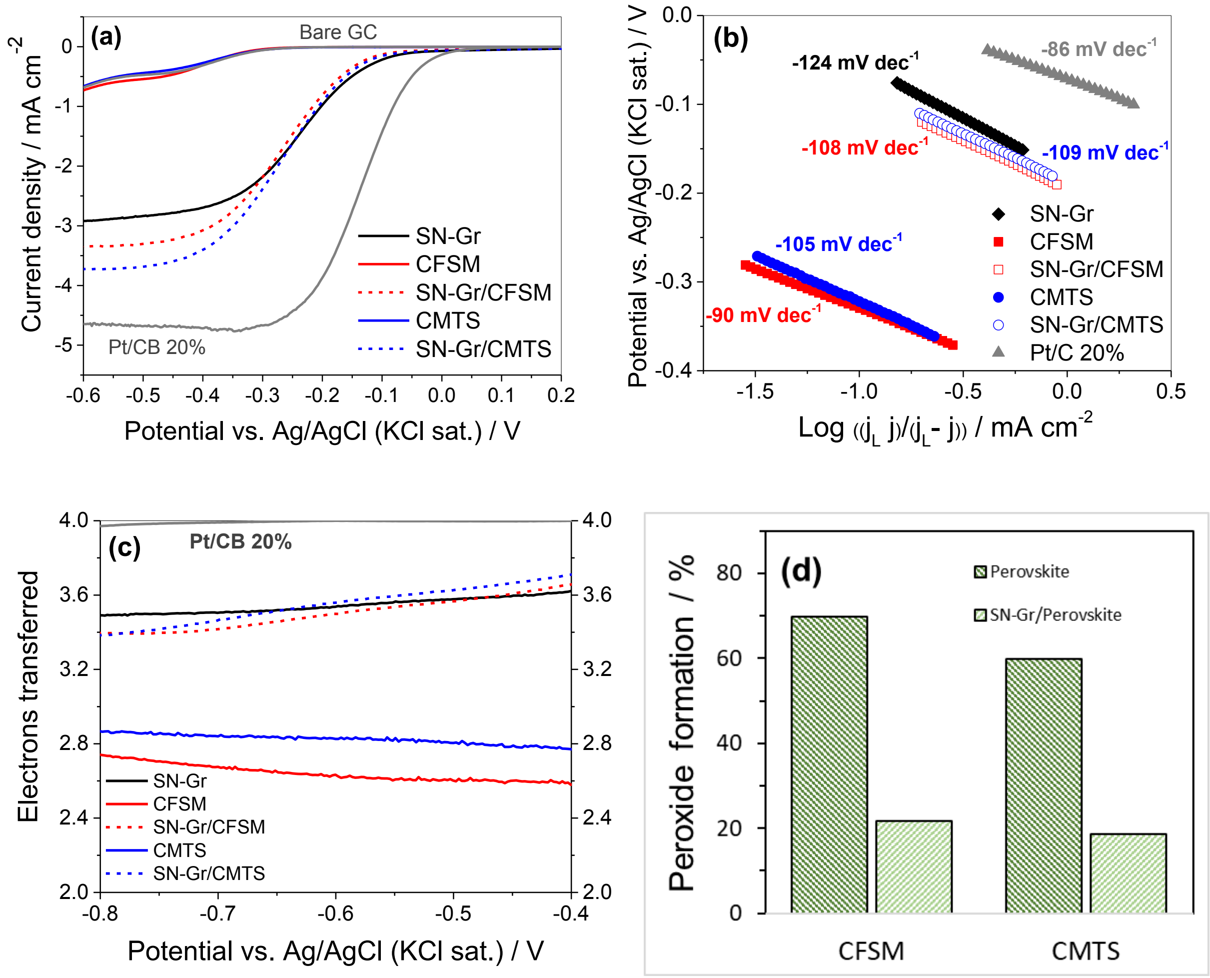

Figure 6.13. *(a) LSV of $CaFe_{0.7}Si_{0.2}Mn_{0.1}O_{3-\delta}$ (CFSM) and $CaMn_{0.7}Ti_{0.2}Si_{0.1}O_{3-\delta}$ (CMTS) perovskites with and without SN-Gr addition (0.2:0.8 ratio), and SN-Gr dual-doped graphene, at different compositions in O_2-saturated 0.1 M KOH. Bare GC electrode and a commercial Pt/C 20% are also shown for comparison. (b) Tafel plots showing the Tafel slope values. (c) Number of electrons transferred vs. potential, obtained from RRDE measurements. (d) Mole fraction (in %) of produced peroxide intermediate.*

Nevertheless, the addition of the dual-doped graphene produces a very significant increase in the electrochemical performance. Although the perovskite-free SN-Gr exhibits a more positive onset potential than both composites, these show higher limited current densities, whose values at -0.6V are -3.34 and -3.72 mA cm^{-2} for SN-

Gr/CFSM and SN-GrCMTS, respectively (for comparison, the perovskite-free SN-Gr exhibited a limited current density of -2.92 mA cm^{-2}).

The calculated Tafel plots are displayed in Figure 6.13b. For the CMTS perovskite, the addition of the dual-doped graphene does not provide a significant change in the value of the Tafel slope (around -105 mV dec^{-1}), which is closed to -120 mV dec^{-1} associated to the electron-transfer Reaction *2.23* as rds. The Tafel slope of CFSM is calculated to be -90 mV dec^{-1}, which determines a rds with a mixed behaviour between Reaction *2.23* and Reaction *2.24*. In this case, the addition of SN-Gr significantly shifts the Tafel slope to -108 mV dec^{-1}, which makes the electron-transfer Reaction *2.23* the rds for the SN-Gr/CFSM hybrid catalyst.

With regard to the number of electrons involved in the reaction, Figure 6.13c shows that CFSM exhibits a lower n than CMTS, with values at -0.5 V of 2.60 and 2.81, respectively. This feature improves with the addition of the dual-doped graphene to reach a similar value than SN-Gr, yielding values of n of 3.57 for SN-Gr/CFSM and 3.63 for SN-Gr/CMTS, both around the value of 3.58 calculated for the perovskite-free dual-doped graphene. These results clearly confirm that the number of electrons involved in the ORR are determined by the SN-Gr in these doped-graphene perovskite hybrids. Concerning to the peroxide production rate, it is observed in Figure 6.13d that both composites yield around 20% peroxide production, although SN-Gr/CMTS displays a slightly lower peroxide production. Nevertheless, SN-Gr/CFSM exhibits a greater lowering in peroxide produced with respect to its single perovskite with a decrease of 48.3%, whereas this value is 41.1% for SN-Gr/CMTS.

These results reveal that, even though the differences are not very pronounced, the doped-graphene/perovskite composite containing Ti and higher levels of Mn in the B-site of the perovskite displays better catalytic activity in terms of limited current density and lower peroxide production. Significantly, both perovskites show a similarly low catalytic activity in absence of doped-graphene. This clearly points to some type of perovskite-carbon interaction.

If we attend to the nature of the single perovskite, the Sabatier principle claims that the best ORR performance is achieved when the interaction between the O_2 adsorbed species and the catalyst is neither too strong nor too weak [352]. It has been demonstrated that the catalytic behaviour of perovskites towards the ORR is linked to the σ*-orbital (e_g) occupation of the transition-metal of B-cation sites [353], showing the metals with e_g occupation around unity the best ORR performance [195]. In the present study, the main transition-metals in the B-sites of CFSM and CMTS are Fe and Mn, respectively, both representing 70% of the B-cation composition. Considering that Fe is reported to have too much orbital occupation ($e_g \approx 2$), whereas Mn shows an orbital occupation near to unity ($e_g \approx 1$) [195], this can explain why the SN-Gr/CMTS composite exhibits better performance in terms of limited current density than SN-Gr/CFMS. Nevertheless, it should be noted that the low conductivity of both perovskites makes that this difference in the catalytic behaviour is only highlighted when the conductive graphene is added.

Another possible explanation could be a direct graphene-perovskite interaction. It has been proposed that the carbon could affect the electronic structure of B-site transition metal of perovskite [194]. Some authors have demonstrated that the addition of carbon to perovskites can modify the oxidation state of the B-site transition metal, for example Co, which is linked to enhanced catalytic activity [354], although this is not observed for Fe [336]. Another study reveals that higher Co contents in carbon-supported $Ba_{0.5}Sr_{0.5}Co_xFe_{1-x}O_{3-\delta}$ perovskites favour the ORR performance, whereas high Fe contents are associated to lower catalytic activity [355]. On the other hand, high Mn-content $LaMn_{0.9}Co_{0.1}O_3$/graphene composites exhibit an impressive catalytic behaviour, with an electron transfer number calculated to be 3.87. XRD measurements demonstrate that this improved ORR activity is not ascribed to any change in the perovskite structure due to the presence of graphene, but the coexistence of Mn^{3+} and Mn^{4+} species (detected by XPS analysis) influenced by the presence of graphene, which implies a surface charge storage and subsequent enhanced catalytic activity [202]. This could explain why the SN-Gr/CMTS composite displays a superior catalytic activity with respect to the Fe-containing SN-Gr/CFMS system.

Moreover, the presence of Ti in the CMTS perovskite may also contribute to the better catalytic performance observed in the SN-Gr/CMTS composite. It has been demonstrated that the {001} facets of anatase TiO_2 crystals favour the oxygen adsorption and subsequent dissociative activation. In addition, the combination of Ti^{3+} and oxygen vacancies create a defect-centred mechanism that enhances the ORR activity [356]. Another study has confirmed that Ti-containing perovskites exhibit improved ORR activity linked to the presence of oxygen vacancies in the perovskite structure, with XPS analysis indicating an oxygen-deficient stoichiometry of $BaTiO_{2.76}$ in that particular case [349].

6.3 Conclusions

In this chapter, a complete study of the catalytic activity of doped-graphene/metal hybrid catalysts has been carried out. First, a transition metal (Fe) has been incorporated into a N-doped graphene, demonstrating this hybrid catalyst an enhanced catalytic activity with respect to its metal-free equivalent. Moreover, the presence of Fe seems to promote the direct 4e mechanism and reduce dramatically the peroxide intermediate production.

Secondly, dual-doped graphene/perovskite oxide composites have been evaluated in terms of ORR performance. The electrochemical tests have revealed that such hybrid systems exhibit an improved catalytic activity with respect to their separated components. This catalytic behaviour has been shown to be dependent on the relative doped graphene-perovskite composition, being 20% the optimal perovskite content. These conclusions can be extended to different dual-doped graphenes, achieving the PN-Gr/$La_{0.8}Sr_{0.2}MnO_3$ composite the highest catalytic activity, with a limited current density yielding 84% of that measured for a commercial Pt/C 20% catalyst and the calculated electron transfer number being 3.75.

Several mechanisms behind this excellent catalytic activity have been proposed and discussed. First, the improved electrical conductivity due to the addition of highly conductive graphene into perovskites has been dismissed as the main factor contributing to the enhanced ORR performance. In addition, a proposed two-step mechanism in which the dual-doped graphene would reduce the adsorbed O_2 into peroxide intermediate, followed by a further reduction to OH^- in the perovskite catalyst, is also ruled out as the only valid explanation due to the low peroxide intermediate production of the dual-doped graphene catalysts in their own.

The possible interaction between the dual-doped graphene and the perovskite has been proposed as the most important factor contributing to the high catalytic activity reported. This interaction can be expressed as a ligand effect, in which an electronic transfer from the graphene towards the transition-metal B-cation site of the perovskite results in positively charged carbon sites that favour the O-O bonding dissociation. Another mechanism associated to enhanced catalytic activity is the spillover effect, where the products of the ORR are attracted due to the affinity of the perovskite surface, thus favouring the release of active sites in the functionalised graphene for further O_2 adsorption and reduction. These two mechanisms are believed to be the origin of the synergistic effect observed in dual-doped graphene/perovskite composites.

Finally, the effect of the perovskite composition on the ORR performance has been also analysed. It is concluded that the transition-metal composition of the B-cation sites has a bigger influence in the final catalytic behaviour than the A-cation sites variability. As a consequence of the application of the Sabatier principle, Mn is reported to be a very active candidate as B-cation transition-metal, due to an orbital occupation near to unity. The crystalline structure of the B-transition metal seems to have also an influence in the O_2 adsorption, as well as the creation of oxygen vacancies linked to enhanced catalytic activity.

7 CONCLUSIONS AND FURTHER WORK

7.1 Conclusions

An integral study on the application of graphene-derived materials as catalysts (or catalyst supports) for the ORR in alkaline media has been carried out. Some promising conclusions have been extracted, which could have implications in the field of the oxygen reduction catalysis.

Regarding its behaviour as catalyst support, graphene has demonstrated to possess catalytic activity by itself. This implies that the ORR follows a mixed mechanism between the proposed 4-electron and the 2+2-electron pathways in platinum supported on graphene-derived catalysts (including multi-walled carbon nanotubes). In contrast, platinum supported in Carbon Black follows a *quasi* 4-electron mechanism, since Carbon Black is inactive towards the ORR and only platinum catalyses the reaction. With respect to the Pt deposition method, the reduction of potassium hexachloroplatinate with sodium borohydride has demonstrated to be a more efficient method than a microwave-assisted polyol reduction procedure.

The systematic study of synthesised single, dual, ternary and quaternary “metal-free” graphene catalysts doped with boron, nitrogen, phosphorus and sulphur, has yielded that only dual-doped graphenes can improve the ORR activity with respect to a dopant-free reduced-graphene oxide catalyst produced under the same conditions. The reasons behind this discovery have been proposed to be related to the fact of that the variability in the electronegativity of the dopants creates a charge distribution asymmetry that favours the ORR activity. The excess of dopant heteroatoms in ternary and quaternary-doped graphenes seems to attenuate this synergistic effect, thus decreasing the ORR performance. The reduction of graphene oxide has been evaluated by two different methods, resulting that an annealing procedure is more efficient than the chemical reduction with L-ascorbic acid.

Metal/graphene hybrid catalysts have been also evaluated. A graphene catalyst doped with N and Fe transition-metal has demonstrated to favour the 4-electron pathway with respect to its Fe-free N-Gr counterpart. In addition, several dual-doped graphenes have been evaluated in combination with a $La_{0.8}Sr_{0.2}MnO_3$ (LSM) perovskite oxide, proving these hybrid catalysts an improved catalytic activity with respect to their separate individual components, and decreasing the peroxide production to levels lower than 10%. Several reasons have been proposed to be behind this finding. First, a “ligand effect”, where the doped-graphene covalently transfer electrons to the transition metal acting as the perovskite B-cation, would favour the splitting of O-O bond in the positive sites formed in the graphene lattice. In addition, the “spillover effect”, in which the affinity of the perovskite towards the peroxide intermediates produced during the ORR would release catalytically active sites in the dual-doped graphene, could also explain the improved ORR activity of these hybrid catalysts. Nevertheless, the increased conductivity of these hybrids due to the addition of a highly conductive graphene-derived material has been dismissed as the main contributor to the excellent catalytic activity observed.

Finally, the metal free doped-graphene catalysts have proven to suffer a lower degradation after continuous activity and much higher tolerance to methanol than a commercial Pt/C catalyst, which can have important implications in the use of these new catalysts for practical applications.

7.2 Further work

- The graphene-derived materials used in this study are synthesised from graphite using as intermediate step the Hummers' method, as the most of the literature available on the topic. As explained, it is well-known that this procedure generates some metal traces (mainly manganese) in the as-produced graphene which may interfere with the electrochemical results in the ORR tests. The development of a method as efficient as the Hummers' procedure but producing metal trace-free graphene oxide is encouraged. In addition, the design of electrochemical experiments that permit to separate the graphene-derived activity from the catalytic contribution of its metal impurities is still challenging.

- In the present study, dual-doped graphene has yielded the optimal ORR activity with respect to single, ternary and quaternary graphene catalysts. Nevertheless, the theoretical mechanism behind this finding needs to be confirmed by further experiments.

- A deeper investigation is required in order to elucidate the mechanisms behind the improved catalytic activity demonstrated by the dual-doped graphene/perovskite hybrid catalysts. In this work, the increased conductivity has been dismissed as the main reason for the excellent ORR performance, and some mechanisms, such as the spillover effect or the ligand effect, have been proposed, but further experiments need to be designed to investigate the main contributor.

- This work has proposed the development of doped-graphene/metal hybrid catalysts as promising alternatives to platinum in ORR catalysis, using transition metals and perovskite oxides as the metal components. This line of investigation can be further explored by combining doped-graphene with other types of metals, such as spinels (previously reported but still relatively unexplored) and transition-metals other than iron and cobalt.

- *In-situ* MEA tests have been carried out in the present study for the carbon-supported Pt catalysts studied in Chapter 4, in order to evaluate the performance of the different catalysts under practical conditions. As discussed in Section 4.3, the results are in good agreement with the observations reported for the *ex-situ* experiments conducted with the same catalysts. Nevertheless, due to time limitations, the same experiment has not been performed for the doped-graphene and metal/doped-graphene catalysts described in Chapters 5 and 6, respectively. It is strongly suggested to perform this type of MEA experiments for doped-graphene catalysts (with and without the addition of transition metals and perovskites) to analyse if the results obtained in the *ex-situ* CV and LSV experiments reflect accurately the behaviour of these catalysts for practical applications.

APPENDICES

Appendix 1. Determination of the kinetic current density from the equation of measured current density

$$\frac{1}{j} = \frac{1}{j_K} + \frac{1}{j_L} \qquad \text{(Ap. 1.1)}$$

$$\frac{1}{j} = \frac{j_L + j_K}{j_K\, j_L} \qquad \text{(Ap. 1.2)}$$

$$j_K\, j_L = j\,(j_L + j_K) \qquad \text{(Ap. 1.3)}$$

$$j_K\, j_L = j\, j_L + j\, j_K \qquad \text{(Ap. 1.4)}$$

$$j_K\, j_L - j\, j_K = j\, j_L \qquad \text{(Ap. 1.5)}$$

$$j_K\,(j_L - j) = j\, j_L \qquad \text{(Ap. 1.6)}$$

$$\boldsymbol{j_K = \frac{j\, j_L}{j_L - j}} \qquad \text{(Ap. 1.7)}$$

where j is the measured current density, j_K is the kinetic current density (the component of the measured current that should be plotted in the abscissa axis to obtain the Tafel plot) and j_L is the limited current density.

Appendix 2. Comparison of C1s deconvoluted peak compositions for GO, rGO (obtained reducing GO with L-ascorbic acid), Pt/GO and Pt/rGO (values expressed as percentage).

	C-C/C=C	**-C-OH**	**-C-O-C-**	**>C=O**	**-COOH**
GO	35.9	14.8	30.3	15.1	3.9
rGO	45.1	17.6	19.4	9.7	8.2
Pt/GO	37.7	14.2	11.5	24.7	11.9
Pt/rGO	66.0	8.9	14.1	6.2	4.8

Appendix 3. Comparison of C1s deconvoluted peak compositions for GO, rGO (L-ascorbic acid) and rGO (Annealing) (values expressed as percentage).

	C-C/C=C	**-C-OH**	**-C-O-C-**	**>C=O**	**-COOH**
GO	35.9	14.8	30.3	15.1	3.9
rGO (L-ascorbic acid)	45.1	17.6	19.4	9.7	8.2
rGO (annealing)	72.7	14.7	7.5	2.2	2.9

Appendix 4. Comparison of B1s, N1s, P2p and S2p deconvoluted peak compositions for all the doped-graphene catalysts (values expressed as percentage).

B1s

	B_4C	B-C_3	C-BO	C-BNO	C-BO_2	B_2O_3
B-Gr		4.1	8.5		76.6	10.8
BN-Gr		14.0	32.6	31.4	17.6	4.4
BNS-Gr		9.3	24.1	41.7	22.2	2.7
BPS-Gr[a]	8.9	10.9	12.8		53.3	14.1
BNPS-Gr[a]	3.2	11.1	34.0	22.1	28.0	1.6

[a] *After P2s subtraction*

N1s

	C-BNO	Pyridinic	Pyrrolic	Quaternary	Pyridinic N-oxide
N-Gr		40.0	14.2	21.8	24.0
BN-Gr	19.3	33.5	20.3	14.1	12.8
PN-Gr		34.9[b]	15.9	29.7	19.5
SN-Gr		48.0	10.2	23.1	18.7
BNS-Gr	48.8	22.8	17.6	7.1	3.7
BNPS-Gr	23.4	38.2[b]	14.4	14.0	10.0
Fe-N-Gr		49.2	9.7	24.4	16.7

[b] N-pyridinic peaks have contribution of P-N bonds appearing at the same binding energy.

P2p

	P-C	P-N	Metaphosphates	Phosphates
P-Gr	3.5		38.7	57.8
PN-Gr	4.9	24.8	31.4	38.9
BPS-Gr	5.8		68.1	26.1
BNPS-Gr	6.8	13.5	19.3	60.4

S2p

	$S2p_{3/2}$	$S2p_{1/2}$	-C-SO_2-C-	-C-SO_3-C-	-C-SO_4-C-
S-Gr	47.0	26.6	15.9	6.7	3.8
SN-Gr	41.2	30.3	16.3	6.3	5.9
BNS-Gr	44.4	34.7	11.2	4.4	5.3
BPS-Gr	45.4	33.2	13.0	4.0	4.4
BNPS-Gr	43.7	31.8	12.6	6.1	5.7

Fe2p

	Fe^{3+} $2p_{3/2}$	Fe^{2+} $2p_{3/2}$	Satellite	Fe^{2+} $2p_{1/2}$	Fe^{2+}, Fe^{3+} $2p_{1/2}$
Fe-N-Gr	41.6	20.0	12.8	11.8	13.8

REFERENCES

[1] J. Hou, Y. Shao, M.W. Ellis, R.B. Moore, B. Yi, Graphene-based electrochemical energy conversion and storage: fuel cells, supercapacitors and lithium ion batteries, Phys. Chem. Chem. Phys. 13 (2011) 15384. doi:10.1039/c1cp21915d.

[2] M. Shao, Q. Chang, J.-P. Dodelet, R. Chenitz, Recent Advances in Electrocatalysts for Oxygen Reduction Reaction, Chem. Rev. 116 (2016) 3594–3657. doi:10.1021/acs.chemrev.5b00462.

[3] S. Gamburzev, A.J. Appleby, Recent progress in performance improvement of the proton exchange membrane fuel cell (PEMFC), J. Power Sources. 107 (2002) 5–12. doi:10.1016/S0378-7753(01)00970-3.

[4] X. Ge, A. Sumboja, D. Wuu, T. An, B. Li, F.W.T. Goh, T.S.A. Hor, Y. Zong, Z. Liu, Oxygen Reduction in Alkaline Media: From Mechanisms to Recent Advances of Catalysts, ACS Catal. 5 (2015) 4643–4667. doi:10.1021/acscatal.5b00524.

[5] G. Sandstede, E.J. Cairns, V.S. Bagotsky, K. Wiesener, History of low temperature fuel cells, in: Handb. Fuel Cells, American Cancer Society, 2010. doi:10.1002/9780470974001.f104011.

[6] J. Larminie, A. Dicks, Fuel Cell Systems Explained, 2001. doi:10.1016/S0378-7753(00)00571-1.

[7] U. Carrette, L. , Friedrich, K. A. and Stimming, Fuel Cells – Fundamentals and Applications., 2001. doi:10.1002/1615-6854(200105)1:1<5::AID-FUCE5>3.0.CO;2-G.

[8] Hydrogen Cars Now, (2018). http://www.hydrogencarsnow.com/index.php/gm-electrovan/ (accessed April 6, 2018).

[9] Honda, New Releases 2002. (2018). http://world.honda.com/news/2002/4021122-fcx-eng.html (accessed April 6, 2018).

[10] Hydrogen Cars Now, Audi Q5 Hybrid Fuel Cell Unveiled Berlin. (2018). http://www.hydrogencarsnow.com/index.php/hydrogen-cars/audi-q5-hybrid-fuel-cell-hfc-unveiled-in-berlin/ (accessed April 6, 2018).

[11] J.R. Varcoe, P. Atanassov, D.R. Dekel, A.M. Herring, M. a. Hickner, P. a. Kohl, A.R. Kucernak, W.E. Mustain, K. Nijmeijer, K. Scott, T. Xu, L. Zhuang, Anion-exchange membranes in electrochemical energy systems, Energy Environ. Sci. 7 (2014) 3135–3191. doi:10.1039/b000000x.

[12] I. Kruusenberg, L. Matisen, Q. Shah, a. M. Kannan, K. Tammeveski, Non-platinum cathode catalysts for alkaline membrane fuel cells, Int. J. Hydrogen Energy. 37 (2012) 4406–4412. doi:10.1016/j.ijhydene.2011.11.143.

[13] A. a. Gewirth, M.S. Thorum, Electroreduction of dioxygen for fuel-cell applications: Materials and challenges, Inorg. Chem. 49 (2010) 3557–3566. doi:10.1021/ic9022486.

[14] J. Pan, S. Lu, Y. Li, A. Huang, L. Zhuang, J. Lu, High-Performance alkaline polymer electrolyte for fuel cell applications, Adv. Funct. Mater. 20 (2010) 312–319. doi:10.1002/adfm.200901314.

[15] D.P. Tang, J. Pan, S.F. Lu, L. Zhuang, J.T. Lu, Alkaline Polymer electrolyte fuel cells: Principle, challenges, and recent progress, Sci. China Chem. 53 (2010) 357–364. doi:10.1007/s11426-010-0080-5.

[16] B.B. Blizanac, P.N. Ross, N.M. Markovic, Oxygen electroreduction on Ag(111): The pH effect, Electrochim. Acta. 52 (2007) 2264–2271. doi:https://doi.org/10.1016/j.electacta.2006.06.047.

[17] N. Ramaswamy, S. Mukerjee, Fundamental mechanistic understanding of electrocatalysis of oxygen reduction on Pt and non-Pt surfaces: Acid versus alkaline media, Adv. Phys. Chem. 2012 (2012). doi:10.1155/2012/491604.

[18] E.P. Randviir, D.A.C. Brownson, C.E. Banks, A decade of graphene research: Production, applications and outlook, Mater. Today. 17 (2014) 426–432. doi:10.1016/j.mattod.2014.06.001.

[19] K.S. Novoselov, V.I. Fal′ko, L. Colombo, P.R. Gellert, M.G. Schwab, K. Kim, A roadmap for graphene, Nature. 490 (2012) 192–200. doi:10.1038/nature11458.

[20] K.S. Novoselov, A.K. Geim, S. V Morozov, D. Jiang, Y. Zhang, S. V Dubonos, I. V Grigorieva, A.A. Firsov, Electric Field Effect in Atomically Thin Carbon Films, Science (80-.). 306 (2004) 666–669. doi:10.1126/science.1102896.

[21] C.R. Dean, A.F. Young, I. Meric, C. Lee, L. Wang, S. Sorgenfrei, K. Watanabe, T. Taniguchi, P. Kim, K.L. Shepard, J. Hone, Boron nitride substrates for high-quality graphene electronics, Nat. Nanotechnol. 5 (2010) 722–726. doi:10.1038/nnano.2010.172.

[22] M. Allen, Honeycomb carbon -- A study of graphene, Am. Chem. Soc. (2009) 184. doi:10.1021/cr900070d.

[23] V. Singh, D. Joung, L. Zhai, S. Das, S.I. Khondaker, S. Seal, Graphene based materials: Past, present and future, Prog. Mater. Sci. 56 (2011) 1178–1271. doi:10.1016/j.pmatsci.2011.03.003.

[24] D.R. Dreyer, R.S. Ruoff, C.W. Bielawski, From conception to realization: An historial account of graphene and some perspectives for its future, Angew. Chemie - Int. Ed. 49 (2010) 9336–9344. doi:10.1002/anie.201003024.

[25] S. Of, G.I.C. With, S.Z. State, Na , K and have been For the were C8K the superconducting c transitions and cl for the © Elsevier Sequoia / Printed in The Netherlands, 34 (1989) 455–460.

[26] A.K. Geim, K.S. Novoselov, The rise of graphene, Nat. Mater. 6 (2007) 183.

http://dx.doi.org/10.1038/nmat1849.

[27] H.P. Boehm, R. Setton, E. Stumpp, Nomenclature and terminology of graphite intercalation compounds, Carbon,. 24 (1986) 241–245. doi:10.1016/0008-6223(86)90126-0.

[28] X. Lu, M. Yu, H. Huang, R.S. Ruoff, Tailoring graphite with the goal of achieving single sheets, Nanotechnology. 10 (1999) 269. http://stacks.iop.org/0957-4484/10/i=3/a=308.

[29] S. Park, R.S. Ruoff, Chemical methods for the production of graphenes, Nat. Nanotechnol. 4 (2009) 217–224. doi:10.1038/nnano.2009.58.

[30] F. Cheng, J. Chen, Metal–air batteries: from oxygen reduction electrochemistry to cathode catalysts, Chem. Soc. Rev. 41 (2012) 2172. doi:10.1039/c1cs15228a.

[31] E. Yeager, Dioxygen electrocatalysis: mechanisms in relation to catalyst structure, J. Mol. Catal. 38 (1986) 5–25. doi:10.1016/0304-5102(86)87045-6.

[32] J.S. Spendelow, A. Wieckowski, Electrocatalysis of oxygen reduction and small alcohol oxidation in alkaline media., Phys. Chem. Chem. Phys. 9 (2007) 2654–2675. doi:10.1039/b703315j.

[33] J.O.B. A. Damjanovic, M. A. Genshaw, The mechanism of oxygen reduction at platinum in alkaline solutions with special reference to H_2O_2, J. Electrochem. Soc. Electrochem. Sci. 114 (1967) 1107–1112.

[34] K.F. Blurton, E. McMullin, The Cathodic Reduction of Oxygen on Platinum in Alkaline Solutions, J. Electrochem. Soc. 116 (1969) 1476. doi:10.1149/1.2411574.

[35] Nenad M. Markovic, H. a. Gasteiger, P.N. Ross, Oxygen Reduction on Platinum Low-Index Single-Crystal Surfaces in Sulfuric Acid Solution: Rotating Ring-Pt(hkZ) Disk Studies, J. Phys. Chem. 99 (1995) 3411. doi:10.1021/j100011a001.

[36] E. Claude, T. Addou, J. Latour, P. Aldebert, A new method for electrochemical screening based on the rotating ring disc electrode and its application to oxygen reduction catalysts, J. Appl. Electrochem. 28 (1998) 57–64. doi:10.1023/A:1003297718146.

[37] N.A. Anastasijević, V. Vesović, R.R. Adžić, Determination of the kinetic parameters of the oxygen reduction reaction using the rotating ring-disk electrode: Part I. Theory, J. Electroanal. Chem. Interfacial Electrochem. 229 (1987) 305–316. doi:10.1016/0022-0728(87)85148-3.

[38] T. Shinagawa, A.T. Garcia-Esparza, K. Takanabe, Insight on Tafel slopes from a microkinetic analysis of aqueous electrocatalysis for energy conversion, Sci. Rep. 5 (2015) 1–21. doi:10.1038/srep13801.

[39] G. Couturier, D.W. Kirk, P.J. Hyde, S. Srinivasan, Electrocatalysis of the hydrogen oxidation and of the oxygen reduction reactions of Pt and some alloys in alkaline medium, Electrochim. Acta. 32 (1987) 995–1005. doi:10.1016/0013-

4686(87)90024-7.

[40] K. Tammeveski, M. Arulepp, T. Tenno, C. Ferrater, J. Claret, Oxygen electroreduction on titanium-supported thin Pt films in alkaline solution, Electrochim. Acta. 42 (1997) 2961–2967. doi:10.1016/S0013-4686(97)00119-9.

[41] A. Damjanovic, V. Brusic, Electrode kinetics of oxygen reduction on oxide-free platinum electrodes, Electrochim. Acta. 12 (1967) 615–628. doi:10.1016/0013-4686(67)85030-8.

[42] O.T. Holton, J.W. Stevenson, The Role of Platinum in Proton Exchange Membrane Fuel Cells Evaluation of platinum's unique properties for use in both the anode and cathode of a proton exchange membrane fuel cell, @BULLETPlatinum Met. Rev. 57 (2013) 259–271. doi:10.1595/147106713X671222.

[43] T. Deutschmann, Olaf; Knozinger, Helmut; Kochloefl, Karl; Turek, Heterogeneous catalysis and solid catalysts, 1. Fundamentals, 2012. doi:10.1002/14356007.a05.

[44] J.K. Nørskov, J. Rossmeisl, A. Logadottir, L. Lindqvist, J.R. Kitchin, T. Bligaard, H. Jónsson, Origin of the overpotential for oxygen reduction at a fuel-cell cathode, J. Phys. Chem. B. 108 (2004) 17886–17892. doi:10.1021/jp047349j.

[45] I. Katsounaros, W.B. Schneider, J.C. Meier, U. Benedikt, P.U. Biedermann, A.A. Auer, K.J.J. Mayrhofer, Hydrogen peroxide electrochemistry on platinum: towards understanding the oxygen reduction reaction mechanism, Phys. Chem. Chem. Phys. 14 (2012) 7384. doi:10.1039/c2cp40616k.

[46] H. a. Gasteiger, S.S. Kocha, B. Sompalli, F.T. Wagner, Activity benchmarks and requirements for Pt, Pt-alloy, and non-Pt oxygen reduction catalysts for PEMFCs, Appl. Catal. B Environ. 56 (2005) 9–35. doi:10.1016/j.apcatb.2004.06.021.

[47] E. Billy, F. Maillard, a. Morin, L. Guetaz, F. Emieux, C. Thurier, P. Doppelt, S. Donet, S. Mailley, Impact of ultra-low Pt loadings on the performance of anode/cathode in a proton-exchange membrane fuel cell, J. Power Sources. 195 (2010) 2737–2746. doi:10.1016/j.jpowsour.2009.10.101.

[48] P. Parthasarathy, A. V. Virkar, Electrochemical Ostwald ripening of Pt and Ag catalysts supported on carbon, J. Power Sources. 234 (2013) 82–90. doi:10.1016/j.jpowsour.2013.01.115.

[49] J.Y.T.R. Ct, D. Guay, J.P. Dodelet, G. Den, Carbon monoxide poisoning of platinum-graphite catalysts for polymer electrolyte fuel cells: comparison between platinum-supported on graphite and intercalated in graphite, 61 (n.d.) 193–200.

[50] P. Trens, R. Durand, B. Coq, C. Coutanceau, S. Rousseau, C. Lamy, Poisoning of Pt/C catalysts by CO and its consequences over the kinetics of hydrogen chemisorption, Appl. Catal. B Environ. 92 (2009) 280–284.

doi:10.1016/j.apcatb.2009.08.004.

[51] G. a. Camara, E. a. Ticianelli, S. Mukerjee, S.J. Lee, J. McBreen, The CO Poisoning Mechanism of the Hydrogen Oxidation Reaction in Proton Exchange Membrane Fuel Cells, J. Electrochem. Soc. 149 (2002) A748. doi:10.1149/1.1473775.

[52] J. Liu, F.R. Lucci, M. Yang, S. Lee, M.D. Marcinkowski, A.J. Therrien, C.T. Williams, E.C.H. Sykes, M. Flytzani-Stephanopoulos, Tackling CO Poisoning with Single-Atom Alloy Catalysts, J. Am. Chem. Soc. 138 (2016) 6396–6399. doi:10.1021/jacs.6b03339.

[53] X.-K. Kong, C.-L. Chen, Q.-W. Chen, Doped graphene for metal-free catalysis, Chem. Soc. Rev. 43 (2014) 2841–2857. doi:10.1039/c3cs60401b.

[54] E.C. Weigert, A.L. Stottlemyer, M.B. Zellner, J.G. Chen, Tungsten monocarbide as potential replacement of platinum for methanol electrooxidation, J. Phys. Chem. C. 111 (2007) 14617–14620. doi:10.1021/jp075504z.

[55] S. Sharma, B.G. Pollet, Support materials for PEMFC and DMFC electrocatalysts - A review, J. Power Sources. 208 (2012) 96–119. doi:10.1016/j.jpowsour.2012.02.011.

[56] J. McBreen, H. Olender, S. Srinivasan, K. V Kordesch, Carbon supports for phosphoric acid fuel cell electrocatalysts: alternative materials and methods of evaluation, J. Appl. Electrochem. 11 (1981) 787–796. doi:10.1007/BF00615184.

[57] D. Pantea, H. Darmstadt, S. Kaliaguine, C. Roy, Electrical conductivity of conductive carbon blacks: Influence of surface chemistry and topology, Appl. Surf. Sci. 217 (2003) 181–193. doi:10.1016/S0169-4332(03)00550-6.

[58] E. Antolini, Carbon supports for low-temperature fuel cell catalysts, Appl. Catal. B Environ. 88 (2009) 1–24. doi:10.1016/j.apcatb.2008.09.030.

[59] K. Hartl, M. Hanzlik, M. Arenz, IL-TEM investigations on the degradation mechanism of Pt/C electrocatalysts with different carbon supports, Energy Environ. Sci. 4 (2011) 234–238. doi:10.1039/c0ee00248h.

[60] E. Bailón-García, F. Maldonado-Hódar, A. Pérez-Cadenas, F. Carrasco-Marín, Catalysts Supported on Carbon Materials for the Selective Hydrogenation of Citral, Catalysts. 3 (2013) 853–877. doi:10.3390/catal3040853.

[61] S. Tang, G. Sun, J. Qi, S. Sun, J. Guo, Q. Xin, G.M. Haarberg, Review of New Carbon Materials as Catalyst Supports in Direct Alcohol Fuel Cells, Chinese J. Catal. 31 (2010) 12–17. doi:10.1016/S1872-2067(09)60034-6.

[62] Y. Takasu, T. Kawaguchi, W. Sugimoto, Y. Murakami, Effects of the surface area of carbon support on the characteristics of highly-dispersed Pt-Ru particles as catalysts for methanol oxidation, Electrochim. Acta. 48 (2003) 3861–3868. doi:10.1016/S0013-4686(03)00521-8.

[63] V. Rao, P. a. Simonov, E.R. Savinova, G. V. Plaksin, S. V. Cherepanova, G.N.

Kryukova, U. Stimming, The influence of carbon support porosity on the activity of PtRu/Sibunit anode catalysts for methanol oxidation, J. Power Sources. 145 (2005) 178–187. doi:10.1016/j.jpowsour.2004.12.064.

[64] B. Fang, N.K. Chaudhari, M.-S. Kim, J.H. Kim, J.-S. Yu, Homogeneous Deposition of Platinum Nanoparticles on Carbon Black for Proton Exchange Membrane Fuel Cell, J. Am. Chem. Soc. 131 (2009) 15330–15338. doi:10.1021/ja905749e.

[65] K. Yasuda, Y. Nishimura, The deposition of ultrafine platinum particles on carbon black by surface ion exchange - Increase in loading amount, Mater. Chem. Phys. 82 (2003) 921–928. doi:10.1016/j.matchemphys.2003.08.020.

[66] J. Perez, E.R. Gonzalez, E.A. Ticianelli, Oxygen electrocatalysis on thin porous coating rotating platinum electrodes, Electrochim. Acta. 44 (1998) 1329–1339. doi:10.1016/S0013-4686(98)00255-2.

[67] V. Grozovski, H. Kasuk, J. Nerut, E. Härk, R. Jäger, I. Tallo, E. Lust, Oxygen Reduction at Shape-Controlled Platinum Nanoparticles and Composite Catalysts Based on (100)Pt Nanocubes on Microporous-Mesoporous Carbon Supports, ChemElectroChem. 2 (2015) 847–851. doi:10.1002/celc.201500021.

[68] E. Antolini, E.R. Gonzalez, Carbon supports for low-temperature fuel cell catalysts, Appl. Catal. B Gen. 88 (2009) 1–24. doi:10.1016/j.apcata.2009.05.045.

[69] P. Trogadas, T.F. Fuller, P. Strasser, Carbon as catalyst and support for electrochemical energy conversion, Carbon,. 75 (2014) 5–42. doi:10.1016/j.carbon.2014.04.005.

[70] N. Seselj, C. Engelbrekt, J. Zhang, Graphene-supported platinum catalysts for fuel cells, Sci. Bull. 60 (2015) 864–876. doi:10.1007/s11434-015-0745-8.

[71] B. Seger, P. V Kamat, Electrocatalytically Active Graphene-Platinum Nanocomposites . Role of 2-D Carbon Support in PEM Fuel Cells, J. Phys. Chem. C. 113 (2009) 7990–7995. doi:10.1021/jp900360k.

[72] A. Marinkas, F. Arena, J. Mitzel, G.M. Prinz, A. Heinzel, V. Peinecke, H. Natter, Graphene as catalyst support: The influences of carbon additives and catalyst preparation methods on the performance of PEM fuel cells, Carbon,. 58 (2013) 139–150. doi:10.1016/j.carbon.2013.02.043.

[73] M.H. Seo, S.M. Choi, J.K. Seo, S.H. Noh, W.B. Kim, B. Han, The graphene-supported palladium and palladium-yttrium nanoparticles for the oxygen reduction and ethanol oxidation reactions: Experimental measurement and computational validation, Appl. Catal. B Environ. 129 (2013) 163–171. doi:10.1016/j.apcatb.2012.09.005.

[74] C. Mattevi, G. Eda, S. Agnoli, S. Miller, K.A. Mkhoyan, O. Celik, D. Mastrogiovanni, C. Cranozzi, E. Carfunkel, M. Chhowalla, Evolution of electrical, chemical, and structural properties of transparent and conducting chemically

derived craphene thin films, Adv. Funct. Mater. 19 (2009) 2577–2583. doi:10.1002/adfm.200900166.

[75] J. Song, X. Wang, C.-T. Chang, Preparation and characterization of graphene oxide, J. Nanomater. 2014 (2014) 1–6. doi:10.1155/2014/276143.

[76] S. Pei, H.M. Cheng, The reduction of graphene oxide, Carbon,. 50 (2012) 3210–3228. doi:10.1016/j.carbon.2011.11.010.

[77] I. Jung, D. a. Dikin, R.D. Piner, R.S. Ruoff, Tuneable Electrical Conductivity of Individual Graphene Oxide Sheets Reduced at “Low” Temperatures, Nano Lett. 8 (2008) 4283–4287.

[78] D.R. Dreyer, S. Park, C.W. Bielawski, R.S. Ruoff, The chemistry of graphene oxide., Chem. Soc. Rev. 39 (2010) 228–240. doi:10.1039/b920539j.

[79] E.J. Lim, S.M. Choi, M.H. Seo, Y. Kim, S. Lee, W.B. Kim, Highly dispersed Ag nanoparticles on nanosheets of reduced graphene oxide for oxygen reduction reaction in alkaline media, Electrochem. Commun. 28 (2013) 100–103. doi:10.1016/j.elecom.2012.12.016.

[80] A. Ambrosi, A. Bonanni, Z. Sofer, J.S. Cross, M. Pumera, Electrochemistry at chemically modified graphenes, Chem. - A Eur. J. 17 (2011) 10763–10770. doi:10.1002/chem.201101117.

[81] M.J. Fernández-Merino, L. Guardia, J.I. Paredes, S. Villar-Rodil, P. Solís-Fernández, a. Martínez-Alonso, J.M.D. Tascón, Vitamin C is an ideal substitute for hydrazine in the reduction of graphene oxide suspensions, J. Phys. Chem. C. 114 (2010) 6426–6432. doi:10.1021/jp100603h.

[82] C. Jiménez-Cervantes, Edgar; López-Barroso, Juventino; Martínez-Hernández, Ana Laura; Velasco-Santos, Recent advances in graphene research, Intech, 2016.

[83] L. Tao, Q. Wang, S. Dou, Z. Ma, J. Huo, S. Wang, L. Dai, Edge-rich and dopant-free graphene as a highly efficient metal-free electrocatalyst for the oxygen reduction reaction, Chem. Commun. 52 (2016) 2764–2767. doi:10.1039/c5cc09173j.

[84] X. Gao, J. Jang, S. Nagase, Hydrazine and Thermal Reduction of Graphene Oxide : Reaction Mechanisms and Design, J. Phys. Chem. C. 114 (2010) 832–842. doi:10.1021/jp909284g.

[85] M.D. Stoller, S. Park, Y. Zhu, J. An, R.S. Ruoff, Graphene-Based Ultracapacitors, Nano Lett. 8 (2008) 3498–3502. doi:10.1021/nl802558y.

[86] L. Tammeveski, H. Erikson, A. Sarapuu, J. Kozlova, P. Ritslaid, V. Sammelselg, K. Tammeveski, Electrocatalytic oxygen reduction on silver nanoparticle/multi-walled carbon nanotube modified glassy carbon electrodes in alkaline solution, Electrochem. Commun. 20 (2012) 15–18. doi:10.1016/j.elecom.2012.04.003.

[87] Y.W. Ma, Z.R. Liu, B.L. Wang, L. Zhu, J.P. Yang, X.A. Li, Preparation of

graphene-supported Pt-Co nanoparticles and their use in oxygen reduction reactions, Xinxing Tan Cailiao/New Carbon Mater. 27 (2012) 250–257. doi:10.1016/S1872-5805(12)60016-X.

[88] M. Zhang, Y. Yan, K. Gong, L. Mao, Z. Guo, Y. Chen, Electrostatic layer-by-layer assembled carbon nanotube multilayer film and its electrocatalytic activity for O 2 reduction, Langmuir. 20 (2004) 8781–8785. doi:10.1021/la0489231.

[89] L. Wang, M. Pumera, Residual metallic impurities within carbon nanotubes play a dominant role in supposedly “metal-free” oxygen reduction reactions, Chem. Commun. 50 (2014) 12662–12664. doi:10.1039/C4CC03271C.

[90] A. Choudhary, Veena; Gupta, Polymer/Carbon Nanotube Nanocomposites, Carbon Nanotubes - Polymer Nanocomposites, 2011. doi:10.5772/711.

[91] J.M. Chem, J. Prasek, J. Drbohlavova, J. Chomoucka, J. Hubalek, O. Jasek, R. Kizek, Methods for carbon nanotubes synthesis — review, (2011) 15872–15884. doi:10.1039/c1jm12254a.

[92] R.H. Baughman, Carbon Nanotubes — the Route Toward, Science (80-.). 297 (2002) 787–792. doi:10.1126/science.1060928.

[93] M. Kumar, Y. Ando, Chemical Vapor Deposition of Carbon Nanotubes : A Review on Growth Mechanism and Mass Production, 10 (2010) 3739–3758. doi:10.1166/jnn.2010.2939.

[94] A.L. Kalamkarov, A. V. Georgiades, S.K. Rokkam, V.P. Veedu, M.N. Ghasemi-Nejhad, Analytical and numerical techniques to predict carbon nanotubes properties, Int. J. Solids Struct. 43 (2006) 6832–6854. doi:10.1016/j.ijsolstr.2006.02.009.

[95] L. Dai, J. Shui, Zigzag carbon as efficient and stable oxygen reduction electrocatalyst for proton exchange membrane fuel cells, Nat. Commun. (n.d.) 2–9. doi:10.1038/s41467-018-06279-x.

[96] M.S. Dresselhaus, G. Dresselhaus, R. Saito, Physics of carbon nanotubes, Carbon N. Y. 33 (1995) 883–891. doi:10.1016/0008-6223(95)00017-8.

[97] A. Dumitru, M. Mamlouk, K. Scott, Effect of different chemical modification of carbon nanotubes for the oxygen reduction reaction in alkaline media, Electrochim. Acta. 135 (2014) 428–438. doi:10.1016/j.electacta.2014.04.123.

[98] K. Lee, J. Zhang, H. Wang, D.P. Wilkinson, Progress in the synthesis of carbon nanotube- and nanofiber-supported Pt electrocatalysts for PEM fuel cell catalysis, J. Appl. Electrochem. 36 (2006) 507–522. doi:10.1007/s10800-006-9120-4.

[99] Y. Sha, T.H. Yu, B. V. Merinov, P. Shirvanian, W. a. Goddard, Mechanism for Oxygen Reduction Reaction on Pt_3Ni Alloy Fuel Cell Cathode, J. Phys. Chem. C. 116 (2012) 21334–21342. doi:10.1021/jp303966u.

[100] K. Shimizu, L. Sepunaru, R.G. Compton, Innovative catalyst design for the

oxygen reduction reaction for fuel cells, Chem. Sci. 7 (2016) 3364–3369. doi:10.1039/C6SC00139D.

[101] C. Huang, C. Li, G. Shi, Graphene based catalysts, Energy Environ. Sci. 5 (2012) 8848–8868. doi:10.1039/c2ee22238h.

[102] X. Li, H. Wang, J.T. Robinson, H. Sanchez, G. Diankov, H. Dai, Simultaneous nitrogen doping and reduction of graphene oxide, J. Am. Chem. Soc. 131 (2009) 15939–15944. doi:10.1021/ja907098f.

[103] L. Qu, Y. Liu, J.-B. Baek, L. Dai, Nitrogen-doped Graphene as Efficient Metal-Free Electrocatalyst for Oxygen Reduction in Fuel Cells, ACS Nano. 4 (2010) 1321–1326. doi:10.1039/c3ra22161j.

[104] D. Higgins, Z. Chen, D.U. Lee, Z. Chen, Activated and nitrogen-doped exfoliated graphene as air electrodes for metal–air battery applications, J. Mater. Chem. A. 1 (2013) 2639–2645. doi:10.1039/c2ta00944g.

[105] T.N. Huan, T. Van Khai, Y. Kang, K.B. Shim, H. Chung, Enhancement of quaternary nitrogen doping of graphene oxide via chemical reduction prior to thermal annealing and an investigation of its electrochemical properties, J. Mater. Chem. 22 (2012) 14756–14762. doi:10.1039/c2jm31158e.

[106] L. Lai, J.R. Potts, D. Zhan, L. Wang, C.K. Poh, C. Tang, H. Gong, Z. Shen, J. Lin, R.S. Ruoff, Exploration of the active center structure of nitrogen-doped graphene-based catalysts for oxygen reduction reaction, Energy Environ. Sci. 5 (2012) 7936–7942. doi:10.1039/c2ee21802j.

[107] H. Wang, M. Xie, L. Thia, A. Fisher, X. Wang, Strategies on the Design of Nitrogen-Doped Graphene, J. Phys. Chem. Lett. 5 (2014) 119–125. doi:10.1021/jz402416a.

[108] R. Vishwakarma, G. Kalita, S.M. Shinde, Y. Yaakob, C. Takahashi, M. Tanemura, Structure of nitrogen-doped graphene synthesized by combination of imidazole and melamine solid precursors, Mater. Lett. 177 (2016) 89–93. doi:10.1016/j.matlet.2016.04.155.

[109] Y.A. Kim, K. Fujisawa, H. Muramatsu, T. Hayashi, M. Endo, T. Fujimori, K. Kaneko, M. Terrones, J. Behrends, A. Eckmann, C. Casiraghi, K.S. Novoselov, R. Saito, M.S. Dresselhaus, Raman spectroscopy of boron-doped single-layer graphene, ACS Nano. 6 (2012) 6293–6300. doi:10.1021/nn301728j.

[110] D.-Y. Yeom, W. Jeon, N.D.K. Tu, S.Y. Yeo, S.-S. Lee, B.J. Sung, H. Chang, J.A. Lim, H. Kim, High-concentration boron doping of graphene nanoplatelets by simple thermal annealing and their supercapacitive properties, Sci. Rep. 5 (2015) 9817. doi:10.1038/srep09817.

[111] S. Agnoli, M. Favaro, Doping graphene with boron: a review of synthesis methods, physicochemical characterization, and emerging applications, J. Mater. Chem. A. 4 (2016) 5002–5025. doi:10.1039/C5TA10599D.

[112] L. Niu, Z. Li, W. Hong, J. Sun, Z. Wang, L. Ma, J. Wang, S. Yang, Pyrolytic synthesis of boron-doped graphene and its application aselectrode material for supercapacitors, Electrochim. Acta. 108 (2013) 666–673. doi:10.1016/j.electacta.2013.07.025.

[113] V. Thirumal, A. Pandurangan, R. Jayavel, R. Ilangovan, Synthesis and characterization of boron doped graphene nanosheets for supercapacitor applications, Synth. Met. 220 (2016) 524–532. doi:10.1016/j.synthmet.2016.07.011.

[114] Z.W. Liu, F. Peng, H.J. Wang, H. Yu, W.X. Zheng, J. Yang, Phosphorus-doped graphite layers with high electrocatalytic activity for the O_2 reduction in an alkaline medium, Angew. Chemie - Int. Ed. 50 (2011) 3257–3261. doi:10.1002/anie.201006768.

[115] C. Zhang, N. Mahmood, H. Yin, F. Liu, Y. Hou, Synthesis of phosphorus-doped graphene and its multifunctional applications for oxygen reduction reaction and lithium ion batteries, Adv. Mater. 25 (2013) 4932–4937. doi:10.1002/adma.201301870.

[116] J. Wu, C. Jin, Z. Yang, J. Tian, R. Yang, Synthesis of phosphorus-doped carbon hollow spheres as efficient metal-free electrocatalysts for oxygen reduction, Carbon N. Y. 82 (2015) 562–571. doi:10.1016/j.carbon.2014.11.008.

[117] L. Zhang, J. Niu, M. Li, Z. Xia, Catalytic mechanisms of sulfur-doped graphene as efficient oxygen reduction reaction catalysts for fuel cells, J. Phys. Chem. C. 118 (2014) 3545–3553. doi:10.1021/jp410501u.

[118] M. Klingele, C. Pham, K.R. Vuyyuru, B. Britton, S. Holdcroft, A. Fischer, S. Thiele, Sulfur doped reduced graphene oxide as metal-free catalyst for the oxygen reduction reaction in anion and proton exchange fuel cells, Electrochem. Commun. 77 (2017) 71–75. doi:10.1016/j.elecom.2017.02.015.

[119] Z. Yang, Z. Yao, G. Li, G. Fang, H. Nie, Z. Liu, X. Zhou, X. Chen, S. Huang, Sulfur-Doped Graphene as an E ffi cient Metal-free Cathode Catalyst for, ACS Nano. 6 (2012) 205–211. doi:10.1021/nn203393d.

[120] Z. Ma, S. Dou, A. Shen, L. Tao, L. Dai, S. Wang, Sulfur-doped graphene derived from cycled lithium-sulfur batteries as a metal-free electrocatalyst for the oxygen reduction reaction, Angew. Chemie - Int. Ed. 54 (2015) 1888–1892. doi:10.1002/anie.201410258.

[121] F. Razmjooei, K.P. Singh, D.-S. Yang, W. Cui, Y.H. Jang, J.-S. Yu, Fe-Treated Heteroatom (S/N/B/P)-Doped Graphene Electrocatalysts for Water Oxidation, ACS Catal. 7 (2017) 2381–2391. doi:10.1021/acscatal.6b03291.

[122] E.H. Yu, X. Wang, U. Krewer, L. Li, K. Scott, Direct oxidation alkaline fuel cells: from materials to systems, Energy Environ. Sci. 5 (2012) 5668. doi:10.1039/c2ee02552c.

[123] X. Wang, G. Sun, P. Routh, D.-H. Kim, W. Huang, P. Chen, Heteroatom-doped

graphene materials: syntheses, properties and applications, Chem. Soc. Rev. 43 (2014) 7067–7098. doi:10.1039/C4CS00141A.

[124] H. Zhao, K.S. Hui, K.N. Hui, Synthesis of nitrogen-doped multilayer graphene from milk powder with melamine and their application to fuel cells, Carbon,. 76 (2014) 1–9. doi:10.1016/j.carbon.2014.04.007.

[125] D. Long, W. Li, L. Ling, J. Miyawaki, I. Mochida, S.H. Yoon, Preparation of nitrogen-doped graphene sheets by a combined chemical and hydrothermal reduction of graphene oxide, Langmuir. 26 (2010) 16096–16102. doi:10.1021/la102425a.

[126] Y. Gong, H. Fei, X. Zou, W. Zhou, S. Yang, G. Ye, Z. Liu, P.M. Ajayan, Boron- and Nitrogen-Substituted Graphene Nanoribbons as Efficient Catalysts for Oxygen Reduction Reaction, Chem. Mater. 27 (2015) 1181–1186. doi:10.1021/cm5037502.

[127] X. Ma, G. Ning, C. Qi, C. Xu, J. Gao, Phosphorus and Nitrogen Dual-Doped Few-Layered Porous Graphene : A High-Performance Anode Material for Lithium-Ion Batteries, (2014).

[128] J. Liang, Y. Jiao, M. Jaroniec, S.Z. Qiao, Sulfur and nitrogen dual-doped mesoporous graphene electrocatalyst for oxygen reduction with synergistically enhanced performance, Angew. Chemie - Int. Ed. 51 (2012) 11496–11500. doi:10.1002/anie.201206720.

[129] H.S. Kim, S.S. Kim, H.S. Kim, Y. Kim, Anomalous transport properties in boron and phosphorus co-doped armchair graphene nanoribbons, (n.d.).

[130] F. Razmjooei, K.P. Singh, M.Y. Song, J.S. Yu, Enhanced electrocatalytic activity due to additional phosphorous doping in nitrogen and sulfur-doped graphene: A comprehensive study, Carbon,. 78 (2014) 257–267. doi:10.1016/j.carbon.2014.07.002.

[131] X. Yu, Y. Kang, H.S. Park, Sulfur and phosphorus co-doping of hierarchically porous graphene aerogels for enhancing supercapacitor performance, Carbon,. 101 (2016) 49–56. doi:10.1016/j.carbon.2016.01.073.

[132] J. Zhang, L. Dai, Nitrogen, Phosphorus, and Fluorine Tri-doped Graphene as a Multifunctional Catalyst for Self-Powered Electrochemical Water Splitting, Angew. Chemie - Int. Ed. 55 (2016) 13296–13300. doi:10.1002/anie.201607405.

[133] L. Tsetseris, S.T. Pantelides, Graphene: An impermeable or selectively permeable membrane for atomic species?, Carbon,. 67 (2014) 58–63. doi:10.1016/j.carbon.2013.09.055.

[134] L.S. Panchakarla, K.S. Subrahmanyam, S.K. Saha, A. Govindaraj, H.R. Krishnamurthy, U. V. Waghmare, C.N.R. Rao, Synthesis, structure, and properties of boron- and nitrogen-doped graphene, Adv. Mater. 21 (2009) 4726–4730. doi:10.1002/adma.200901285.

[135] Z. Tian, C. Xu, J. Li, G. Zhu, J. Wu, Z. Shi, Y. Wang, A facile preparation route for highly conductive borate cross-linked reduced graphene oxide paper, New J. Chem. 39 (2015) 6907–6913. doi:10.1039/C5NJ00906E.

[136] S.M. Jung, E.K. Lee, M. Choi, D. Shin, I.Y. Jeon, J.M. Seo, H.Y. Jeong, N. Park, J.H. Oh, J.B. Baek, Direct solvothermal synthesis of B/N-doped graphene, Angew. Chemie - Int. Ed. 53 (2014) 2398–2401. doi:10.1002/anie.201310260.

[137] N.G. Overzmyradov, M.; Magedov, I. V.; Frolova, L. V.; Chandler, G.; Garcia, J.; Bethke, D.; Shaner, E. A.; Kalugin, Chemical Vapor Deposition of Phosphorous- and Boron-Doped Graphene Using Phenyl-Containing Molecules, J. Nanosci. Nanotechnol. 15 (2015) 4883.

[138] H. Fang, C. Yu, T. Ma, J. Qiu, Boron-doped graphene as a high-efficiency counter electrode for dye-sensitized solar cells, Chem. Commun. 50 (2014) 3328. doi:10.1039/c3cc48258h.

[139] Z.H. Sheng, H.L. Gao, W.J. Bao, F. Bin Wang, X.H. Xia, Synthesis of boron doped graphene for oxygen reduction reaction in fuel cells, J. Mater. Chem. 22 (2012) 390–395. doi:10.1039/C1JM14694G.

[140] W. Norimatsu, K. Hirata, Y. Yamamoto, S. Arai, M. Kusunoki, Epitaxial growth of boron-doped graphene by thermal decomposition of B 4C, J. Phys. Condens. Matter. 24 (2012). doi:10.1088/0953-8984/24/31/314207.

[141] Z.S. Wu, W. Ren, L. Xu, F. Li, H.M. Cheng, Doped graphene sheets as anode materials with superhigh rate and large capacity for lithium ion batteries, ACS Nano. 5 (2011) 5463–5471. doi:10.1021/nn2006249.

[142] B.R. Sathe, X. Zou, T. Asefa, Metal-free B-doped graphene with efficient electrocatalytic activity for hydrogen evolution reaction, Catal. Sci. Technol. 4 (2014) 2023–2030. doi:10.1039/C4CY00075G.

[143] J. Sanetuntikul, S. Shanmugam, High Pressure Pyrolyzed Non-precious Oxygen Reduction Catalysts for Alkaline Polymer Electrolyte Membrane Fuel Cells, Nanoscale. (2015) 7644–7650. doi:10.1039/C5NR00311C.

[144] D.Y. Usachov, A. V Fedorov, A.E. Petukhov, O.Y. Vilkov, A.G. Rybkin, M.M. Otrokov, A. Arnau, E. V Chulkov, L. V Yashina, M. Farjam, V.K. Adamchuk, B. V Senkovskiy, C. Laubschat, D. V Vyalikh, Epitaxial B-Graphene: Large-Scale Growth and Atomic Structure, ACS Nano. 9 (2015) 7314–7322. doi:10.1021/acsnano.5b02322.

[145] M. Cattelan, S. Agnoli, M. Favaro, D. Garoli, F. Romanato, M. Meneghetti, A. Barinov, P. Dudin, G. Granozzi, Microscopic view on a chemical vapor deposition route to boron-doped graphene nanostructures, Chem. Mater. 25 (2013) 1490–1495. doi:10.1021/cm302819b.

[146] L. Yang, S. Jiang, Y. Zhao, L. Zhu, S. Chen, X. Wang, Q. Wu, J. Ma, Y. Ma, Z. Hu, Boron-doped carbon nanotubes as metal-free electrocatalysts for the oxygen reduction reaction, Angew. Chemie - Int. Ed. 50 (2011) 7132–7135.

doi:10.1002/anie.201101287.

[147] Z.-H. Sheng, H.-L. Gao, W.-J. Bao, F.-B. Wang, X.-H. Xia, Synthesis of boron doped graphene for oxygen reduction reaction in fuel cells, J. Mater. Chem. 22 (2012) 390–395. doi:10.1039/C1JM14694G.

[148] W. Shen, W. Fan, Nitrogen-containing porous carbons: synthesis and application, J. Mater. Chem. A. 1 (2013) 999–1013. doi:10.1039/C2TA00028H.

[149] D. Wei, Y. Liu, Y. Wang, H. Zhang, L. Huang, G. Yu, Synthesis of N-doped graphene by chemical vapor deposition and its electrical properties., Nano Lett, (2009).

[150] C. Zhang, L. Fu, N. Liu, M. Liu, Y. Wang, Z. Liu, Synthesis of nitrogen-doped graphene using embedded carbon and nitrogen sources, Adv. Mater. 23 (2011) 1020–1024. doi:10.1002/adma.201004110.

[151] D. Deng, X. Pan, L. Yu, Y. Cui, Y. Jiang, J. Qi, W.X. Li, Q. Fu, X. Ma, Q. Xue, G. Sun, X. Bao, Toward N-doped graphene via solvothermal synthesis, Chem. Mater. 23 (2011) 1188–1193. doi:10.1021/cm102666r.

[152] B. Guo, Q. Liu, E. Chen, H. Zhu, L. Fang, J.R. Gong, Controllable N-doping of graphene, Nano Lett. 10 (2010) 4975–4980. doi:10.1021/nl103079j.

[153] H. Wang, T. Maiyalagan, X. Wang, Review on recent progress in nitrogen-doped graphene: Synthesis, characterization, and its potential applications, ACS Catal. 2 (2012) 781–794. doi:10.1021/cs200652y.

[154] H.M. Jeong, J.W. Lee, W.H. Shin, Y.J. Choi, H.J. Shin, J.K. Kang, J.W. Choi, Nitrogen-doped graphene for high-performance ultracapacitors and the importance of nitrogen-doped sites at basal planes, Nano Lett. 11 (2011) 2472–2477. doi:10.1021/nl2009058.

[155] S. Hou, X. Cai, H. Wu, X. Yu, M. Peng, K. Yan, D. Zou, Nitrogen-doped graphene for dye-sensitized solar cells and the role of nitrogen states in triiodide reduction, Energy Environ. Sci. 6 (2013) 3356–3362. doi:10.1039/c3ee42516a.

[156] Z. Xing, Z. Ju, Y. Zhao, J. Wan, Y. Zhu, Y. Qiang, Y. Qian, One-pot hydrothermal synthesis of Nitrogen-doped graphene as high-performance anode materials for lithium ion batteries, Sci. Rep. 6 (2016) 1–10. doi:10.1038/srep26146.

[157] J.I. Aihara, Reduced HOMO-LUMO Gap as an Index of Kinetic Stability for Polycyclic Aromatic Hydrocarbons, J. Phys. Chem. A. 103 (1999) 7487–7495. doi:10.1021/jp990092i.

[158] L. Zhang, Z. Xia, Mechanisms of oxygen reduction reaction on nitrogen-doped graphene for fuel cells, J. Phys. Chem. C. 115 (2011) 11170–11176. doi:10.1021/jp201991j.

[159] P. Wang, Z. Wang, L. Jia, Z. Xiao, Origin of the catalytic activity of graphite nitride for the electrochemical reduction of oxygen: geometric factors vs. electronic factors, Phys. Chem. Chem. Phys. 11 (2009) 2730. doi:10.1039/b818408a.

[160] D.S. Yang, D. Bhattacharjya, S. Inamdar, J. Park, J.S. Yu, Phosphorus-doped ordered mesoporous carbons with different lengths as efficient metal-free electrocatalysts for oxygen reduction reaction in alkaline media, J. Am. Chem. Soc. 134 (2012) 16127–16130. doi:10.1021/ja306376s.

[161] J.C. Han, A.P. Liu, J.Q. Zhu, M.L. Tan, H.P. Wu, Effect of phosphorus content on structural properties of phosphorus incorporated tetrahedral amorphous carbon films, Appl. Phys. A. 88 (2007) 341–345. doi:10.1007/s00339-007-3938-4.

[162] M. Shumba, T. Nyokong, Development of nanocomposites of phosphorus-nitrogen co-doped graphene oxide nanosheets and nanosized cobalt phthalocyanines for electrocatalysis, Electrochim. Acta. 213 (2016) 529–539. doi:10.1016/j.electacta.2016.07.079.

[163] R. Li, Z. Wei, X. Gou, Nitrogen and Phosphorus Dual-Doped Graphene/Carbon Nanosheets as Bifunctional Electrocatalysts for Oxygen Reduction and Evolution, ACS Catal. 5 (2015) 4133–4142. doi:10.1021/acscatal.5b00601.

[164] C. Yu, Z. Liu, X. Meng, B. Lu, D. Cui, J. Qiu, Nitrogen and phosphorus dual-doped graphene as a metal-free high-efficiency electrocatalyst for triiodide reduction, Nanoscale. 8 (2016) 17458–17464. doi:10.1039/C6NR00839A.

[165] X. Qiao, S. Liao, C. You, R. Chen, Phosphorus and Nitrogen Dual Doped and Simultaneously Reduced Graphene Oxide with High Surface Area as Efficient Metal-Free Electrocatalyst for Oxygen Reduction, Catalysts. 5 (2015) 981–991. doi:10.3390/catal5020981.

[166] H. Lin, L. Chu, X. Wang, Z. Yao, F. Liu, Y. Ai, X. Zhuang, S. Han, Boron, nitrogen, and phosphorous ternary doped graphene aerogel with hierarchically porous structures as highly efficient electrocatalysts for oxygen reduction reaction, New J. Chem. 40 (2016) 6022–6029. doi:10.1039/C5NJ03390J.

[167] J. Wu, X. Zheng, C. Jin, J. Tian, R. Yang, Ternary doping of phosphorus, nitrogen, and sulfur into porous carbon for enhancing electrocatalytic oxygen reduction, Carbon,. 92 (2015) 327–338. doi:10.1016/j.carbon.2015.05.013.

[168] P.A. Denis, Band gap opening of monolayer and bilayer graphene doped with aluminium, silicon, phosphorus, and sulfur, Chem. Phys. Lett. 492 (2010) 251–257. doi:10.1016/j.cplett.2010.04.038.

[169] V. V. Strelko, V.S. Kuts, P.A. Thrower, On the mechanism of possible influence of heteroatoms of nitrogen, boron and phosphorus in a carbon matrix on the catalytic activity of carbons in electron transfer reactions, Carbon,. 38 (2000) 1499–1503. doi:10.1016/S0008-6223(00)00121-4.

[170] S. Some, J. Kim, K. Lee, A. Kulkarni, Y. Yoon, S. Lee, T. Kim, H. Lee, Highly air-stable phosphorus-doped n-type graphene field-effect transistors, Adv. Mater. 24 (2012) 5481–5486. doi:10.1002/adma.201202255.

[171] O. El Zubir, I. Barlow, G.J. Leggett, N.H. Williams, Fabrication of molecular

nanopatterns at aluminium oxide surfaces by nanoshaving of self-assembled monolayers of alkylphosphonates, Nanoscale. 5 (2013) 11125–11131. doi:10.1039/c3nr04701f.

[172] C. Wang, L. Sun, Y. Zhou, P. Wan, X. Zhang, J. Qiu, P/N co-doped microporous carbons from H_3PO_4-doped polyaniline by in situ activation for supercapacitors, Carbon,. 59 (2013) 537–546. doi:10.1016/j.carbon.2013.03.052.

[173] J.P. Paraknowitsch, Y. Zhang, B. Wienert, A. Thomas, Nitrogen- and phosphorus-co-doped carbons with tunable enhanced surface areas promoted by the doping additives, Chem. Commun. 49 (2013) 1208–1210. doi:10.1039/c2cc37398j.

[174] J.P. Paraknowitsch, A. Thomas, J. Schmidt, Microporous sulfur-doped carbon from thienyl-based polymer network precursors., Chem. Commun. (Camb). 47 (2011) 8283–5. doi:10.1039/c1cc12272j.

[175] C. Chen, W. Fan, Q. Zhang, X. Fu, H. Wu, One-step hydrothermal synthesis of nitrogen and sulfur co-doped graphene for supercapacitors with high electrochemical capacitance performance, Ionics (Kiel). 21 (2015) 3233–3238. doi:10.1007/s11581-015-1522-z.

[176] H. Zhang, X. Liu, G. He, X. Zhang, S. Bao, W. Hu, Bioinspired synthesis of nitrogen/sulfur co-doped graphene as an efficient electrocatalyst for oxygen reduction reaction, J. Power Sources. 279 (2015) 252–258. doi:10.1016/j.jpowsour.2015.01.016.

[177] F. Pan, Y. Duan, X. Zhang, J. Zhang, A Facile Synthesis of Nitrogen/Sulfur Co-Doped Graphene for the Oxygen Reduction Reaction, ChemCatChem. 8 (2016) 163–170. doi:10.1002/cctc.201500893.

[178] Y. Su, Y. Zhang, X. Zhuang, S. Li, D. Wu, F. Zhang, X. Feng, Low-temperature synthesis of nitrogen/sulfur co-doped three-dimensional graphene frameworks as efficient metal-free electrocatalyst for oxygen reduction reaction, Carbon N. Y. 62 (2013) 296–301. doi:10.1016/j.carbon.2013.05.067.

[179] H. Gao, Z. Liu, L. Song, W. Guo, W. Gao, L. Ci, A. Rao, W. Quan, R. Vajtai, P.M. Ajayan, Synthesis of S-doped graphene by liquid precursor, Nanotechnology. 23 (2012). doi:10.1088/0957-4484/23/27/275605.

[180] A. Das, S. Pisana, B. Chakraborty, S. Piscanec, S.K. Saha, U. V. Waghmare, K.S. Novoselov, H.R. Krishnamurthy, A.K. Geim, A.C. Ferrari, A.K. Sood, Monitoring dopants by Raman scattering in an electrochemically top-gated graphene transistor, Nat. Nanotechnol. 3 (2008) 210–215. doi:10.1038/nnano.2008.67.

[181] H.W. Liang, W. Wei, Z.S. Wu, X. Feng, K. Mullen, Mesoporous metal-nitrogen-doped carbon electrocatalysts for highly efficient oxygen reduction reaction, J. Am. Chem. Soc. 135 (2013) 16002–16005. doi:10.1021/ja407552k.

[182] H. Wang, X. Bo, A. Wang, L. Guo, Cobalt doped nanoporous hollow carbon

spheres as novel non-precious metal oxygen reduction electrocatalysts, Electrochem. Commun. 36 (2013) 75–79. doi:10.1016/j.elecom.2013.09.022.

[183] M. Lefèvre, E. Proietti, F. Jaouen, J.-P. Dodelet, Iron-Based Catalysts with Improved Oxygen Reduction Activity in Polymer Electrolyte Fuel Cells, Science (80-.). 324 (2009) 71–74. doi:10.1126/science.1170051.

[184] H. Peng, Z. Mo, S. Liao, H. Liang, L. Yang, F. Luo, H. Song, Y. Zhong, B. Zhang, High Performance Fe- and N- Doped Carbon Catalyst with Graphene Structure for Oxygen Reduction, Sci. Rep. 3 (2013) 1765. doi:10.1038/srep01765.

[185] E. Yeager, Electrocatalysts for O_2 reduction, Electrochim. Acta. 29 (1984) 1527–1537. doi:10.1016/0013-4686(84)85006-9.

[186] J.D. Wiggins-Camacho, K.J. Stevenson, Mechanistic discussion of the oxygen reduction reaction at nitrogen-doped carbon nanotubes, J. Phys. Chem. C. 115 (2011) 20002–20010. doi:10.1021/jp205336w.

[187] Q. Dong, X. Zhuang, Z. Li, B. Li, B. Fang, C. Yang, H. Xie, F. Zhang, X. Feng, Efficient approach to iron/nitrogen co-doped graphene materials as efficient electrochemical catalysts for the oxygen reduction reaction, J. Mater. Chem. A. 3 (2015) 7767–7772. doi:10.1039/C5TA00556F.

[188] X.H. Yan, B.Q. Xu, Mesoporous carbon material co-doped with nitrogen and iron (Fe–N–C): high-performance cathode catalyst for oxygen reduction reaction in alkaline electrolyte, J. Mater. Chem. A. 2 (2014) 8617–8622. doi:10.1039/C3TA15300B.

[189] M. Risch, Perovskite Electrocatalysts for the Oxygen Reduction Reaction in Alkaline Media, Catalysts. 7 (2017) 154. doi:10.3390/CATAL7050154.

[190] D. Chen, C. Chen, Z. Zhang, Z.M. Baiyee, F. Ciucci, Z. Shao, Compositional engineering of perovskite oxides for highly efficient oxygen reduction reactions, ACS Appl. Mater. Interfaces. 7 (2015) 8562–8571. doi:10.1021/acsami.5b00358.

[191] D. Chen, C. Chen, Z.M. Baiyee, Z. Shao, F. Ciucci, Nonstoichiometric Oxides as Low-Cost and Highly-Efficient Oxygen Reduction/Evolution Catalysts for Low-Temperature Electrochemical Devices, Chem. Rev. 115 (2015) 9869–9921. doi:10.1021/acs.chemrev.5b00073.

[192] V.M. Goldschmidt, Die Gesetze der Krystallochemie, Naturwissenschaften. 14 (1926) 477–485. doi:10.1007/BF01507527.

[193] Y. Zhu, W. Zhou, J. Yu, Y. Chen, M. Liu, Z. Shao, Enhancing Electrocatalytic Activity of Perovskite Oxides by Tuning Cation Deficiency for Oxygen Reduction and Evolution Reactions, Chem. Mater. 28 (2016) 1691–1697. doi:10.1021/acs.chemmater.5b04457.

[194] Y. Zhu, W. Zhou, Z. Shao, Perovskite/Carbon Composites: Applications in Oxygen Electrocatalysis, Small. 13 (2017) 1603793.

doi:10.1002/smll.201603793.

[195] J. Suntivich, H. a Gasteiger, N. Yabuuchi, H. Nakanishi, J.B. Goodenough, Y. Shao-Horn, Design principles for oxygen-reduction activity on perovskite oxide catalysts for fuel cells and metal-air batteries., Nat. Chem. 3 (2011) 546–550. doi:10.1038/nchem.1069.

[196] P.P. Patel, M.K. Datta, O.I. Velikokhatnyi, R. Kuruba, Noble metal-free bifunctional oxygen evolution and oxygen reduction acidic media electro-catalysts, Sci. Rep. 6 (2016) 28367. doi:10.1038/srep28367.

[197] E. Fabbri, R. Mohamed, P. Levecque, O. Conrad, R. Kötz, T.J. Schmidt, Composite Electrode Boosts the Activity of $Ba_{0.5}Sr_{0.5}Co_{0.8}Fe_{0.2}O_{3-\delta}$ Perovskite and Carbon toward Oxygen Reduction in Alkaline Media, ACS Catal. 4 (2014) 1061–1070. doi:10.1021/cs400903k.

[198] X. Li, W. Qu, J. Zhang, H. Wang, Electrocatalytic Activities of $La_{0.6}Ca_{0.4}CoO_3$ and $La_{0.6}Ca_{0.4}CoO_3$-Carbon Composites Toward the Oxygen Reduction Reaction in Concentrated Alkaline Electrolytes, J. Electrochem. Soc. 158 (2011) A597. doi:10.1149/1.3560170.

[199] V. Hermann, D. Dutriat, S. Müller, C. Comninellis, Mechanistic studies of oxygen reduction at $La_{0.6}Ca_{0.4}CoO_3$-activated carbon electrodes in a channel flow cell, Electrochim. Acta. 46 (2000) 365–372. doi:10.1016/S0013-4686(00)00593-4.

[200] J. Hu, L. Wang, L. Shi, H. Huang, Preparation of $La_{1-x}Ca_xMnO_3$ perovskite-graphene composites as oxygen reduction reaction electrocatalyst in alkaline medium, J. Power Sources. 269 (2014) 144–151. doi:10.1016/j.jpowsour.2014.07.004.

[201] T. Poux, A. Bonnefont, G. Kéranguéven, G.A. Tsirlina, E.R. Savinova, Electrocatalytic oxygen reduction reaction on perovskite oxides: Series versus direct pathway, ChemPhysChem. 15 (2014) 2108–2120. doi:10.1002/cphc.201402022.

[202] J. Hu, L. Wang, L. Shi, H. Huang, Oxygen reduction reaction activity of $LaMn_{1-x}Co_xO_3$-graphene nanocomposite for zinc-air battery, Electrochim. Acta. 161 (2015) 115–123. doi:10.1016/j.electacta.2015.02.048.

[203] W.G. Hardin, D.A. Slanac, X. Wang, S. Dai, K.P. Johnston, K.J. Stevenson, Highly active, nonprecious metal perovskite electrocatalysts for bifunctional metal-air battery electrodes, J. Phys. Chem. Lett. 4 (2013) 1254–1259. doi:10.1021/jz400595z.

[204] J. Wang, H. Zhao, Y. Gao, D. Chen, C. Chen, M. Saccoccio, F. Ciucci, $Ba_{0.5}Sr_{0.5}Co_{0.8}Fe_{0.2}O_{3-\delta}$ on N-doped mesoporous carbon derived from organic waste as a bi-functional oxygen catalyst, Int. J. Hydrogen Energy. 41 (2016) 10744–10754. doi:10.1016/j.ijhydene.2016.04.049.

[205] H.W. Park, D.U. Lee, P. Zamani, M.H. Seo, L.F. Nazar, Z. Chen, Electrospun porous nanorod perovskite oxide/nitrogen-doped graphene composite as a bi-

functional catalyst for metal air batteries, Nano Energy. 10 (2014) 192–200. doi:10.1016/j.nanoen.2014.09.009.

[206] K. Elumeeva, J. Masa, J. Sierau, F. Tietz, M. Muhler, W. Schuhmann, Perovskite-based bifunctional electrocatalysts for oxygen evolution and oxygen reduction in alkaline electrolytes, Electrochim. Acta. 208 (2016) 25–32. doi:10.1016/j.electacta.2016.05.010.

[207] X. Ge, F.W.T. Goh, B. Li, T.S.A. Hor, J. Zhang, P. Xiao, X. Wang, Y. Zong, Z. Liu, Efficient and durable oxygen reduction and evolution of a hydrothermally synthesized $La(Co_{0.55}Mn_{0.45})_{0.99}O_{3-\delta}$ nanorod/graphene hybrid in alkaline media, Nanoscale. 7 (2015) 9046–9054. doi:10.1039/C5NR01272D.

[208] M. Prabu, P. Ramakrishnan, P. Ganesan, A. Manthiram, S. Shanmugam, $LaTi_{0.65}Fe_{0.35}O_{3-\delta}$ nanoparticle-decorated nitrogen-doped carbon nanorods as an advanced hierarchical air electrode for rechargeable metal-air batteries, Nano Energy. 15 (2015) 92–103. doi:10.1016/j.nanoen.2015.04.005.

[209] C. Kim, O. Gwon, I.-Y. Jeon, Y. Kim, J. Shin, Y.-W. Ju, J.-B. Baek, G. Kim, Cloud-like graphene nanoplatelets on Nd0.5Sr0.5CoO3−δ nanorods as an efficient bifunctional electrocatalyst for hybrid Li–air batteries, J. Mater. Chem. A. 4 (2016) 2122–2127. doi:10.1039/C5TA08493H.

[210] T. Poux, F.S. Napolskiy, T. Dintzer, G. Kéranguéven, S.Y. Istomin, G.A. Tsirlina, E. V. Antipov, E.R. Savinova, Dual role of carbon in the catalytic layers of perovskite/carbon composites for the electrocatalytic oxygen reduction reaction, Catal. Today. 189 (2012) 83–92. doi:10.1016/j.cattod.2012.04.046.

[211] J.P. Coats, A. W.; Redfern, Thermogravimetric Analysis: A review, Analyst. 88 (1963) 906–924. doi:10.1039/AN9638800906.

[212] Thermogravimetric Analysis: A Begginers Guide, PerkinElmer. (2010). https://www.perkinelmer.com/CMSResources/Images/44-74556GDE_TGABeginnersGuide.pdf (accessed April 12, 2018).

[213] M.W. Spring, Kenneth R.; Davidson, Depth of Field and Depth of Focus, Microsc. U. (2018). https://www.microscopyu.com/microscopy-basics/depth-of-field-and-depth-of-focus (accessed April 12, 2018).

[214] Microscopy, John Innes Cent. (n.d.). https://www.jic.ac.uk/microscopy/intro_EM.html (accessed April 9, 2018).

[215] K. Matsutani, K. Hayakawa, T. Tada, Effect of particle size of platinum and platinum-cobalt catalysts on stability against load cycling: Towards the development of high performance, stable fuel cell catalysts with low platinum loadings, Platin. Met. Rev. 54 (2010) 223–232. doi:10.1595/147106710X523698.

[216] A. La Torre, Introduction to Energy Dispersive X-Ray Spectrometry (EDS), Science (80-.). 3 (2017) 2300–2340. doi:http://dx.doi.org/10.1590/S0104-66322011000100011.

[217] K.S. Walton, R.Q. Snurr, Applicability of the BET method for determining surface areas of microporous metal-organic frameworks, J. Am. Chem. Soc. 129 (2007) 8552–8556. doi:10.1021/ja071174k.

[218] Y.H. Tan, J.A. Davis, K. Fujikawa, N.V. Ganesh, A. V Demchenko, K.J. Stine, Surface area and pore size characteristics of nanoporous gold subjected to thermal{,} mechanical{,} or surface modification studied using gas adsorption isotherms{,} cyclic voltammetry{,} thermogravimetric analysis{,} and scanning electron microscopy, J. Mater. Chem. 22 (2012) 6733–6745. doi:10.1039/C2JM16633J.

[219] K.S.W. Sing, Reporting physisorption data for gas/solid systems with special reference to the determination of surface area and porosity (Recommendations 1984), Pure Appl. Chem. 57 (1985) 603–619. doi:10.1351/pac198557040603.

[220] M. Khalfaoui, S. Knani, M.A. Hachicha, A. Ben Lamine, New theoretical expressions for the five adsorption type isotherms classified by BET based on statistical physics treatment, J. Colloid Interface Sci. 263 (2003) 350–356. doi:10.1016/S0021-9797(03)00139-5.

[221] E.P. Barrett, L.G. Joyner, P.P. Halenda, The Determination of Pore Volume and Area Distributions in Porous Substances. I. Computations from Nitrogen Isotherms, J. Am. Chem. Soc. 73 (1951) 373–380. doi:10.1021/ja01145a126.

[222] O. Faix, Fourier Transform Infrared Spectroscopy, in: S.Y. Lin, C.W. Dence (Eds.), Methods Lignin Chem., Springer Berlin Heidelberg, Berlin, Heidelberg, 1992: pp. 83–109. doi:10.1007/978-3-642-74065-7_7.

[223] Infra-red Absorption Spectroscopy, Sheff. Hallam Univ. (n.d.). http://teaching.shu.ac.uk/hwb/chemistry/tutorials/molspec/irspec1.htm (accessed April 6, 2018).

[224] X-Ray Fluorescence, Sci. Educ. Resour. Cent. Carlet. Coll. (n.d.). https://serc.carleton.edu/research_education/geochemsheets/techniques/XRF.html (accessed April 3, 2018).

[225] M. Planck, On the law of the energy distribution in the normal spectrum, Ann. Phys. 4 (1901) 1–11. doi:10.1002/andp.19013090310.

[226] R. Sitko, P. Janik, B. Zawisza, E. Talik, E. Margui, I. Queralt, Green Approach for Ultratrace Determination of Divalent Metal Ions and Arsenic Species Using Total-Reflection X-ray Fluorescence Spectrometry and Mercapto-Modified Graphene Oxide Nanosheets as a Novel Adsorbent, Anal. Chem. 87 (2015) 3535–3542. doi:10.1021/acs.analchem.5b00283.

[227] P. Ewald, The Principles of X-ray Diffraction, Fifty Years X-Ray Diffr. (1962) 82–101. doi:10.1007/978-1-4615-9961-6_6.

[228] Veqter, X-ray Diffraction, (2018). http://www.veqter.co.uk/residual-stress-measurement/x-ray-diffraction (accessed April 11, 2018).

[229] G. Wang, J. Yang, J. Park, X. Gou, B. Wang, H. Liu, J. Yao, Facile synthesis and characterization of graphene nanosheets, Phys. Chem C. 112 (2008) 8192–8195. doi:10.1021/jp710931h.

[230] Z. Sheng, L. Shao, J. Chen, W. Bao, F. Wang, X. Xia, Catalyst-Free Synthesis of Nitrogen-Doped Graphene via Thermal Annealing Graphite Oxide with Melamine and Its Excellent Electrocatalysis, ACS Nano. 5 (2011) 4350–4358. doi:10.1021/nn103584t.

[231] S. Devanarayanan, RAMAN SPECTROSCOPY – FUNDAMENTALS, Trivandrum (India), 2015. doi:10.13140/RG.2.1.5182.2243.

[232] Z. Zafar, Z.H. Ni, X. Wu, Z.X. Shi, H.Y. Nan, J. Bai, L.T. Sun, Evolution of Raman spectra in nitrogen doped graphene, Carbon,. 61 (2013) 57–62. doi:10.1016/j.carbon.2013.04.065.

[233] Nobelpirze.org, The Nobel Prize in Physics 1921, (n.d.). https://www.nobelprize.org/nobel_prizes/physics/laureates/1921/ (accessed April 12, 2018).

[234] M.C. Biesinger, X-Ray Photoelectron Spectroscopy (XPS) Reference Pages, (n.d.). http://www.xpsfitting.com/2008/09/xps-fundamentals.html (accessed April 8, 2018).

[235] Theory of X-Ray Photoelectron Spectroscopy, CoreTech Integr. Ltd. (n.d.). http://www.coretechint.com/technical_info-xps.php (accessed April 5, 2018).

[236] XPS Applications, Thermo Fish. Sci. Inc. (2013). https://xpssimplified.com/applications.php (accessed April 12, 2018).

[237] N. Wakabayashi, M. Takeichi, M. Itagaki, H. Uchida, M. Watanabe, Temperature-dependence of oxygen reduction activity at a platinum electrode in an acidic electrolyte solution investigated with a channel flow double electrode, J. Electroanal. Chem. 574 (2005) 339–346. doi:10.1016/j.jelechem.2004.08.013.

[238] N. Elgrishi, K.J. Rountree, B.D. McCarthy, E.S. Rountree, T.T. Eisenhart, J.L. Dempsey, A Practical Beginner’s Guide to Cyclic Voltammetry, J. Chem. Educ. 95 (2018) 197–206. doi:10.1021/acs.jchemed.7b00361.

[239] The Ag/AgCl Reference Electrode, Res. Solut. Resour. LLC. (2014). http://www.consultrsr.net/resources/ref/agcl.htm (accessed April 8, 2018).

[240] L. Chen, Y. Tang, K. Wang, C. Liu, S. Luo, Direct electrodeposition of reduced graphene oxide on glassy carbon electrode and its electrochemical application, Electrochem. Commun. 13 (2011) 133–137. doi:10.1016/j.elecom.2010.11.033.

[241] A.J. Bard, L.R. Faulkner, N. York, C. @Bullet, W. Brisbane, S.E. Toronto, ELECTROCHEMICAL METHODS Fundamentals and Applications, 1944. doi:10.1016/B978-0-12-381373-2.00056-9.

[242] S. Treimer, A. Tanga, D. Johnson, Consideration of the Application of Koutecky-Levich Plots in the Diagnoses of Charge-Transfer Mechanisms at Rotated Disk

Electrodes, Electroanalysis. 14 (2002) 165–171.

[243] R. Zhou, Y. Zheng, M. Jaroniec, S.-Z. Qiao, Determination of the Electron Transfer Number for the Oxygen Reduction Reaction: From Theory to Experiment, ACS Catal. 6 (2016) 4720–4728. doi:10.1021/acscatal.6b01581.

[244] J. Masa, C. Batchelor-McAuley, W. Schuhmann, R.G. Compton, Koutecky-Levich analysis applied to nanoparticle modified rotating disk electrodes: Electrocatalysis or misinterpretation, Nano Res. 7 (2014) 71–78. doi:10.1007/s12274-013-0372-0.

[245] S. V. Sokolov, L. Sepunaru, R.G. Compton, Taking cues from nature: Hemoglobin catalysed oxygen reduction, Appl. Mater. Today. 7 (2017) 82–90. doi:10.1016/j.apmt.2017.01.005.

[246] J.E. Newton, J. a Preece, N. V Rees, S.L. Horswell, Nanoparticle catalysts for proton exchange membrane fuel cells: can surfactant effects be beneficial for electrocatalysis?, Phys. Chem. Chem. Phys. 16 (2014) 11435–46. doi:10.1039/c4cp00991f.

[247] K.J.J. Mayrhofer, D. Strmcnik, B.B. Blizanac, V. Stamenkovic, M. Arenz, N.M. Markovic, Measurement of oxygen reduction activities via the rotating disc electrode method: From Pt model surfaces to carbon-supported high surface area catalysts, Electrochim. Acta. 53 (2008) 3181–3188. doi:10.1016/j.electacta.2007.11.057.

[248] T. Binninger, E. Fabbri, R. Kotz, T.J. Schmidt, Determination of the Electrochemically Active Surface Area of Metal-Oxide Supported Platinum Catalyst, J. Electrochem. Soc. 161 (2013) H121–H128. doi:10.1149/2.055403jes.

[249] M. Lukaszewski, M. Soszko, A. Czerwiński, Electrochemical methods of real surface area determination of noble metal electrodes - an overview, Int. J. Electrochem. Sci. 11 (2016) 4442–4469. doi:10.20964/2016.06.71.

[250] F.P. Lohmann-Richters, B. Abel, Á. Varga, In situ determination of the electrochemically active platinum surface area: Key to improvement of solid acid fuel cells, J. Mater. Chem. A. 6 (2018) 2700–2707. doi:10.1039/c7ta10110d.

[251] W. Li, A.M. Lane, Resolving the H_{UPD} and H_{OPD} by DEMS to determine the ECSA of Pt electrodes in PEM fuel cells, Electrochem. Commun. 13 (2011) 913–916. doi:10.1016/j.elecom.2011.05.028.

[252] X. Yuan, H. Wang, J.C. Sun, J. Zhang, AC impedance technique in PEM fuel cell diagnosis — A review, Int. J. Hydrogen Energy. 32 (2007) 4365–4380. doi:10.1016/j.ijhydene.2007.05.036.

[253] R.O.S.-W. Cha, W. Colella, F.B. Prinz, Chapter 7: Fuel Cell Characterization, in: Fuel Cell Fundam., Wiley-Blackwell, 2016: pp. 237–270. doi:10.1002/9781119191766.ch7.

[254] K.R. Cooper, M. Smith, Electrical test methods for on-line fuel cell ohmic resistance measurement, J. Power Sources. 160 (2006) 1088–1095. doi:10.1016/j.jpowsour.2006.02.086.

[255] J. Zhang, H. Yang, G. Shen, P. Cheng, J. Zhang, S. Guo, Reduction of graphene oxide via L-ascorbic acid., Chem. Commun. (Camb). 46 (2010) 1112–1114. doi:10.1039/b917705a.

[256] W. Yu, W. Tu, H. Liu, Synthesis of Nanoscale Platinum Colloids by Microwave Dielectric Heating, Langmuir. 15 (1999) 6–9. doi:10.1021/la9806505.

[257] B. Fang, N.K. Chaudhari, M.-S. Kim, J.H. Kim, J.-S. Yu, Homogeneous deposition of platinum nanoparticles on carbon black for proton exchange membrane fuel cell., J. Am. Chem. Soc. 131 (2009) 15330–15338. doi:10.1021/ja905749e.

[258] Y. Garsany, I.L. Singer, K.E. Swider-Lyons, Impact of film drying procedures on RDE characterization of Pt/VC electrocatalysts, J. Electroanal. Chem. 662 (2011) 396–406. doi:10.1016/j.jelechem.2011.09.016.

[259] J. Sunarso, A. a J. Torriero, W. Zhou, P.C. Howlett, M. Forsyth, Oxygen reduction reaction activity of La-based perovskite oxides in alkaline medium: A thin-film rotating ring-disk electrode study, J. Phys. Chem. C. 116 (2012) 5827–5834. doi:10.1021/jp211946n.

[260] D. Bom, R. Andrews, D. Jacques, J. Anthony, B. Chen, M.S. Meier, J.P. Selegue, Thermogravimetric Analysis of the Oxidation of Multiwalled Carbon Nanotubes: Evidence for the Role of Defect Sites in Carbon Nanotube Chemistry, Nano Lett. 2 (2002) 615–619. doi:10.1021/nl020297u.

[261] E.F. Antunes, V.G. De Resende, U. a. Mengui, J.B.M. Cunha, E.J. Corat, M. Massi, Analyses of residual iron in carbon nanotubes produced by camphor/ferrocene pyrolysis and purified by high temperature annealing, Appl. Surf. Sci. 257 (2011) 8038–8043. doi:10.1016/j.apsusc.2011.04.090.

[262] A. Ganguly, S. Sharma, P. Papakonstantinou, J. Hamilton, Probing the Thermal Deoxygenation of Graphene Oxide using High Resolution In Situ X-Ray based Spectroscopies, J. Phys. Chem. (2011) 17009–17019. doi:10.1021/jp203741y.

[263] N. Du, M.M. Dal-Cin, G.P. Robertson, M.D. Guiver, Decarboxylation-induced cross-linking of Polymers of Intrinsic Microporosity (PIMs) for membrane gas separation, Macromolecules. 45 (2012) 5134–5139. doi:10.1021/ma300751s.

[264] J. Chen, B. Lim, E.P. Lee, Y. Xia, Shape-controlled synthesis of platinum nanocrystals for catalytic and electrocatalytic applications, Nano Today. 4 (2009) 81–95. doi:10.1016/j.nantod.2008.09.002.

[265] R. Yu, L. Chen, Q. Liu, J. Lin, K. Tan, S.C. Ng, H.S.O. Chan, G. Xu, T.S.A. Hor, Platinum Deposition on Carbon Nanotubes via Chemical Modification, Chem. Mater. 10 (1998) 718–722.

[266] E. Lebegue, S. Baranton, C. Coutanceau, Polyol synthesis of nanosized Pt/C electrocatalysts assisted by pulse microwave activation, J. Power Sources. 196 (2011) 920–927. doi:10.1016/j.jpowsour.2010.08.107.

[267] W. Li, C. Liang, W. Zhou, J. Qiu, Z. Zhou, G. Sun, Q. Xin, Preparation and Characterization of Multiwalled Carbon Nanotube-Supported Platinum for Cathode Catalysts of Direct Methanol Fuel Cells, J. Phys. Chem. B. 107 (2003) 6292–6299. doi:10.1021/jp022505c.

[268] X. Zhang, H. Li, Y. Yang, Determination of impurities in highly pure platinum by inductively coupled plasma-atomic emission spectrometry, Talanta. 42 (1995) 1959–1963. doi:10.1016/0039-9140(95)01675-9.

[269] M. Ghosh, K.K. Swain, P.S. Remya Devi, T.A. Chavan, A.K. Singh, M.K. Tiwari, R. Verma, Determination of impurities in graphite using synchrotron radiation based X-ray fluorescence spectrometry, Appl. Radiat. Isot. 128 (2017) 210–215. doi:10.1016/j.apradiso.2017.07.025.

[270] R.M. Dixit, S.S. Deshpande, An XRF Method for the Determination of Common Rare Earth Impurities in High Purity Yttrium Oxide, Fresenius Zeitschrift Fur Anal. Chemie. 288 (1977) 180–182.

[271] C. Te Hsieh, W.Y. Chen, D.Y. Tzou, A.K. Roy, H.T. Hsiao, Atomic layer deposition of Pt nanocatalysts on graphene oxide nanosheets for electro-oxidation of formic acid, Int. J. Hydrogen Energy. 37 (2012) 17837–17843. doi:10.1016/j.ijhydene.2012.08.139.

[272] F. Li, Y. Guo, T. Wu, Y. Liu, W. Wang, J. Gao, Platinum nano-catalysts deposited on reduced graphene oxides for alcohol oxidation, Electrochim. Acta. 111 (2013) 614–620. doi:10.1016/j.electacta.2013.08.058.

[273] K. Sheng, Y. Sun, C. Li, W. Yuan, G. Shi, Ultrahigh-rate supercapacitors based on eletrochemically reduced graphene oxide for ac line-filtering, Sci. Rep. 2 (2012) 3–7. doi:10.1038/srep00247.

[274] R. Nie, J. Wang, L. Wang, Y. Qin, P. Chen, Z. Hou, Platinum supported on reduced graphene oxide as a catalyst for hydrogenation of nitroarenes, Carbon,. 50 (2012) 586–596. doi:10.1016/j.carbon.2011.09.017.

[275] M. Kheirmand, A. Eshghi, Electro deposition of platinum nanoparticles on reduced graphene oxide as an efficient catalyst for oxygen reduction reaction, Iran. J. Hydrog. Fuel Cell. 1 (2015) 7–12.

[276] J.W. Ma, a Habrioux, Y. Luo, G. Ramos-Sanchez, L. Calvillo, G. Granozzi, P.B. Balbuena, N. Alonso-Vante, Electronic interaction between platinum nanoparticles and nitrogen-doped reduced graphene oxide: effect on the oxygen reduction reaction, J. Mater. Chem. A. 3 (2015) 11891–11904. doi:10.1039/c5ta01285f.

[277] M. Nesselberger, S. Ashton, J.C. Meier, I. Katsounaros, K.J.J. Mayrhofer, M. Arenz, The particle size effect on the oxygen reduction reaction activity of Pt

catalysts: influence of electrolyte and relation to single crystal models., J. Am. Chem. Soc. 133 (2011) 17428–33. doi:10.1021/ja207016u.

[278] K. Kinoshita, Particle Size Effects for Oxygen Reduction on Highly Dispersed Platinum in Acid Electrolytes, J. Electrochem. Soc. 137 (1990) 845. doi:10.1149/1.2086566.

[279] H. Yano, J. Inukai, H. Uchida, M. Watanabe, P.K. Babu, T. Kobayashi, J.H. Chung, E. Oldfield, A. Wieckowski, Particle-size effect of nanoscale platinum catalysts in oxygen reduction reaction: an electrochemical and 195Pt EC-NMR study., Phys. Chem. Chem. Phys. 8 (2006) 4932–4939. doi:10.1039/b610573d.

[280] T. Szabó, O. Berkesi, I. Dékány, DRIFT study of deuterium-exchanged graphite oxide, Carbon N. Y. 43 (2005) 3186–3189. doi:10.1016/j.carbon.2005.07.013.

[281] V. Loryuenyong, K. Totepvimarn, P. Eimburanapravat, W. Boonchompoo, A. Buasri, Preparation and characterization of reduced graphene oxide sheets via water-based exfoliation and reduction methods, Adv. Mater. Sci. Eng. 2013 (2013). doi:10.1155/2013/923403.

[282] E. Fuente, J. a. Menéndez, M. a. Díez, D. Suárez, M. a. Montes-Morán, Infrared Spectroscopy of Carbon Materials: A Quantum Chemical Study of Model Compounds, J. Phys. Chem. B. 107 (2003) 6350–6359. doi:10.1021/jp027482g.

[283] R. Blume, D. Rosenthal, J.P. Tessonnier, H. Li, A. Knop-Gericke, R. Schlögl, Characterizing Graphitic Carbon with X-ray Photoelectron Spectroscopy: A Step-by-Step Approach, ChemCatChem. 7 (2015) 2871–2881. doi:10.1002/cctc.201500344.

[284] K.G. Neoh, E.T. Kang, K.L. Tan, Limitations of the X-ray Photoelectron Spectroscopy Technique in the Study of Electroactive Polymers, J. Phys. Chem. B. 101 (1997) 726–731. doi:10.1021/jp962497y.

[285] Y.S. Kim, J. Shin, J.H. Cho, G.A. Ten Eyck, D.L. Liu, S. Pimanpang, T.M. Lu, J.J. Senkevich, H.S. Shin, Surface characterization of copper electroless deposition on atomic layer deposited palladium on iridium and tungsten, Surf. Coatings Technol. 200 (2006) 5760–5766. doi:10.1016/j.surfcoat.2005.08.142.

[286] A. Bagri, C. Mattevi, M. Acik, Y.J. Chabal, M. Chhowalla, V.B. Shenoy, Structural evolution during the reduction of chemically derived graphene oxide., Nat. Chem. 2 (2010) 581–587. doi:10.1038/nchem.686.

[287] T. Szab, O. Berkesi, P. Forg, K. Josepovits, Y. Sanakis, D. Petridis, I. Dkny, Evolution of Surface Functional Groups in a Series of Progressively Oxidized Graphite Oxides Evolution of Surface Functional Groups in a Series of Progressively Oxidized Graphite Oxides, Chem. Mater. 18 (2006) 2740–2749. doi:10.1021/cm060258.

[288] S. Li, E.T. Kang, K.G. Neoh, Z.H. Ma, K.L. Tan, W. Huang, In situ XPS studies of thermally deposited potassium on poly(p-phenylene vinylene) and its ring-substituted derivatives, Appl. Surf. Sci. 181 (2001) 201–210. doi:10.1016/S0169-

4332(01)00397-X.

[289] Z. Li, Q. Gao, H. Zhang, W. Tian, Y. Tan, W. Qian, Z. Liu, Low content Pt nanoparticles anchored on N-doped reduced graphene oxide with high and stable electrocatalytic activity for oxygen reduction reaction, Sci. Rep. 7 (2017) 1–9. doi:10.1038/srep43352.

[290] C.F. Zinola, A.M. Castro Luna, W.E. Triaca, A.J. Arvia, Kinetics and mechanism of the electrochemical reduction of molecular oxygen on platinum in KOH: influence of preferred crystallographic orientation, J. Appl. Electrochem. 24 (1994) 531–541. doi:10.1007/BF00249854.

[291] Y. Li, W. Zhou, H. Wang, L. Xie, Y. Liang, F. Wei, J. Idrobo, S.J. Pennycook, H. Dai, An oxygen reduction electrocatalyst based on carbon nanotube-graphene complexes, Nat. Nanotechnol. 7 (2012) 394–400. doi:10.1038/nnano.2012.72.

[292] P. Gayathri, A. Senthil, An Iron Impurity in Multiwalled Carbon Nanotube Complexes with Chitosan that Biomimics the Heme-Peroxidase Function, Chem. - A Eur. J. 19 (2013) 17103–17112. doi:10.1002/chem.201303075.

[293] V.A. Online, M. Pumera, E. Lay, K. Chng, H.L. Poh, Purification of carbon nanotubes by high temperature chlorine gas treatment, Phys. Chem. Chem. Phys. 15 (2013) 5615–5619. doi:10.1039/c3cp50348h.

[294] K.M. Samant, V.S. Joshi, K.R. Patil, Role of iron oxide impurities in electrocatalysis by multiwall carbon nanotubes : An investigation using a novel magnetically modified ITO, Bull. Mater. Sci. 37 (2014) 221–226. doi:10.1007/s12034-014-0658-1.

[295] T. Kolodiazhnyi, M. Pumera, Impurities in carbon nanotubes Towards an Ultrasensitive Method for the Determination of Metal Impurities in Carbon Nanotubes, Small. 4 (2008) 1476–1484. doi:10.1002/smll.200800125.

[296] J. Kruusma, N. Mould, K. Jurkschat, A. Crossley, C.E. Banks, Single walled carbon nanotubes contain residual iron oxide impurities which can dominate their electrochemical activity, Electrochem. Commun. 9 (2007) 2330–2333. doi:10.1016/j.elecom.2007.06.024.

[297] L. Wang, M. Pumera, Residual metallic impurities within carbon nanotubes play a dominant role in supposedly "'metal-free'" oxygen reduction reactions, Chem. Commun. 50 (2014) 12662–12664. doi:10.1039/C4CC03271C.

[298] G. Ju, K. Tammeveski, Electroreduction of oxygen on multi-walled carbon nanotubes modified highly oriented pyrolytic graphite electrodes in alkaline solution, J. Electroanal. Chem. 597 (2006) 119–126. doi:10.1016/j.jelechem.2006.09.002.

[299] S.K. Bikkarolla, P. Cumpson, P. Joseph, P. Papakonstantinou, Oxygen reduction reaction by electrochemically reduced graphene oxide, Faraday Discuss. 173 (2014) 415–428. doi:10.1039/c4fd00088a.

[300] C. Song, J. Zhang, Electrocatalytic Oxygen Reduction Reaction, PEM Feul Cell Electrocatal. Catal. Layers. Fundam. Appl. (2008) 89–134. doi:10.1007/978-1-84800-936-3.

[301] A. Alazmi, S. Rasul, S.P. Patole, P.M.F.J. Costa, Comparative study of synthesis and reduction methods for graphene oxide, Polyhedron. 116 (2016) 153–161. doi:10.1016/j.poly.2016.04.044.

[302] W.W. Wang, J.S. Dang, X. Zhao, S. Nagase, Formation Mechanisms of Graphitic-N: Oxygen Reduction and Nitrogen Doping of Graphene Oxides, J. Phys. Chem. C. 120 (2016) 5673–5681. doi:10.1021/acs.jpcc.5b10607.

[303] S. Kumar, S. Gonen, A. Friedman, L. Elbaz, G.D. Nessim, Doping and reduction of graphene oxide using chitosan-derived volatile N-heterocyclic compounds for metal-free oxygen reduction reaction, Carbon,. 120 (2017) 419–426. doi:10.1016/j.carbon.2017.05.071.

[304] S.Y. Huang, B. Zhao, K. Zhang, M.M.F. Yuen, J. Bin Xu, X.Z. Fu, R. Sun, C.P. Wong, Enhanced Reduction of Graphene Oxide on Recyclable Cu Foils to Fabricate Graphene Films with Superior Thermal Conductivity, Sci. Rep. 5 (2015) 1–11. doi:10.1038/srep14260.

[305] L. David, G. Singh, Reduced graphene oxide paper electrode: Opposing effect of thermal annealing on Li and Na cyclability, J. Phys. Chem. C. 118 (2014) 28401–28408. doi:10.1021/jp5080847.

[306] J.P. Paraknowitsch, A. Thomas, Doping carbons beyond nitrogen: an overview of advanced heteroatom doped carbons with boron, sulphur and phosphorus for energy applications, Energy Environ. Sci. 6 (2013) 2839. doi:10.1039/c3ee41444b.

[307] M.A. Hoque, F.M. Hassan, M.H. Seo, J.Y. Choi, M. Pritzker, S. Knights, S. Ye, Z. Chen, Optimization of sulfur-doped graphene as an emerging platinum nanowires support for oxygen reduction reaction, Nano Energy. 19 (2016) 27–38. doi:10.1016/j.nanoen.2015.11.004.

[308] Y. Li, J. Yang, J. Huang, Y. Zhou, K. Xu, N. Zhao, X. Cheng, Soft template-assisted method for synthesis of nitrogen and sulfur co-doped three-dimensional reduced graphene oxide as an efficient metal free catalyst for oxygen reduction reaction, Carbon,. 122 (2017) 237–246. doi:10.1016/j.carbon.2017.06.046.

[309] A.S. Al-Sherbini, M. Bakr, I. Ghoneim, M. Saad, Exfoliation of graphene sheets via high energy wet milling of graphite in 2-ethylhexanol and kerosene, J. Adv. Res. 8 (2017) 209–215. doi:10.1016/j.jare.2017.01.004.

[310] A.C. Ferrari, J. Robertson, Interpretation of Raman spectra of disordered and amorphous carbon, Phys. Rev. B. 61 (2000) 14095–14107. doi:10.1103/PhysRevB.61.14095.

[311] Y. Li, J. Yang, N. Zhao, J. Huang, Y. Zhou, K. Xu, N. Zhao, Facile fabrication of N-doped three-dimensional reduced graphene oxide as a superior

electrocatalyst for oxygen reduction reaction, Appl. Catal. A Gen. 534 (2017) 30–39. doi:10.1016/j.apcata.2017.01.014.

[312] P. Mallet-Ladeira, P. Puech, C. Toulouse, M. Cazayous, N. Ratel-Ramond, P. Weisbecker, G.L. Vignoles, M. Monthioux, A Raman study to obtain crystallite size of carbon materials: A better alternative to the Tuinstra-Koenig law, Carbon,. 80 (2014) 629–639. doi:10.1016/j.carbon.2014.09.006.

[313] Z. Jiang, X. Zhao, X. Tian, L. Luo, J. Fang, H. Gao, Z.J. Jiang, Hydrothermal Synthesis of Boron and Nitrogen Codoped Hollow Graphene Microspheres with Enhanced Electrocatalytic Activity for Oxygen Reduction Reaction, ACS Appl. Mater. Interfaces. 7 (2015) 19398–19407. doi:10.1021/acsami.5b05585.

[314] G.-L. Chai, K. Qiu, M. Qiao, M.-M. Titirici, C. Shang, Z. Guo, Active sites engineering leads to exceptional ORR and OER bifunctionality in P,N Co-doped graphene frameworks, Energy Environ. Sci. 10 (2017) 1186–1195. doi:10.1039/C6EE03446B.

[315] C.H. Choi, S.H. Park, S.I. Woo, Binary and ternary doping of nitrogen, boron, and phosphorus into carbon for enhancing electrochemical oxygen reduction activity, ACS Nano. 6 (2012) 7084–7091. doi:10.1021/nn3021234.

[316] M. Chisaka, T. Iijima, Y. Ishihara, Y. Suzuki, R. Inada, Y. Sakurai, Carbon catalyst codoped with boron and nitrogen for oxygen reduction reaction in acid media, Electrochim. Acta. 85 (2012) 399–410. doi:10.1016/j.electacta.2012.07.131.

[317] L. Sun, L. Wang, C. Tian, T. Tan, Y. Xie, K. Shi, M. Li, H. Fu, Nitrogen-doped graphene with high nitrogen level via a one-step hydrothermal reaction of graphene oxide with urea for superior capacitive energy storage, RSC Adv. 2 (2012) 4498–4506. doi:10.1039/c2ra01367c.

[318] S. Zhao, J. Liu, C. Li, W. Ji, M. Yang, H. Huang, Y. Liu, Z. Kang, Tunable Ternary (N , P , B) -Doped Porous Nanocarbons and Their Catalytic Properties for Oxygen Reduction Reaction, ACS Appl. Mater. Interfaces. 6 (2014) 22297–22304.

[319] C. Liang, Z. Li, S. Dai, Mesoporous carbon materials: Synthesis and modification, Angew. Chemie - Int. Ed. 47 (2008) 3696–3717. doi:10.1002/anie.200702046.

[320] L.A. Hutton, G.D. O'Neil, T.L. Read, Z.J. Ayres, M.E. Newton, J. V. MacPherson, Electrochemical X-ray fluorescence spectroscopy for trace heavy metal analysis: Enhancing X-ray fluorescence detection capabilities by four orders of magnitude, Anal. Chem. 86 (2014) 4566–4572. doi:10.1021/ac500608d.

[321] L. Tang, X. Li, R. Ji, K.S. Teng, G. Tai, J. Ye, C. Wei, S.P. Lau, Bottom-up synthesis of large-scale graphene oxide nanosheets, J. Mater. Chem. 22 (2012) 5676. doi:10.1039/c2jm15944a.

[322] M.H. Al-Abboodi, F.N. Ajeel, A.M. Khudhair, Influence of oxygen impurities on

the electronic properties of graphene nanoflakes, Phys. E Low-Dimensional Syst. Nanostructures. 88 (2017) 1–5. doi:10.1016/j.physe.2016.11.023.

[323] L. Wang, A. Ambrosi, M. Pumera, “Metal-free” catalytic oxygen reduction reaction on heteroatom-doped graphene is caused by trace metal impurities, Angew. Chemie - Int. Ed. 52 (2013) 13818–13821. doi:10.1002/anie.201309171.

[324] A. Heinzel, V.M. Barragán, A review of the state-of-the-art of the methanol crossover in direct methanol fuel cells, J. Power Sources. 84 (1999) 70–74. doi:10.1016/S0378-7753(99)00302-X.

[325] K. Scott, W.M. Taama, P. Argyropoulos, K. Sundmacher, The impact of mass transport and methanol crossover on the direct methanol fuel cell, J. Power Sources. 83 (1999) 204–216. doi:10.1016/S0378-7753(99)00303-1.

[326] D.Y. Chung, H. Kim, Y.-H. Chung, M.J. Lee, S.J. Yoo, A.D. Bokare, W. Choi, Y.-E. Sung, Inhibition of CO poisoning on Pt catalyst coupled with the reduction of toxic hexavalent chromium in a dual-functional fuel cell, Sci. Rep. 4 (2014) 7450. doi:10.1038/srep07450.

[327] Y. Lu, L. Wang, K. Preuß, M. Qiao, M.M. Titirici, J. Varcoe, Q. Cai, Halloysite-derived nitrogen doped carbon electrocatalysts for anion exchange membrane fuel cells, J. Power Sources. 372 (2017) 82–90. doi:10.1016/j.jpowsour.2017.10.037.

[328] J.-S. Li, S.-L. Li, Y.-J. Tang, K. Li, L. Zhou, N. Kong, Y.-Q. Lan, J.-C. Bao, Z.-H. Dai, Heteroatoms ternary-doped porous carbons derived from MOFs as metal-free electrocatalysts for oxygen reduction reaction, Sci. Rep. 4 (2015) 5130. doi:10.1038/srep05130.

[329] C.H. Choi, M.W. Chung, S.H. Park, S.I. Woo, Additional doping of phosphorus and/or sulfur into nitrogen-doped carbon for efficient oxygen reduction reaction in acidic media, Phys. Chem. Chem. Phys. 15 (2013) 1802–1805. doi:10.1039/C2CP44147K.

[330] J. Liu, X. Sun, P. Song, Y. Zhang, W. Xing, W. Xu, High-Performance Oxygen Reduction Electrocatalysts based on Cheap Carbon Black, Nitrogen, and Trace Iron, Adv. Mater. 25 (2013) 6879–6883. doi:10.1002/adma.201302786.

[331] K.A. Stoerzinger, M. Risch, B. Han, Y. Shao-Horn, Recent Insights into Manganese Oxides in Catalyzing Oxygen Reduction Kinetics, ACS Catal. 5 (2015) 6021–6031. doi:10.1021/acscatal.5b01444.

[332] K.L. Hsueh, D.T. Chin, S. Srinivasan, Electrode kinetics of oxygen reduction. A theoretical and experimental analysis of the rotating ring-disk electrode method, J. Electroanal. Chem. Interfacial Electrochem. 153 (1983) 79–95. doi:10.1016/0368-1874(83)80358-x.

[333] N.A. Anastasijević, Z.M. Dimitrijević, R.R. Adžić, Oxygen reduction on a ruthenium electrode in acid electrolytes, Electrochim. Acta. 31 (1986) 1125–1130. doi:10.1016/0013-4686(86)80124-4.

[334] L. Vicarelli, S.J. Heerema, C. Dekker, H.W. Zandbergen, Controlling defects in graphene for optimizing the electrical properties of graphene nanodevices, ACS Nano. 9 (2015) 3428–3435. doi:10.1021/acsnano.5b01762.

[335] R. Beams, L.G. Canç Ado, L. Novotny, Raman characterization of defects and dopants in graphene, J. Phys. Condens. Matter. 27 (2015) 83002. doi:10.1088/0953-8984/27/8/083002.

[336] E. Fabbri, M. Nachtegaal, X. Cheng, T.J. Schmidt, Superior Bifunctional Electrocatalytic Activity of Insight into the Local Electronic Structure, Adv. Energy Mater. 5 (2015) 1–5. doi:10.1002/aenm.201402033.

[337] W.G. Hardin, J.T. Mefford, D.A. Slanac, B.B. Patel, X. Wang, S. Dai, X. Zhao, R.S. Ruoff, K.P. Johnston, K.J. Stevenson, Tuning the electrocatalytic activity of perovskites through active site variation and support interactions, Chem. Mater. 26 (2014) 3368–3376. doi:10.1021/cm403785q.

[338] L. Dai, M. Liu, Y. Song, J. Liu, F. Wang, Mn3O4-decorated Co3O4 nanoparticles supported on graphene oxide: Dual electrocatalyst system for oxygen reduction reaction in alkaline medium, Nano Energy. 27 (2016) 185–195. doi:10.1016/j.nanoen.2016.07.007.

[339] Z. Yang, X. Zhou, H. Nie, Z. Yao, S. Huang, Facile construction of manganese oxide doped carbon nanotube catalysts with high activity for oxygen reduction reaction and investigations into the origin of their activity enhancement, ACS Appl. Mater. Interfaces. 3 (2011) 2601–2606. doi:10.1021/am200426q.

[340] X. Li, Y. Fang, X. Lin, M. Tian, X. An, Y. Fu, R. Li, J. Jin, J. Ma, MOF derived Co_3O_4 nanoparticles embedded in N-doped mesoporous carbon layer/MWCNT hybrids: extraordinary bi-functional electrocatalysts for OER and ORR, J. Mater. Chem. A. 3 (2015) 17392–17402. doi:10.1039/C5TA03900B.

[341] M.R. Gao, X. Cao, Q. Gao, Y.F. Xu, Y.R. Zheng, J. Jiang, S.H. Yu, Nitrogen-doped graphene supported $CoSe_2$ nanobelt composite catalyst for efficient water oxidation, ACS Nano. 8 (2014) 3970–3978. doi:10.1021/nn500880v.

[342] N.R. Elezović, B.M. Babić, V.R. Radmilović, S.L. Gojković, N. V. Krstajić, L.M. Vračar, Pt/C doped by MoOx as the electrocatalyst for oxygen reduction and methanol oxidation, J. Power Sources. 175 (2008) 250–255. doi:10.1016/j.jpowsour.2007.09.011.

[343] J. Shim, C.-R. Lee, H.-K. Lee, J.-S. Lee, E.J. Cairns, Electrochemical characteristics of Pt–WO_3/C and Pt–TiO_2/C electrocatalysts in a polymer electrolyte fuel cell, J. Power Sources. 102 (2001) 172–177.

[344] Z. Awaludin, M. Suzuki, J. Masud, T. Okajima, T. Ohsaka, Enhanced electrocatalysis of oxygen reduction on Pt/TaO_x/GC, J. Phys. Chem. C. 115 (2011) 25557–25567. doi:10.1021/jp209347r.

[345] Y. Zhu, C. Su, X. Xu, W. Zhou, R. Ran, Z. Shao, A universal and facile way for the development of superior bifunctional electrocatalysts for oxygen reduction

and evolution reactions utilizing the synergistic effect, Chem. - A Eur. J. 20 (2014) 13533–13542. doi:10.1002/chem.201403192.

[346] G.L. Luque, N.F. Ferreyra, A.G. Leyva, G.A. Rivas, Characterization of carbon paste electrodes modified with manganese based perovskites-type oxides from the amperometric determination of hydrogen peroxide, Sensors Actuators, B Chem. 142 (2009) 331–336. doi:10.1016/j.snb.2009.07.038.

[347] J. Kim, X. Yin, K.C. Tsao, S. Fang, H. Yang, $Ca_2Mn_2O_5$ as Oxygen-Deficient Perovskite Electrocatalyst for Oxygen Evolution Reaction, J. Am. Chem. Soc. 136 (2014) 14646–14649. doi:10.1021/ja506254g.

[348] J. Du, T. Zhang, F. Cheng, W. Chu, Z. Wu, J. Chen, Nonstoichiometric perovskite $CaMnO_{3-\delta}$ for oxygen electrocatalysis with high activity, Inorg. Chem. 53 (2014) 9106–9114. doi:10.1021/ic501631h.

[349] C.F. Chen, G. King, R.M. Dickerson, P.A. Papin, S. Gupta, W.R. Kellogg, G. Wu, Oxygen-deficient $BaTiO_{3-x}$ perovskite as an efficient bifunctional oxygen electrocatalyst, Nano Energy. 13 (2015) 423–432. doi:10.1016/j.nanoen.2015.03.005.

[350] A.M. Duprat, P. Alphonse, Nonstoichiometry-activity relationship in perovskite-like manganites, Mater. Chem. Phys. 37 (1994) 76–81. doi:10.1016/0254-0584(94)90074-4.

[351] L. Li, X. Feng, Y. Nie, S. Chen, F. Shi, K. Xiong, W. Ding, X. Qi, J. Hu, Z. Wei, L.-J. Wan, M. Xia, Insight into the Effect of Oxygen Vacancy Concentration on the Catalytic Performance of MnO_2, ACS Catal. 5 (2015) 4825–4832. doi:10.1021/acscatal.5b00320.

[352] A.B. Laursen, I.C. Man, O.L. Trinhammer, J. Rossmeisl, S. Dahl, The Sabatier principle illustrated by catalytic H_2O_2 decomposition on metal surfaces, J. Chem. Educ. 88 (2011) 1711–1715. doi:10.1021/ed101010x.

[353] Y. Matsumoto, H. Yoneyama, H. Tamura, Catalytic activity for electrochemical reduction of oxygen of lanthanum nickel oxide and related oxides, J. Electroanal. Chem. 79 (1977) 319–326. doi:10.1016/S0022-0728(77)80453-1.

[354] O. Haas, F. Holzer, S. Müller, J.M. McBreen, X.Q. Yang, X. Sun, M. Balasubramanian, X-ray absorption and diffraction studies of $La_{0.6}Ca_{0.4}CoO_3$ perovskite, a catalyst for bifunctional oxygen electrodes, Electrochim. Acta. 47 (2002) 3211–3217. doi:10.1016/S0013-4686(02)00241-4.

[355] V. Celorrio, D. Tiwari, D.J. Fermin, Composition-Dependent Reactivity of $Ba_{0.5}Sr_{0.5}Co_xFe_{1-x}O_{3-\delta}$ toward the Oxygen Reduction Reaction, J. Phys. Chem. C. 120 (2016) 22291–22297. doi:10.1021/acs.jpcc.6b04781.

[356] D.N. Pei, L. Gong, A.Y. Zhang, X. Zhang, J.J. Chen, Y. Mu, H.Q. Yu, Defective titanium dioxide single crystals exposed by high-energy {001} facets for efficient oxygen reduction, Nat. Commun. 6 (2015) 1–10. doi:10.1038/ncomms9696.